Nanoparticle Encapsulation and Aggregation Control for Anti-reflection Coatings and Organic Photovoltaics

Jonathan S. Metzman

Dissertation submitted to the faculty of the Virginia Polytechnic Institute and State University in partial fulfillment of the requirements for the degree of

Doctor of Philosophy

In

Materials Science & Engineering

James R. Heflin, Committee Chair

Richey M. Davis

Guo-Quan Lu

Gary R. Pickrell

September 10th, 2018

Blacksburg, VA

Keywords: Anti-reflection coatings, Organic photovoltaics, Ionic Self-Assembled Multilayers, Nanoparticles, Polymers, Nanocomposites, Stability, Plasmonics

Nanoparticle Encapsulation and Aggregation Control for Anti-reflection Coatings and Organic Photovoltaics

Jonathan S. Metzman

Abstract

Nanoparticles present a myriad of physical, optical, electrical, and chemical properties that provide valuable functionality to thin-film technologies. In order to successfully exploit these aspects of nanoparticles, appropriate dispersion and stability measures must be implemented. In this dissertation, different types of nanoparticles are coated with polymer and metallic layers to enable their effectiveness in both anti-reflection coatings (ARCs) and organic photovoltaics (OPVs).

Ionic self-assembled multilayers (ISAMs) fabrication of poly(allylamine hydrochloride) (PAH) and silica nanoparticles (SiO_2 NPs) results in highly-transparent, porous ARCs. However, the ionic bonding and low contact area between the film constituents lack sufficient mechanical and chemical stability necessary for commercial application. Chemical stability was established in the film by the encapsulation of SiO_2 NPs by a photo-crosslinkable polyelectrolyte, diazo-resin (DAR) to make modified silica nanoparticles (MSNPs). UV-irradiation induced decomposition of the diazonium group and the development of covalent bonds with polyanions. Crosslinked MSNP/poly(styrene sulfonate) (PSS) ISAMs exhibited excellent anti-reflectivity (transmittance >98%, reflectance <0.2% in the visible range) and chemical stability against dissolution in a ternary solvent. Mechanical stability was also achieved by the incorporation of two additional PAH and poly(acrylic acid) (PAA) layers to create PAH/PAA/PAH/SiO_2 NP interlayer ISAM ARCs. Thermal crosslinking of PAH and PAA facilitates the formation of covalent amide bonds between the two polyelectrolytes, as confirmed by FTIR. Since PAH and PAA are both weak polyelectrolytes, adjustment of the solution pH causes significant variations in the polymer chain charge densities. At low PAA pH, the decreased chain charge densities caused large SiO_2 NP encapsulation thicknesses in the film with great mechanical stability, but poor anti-reflection

(≤97% transmittance). At high PAA pH, the high chain charge densities induced thin encapsulation layers, insufficient mechanical stability, but excellent anti-reflection. At trade-off between the two extremes was founded at a PAA pH of 5.2 with excellent anti-reflection (≥99% transmittance) and sufficient mechanical stability. The normal force required for scratch initiation was increased by a factor of seven for films made from a pH of 5.2 compared to those made from a pH of 6.0.

Organic photovoltaics (OPVs) are an attractive area of solar cell research due to their inexpensive nature, ease of large-scale fabrication, flexibility, and low-weight. The introduction of the bulk heterojunction greatly improved charge transport and OPV performance by the blending of the active layer electron donor and acceptor materials, poly(3-hexylthiophene) (P3HT) and [6,6]-phenyl-C61-butyric acid methyl ester (PCBM), into an interpenetrating network with high interfacial area between adjacent nanodomains. However, constrained active layer thicknesses restrict the total optical absorption and device performance. The localized surface plasmon resonance (LSPR) of plasmonic nanoparticles, such as anisotropic silver nanoplates (AgNPs), provides large local field enhancements and in coupling with the active layer, substantial optical absorption improvements can be realized. AgNPs were first integrated into the hole-transport layer (PEDOT:PSS) by ISAM deposition. Here, PEDOT:PSS was used as a negatively-charged ISAM layer. Encapsulation of the AgNPs by PAH (ENPs) provided a positive surface charge and allowed for the creation of ENP/PEDOT:PSS ISAMs. Stability against acidic etching by PEDOT:PSS was imparted to the AgNPs by coating the edges with gold (AuAgNPs). The AuAgNP ISAMs substantially improved the optical absorption, but were ineffective at increasing the device performance. The dispersion effects of functionalized polymer coatings on AgNPs were also deeply investigated. Functionalized AgNPs were dispersed in methanol and spin-coated onto the active layer. When the AgNPs possessed hydrophilic properties, such as unfunctionalized or functionalized by poly(ethylene glycol) methyl ether thiol (PEG-SH), they formed large aggregates due to unfavorable interactions with the hydrophobic P3HT:PCBM layer. However, the hydrophobic functionalization of AgNPs with thiol-terminated polystyrene (PS-SH) (PS-AgNPs) resulted in excellent dispersion, optical absorption enhancements, and device performance improvements. At a PS-AgNP concentration of 0.57 nM, the device efficiency was increased by 32% over the reference devices.

Nanoparticle Encapsulation and Aggregation Control for Improved Stability and Performance in Anti-reflection Coatings and Organic Photovoltaics

Jonathan S. Metzman

General Audience Abstract

Investigations are presented on the quality of distribution or dispersion of functional inorganic (composed of silicon dioxide or silver) particles that have dimensions of less than 100 nanometers, called nanoparticles. The nanoparticle surfaces were covered with polymer layers, where polymers are organic materials with repeating molecular structures.

The study of these nanoparticle distribution effects were first examined in anti-reflection coatings (ARCs). ARCs induce transparency of windows or glasses through a reduction in the reflection of light. Here, the ARCs were fabricated as self-assembled thin-films (films with thicknesses ranging from 1 to 2000 nanometers). The self-assembly process here was carried out by immersing a charged substrate (microscope slide) into a solution with an oppositely-charged material. The attraction of the material to the substrate leads to thin-film growth. The process can continue by sequentially immersing the thin-film into oppositely-charged solutions for a desired number of thin-film layers. This technique is called ionic self-assembled multilayers (ISAMs). ARCs created by ISAM with charged polymers (polyelectrolytes) and silicon dioxide nanoparticles (SiO_2 NPs) can lead to highly-transparent films, but unfortunately, they lack the stability and scratch-resistance necessary for commercial applications.

In this dissertation, we address the lack of stability in the ISAM ARCs by adding additional polyelectrolyte layers that can develop strong, covalent bonds, while also examining nanoparticle dispersive properties. First, SiO_2 NP surfaces were coated in solution with a polyelectrolyte called diazo-resin, which can form covalent bonds by UV-light exposure of the film. After tuning the concentration for the added diazo-resin, the coated SiO_2 NPs were used to make ARCs ISAM films. The ARCs had excellent nanoparticle dispersion, high levels of transparency, and chemical stability. Chemically stability entails that the integrity of the film was unaffected by exposure to polar organic solvents or strong polyelectrolytes. In a second method, two additional

polyelectrolyte layers were added into the original polyelectrolyte/SiO_2 NP design. Here, heating of the film to 200 ^oC temperatures induced strong covalent bonding between the polyelectrolytes. Variation of the solution pH dramatically changed the polyelectrolyte thickness, the nanoparticle dispersion, the scratch-resistance, and the anti-reflection. An optimum trade-off was discovered at a pH of 5.2, where the anti-reflection was excellent (amount of transmitted light over 99%), along with a substantially improved scratch-resistance. A change of pH from 6.0 (highest tested pH) to 5.2 (optimal) caused a difference in the scratch-resistance by a factor of seven. In these findings, we introduce stability enhancing properties from films composed purely of polyelectrolytes into nanoparticle-containing ISAM films. We also show that a simple adjustment of solution parameters, such as the pH value, can cause substantial differences in the film properties.

Nanoparticle dispersion properties were next investigated in organic photovoltaics (OPVs) OPVs use semiconducting polymers to convert sunlight into usable electricity. They have many advantages over traditional solar cells, including their simple processing, low-cost, flexibility, and lightweight. However, OPVs are limited by their total optical absorption or the amount of light that can potentially be converted to electricity. The addition of plasmonic nanoparticles into an OPV device is a suitable way to increase optical absorption without changing the other device properties. Plasmonic nanoparticles, which are composed of noble metals (such as silver or gold), act as "light antennas" that concentrate incoming light and radiate it around the particle. In this dissertation, we investigate the dispersion and stability effects of polymer or metallic layers on silver nanoplates (AgNPs). The stability of the AgNPs was found to be greatly enhanced by coating the nanoparticle edges with a thin gold layer (AuAgNPs). AuAgNPs could then be introduced into a conductive, acidic layer of the OPVs (PEDOT:PSS) to increase the overall light absorption, which otherwise would be impossible with uncoated AgNPs. Next, the AgNPs were distributed on top of the photoactive layer or the layer that is responsible for absorbing light. Coating the AgNPs with a polystyrene polymer layer (PS-AgNPs) allowed for excellent dispersion on this layer and contrastingly, dispersion of the uncoated AgNPs was poor. An increased amount PS-AgNPs added on top of the photoactive layer progressively increased the optical absorption of the OPV devices. However, trends were quite different for the power conversion efficiency or the ratio of electricity power to sunlight power in the OPV device. The greatest PCE enhancements (27 – 32%) were found at a relatively low coverage level (using a solution concentration of 0.29 to 0.57 nM) of the PS-AgNPs on the photoactive layer.

This dissertation is dedicated to my family, Eric, Helen, and Elana.

Thank you for your patience, love, and support.

Acknowledgements

This research and writing of this dissertation was only possible with the gracious support from the many people who provided me assistance along the way. I would not be where I am today without the people included below.

First, I would like to express my utmost gratitude to my advisor Dr. Randy Heflin who allowed me to join his group and introduced me to this field of scientific research. He provided me the opportunity, the resources, and the generous lab space to work on two exciting projects, as well as the ample freedom to explore new ideas within my research. Because of his vast knowledge and intuition from years of experience in the field, he was always quick to voice an excellent solution or a plan to nearly any problem we faced. He was also an influential teacher, and I have gained a tremendous amount from working under him.

I am also very grateful to have worked closely with Dr. Guoliang (Greg) Liu who was my primary research collaboration advisor on all of the work related to silver nanoplates in organic photovoltaics. Dr. Liu allowed me to spend a significant amount of time working in his lab and using his resources to synthesize inorganic nanoparticles. He helped me understand a substantial amount about experimental chemistry. He also spent many hours meeting with me to review results and the publication. I am grateful for his providing of extra excitement and motivation for the research.

Assad Khan in Dr. Liu's group assisted me tremendously with the synthesis of silver nanoplates and their incorporation into organic photovoltaics. He contributed significantly to the project and was always open for discussion. He also provided a substantial amount of help with TEM and SEM characterization.

I am also highly appreciative of all my other collaborators who assisted in critical measurements throughout my research including Dr. John Morris, Guanyu Wang, Brenden Magill, and Dr. Giti Khodaparast.

Next, I would like to acknowledge Jason Ridley and Manpreet Kaur from Dr. Heflin's group who prepared me to do experimental work with anti-reflection coatings and organic photovoltaics, respectively. Their training brought me up to speed on the instrumentation and protocols, which I am very appreciative of.

I would also like to thank everyone else from Dr. Heflin's group who I worked with and interacted with over the years, including Chalongrat Daengngam, Moataz Khalifa, Jeong-Ah Lee, Yanlong Li, Kelly McCutcheon, Reza Montazami, Shane Seaman, Dong Wang, and Ziwei Zuo. The members of the group provided assistance and moral support, as well as fostered a productive environment for research.

The Materials Science and Engineering faculty and staff did a remarkable job at supporting and assisting my development as a Ph.D. student. Kim Grandstaff was above and beyond what anyone could expect from a student advisor. She provided an incredible amount of support for all my exams, in terms of technicalities, scheduling, and morale. Her benevolence and selflessness was extraordinary when times were tough and stressful. I would like to express my sincerest gratitude to Dr. David Clark and Dr. Bill Reynolds for providing a substantial amount of financial assistance to me, which kept our project moving forward.

I am also very grateful for my excellent graduate committee members, including Dr. Richey M. Davis, Dr. Guo-Quan Lu, Dr. Gary R. Pickrell. I learned an immense amount from their discussions. They adequately challenged me during my committee meetings, which helped me grow as a scientist and also a person.

Throughout my time as a Ph.D. student, I also received a significant amount of instrumentation assistance from those listed below, which I am extremely grateful for.

Eric Carlson, Don Leber, and Michael Bouchard (from Ladd Research) all spent a substantial amount of time helping me fix and troubleshoot our thermal evaporator. In their assistance, they also supplied me with a great deal of knowledge about the technical aspects of the systems, which I will surely use in the future. Eric and Don also assisted me with using the E-beam evaporator in the Whittemore Hall cleanroom, and I am very grateful for that experience.

Steve McCartney and Chris Winkler both provided an immense amount of assistance in the NCFL on the AFM, SEM, and TEM. Jacob Noble (from Hysitron) and Jay Tuggle helped me with using and interpreting data from the Hysitron TriboIndenter. I am thankful for their support.

I would also like to thank Neha Singh from J.A. Woollam Co. for essentially training me over the phone on the Ellipsometer. Nina Hong, also from J.A. Woollam Co., gave me much assistance on the instrument in-person.

I am very thankful that Erich Seeh assisted me in depositing gold for FTIR measurements. Also, I am very appreciative that Min Gao and Dr. Dwight D. Viehland allowed me to use their AFM. I

would like to express my gratitude to Hadi Mohammadi and Dr. Herve Marand for giving me access and assistance to their BYK Gardner Hazer Meter. I am highly grateful that Dr. Hans Robinson allowed me to use his motorized translational stage for macroscopic scratch testing. I thank Tom Wertalik for cutting all of the ITO substrates over the years for use in the organic photovoltaic project.

I would like to give a special thanks to Sherri Collins, Michele Strauss, Tammy Jo Hiner, and Mary Jane Smith for assistance with ordering laboratory supplies and with Hokiemart. Finally, I would like to acknowledge the Army Research Lab for their funding support on the anti-reflection coatings, under Cooperative Agreement Number W911NF-06-2-0014.

I would like to personally thank Alyssa Johnson for all of her laboratory assistance and her love for bean salad and tacos. Her optimism and support was massive.

I am so appreciative of all my friends in Blacksburg and ~40 roommates that came and went in my house throughout the years. It won't be easy leaving this cozy, happy town tucked away in the mountains of Southwest Virginia after being here for 13 years.

Perhaps most importantly, I would like to thank my loving parents, Eric and Helen, as well as my amazing sister, Elana. Without my family's kindness, unconditional love, and care, I would have never come this far. My parents emphasized the importance of perseverance and hard work, which has become one of my greatest strengths to this day. They helped me build a positive attitude and conscience. They facilitated my interest in science at a very young age, with discussions at the dinner table and suggesting that I investigate the thinning of the ozone layer in middle school. I dedicate my initial interest in photovoltaics to my mother, who helped me with my eight grade science project, where I measured the current from a silicon solar cell under different colored lights. I am also extremely grateful for their financial support growing up and in times of need. I thank my sister for being my best friend for life, putting up with me while we grew up, and also always being there for me. Her freedom with life and exploration has inspired me. I hope that I can return my family's love back to them in the coming years, now that I won't be trapped in the lab anymore!

Table of Contents

List of Figures

Chapter One: Introduction

Chapter Two: Background and Literature Review

Chapter Three: Experimental Methods and Materials

Chapter Four: Stability of Anti-Reflection Coatings via the Self-Assembly Encapsulation of Silica Nanoparticles by Diazo-Resins

Chapter Five: Enhanced Scratch Resistance of Self-Assembled Silica Nanoparticle Anti-Reflection Coatings Using Crosslinked Polyelectrolyte Interlayers

Chapter Six: Self-assembly of the Hole-transport Layer and Encapsulated Silver Nanoplates in Organic Photovoltaics

Chapter Seven: Polystyrene-Coated Plasmonic Silver Nanoplates for Enhancement of Organic Photovoltaics

List of Tables

Chapter Four: Stability of Anti-Reflection Coatings via the Self-Assembly Encapsulation of Silica Nanoparticles by Diazo-Resins

Chapter Five: Enhanced Scratch Resistance of Self-Assembled Silica Nanoparticle Anti-Reflection Coatings Using Crosslinked Polyelectrolyte Interlayers

Chapter Six: Self-assembly of the Hole-transport Layer and Encapsulated Silver Nanoplates in Organic Photovoltaics

Chapter Seven: Polystyrene-Coated Plasmonic Silver Nanoplates for Enhancement of Organic Photovoltaics

Chapter 1

Introduction

1.1 MOTIVATION

Energy is a central aspect in our modern day life. Office lighting, laptops, mobile devices, air conditioning units, and vehicles all use energy. Global energy consumption continues to ramp up annually, especially as more countries become developed and the world becomes more westernized. The Organization for Economic Co-operation and Development (OECD) consists of 36 highly-developed member countries. Projected energy consumption growth for non-OECD (mostly developing) countries is 2.2% annually and these countries will consume 65% of the world's total energy use by 2040 (**Figure 1.1a**).[1-2]

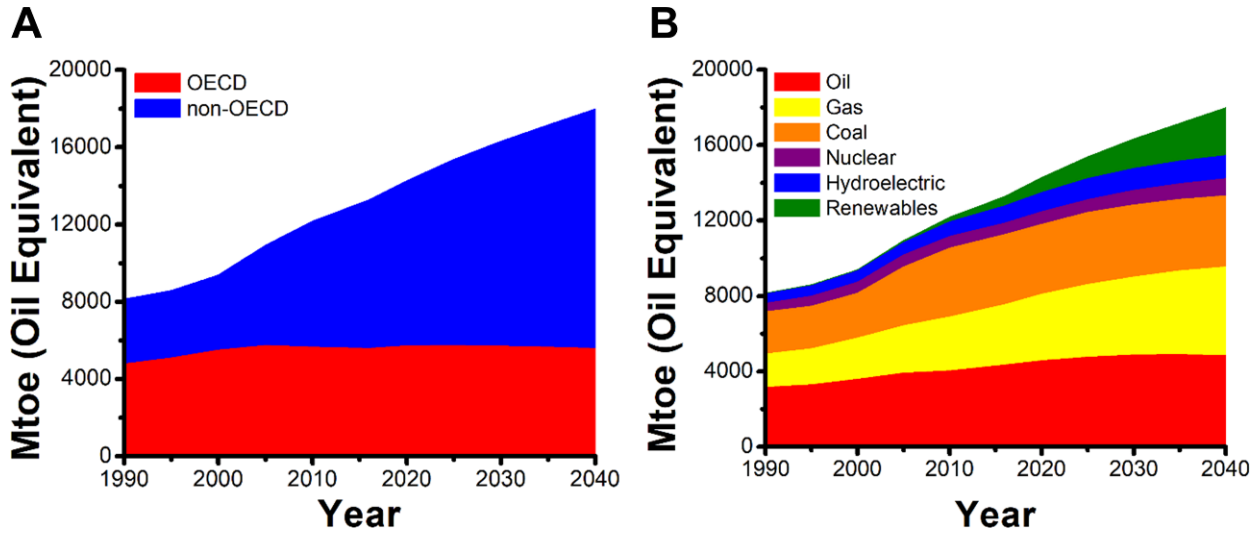

Figure 1.1. Actual and projected global energy consumption from 1990 to 2040 in million tonnes of oil equivalent, according to (**a**) OECD compared to non-OECD countries, and (**b**) separated by energy source. These figures were produced using data gathered from the *BP Statistical Review of World Energy*; 2018.[1]

Nearly 85% of the energy consumed worldwide comes from fossil fuels (oil, gas, coal), and this poses some serious problems in the years to come.[1] The combustion of fossil fuels is used to produce steam in large turbines and ultimately results in the creation of electrical energy. However, fossil fuels are also non-renewable and will eventually be depleted. One study predicts that oil, coal, and gas will be depleted in 35, 107, and 37 years, respectively, and thus, coal will be the only remaining fossil fuel after 2042.[3] Future dependence on fossil fuels (**Figure 1.1b**) would only be feasible if these sources were in infinite supply.

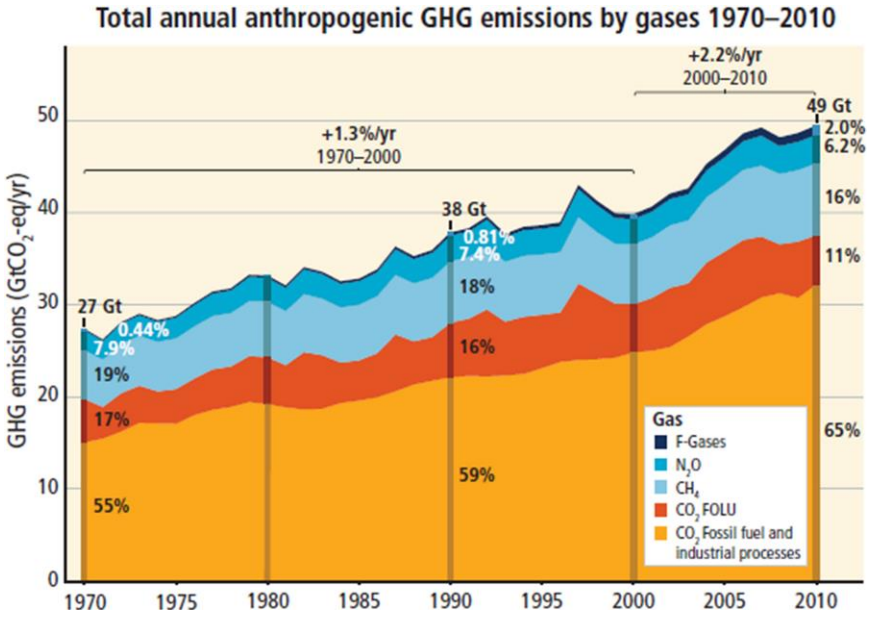

Figure 1.2. Anthropogenic greenhouse gas (GHG) emissions from 1970 to 2010 partitioned based on the gas type. This figure was originally printed as **Figure SPM.2** on page 5 in Pachauri, R. K.; Meyer, L. Ipcc, 2014: Climate Change 2014: Synthesis Report. Contribution of Working Groups I. *II and III to the Fifth Assessment Report of the intergovernmental panel on Climate Change. IPCC, Geneva, Switzerland* **2014**, *151*.[4] IPCC authorizes permission for reproduction.

Even more significant than fossil fuel depletion is the growing threat of global warming, which has largely been attributed to the escalation of anthropogenic greenhouse gas (GHG) emissions

(CO_2, CH_4, NO_2, etc.).[4] Since fossil fuels are mostly composed of hydrocarbons (C-H), their combustion in air creates substantial CO_2 emissions. Ice core data extracted from Antarctica reveal that current CO_2 levels are the highest they have been in the past 800,000 years.[5] In 2017, atmospheric levels surpassed a record-high level of 400 ppm. The total average temperature from 1880 to today has increased by approximately 0.85 ^oC, with the majority of the warming occurring in the past four decades at 0.15 – 0.2 ^oC per decade.[4, 6] Oceans absorb the majority of the thermal energy (~90%), while the atmosphere is reported to only store 1%.[4] In the period of 1901 to 2010, the global sea level has risen 0.19 m and the ocean has increased in acidity by 26% (due to an uptake of CO_2). Out of all the greenhouse gas emissions, the burning of fossil fuels contributes 65% of the total (**Figure 1.2**).[4] Given the pressing circumstances, the need for clean, renewable energy is vital. As is apparent in **Figure 1.1b**, renewables are projected to grow more than any other energy source in the generations to come.

Solar energy is a highly attractive renewable source, as the sun supplies a tremendous amount of energy and with an expected supply for billions of more years. The surface of the earth receives 120,000 terawatts (TW) of power from the sun at any given moment.[7] Compared to the global consumption over the past several decades of 10 – 20 TW, the sun delivers nearly 10 thousand times more power than we currently use. To put things further in perspective, more power arrives from the sun in one hour than the entire planet uses in one year. Since the sun yields more power than any other source, advancements in solar energy harvesting are absolutely imperative.

Solar cells, also known as photovoltaics (PVs), are a form of solar-generated energy that optically absorb a portion of the light spectrum in the form of photons. The absorbed photons cause excitations within the PV material to generate a direct current (DC). After fabrication, PVs require minimal maintenance since there are no moving parts, and they produce zero emissions. PVs can

be wired into an array to generate huge amounts of power, only restricted by the installation area. As long as the sun is shining, there will be generated power. The PV industry is currently increasing faster than any other renewable resource, and PV growth is reported to be more than 40% annually.[8] Crystalline silicon PVs dominate the market by far with 85% of the global sales in 2011.[9] Commercially-sold silicon PVs exhibit efficiencies of 18-22% with maximum laboratory test cell efficiencies reaching upwards of 25% (monocrystalline). At these efficiencies, photovoltaics could supply over 1000 times the world's energy consumption just from the sun. So why do fossil fuels still control the energy market? The answer is cost.

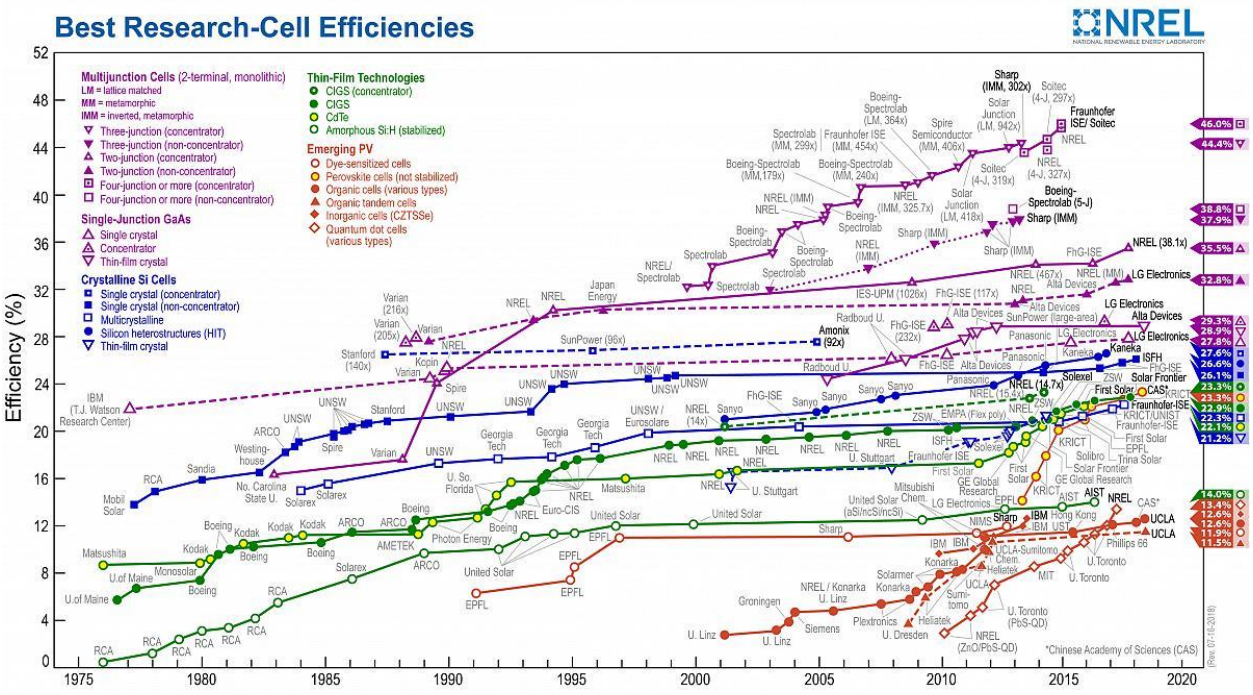

Figure 1.3. Solar cell efficiencies for the many different technologies. OPVs are represented by the closed, red dots on the bottom right-hand portion of the figure. This figure is openly distributed by NREL,[10] which authorizes reproduction as it was developed with government funds.

The cost of PV technology is often compared based on the cost per peak watt ($/$W_p$) or cost per kilowatt-hour ($/kWh).[11-12] The $/$W_p$ is associated with the cost of a PV module (assembly of

solar cells) and the installation. The PV module cost scales inversely with its power conversion efficiency (PCE) since module cost = (material cost per unit area) / (PCE x average midday solar irradiance). $/kWh is more familiar to consumers, but conversion from $/$W_p$ to $/kWh is convoluted. Conversion between the two figures can roughly be approximated by the ratio $/kWh = $/$W_p$ x 0.05. Commercially available Si PVs are approximately $1/$W_p$ or $0.15-0.05/kWh.[11, 13] The conventional electricity cost to consumers (typically from fossil fuel sources) is $0.25 – 0.08/kWh, so PVs are currently on par or cheaper compared to conventional fossil fuel sources (referred to as grid parity).[14] However, since fossil fuel energy sources essentially monopolize the energy infrastructure, reports state that PV cost should equal to a half to a third the cost of conventional energy before it becomes a truly competitive resource.[11] Therefore, there is a strong development push for cheaper alternatives to silicon with higher PCEs (**Figure 1.3**).

Organic photovoltaics (OPVs) could potentially be competitive because of their low fabrication cost, attributed to their inexpensive components and low temperature processing.[15-16] Other advantages of OPVs include their light-weight, flexibility, tunable nature of materials, and printability on a large-scale. Classic OPVs are based on p-type π-conjugated polymers (electron donors) and fullerene derivatives (electron acceptors), however small molecule materials have also received considerable attention more recently. However, OPVs have relatively low PCEs compared to other PVs. Using commercially-available conjugated polymers, such as poly(3-hexylthiophene) (P3HT), PCEs range from 2 to 5%.[17-19] In newer, low bandgap conjugated polymers such as PCDTBT, PTB1, PTB7, or PffBT4T-2OD, higher PCEs can achieved at 6.5 to 11%, but at 3 to 5 times the cost of P3HT.[12, 20-22] Therefore, low-end conjugated polymers can be more appealing for many applications. Furthermore, P3HT-based OPVs are reported to have a 0.004 to 0.02 $/$W_p$, which is substantially cheaper than more efficient conjugated polymers, such

as PTB1 at 0.075 to 0.48 \$/W_p.[12] Since materials cost are difficult to reduce beyond a certain point, the pursuit to increase the PCEs of OPVs is essential to establish their commercial competitiveness.

OPV PCEs are limited by their low charge carrier mobilities and short exciton diffusion lengths.[15-16] Despite high absorption coefficients in conjugated polymers, the optical absorption is also restricted because of trade-offs on the active layer thickness and fill factors. However, OPVs can be enhanced by the inclusion of plasmonic nanoparticles into the devices.[23-27] The electrons within the metallic core of plasmonic nanoparticles resonate upon the exposure of incidence light, which leads to substantial electric field enhancements. This phenomenon is well-known as localized surface plasmon resonance (LSPR). When the frequency of the plasmonic nanoparticle LSPR is coupled closely to the peak absorption frequency of the OPV device, large absorption enhancements can be achieved. In this dissertation, anisotropic silver nanoplates (AgNPs) are integrated into OPV devices for optical absorption enhancements. The AgNPs are coated by polymer or metallic layers, and the dispersion (resistance to aggregation) and stability properties are thoroughly investigated.

Optical absorption in PVs can also be significantly enhanced by reducing the amount of reflected light entering devices. When light is incident at an interface separating a medium of air from a different refractive index medium, the light is split into transmitted, reflected, absorbed, and/or scattering portions. For instance, incident light on silicon (n = 3.5 - 4) in air (n = 1) leads to reflection losses exceeding 30%.[28] Anti-reflection coatings (ARCs) are generally utilized on all types of PVs to diminish reflection loss and substantially improve the performance. ARCs are composed of thin dielectric with an intermediate refractive index between the two separate mediums. The ideal refractive index value for ARCs is the geometric mean for the two mediums, $n = \sqrt{n_0 n_1}$. For silicon in air, the ideal ARC refractive index of n = 1.9 – 2.0 can be achieved

using silicon nitride (SiN_x), which has a tunable refractive index (n = 1.9 – 2.9) when deposited by plasma-enhanced chemical vapor deposition (PECVD) or sputtering.[8, 29-30] With establishment of the proper refractive index, the peak anti-reflection wavelength (destructive interference of the reflected beams) can easily be tuned by variation of the thickness. However, for glass (n = 1.5) in air (n = 1), the ideal refractive index of 1.22 is unattainable using single material coatings. The lowest refractive index material that is practical for ARCs on glass is magnesium fluoride (MgF_2), with a refractive index far from ideal (n = 1.38).

The ideal refractive index can be acquired through porous nanocomposite ARCs. In porous ARCs, the mixing of void space ($n \approx 1$) lowers the overall refractive index further than could be achieved with a single material. In this dissertation, the void space is created as a result of the self-assembled packing of spherical nanoparticles on a film (**Figure 1.4**). Ionic self-assembled multilayers (ISAM) or layer-by-layer (Lbl) deposition is optimal for the fabrication of porous ARCs. ISAM deposition involves the adsorption of two or more oppositely-charged materials onto a charged substrate, driven by electrostatic attraction. Since the only requirement for ISAM is that the materials must possess a charge, a wide range of materials can be deposited and onto any substrate composition or size. The process is inexpensive and the thickness can simply be controlled by the number of layers. Our group previously developed highly-transparent ARCs with poly(allylamine hydrochloride) (PAH) and silica nanoparticle (SiO_2 NP) ISAMs.[31] If used commercially, these ARCs would be highly effective for increasing light transmission on lenses (eyeglasses, binoculars, microscopes, etc.) windows, or computer displays. Another beneficial aspect of ARCs is effective glare reduction. However, because as-assembled ISAMs are comprised solely of ionic bonding, the mechanical (scratch-resistance) and chemical stability of ISAM

nanoparticle films is undesirable for many practical applications because of the relatively low contact areas.

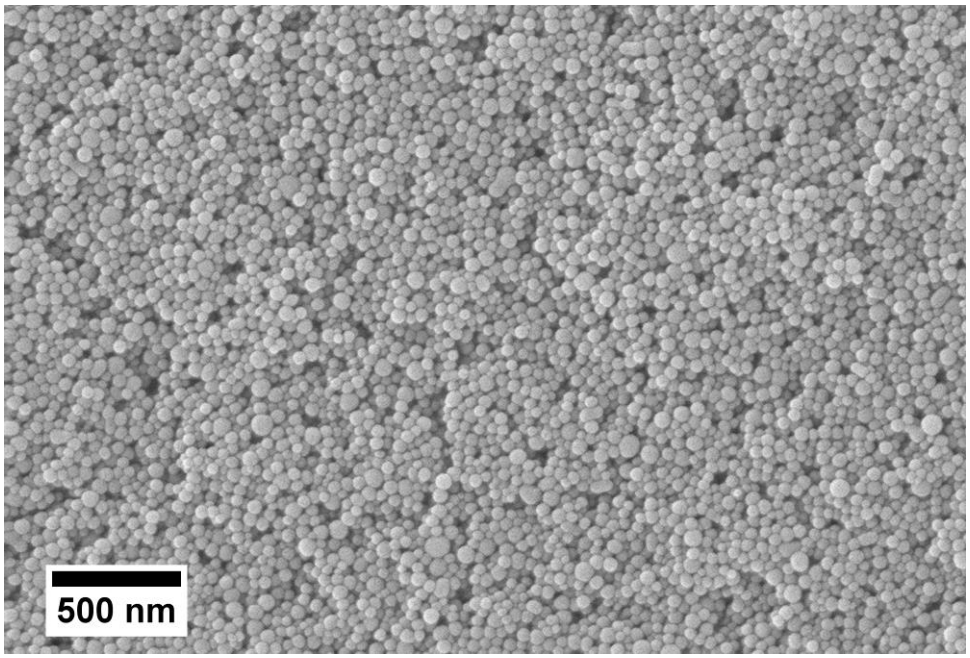

Figure 1.4. SEM image of porous ISAM ARCs composed of PAH/SiO_2 NPs, as developed by our group.

In this dissertation, covalent crosslinking polyelectrolytes are incorporated into porous silica nanoparticle ISAM ARCs in order to provide mechanical and chemical stability enhancements. We investigate fundamental experimental factors, such as pH and solution concentration, on the dispersion and encapsulation properties of the nanoparticles in solution and on the film. These properties are then correlated to the optical and stability characteristics of the ARCs.

1.2 DISSERTATION OUTLINE

Chapter 2 provides background and literature review pertaining to all of the experimental material in this dissertation. The chapter begins with an introduction to self-assembly, followed by a discussion of static and dynamic self-assembly techniques. Langmuir-Blodgett films and self-assembled monolayers (SAMs) are briefly discussed. ISAMs are then reviewed in detail, including

the basis of the technique, history, polyelectrolytes (strong, weak, covalently-crosslinked, linear-growth, and exponential-growth) layers, and nanoparticle layers. The theory of nanoparticles stabilization by electrostatic, steric, and electrosteric means is then thoroughly discussed. Next, ARCs are overviewed in-depth, including theory, history, and fabrication of porous ARCs by ISAMs. A detailed background on OPVs is then presented, including the theoretical principles and device operational mechanisms. Finally, plasmonic nanoparticles are reviewed, as well as their incorporation in OPVs.

Chapter 3 overviews all of the experimental setups and methods used in this dissertation. First, the materials and substrate preparation methods for ARCs are discussed. Next, the ISAM film fabrication and crosslinking methods are thoroughly explained. The instrumentation and characterization for ARCs is then presented in detail. The materials for OPVs are next outlined, including a full discussion on the conjugated polymers and fullerene properties. Then, the OPV solution and substrate preparations are described. The chapter ends with a detailed discussion of OPV fabrication and characterization methodology and instrumentation.

Chapters 4 and **5** are dedicated to the experimental work on improving the stability of ISAM ARCs by the incorporation of covalently-crosslinked polyelectrolytes and the reduction of film agglomerates. In **Chapter 4**, a photo-crosslinkable polyelectrolyte, called diazo-resin or DAR, is focused on. Upon UV irradiation, the diazonium group on DAR partially decomposes, allowing for the formation of covalent crosslinking with nearby sulfonate groups, such as in poly(styrene sulfonate) (PSS). The crosslinking behavior is first inspected and confirmed through the formation of pure DAR/PSS ISAMs. The following section of the chapter overviews the surface coating of silica nanoparticles (SiO_2 NPs) by DAR in solution to develop a modified silica nanoparticle (MSNP) solution. In the chapter, we primarily investigated the necessary conditions to produce a

stable, well-dispersed MSNP solution free from large agglomerates for highly transparent MSNP/PSS ARCs with enhanced stability. To do so, the DAR added to the SiO_2 NPs was altered over a range of concentrations, and the optimum level was determined by ζ-potential and dynamic light scattering (DLS) measurements. After the fabrication and crosslinking of MSNP/PSS ISAM films, the film morphology (scanning electron microscopy; SEM), optical properties (transmittance and reflectance), and chemical stability (solubility resistance in a ternary solvent) were analyzed. MSNP/PSS ISAMs were highly homogeneous (free from agglomerations) with excellent anti-reflection in the visible range, including transmittances >98% and reflectances < 0.2%. After crosslinking by UV-irradiation, the films displayed chemical stability through resistance to etching by a ternary solvent.

Chapter 5 is focused on the fabrication of nanocomposite ARCs with poly(allylamine hydrochloride) (PAH), poly(acrylic acid) (PAA), and SiO_2 NPs. PAH/PAA/PAH/SiO_2 NP interlayer ARCs were produced, which incorporated two extra PAH and PAA interlayers into our standard PAH/SiO_2 ARCs to enhance the mechanical stability. Thermal crosslinking of films containing the PAH amine and PAA carboxylate groups replaced the ionic linkages with covalent amide bonds, as confirmed by FTIR. For this chapter, we studied the effects of PAA pH manipulation on SiO_2 NP encapsulation size (by SEM), along with the resulting differences in both optical and mechanical properties. At low PAA pH, the lowered polymer chain charge density caused elevated encapsulation thicknesses, which resulted in enhanced mechanical stability and degraded anti-reflection. Differently, a high PAA pH increased the polymer charge density, leading to thin encapsulations, excellent anti-reflection, but poor mechanical robustness. An optimal trade-off was established at a PAA pH of 5.2, in which both improved mechanical properties and excellent anti-reflection (transmittance ≥99%) coincided. For example, the normal

force required for scratch initiation as determined by a Triboindenter was increased by a factor of seven for films made from a pH of 5.2 compared to those made from a pH of 6.0.

Chapters 6 and **7** describe the work on OPVs and plasmonic silver nanoplates (AgNPs), as well as the methods for dispersion (aggregation resistance) and stability of AgNPs when integrated into OPVs. The initial section of Chapter 6 is focused on the optimization of baseline OPVs (tuning of the active layer thickness and annealing properties) to maximize the device power conversion efficiency. After the baseline optimization is discussed, the remaining majority of the chapter is aimed at the incorporation of AgNPs into the hole-transport layer (HTL) of OPV devices by ISAM deposition. First, the synthesis of AgNPs is discussed, along with the fabrication of PAH/AgNP ISAMs on glass. Next, the HTL is fabricated with PAH/PEDOT:PSS ISAM films (without AgNPs), along with the examination of the morphology, roughness, optical absorption, sheet resistance, and OPV electrical properties. Following this, the PAH encapsulation of AgNPs process and addition to the HTL is discussed. To protect AgNPs from etching by the acidic PEDOT:PSS, AgNPs are coated with gold (AuAgNPs), which are used for the rest of the chapter. In the final section of the chapter, the hole-transport layer is constructed by PAH/AuAgNP or PAH/PEDOT:PSS/PAH/AuAgNP ISAMs, and the optical absorption and OPV electrical properties are both assessed in detail. The techniques in this chapter did not lead to improved OPV device performances, but established many experimental conclusions that can certainly be expanded on by those with interest in the field. Additionally, we describe detailed methodology for the PAH encapsulation of AgNPs and the etching resistance of AuAgNPs to the acidic PEDOT:PSS, both important for the field of plasmonics.

In Chapter 7, we thoroughly investigate the dispersion effects of thiolated polymer coatings on the AgNPs when included at the organic/cathode interface (between the active layer and aluminum

cathode). This chapter studies AgNPs unfunctionalized, functionalized by poly(ethylene glycol) methyl ether thiol (PEG-SH) (PEG-AgNPs), and functionalized by thiol-terminated polystyrene (PS-SH) (PS-AgNPs). The dispersion for all three types of AgNPs at the interface is examined by AFM and SEM, and the density is controlled by spin-coating solution concentrations. Next, the optical absorption enhancement of the active layer with AgNPs is assessed, before and after thermal annealing. Following this, the photoluminesce behavior of the active layer is presented, to evaluate how the added AgNPs affects the exciton yield. Finally, the OPV electrical device characteristics are discussed in-depth. Integration of the PS-AgNPs into the OPV devices at an optimal concentration of 0.57 nM resulted in a homogeneous film dispersion, significant absorption enhancements, and an increase of the device efficiency by 32%. Unfunctionalized AgNPs and PEG-AgNPs both degraded the device performance due to the creation of detrimental film aggregates.

Chapter 8 finalizes the dissertation with an overview of all the major conclusions, scientific contributions, and the potential future work for further exploration.

REFERENCES

(1) *Bp Statistical Review of World Energy*; 2018.
(2) Peterson, D. Future World Energy Demand Driven by Trends in Developing Countries. https://www.eia.gov/todayinenergy/detail.php?id=14011.
(3) Shafiee, S.; Topal, E. When Will Fossil Fuel Reserves Be Diminished? *Energy policy* **2009,** *37* (1), 181-189.
(4) Pachauri, R. K.; Meyer, L. Ipcc, 2014: Climate Change 2014: Synthesis Report. Contribution of Working Groups I. *II and III to the Fifth Assessment Report of the intergovernmental panel on Climate Change. IPCC, Geneva, Switzerland* **2014,** *151*.
(5) Blunden, J.; Arndt, D. 2017: State of the Climate in 2016. *Bull Amer Meteor Soc* **2017,** *98* (8).
(6) World of Change: Global Temperatures. https://earthobservatory.nasa.gov/WorldOfChange/decadaltemp.php.
(7) Lewis, N. S. Powering the Planet. *MRS bulletin* **2007,** *32* (10), 808-820.
(8) Luque, A.; Hegedus, S. Handbook of Photovoltaic Science and Engineering, *John Wiley & Sons*, **2011**.
(9) Crystalline Silicon Photovoltaics Research. https://www.energy.gov/eere/solar/crystalline-silicon-photovoltaics-research.

(10) Best Research-Cell Efficiencies. https://www.nrel.gov/pv/assets/images/efficiency-chart-20180716.jpg.
(11) Beard, M. C.; Luther, J. M.; Nozik, A. J. The Promise and Challenge of Nanostructured Solar Cells. *Nature nanotechnology* **2014,** *9* (12), 951.
(12) Osedach, T. P.; Andrew, T. L.; Bulović, V. Effect of Synthetic Accessibility on the Commercial Viability of Organic Photovoltaics. *Energy & Environmental Science* **2013,** *6* (3), 711-718.
(13) Fu, R.; Feldman, D. J.; Margolis, R. M.; Woodhouse, M. A.; Ardani, K. B. *Us Solar Photovoltaic System Cost Benchmark: Q1 2017*; National Renewable Energy Lab.(NREL), Golden, CO (United States): 2017.
(14) Electric Power Monthly. https://www.eia.gov/electricity/monthly/epm_table_grapher.php?t=epmt_5_6_a.
(15) Kippelen, B.; Brédas, J.-L. Organic Photovoltaics. *Energy & Environmental Science* **2009,** *2* (3), 251-261.
(16) Nelson, J. Polymer: Fullerene Bulk Heterojunction Solar Cells. *Materials today* **2011,** *14* (10), 462-470.
(17) Kim, Y.; Choulis, S. A.; Nelson, J.; Bradley, D. D.; Cook, S.; Durrant, J. R. Device Annealing Effect in Organic Solar Cells with Blends of Regioregular Poly (3-Hexylthiophene) and Soluble Fullerene. *Applied Physics Letters* **2005,** *86* (6), 063502.
(18) Li, G.; Shrotriya, V.; Yao, Y.; Yang, Y. Investigation of Annealing Effects and Film Thickness Dependence of Polymer Solar Cells Based on Poly (3-Hexylthiophene). *Journal of Applied Physics* **2005,** *98* (4), 043704.
(19) Ma, W.; Yang, C.; Gong, X.; Lee, K.; Heeger, A. J. Thermally Stable, Efficient Polymer Solar Cells with Nanoscale Control of the Interpenetrating Network Morphology. *Advanced Functional Materials* **2005,** *15* (10), 1617-1622.
(20) He, Z.; Zhong, C.; Huang, X.; Wong, W. Y.; Wu, H.; Chen, L.; Su, S.; Cao, Y. Simultaneous Enhancement of Open-Circuit Voltage, Short-Circuit Current Density, and Fill Factor in Polymer Solar Cells. *Advanced Materials* **2011,** *23* (40), 4636-4643.
(21) Liu, Y.; Zhao, J.; Li, Z.; Mu, C.; Ma, W.; Hu, H.; Jiang, K.; Lin, H.; Ade, H.; Yan, H. Aggregation and Morphology Control Enables Multiple Cases of High-Efficiency Polymer Solar Cells. *Nature communications* **2014,** *5* 5293.
(22) Opv Donors and Acceptors. https://www.ossila.com/pages/opv-donors-acceptors.
(23) Atwater, H. A.; Polman, A. Plasmonics for Improved Photovoltaic Devices. *Nat. Mater.* **2010,** *9* (3), 205-213.
(24) Pastoriza-Santos, I.; Liz-Marzán, L. M. Colloidal Silver Nanoplates. State of the Art and Future Challenges. *J. Mater. Chem.* **2008,** *18* (15), 1724-1737.
(25) Kelly, K. L.; Coronado, E.; Zhao, L. L.; Schatz, G. C. The Optical Properties of Metal Nanoparticles: The Influence of Size, Shape, and Dielectric Environment. *J. Phys. Chem. B.* **2003**.
(26) Khan, A. U.; Scruggs, C.; Hicks, D.; Liu, G. Two-Dimensional Plasmonic Nanoparticle as a Nanoscale Sensor to Probe Polymer Brush Formation. *Analytical Chemistry* **2017,** *89* (14), 7541-7548.
(27) Khan, A. U.; Zhao, S.; Liu, G. Key Parameter Controlling the Sensitivity of Plasmonic Metal Nanoparticles: Aspect Ratio. *J. Phys. Chem. C* **2016,** *120* (34), 19353-19364.
(28) Optical Properties of Silicon. https://www.pveducation.org/pvcdrom/materials/optical-properties-of-silicon.

(29) Duttagupta, S.; Ma, F.; Hoex, B.; Mueller, T.; Aberle, A. G. Optimised Antireflection Coatings Using Silicon Nitride on Textured Silicon Surfaces Based on Measurements and Multidimensional Modelling. *Energy Procedia* **2012,** *15* 78-83.
(30) Vetter, M. Surface Passivation of Silicon by Rf Magnetron-Sputtered Silicon Nitride Films. *Thin Solid Films* **1999,** *337* (1-2), 118-122.
(31) Yancey, S.; Zhong, W.; Heflin, J. R.; Ritter, A. L. The Influence of Void Space on Antireflection Coatings of Silica Nanoparticle Self-Assembled Films. *Journal of applied physics* **2006,** *99* (3), 034313.

Chapter 2

Background and Literature Review

2.1 SELF-ASSEMBLY TECHNIQUES

2.1.1 Self-assembly.

Engineering principals can vastly benefit from lessons taught by the natural world. Oligonucleotides elegantly converge into the double helix DNA structure with genetic information for production of proteins and cells. Cells split and coalesce into organ structures that assemble into organisms, such as ourselves. Organisms such as fish create schools and insects form swarms. Bubbles organize into arrays, frozen rain aggregates into hailstones, weather and galaxies produce unique patterns. Nature's design tends to logically process structures through self-assembly. In self-assembly, each component possesses information or characteristics (shape, charge, surface energy, etc.) that support spontaneous convergence into stable, complex structures.[1-3] Since autonomy is fundamental to self-assembly, the components must have the freedom to adjust their structural positions, which is mostly possible in fluids or on smooth surfaces.[1] Therefore, only non-covalent or weakly covalent interactions can exist between self-assembled components, such as electrostatics, van der Waals forces, hydrogen bonds, or hydrophobic interactions.[1-3] Due to the specificity of most interactions, self-assembly automatically corrects structural errors in development, and its components build cooperatively for a high rate of convergence.[3] Self-assembly can be categorized into two broad categories: dynamic and static self-assembly.[1-2]

2.1.1.1 Dynamic Self-assembly. Dynamic self-assembled systems dissipate energy and remain in a non-equilibrium thermodynamic state.[1-2] Additionally, dynamic self-assembly must have an external driving force or the components must be self-propelled.[2] The vast majority of dynamic

self-assembly systems are those from nature, including life. If the energy flux within biological cells or weather patterns stops, then these systems cease to exist. Engineered dynamic self-assembled systems are a relatively new field with work spanning back only to the early 2000's. Earlier in that time frame, Hermanson *et al.* developed dynamic self-assembled microwires by application of a AC field through an aqueous gold nanoparticle (AuNP) solution, which induced dipoles within the AuNPs by dielectrophoresis (**Figure 2.1**).[4] The non-uniform electric field gave rise to electrostatic attraction between nanoparticles and microwire growth. Growth propagated from the tip of the wires at approximately 50 μm/s, attributable to the formation of nanoparticle aggregations (which increased the dielectrophoretic force) and the presence of hydrodynamic interactions. Upon bridging opposite electrodes, the microwire growth ceased, along with a large jump in electrical current. The microwires displayed an ohmic behavior, with a resistivity three orders of magnitude higher than bulk gold because of pores and limited particle contact areas. A key feature of the microwires was their ability to repair themselves, as a small breakage gap resulted in substantial fields that attracted new particles to aggregate and rebuild the wire.

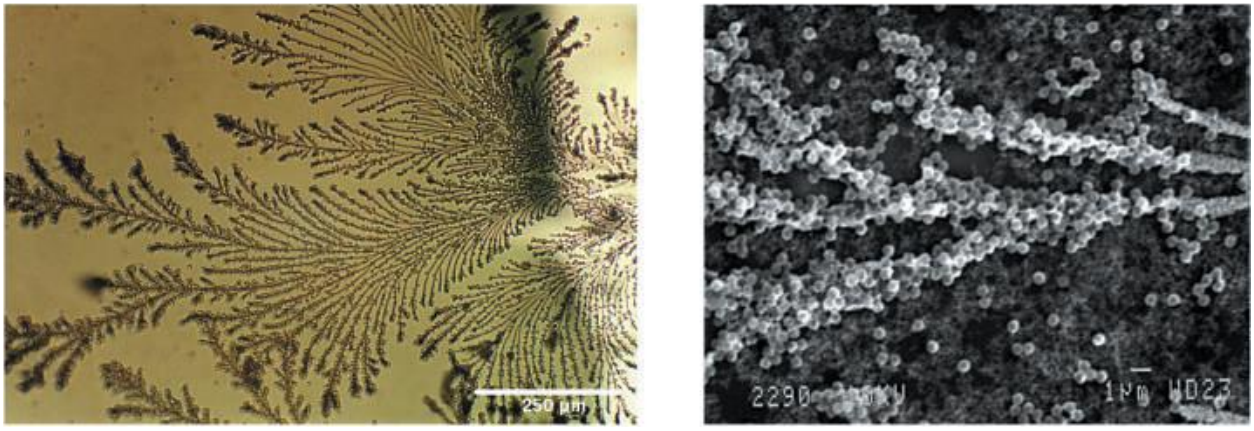

Figure 2.1. SEM micrographs of AuNP microwires dynamically self-assembled by dielectrophoresis. From Hermanson, K. D.; Lumsdon, S. O.; Williams, J. P.; Kaler, E. W.; Velev,

O. D. Dielectrophoretic Assembly of Electrically Functional Microwires from Nanoparticle Suspensions. *Science* **2001**, 294 (5544), pg. 1084.[4] Reprinted with permission from AAAS.

In a more recent study, Lee *et al.* demonstrated dynamic self-assemblies of polystyrene (PS) particle pairs or "trains" in microfluidic channels.[5] Inertial lift forces stabilized the particles into dynamic equilibrium positions within the channels streamlines, where the spacing between the rotating particles oscillated. Hydrodynamic interactions caused the oscillation between particles, which was attributed to the competition between inertial and viscous disturbance flows. Both of these systems represent dynamic self-assembly since they dissipate energy, exist in a non-equilibrium state, and function purely because of a continuous external driving force.

2.1.1.2 Static Self-assembly. Differently from dynamic self-assembly, static self-assembly systems do not dissipate energy and do reach a stable thermodynamic equilibrium.[1-2] The end result of static self-assembled systems is typically a remarkable level of order because of the continuation of rearrangement processes until thermodynamic equilibrium is achieved. Although static self-assembly is predominantly found in engineered systems, it also occurs in natural systems as well, such as crystalline structures, globular proteins, lipid bilayers, or bubble rafts.[1-2] Static self-assembled structures may require an external driving force such as stirring or agitation during processing, but these forces are removed at completion of the structure. The Whitesides group is well-known for their notable work in static self-assembled arrays and structures. Earlier work by Bowden *et al.* in the Whitesides group involved the static self-assembly of polydimethylsiloxane (PDMS) molded components in a mixture of water and perfluorodecalin ($C_{10}F_{18}$).[6] The top surface of the PDMS components were converted from hydrophobic (low surface energy) to hydrophilic (high surface energy) through an O_2 plasma. The $C_{10}F_{18}$ layer wetted the hydrophobic PDMS side with a curved meniscus, and the H_2O layer wetted the oxidized hydrophilic side. The components

maintained a parallel orientation between the two layers at the $C_{10}F_{18}$-H_2O interface due to the interactions and densities differences. After breaking up of component aggregates by agitation, the hydrophobic sides of separate components attracted each other over large distances (approximately 2-3 times their height), into a fully-reversible self-assembled array after 5 to 30 min. The process was applied to hexagonal, cross, and lock-and-key shapes, along with variations in the hydrophilic conversion of the faces to produce different patterned arrays (**Figure 2.2**).

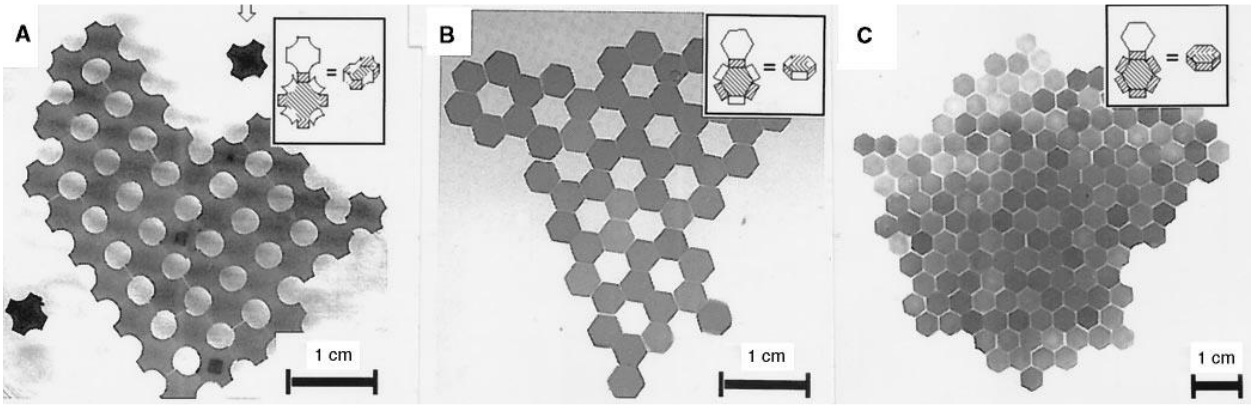

Figure 2.2. Static self-assembly of PDMS components with sides of variable wetting properties for different crystalline array patterns. From Bowden, N.; Terfort, A.; Carbeck, J.; Whitesides, G. M. Self-Assembly of Mesoscale Objects into Ordered Two-Dimensional Arrays. *Science* **1997**, *276* (5310), 233-235.[6] Reprinted with permission from AAAS.

Later, Gracis *et al.* from the Whitesides group used truncated octahedrons (TOs) in the static self-assembly of 3D patterned arrays for LEDs.[7] Configured copper/polyimide sheets were first attached to the TOs with solder dots at their contacts. The TOs were then suspended in an isodense KBr solution and heated to slightly above the solder metling temperature at 47 ºC. For minimization of the interfacial free energy, the solder dots came in contact and fused to establish a 3D integrated circuit with parallel and serial connections. The work done in both of these reports

are classic of static self-assembly as the individual components visibly combined into energetically stable structures at thermodynamic equilibrium.

2.1.2 Langmuir-Blodgett Films.

Besides patterned arrays and crystalline structures, monolayer (or multilayer) films are perhaps the most versatile form of static self-assembly. The earliest record of monolayer films dates back to the Babylonians (18th century BC) pouring oil on water as an act of divination.[8-9] Thousands of years later, Benjamin Franklin noticed that oily water provided a remarkable calmness to choppy water at sea.[8] Franklin later deposited a small quantity of oil to a pond, which then rapidly spread over half an acre to such a small thickness that it became nearly invisible and made the water look as "smooth as a looking glass".[8-9] The effect that Franklin observed was not understood until Lord Rayleigh and Agnes Pockles found that a fatty acid contaminant in soap reduced the surface tension of water, and Rayleigh believed that the film thickness reached the size of one organic molecule.[8-9] Irving Langmuir confirmed Rayleigh's suggestion that fatty acid films extended to one molecular layer based on the volume of oil and area of the film.[8] These floating monolayer films, called Langmuir films, are composed of the amphiphilic material with a hydrophilic polar head group pointed into the water and a hydrophobic nonpolar alkyl (hydrocarbon) tail directed out of the water.[8] Amphiphilic materials are commonly known as surfactants.[9] Several years later, Katharine Blodgett worked with Langmuir to produce monolayer and multilayer assemblies onto solid substrates, which became known as Langmuir-Blodgett (LB) films.[8-9]

The processing of modern LB films involves a trough with computerized and automated functions.[8-9] The amphiphilic molecule is first dissolved into a volatile, organic solvent (typically chloroform) at low concentrations ($\leq$ 1 wt%) and then added to water in the trough.[9-10] The organic solvent evaporates from the amphiphilic molecule to leave a monolayer called the aqueous

subphase.[9] The monolayer is then compressed by a barrier that transitions the molecules from a gaseous to liquid to solid state, also known as the condensed state.[9] In the condensed state, the monolayer is packed tightly at approximately 20 $Å^2$/molecule, the molecules are highly oriented, and the surface pressure is high.[9] A pressure sensor cooperates with the barrier to maintain the condensed state. A hydrophilic or hydrophobic substrate is then vertically immersed into the aqueous subphase, a meniscus forms, and the substrate is slowly withdrawn (~1 mm/s) for monolayer homogeneity.[8] The immersion process is then repeated to grow a series of successive monolayers (multilayers) on the substrate.[8-9] The amphiphilic materials orient in each new layer to maintain hydrophilic-hydrophilic and hydrophobic-hydrophobic interactions throughout the film.[9] For instance, if the hydrophobic side of the previous layer points away from the substrate, then the new layer will orient with the hydrophobic side pointing into the substrate (**Figure 2.3**).

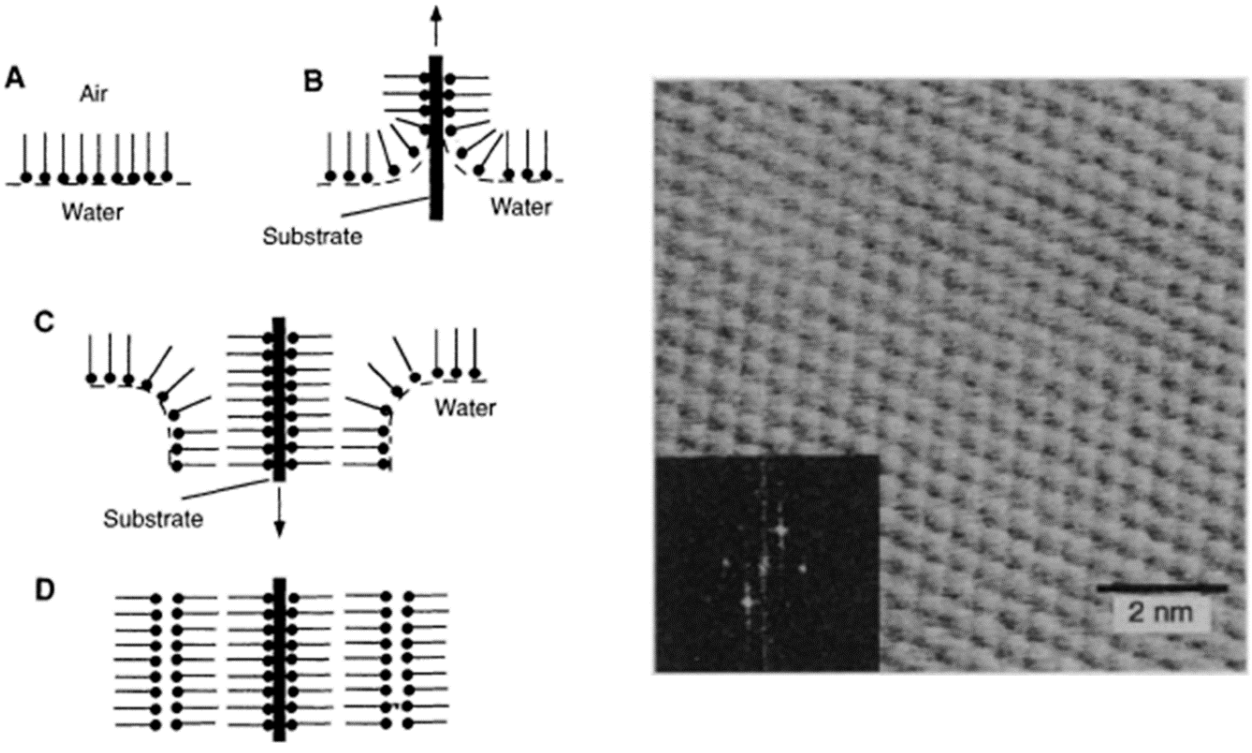

Figure 2.3. Processing schematic of LB films composed of amphiphilic materials and molecular resolution image of a well-ordered seven-layer ZnA_2 LB film on a mica. From Zasadzinski, J.;

Viswanathan, R.; Madsen, L.; Garnaes, J.; Schwartz, D. Langmuir-Blodgett Films. *Science* **1994**, *263* (5154), 1726-1733.[10] Reprinted with permission from AAAS.

Variations in amphiphilic materials and aqueous subphase constituents can strongly influence a range of properties in the LB film. The alkyl chain length is responsible for the differences among fatty acids, such as palmitic ($C_{16}H_{32}O_2$), stearic ($C_{18}H_{36}O_2$), arachidic ($C_{20}H_{40}O_2$), behenic ($C_{22}H_{44}O_2$) acids, and longer chain lengths are more stable because of the increased van der Waals interactions.[9-10] The pH of the aqueous subphase is critical for homogeneous growth.[9-10] Zasadzinski *et al.* showed that high levels of order and packing density in LB films can be achieved through the addition of counterions to the aqueous subphase such as $CdCl_2$, $MnCl_2$, $BaCl_2$, $CaCl_2$, $MgCl_2$, $ZnCl_2$, or $Pb(CH3COO)_2$.[10] The difference in electronegativity of the counterions compared to the oxygen on the carboxylic acid head group resulted in either covalent bonding (<2 difference; e.g. Cd, Mn, Pb) or ionic bonding (>2 difference; e.g. Ba, Ca, Mg). The bonding variations produced different local lattice structures (herringbone, triclinic, hexagonal) and molecular areas on the substrate (from 17.9 $Å^2$ in the most covalent to 22.2 $Å^2$ in the most ionic bonding). Due to the van der Waals interaction between the alkyl chains, the minimum cross-sectional area of the alkyl chains is 18 A^2. Therefore, an increased molecular area between chains caused the chains to tilt from 0^o to 33^o. Upon creation of multilayers with LB films, the development of the bulk lattice structure required three to seven monolayers, based on the lattice matching with the different substrates used. This work was one of the first to show detailed molecular order in the films by scanning probe microscopy (SPM) and atomic force microscopy (AFM). Besides fatty acids, other amphiphilic materials can be used for LB films for various applications such as phospholipids (for biological membranes), fluorocarbons, amphiphilic polymers, and organically capped nanoparticles.[8-9, 11] Several applications for LB films include

anti-reflection coatings (ARCs), nonlinear optical (NLO) films, conductive films, insulating films, passive layers in metal-insulator-semiconductor (MIS) devices, and biosensors.[8-12]

2.1.3 Self-assembled monolayers.

Later monolayer development led to the advent of a more fundamental structure, appropriately named self-assembled monolayers (SAMs). SAMs are similar to LB films as each monolayer is composed of a head group, a fully extended alkyl chain, and often a terminal functional group.[13-14] While LB films physisorb to substrates, SAMs instead exothermically chemisorb to substrates, which significantly increases the molecular adhesion and stability.[15] SAMs assemble into a closely-packed crystalline-like structure, based on the substrate-head group interactions, with a defined lattice spacing, which results in a tilt of the molecules caused by the van der Waals interactions between alkyl chains.[13-14] The thickness of each monolayer is typically 1 – 3 nm, based on the length of the alkyl chain and the tilt angle.[14] In the adsorption process, the first regime lasts only minutes, in which 80-90% of SAMs final thickness is completed.[13] The second adsorption regime involves ordering of the molecules, along with the elimination of defects, and can last hours to days depending on the alkyl chain length.[13-14] Besides adsorption from solution, SAMs can also be less commonly assembled from a gas phase under ultra-high vacuum (UHV).[14] The spontaneous adsorption of SAMs onto a multitude of substrate materials or shapes circumvents the need for special processing equipment.

SAMs are primarily classified based on their head group, which includes fatty acid derivatives (generally carboxylic acid or amines), organosilicon derivatives (alkylsilanes derivatives), and organosulfur derivatives (thiols, disulfides, sulfides).[9, 13] Fatty acid derivatives such as docosanoic acid have previously been reported to have carboxylic acid head groups that adsorb ionically to silver(111) substrates, specifically the native oxide layer (AgO).[13, 16] As determined by X-ray

diffraction, the fatty acid chains assembled into a p(2x2) structure with a lattice spacing of 5.78 Å with a tilt angle of 26° from the surface normal.[13, 16] Fatty acid SAMs can bind to virtually any metal oxide in a similar fashion. SAMs with alkylsilane derivate head groups form silanol groups (Si-OH) on hydroxylated substrates and subsequently, polysiloxanes (Si-O-Si) with neighboring chains.[13] Alkylsilane SAMs on SiO_2 substrates results in an interchain distance of approximately 4.4 Å, and therefore the tilt of alkyl chains is typically nonexistent.[13] Limited water exposure is critical for all alkylsilane SAMs to resist polymerization in solution or at the surface.[13] Alkylsilane derivatives have chemical formulas of $RSiX_3$, R_2SiX_2, or R_3SiX, where R is the alkyl chain with a terminal functional group.[9] The alkylsilane derivative used in this thesis is (3-Mercaptopropyl)trimethoxysilane (MPTS) with formula $HS(CH_2)_3Si(OCH_3)_3$, and in $RSiX_3$, R is $HS(CH_2)_3$ and X is (OCH_3). To deposit the SAMs, glass substrates were first hydroxylated using a piranha solution (H_2SO_4/H_2O_2; 7/3; w/w). MPTS was then dissolved into methanol (MeOH) and the hydroxylated glass substrates were immersed into the solution for 18 h to form SAMs on the surface. After formation of the MPTS SAMs, the thiol (-SH) functional groups were converted to sulfonates by an acetic acid and hydrogen peroxide mixture. In previous reports, hydroxylation of the terminal functional group on alkylsilane SAMs, specifically octadecyltrichlorosilane (OTS), allowed for the creation of multilayer films.[17] OTS multilayers were assembled with 25 consecutive monolayers with an overall film thickness of ~0.1 μm, however, increasing levels of structural disorder was present with a greater number of monolayers.

Besides fatty acid and organosilicon derivatives, perhaps the most studied and used SAM are organosulfur derivatives. SAMs with organosulfur derivatives form strong coordination bonds with a range of metals and semiconductors, such as silver, gold, copper, palladium, platinum, mercury, and GaAs.[13-14] Among the types of organosulfur derivatives, thiols (R-SH) are most

common as they have higher solubility than disulfides (R-S-S-R'), and have greater stability than sulfides (S^{2}-).[14] The reaction of alkanethiolates with metals (e.g. gold) involves the oxidative addition of the R-SH to the surface, followed by a reduction elimination of hydrogen into a gas (H_2),

$$RS - H + Au_n^0 \Rightarrow RS^- - Au^+ + \frac{1}{2}H_2 + Au_n^0 \qquad (\mathbf{2.1})$$

with bonding energies (strengths) for RS-H ≈ 87 kcal mol^{-1}, RS-Au ≈ 40-50 kcal mol^{-1}, H_2 ≈104 kcal mol^{-1}, and the net adsorption energy for alkanethiolates to gold is -5 kcal mol^{-1} (exothermic).[9, 13-14] Despite nearly the same lattice constant for Au(111) and Ag(111) at 2.88 and 2.89 Å, respectively, the structure of alkanethiolates on the two surfaces is drastically different.[13] On Au(111), the energy difference between top and hollow surface sites is ~6.0 kcal mol^{-1}, so alkanethiolates bind to every sixth hollow site with a (√3x√3)R30° overlayer, a hexagonal S···S spacing of 4.97 Å, and with a molecular area of 21.4 $Å^2$ (**Figure 2.4**).[13-14] On Ag(111), the energy difference between top and hollow surface sites is smaller at ~3.3 kcal mol^{-1}, so alkanethiolate adsorption on these sites is more competitive.[13] Alkanethiolate adsorption on Ag(111) forms a (√7x√7)R10.9° structure with S···S spacing of 4.41 Å.[13-14] As a result of the larger spacing in Au(111) compared to Ag(111), the tilt of alkyl chains to the surface normal is 28° and 11-15°, respectively.[14] More detail on thiol-terminated polymer brushes are discussed below.

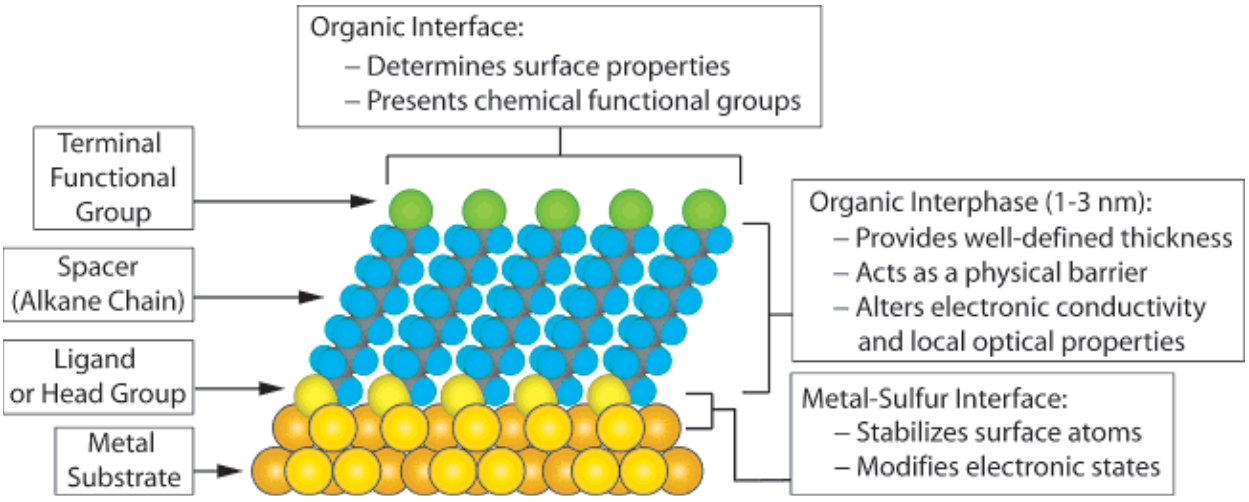

Figure 2.4. Schematic of a crystalline alkanethiolate SAM on Au(111). Reprinted (adapted) with permission from Love, J. C.; Estroff, L. A.; Kriebel, J. K.; Nuzzo, R. G.; Whitesides, G. M. Self-Assembled Monolayers of Thiolates on Metals as a Form of Nanotechnology. *Chemical reviews* **2005**, *105* (4), 1103-1170.[14] Copyright 2005 American Chemical Society.

Functionalization of the alkyl terminal end groups on SAMs are essential for their application in optics, piezoelectrics, chemical sensors, biomaterials, and also for understanding of wetting, adhesion, corrosion, and friction properties.[13-14] The functionalization of terminal end groups after formation of SAMs on a substrate is less convoluted (than prior to assembly) and ensures that the assembly structure will not be compromised.[14]

2.1.4 Ionic Self-assembled Multilayers.

2.1.4.1 Background. Among self-assembled thin-films, no other technique has greater simplicity and robustness than ionic self-assembled multilayers (ISAMs). In the processing of ISAMs, a charged substrate is first immersed into a solution containing an oppositely-charged material (e.g. anionic substrate into a cationic solution). Within seconds of immersion, the dissolved charged material diffuses towards the substrate and adsorbs onto the surface, driven by electrostatic attraction.[18-19] Adsorption continues until the material fully overcompensates and

reverses the surface charge of the substrate. At this point, the buildup of charged material creates a repulsive barrier that terminates further adsorption, and one layer is completed. The single layer ISAM film is then thoroughly rinsed (typically with DI water) to remove weakly bound and solvated material off the surface of the film. Essentially, the rinsing step improves the homogeneity of the film and prevents contamination of further solutions.[18-19] After rinsing, the ISAM film is then immersed into a separate, oppositely-charged solution, which induces the adsorption of a second layer on top of the first one. After completion of the second layer, the ISAM film is again rinsed, and the process is repeated indefinitely, until the desired film thickness is obtained (**Figure 2.5**). In this sense, ISAM films are also referred to as layer-by-layer (LBL) films.

The attraction of ISAM films arises primarily due to their simple nature. Unlike LB films, specialized equipment is not utilized in ISAM film processing; a substrate is simply immersed into a solution for a predefined amount of time. The substrate does not need to be planar for a homogenous ISAM film; it can be of any size, shape, or curvature. Since the basis for ISAM films growth is electrostatic attraction, the sole requirement is that each material has a stable surface charge and every successive layer is of opposite charge. Therefore, precise stoichiometry and chemical reactions are unnecessary to build homogeneous multilayers, as they may be with other self-assembled thin-films (e.g. SAMs).

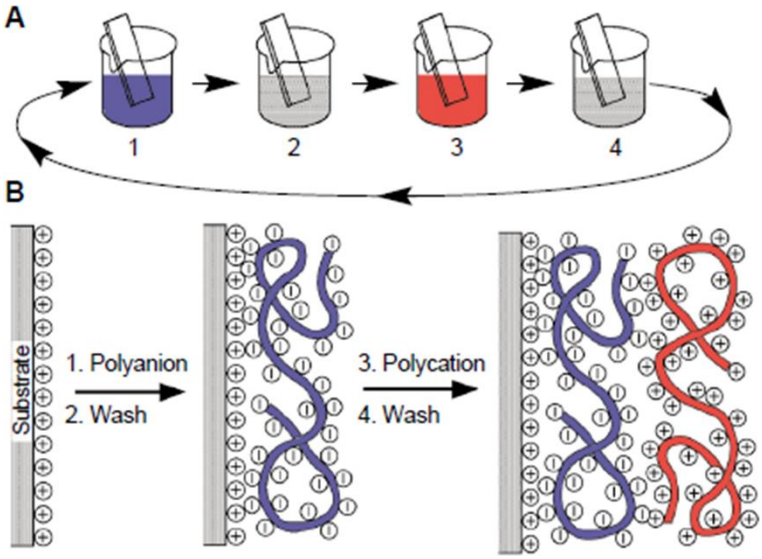

Figure 2.5. Schematic of ISAM film processing. In the schematic, the substrate is cationic, polyelectrolyte solution 1 (blue) is anionic, solution 2 represents a water rinse, polyelectrolyte solution 3 (red) is cationic, and solution 4 represents another water rinse. From Decher, G. Fuzzy Nanoassemblies: Toward Layered Polymeric Multicomposites. Science 1997, 277 (5330), 1232-1237. Reprinted with permission from AAAS.[18]

Any number or combination of charged materials can be used to make ISAM films for any degree of complexity. Consequently, ISAM films can possess a wide range of functionalities and properties, useful for a multitude of applications. Most often, ISAM films are composed of two oppositely charged materials, and the completion of two successive layers is appropriately named a bilayer. The ISAM film's design can be represented as $(A/B)_n$, where A and B are the cationic and anionic materials, respectively, and n is the number of repeat units or bilayers. Another common architecture for ISAM films is $(A/B/C/D)_n$, where A, B, C, and D are represented as cationic solution 1, anionic solution 1, cationic solution 2, and anionic solution 2, respectively, and n is the number of *quadlayers*.

The first report of ISAMs dates back to the 1960's, where Ralph Iler fabricated colloidal multilayers as an alternative to LB films.[20] The ISAM films were composed of cationic boehmite alumina fibrils and anionic silica nanospheres with a diameter of 5 to 6 nm and 100 nm, respectively, on black plate glass. Since the silica formed a packing density of 50 to 60%, the overall refractive index of the films was approximately 1.25. As this refractive index is close to the ideal value for anti-reflection (as discussed more thoroughly later), the films displayed strong optical interference in the visible wavelengths. The thickness of the films was approximated by the peak interference wavelengths and the reflected interference color.

Despite the significant implications in the work done by Iler, further development with ISAM films had a long dormancy period until Gero Decher revitalized them in the 1990's.[18, 21-23] Decher *et al.* produced ISAMs using cationic and anionic bipolar amphiphiles with outer charged functional groups, inner alkyl chains, and a central biphenyl unit.[21] The amphiphile layers were adsorbed onto an aminopropylsilanized cationic substrate and their biphenyl chromophores showed a linear increase in absorption at λ = 262 nm with a greater number of layers. Upon examination of the films by small angle X-ray scattering (SAXS), the thickness of the cationic and anionic layers together was found to be 97.2 Å. Soon thereafter, Decher *et al.* reported the fabrication of ISAM films with cationic and anionic polyelectrolytes (polycations and polyanions), such as poly(styrene sulfonate) (PSS), poly-4-vinylbenzyl-(N-N-diethyl-N-methyl-)-ammonium iodide, poly-(1-(4-(3-carboxy-4-hydroxyphenylazo)-benzenesulphonamido)-1,2-ethanediyl) sodium salt (PAZO), and poly(allylamine) hydrochloride (PAH).[18, 22-23] Similar to the ionic amphiphile ISAM films, polyelectrolyte-based films composed of poly-4-vinylbenzyl-(N-N-diethyl-N-methyl-)-ammonium iodide and PSS showed a linear increase in UV absorption with increased number of layers.[22] However, when these films were first examined under SAXS, the

measurements were devoid of Bragg peaks, which suggested that the structure of the films was different than expected. It was theorized that the lack of Bragg peaks was either due to an electron density similarity between adjacent layers or a "smearing" of the electron density profile as a result of *interpenetration* between neighboring polyelectrolytes.[23] Regardless of the lack of Bragg peaks, the SAXS spectra did exhibit Kiessig fringes which could be used to calculate the overall thicknesses of the films and also revealed that the films had a high level of smoothness (Kiessig fringes are strongly affected by interfacial roughness).[22] In later examined PSS/PAH/PAZO/PAH ISAMs, Bragg peaks finally appeared and intensified with seven or more quadlayers, attributed to an increased contrast in the electron density from the azo dyes of PAZO.[23] Also, it was found that periodic drying after every fourth, sixth, or eighth bilayer of PAH/PSS ISAMs resulted in the formation of Bragg peaks. As ISAM films are generally kept wet until their completion, the drying removed solvated counterions and lead to a rearrangement of the surface polymer chains. The reorganization of polymer chains changed the interfacial roughness, electron density, and created defined "superlattice" structures within the ISAM films, associated with the observed Bragg peaks. Years later, Decher incorporated perdeuterated PSS (labeled with deuterium) into PAH/PSS ISAMs to investigate the configuration of the polyelectrolyte-based films.[18] Surprisingly, Kiessig fringes were again only present in neutron reflectivity (NR) spectra when films were composed of only PAH and perdeuterated PSS. When the perdeuterated PSS was used for every fourth layer, however, the Bragg peaks again appeared. Therefore, it was concluded that the majority of polyelectrolyte-based films are not discrete individual layers, but are rather largely interpenetrated. Interpenetration naturally arises to maintain an equal stoichometry of cationic and anionic groups across the ISAM stratum and corresponds to roughly a 50% overlap of nearby layers with equal charge. These films were thus characterized as "fuzzy layered assemblies", which had important

implications for applications such as the interconnectivity of conductive polyelectrolytes. ISAM film characteristics were found to become prominent only after the film thickness has surpassed the substrate/film interactions. The polyelectrolytes used by Decher opened the door for versatility in ISAMs and therefore were an important milestone.

Polyelectrolytes are a class of polymers with synthetic or natural repeat units that contain ionizable functional groups. When polyelectrolytes are dissolved in aqueous or other polar media, they dissociate into charged polymer chains and oppositely charged counterions. The thickness of polyelectrolyte layers in ISAM films is largely dependent on the charge density of the polymer chains. A fully charged polyelectrolyte maintains a relatively strong level of adhesion because of the large number of formed ionic bonds.[18] Based on their inherent charge characteristics, polyelectrolytes are classified as either "strong" or "weak".[24-29]

2.1.4.2 Strong Polyelectrolytes. Strong polyelectrolytes are those with fixed, permanent charges that dissociate completely in solution and are independent of the solution pH.[28-30] PSS and poly(vinylsulfonic acid) (PVS) are considered strong polyanions, while poly(diallyldimethylammonium chloride) (PDDA) and poly(4-vinylbenzyltrimethylammonium chloride) (PVTAC) are known as strong polycations.[27] The systematic addition of salt, such as NaCl, to solutions is an effective method for the adjustment of the ionic strength and the charge density on strong polyelectrolyte chains.[28, 31-33] When dissolved into solution, salt dissociates into separate cation and anionic ions (e.g. Na^+ and Cl^-), which act as counterions to the electrolyte functional groups. Decher *et al.* showed that the addition of NaCl at concentrations of 1.0, 1.5, 2.0 M to PAH/PSS ISAMs systematically increased the linear-slope of the thickness per bilayer to 17.7, 19.4, and 22.6 Å, respectively.[31] Without the inclusion of salt, the charged chains fully extend into a "flat" conformation as a result of the electrostatic repulsion between the ionic groups (**Figure**

2.6). The increased presence of salt and counterions in the solution induces electrostatic screening of the polyelectrolyte ionic groups, causing the chains to possess an increasingly "loopy" conformation with a greater film thickness. The screening of charges by counterions is referred to as "counterion condensation".[28]

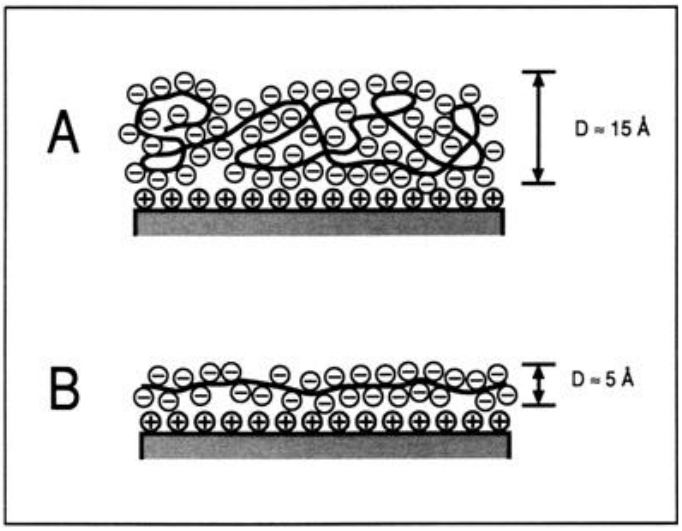

Figure 2.6. Schematic of polyelectrolytes with (**a**) loopy and (**b**) extended conformations. Reprinted by permission from Springer Nature: Decher, G.; Schmitt, J. Fine-Tuning of the Film Thickness of Ultrathin Multilayer Films Composed of Consecutively Alternating Layers of Anionic and Cationic Polyelectrolytes. *Progr. Colloid Polym. Sci.* **1992**, 160-164.[31] Copyright 1992.

Steitz *et al.* found that the thickness of bilayers containing fully-charged strong polyelectrolytes was directly proportional to the square-root of the NaCl concentration ($c_{NaCl}^{1/2}$).[32-33] It was also revealed that wet ISAM films hold a considerable amount of water (water content ≈ 42 – 56%) that scales with bilayer thickness, and the drying of films decreases the thickness by 30%.[33] Steitz *et al.* developed a copolymer with varying ratios of the cationic monomer, PDDA, and the neutral monomer, *N*-methyl-*N*-vinylacetamide (NMVA), in order to investigate the effect of charge

density on polyelectrolyte thickness.[32] The thickness of ten bilayer PSS/P(DAC-NMVA) films remained relatively small (~75 Å) at very low charge densities (<50%) and increased dramatically at a critical charge density of 50% (~660 Å). As the charge density was increased above 50%, the film thickness and the roughness gradually decreased due to the heightened levels of charge repulsion within the chains. Counterions had a significant effect on the highly-charged polyelectrolyte thickness and a negligible effect on the lowly-charged polyelectrolyte thickness. It was also demonstrated that the charge density on strong polyelectrolyte chains must be ≥50% for charge overcompensation in ISAM growth. Lourenço *et al.* discovered through XPS that counterions were distributed throughout the bulk of PAH/PSS ISAM films during and after processing, and associated closely to the polyelectrolyte ionic groups.[34] The counterion concentrations in the bulk of the films scaled proportionally with the NaCl solution concentrations and polyelectrolyte adsorption per monolayer.

2.1.4.3 Weak Polyelectrolytes. Weak polyelectrolytes feature functional groups with variable charge states that can easily be adjusted through solution pH. PAH and poly(acrylic acid) (PAA) are perhaps the most studied weak polyelectrolytes, notably by Rubner's group.[24-27] PAH and PAA contain cationic amine groups (NH_3^+) and anionic carboxylate groups (COO^-), respectively. In an early report by Rubner's group, Decher's previous investigation on polyelectrolyte interpenetration was revisited by exploring the wettability of PAH/PAA ISAMs for a range of monolayer thicknesses.[24] Since PAH is cationic, a lower and higher pH of PAH solution increases and decreases the linear charge density of the polyelectrolyte chains, respectively. This pH to linear charge density relationship is the opposite for PAA, as it is anionic. Similar to strong polyelectrolytes, a higher linear charge density increases electrostatic repulsion between ionized groups, and the chains adopt an extended, "flat" conformation upon adsorption. Contrarily, a low

linear charge density reduces segmental electrostatic repulsion between ionized groups, resulting in an increasingly "loopy" structure with an elevated population of polymer loops and tails. In the ISAM film, the loops from the underlying layer interpenetrate into neighboring layers. The easily manipulated charge properties of weak polyelectrolytes by alteration of the solution pH allow for a precise control over layer thickness. Since PAH and PAA films have considerably different contact angles (PAH = 50 – 55°, PAA < 5°), the film's combined contact angle could be adjusted by changing the thicknesses of the two layers, which tuned the proportions from each polymer. Along with contact angle measurements, a positively-charged dye called methylene blue was deposited onto the films and its absorption intensity was reported to scale proportionally to the level of available ionic carboxylate groups on PAA. The methylene blue staining emphasized 1) a higher charge density on PAA (higher PAA pH) resulted in decreased methylene blue absorption as greater number of carboxylate groups had formed ionic pairs, and 2) thinner outermost PAH layers (lower PAH pH) showed enhanced methylene blue absorption from a higher degree of interpenetration by PAA. By the same regard, thinner outermost PAA layers also allowed for greater PAH interpenetration. A following report by Shiratori *et al.* from Rubner's group more systematically explored the relationship between pH and PAH/PAA thickness.[25] The pH of PAH and PAA were both separately varied from 2.5 to 9.0 to develop a 3-D column chart for every possible pH combination with bilayer thicknesses ranging from very thin (<10 Å) to very thick (>120 Å) (**Figure 2.7**). Additionally, the pH of both PAH and PAA were modified in unison (along the diagonal on the 3-D column chart) to unveil four pH regions. It was noted that PAA has a 20-30% degree of ionization at pH 2.5 and is close to 100% ionized at pH 6.5, whereas for PAH, the chains are fully ionized until pH 7.0, and deprotonation occurred above this pH. In "Region I" (pH 2.5 – 4.5), an increase in the PAA pH results in an increase of the linear charge density that leads

to thinner PAA layers and thicker PAH layers, as more PAH chains are required to overcompensate the PAA surface charge. In "Region III" (pH 6.0 – 7.5), both PAH and PAA are fully ionized and the thickness is ~3-5 Å per layer, the lowest out of all the regions. Both "Region II" (pH 4.5 – 6.0) and "Region IV" (pH 7.5 – 9.0) present a unique situation in which a fully-ionized polyelectrolyte is deposited with a *nearly* fully-ionized polyelectrolyte. This situation results in dramatically thick layers that are uncharacteristic for the other two regions. A fully-ionized chain with high charge density is expected to have a flat conformation since the enthalpic gain in the adsorption free energy is larger than the entropy cost for extending the chain. Differently, the enthalpic gain in a *nearly* fully-ionized chain is inadequate for spreading the chain, so the conformation is loopy, and the overall bilayer is remarkably thick. As related to the polymer conformations, increased layer thickness correlated directly to heightened layer roughness values. The underlying layer conformations and surface effects were found to be highly influential to the following adsorbed layers. When fully-ionized polyelectrolytes from Region III (pH 6.5 for PAH and PAA) were deposited on top of layers from Region I, it required nearly 30 bilayers for the layer thickness and roughness values to reach similar magnitudes for the layers deposited on a bare substrate. This report also highlighted an interesting phenomenon in which lowly-charged PAA chains (pH 2.5 – 4.5) will increase their ionization when deposited on highly-charged PAH chains to neutralize the high surface charge density. The change in ionization causes PAA to have a substantially different pK_a in a PAH/PAA film than in solution.

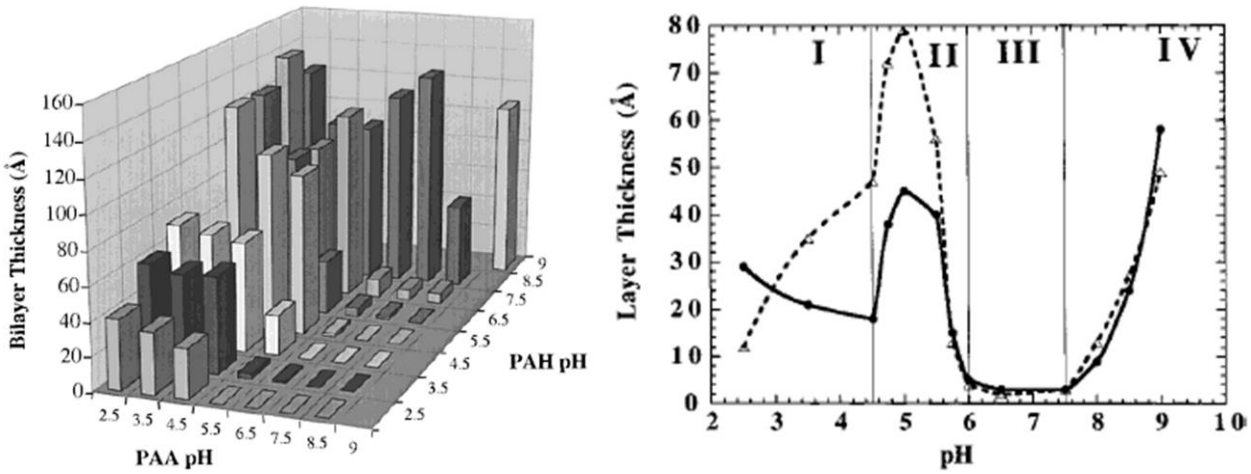

Figure 2.7. Graphical representation 3-D column chart of bilayer thickness dependency on PAH and PAA pH ranging from 2.5 to 9.0. Monolayer thickness of PAH and PAA when the pH of the two polyelectrolytes is varied together (along the diagonal of the 3-D column chart), representing Regions I, II, III, and IV. Reprinted (adapted) with permission from Shiratori, S. S.; Rubner, M. F. pH-Dependent Thickness Behavior of Sequentially Adsorbed Layers of Weak Polyelectrolytes. *Macromolecules* **2000**, 33 (11), 4213-4219.[25] Copyright 2000 American Chemical Society.

Mendelsohn *et al.* from Rubner's group next reported that for PAH/PAA ISAMs: 1) fully-charged (Region III, pH 7.0) had a "ladder-like" structure with "cooperatively stitched segments", 2) lowly-charged (PAH pH 7.5, PAA pH 3.5) had a "scrambled salt" structure with randomly stitched and mixed loopy segments, and 3) *nearly* fully-charged (Region II, pH 5.0) contained both "cooperatively stitched segments" and "scrambled salt" domains.[26] Upon immersing PAH/PAA ISAMs with lowly-charged polyelectrolytes into an acidic solution with pH $\leq$ 2.50, the film thicknesses swelled by ~100 – 200 %, the refractive index dropped substantially (1.54 to 1.18). In this situation, AFM revealed that the films drastically shifted from a contiguous structure (pore volume $\approx$ 0%) to a microporous structure (pore volume $\approx$ 60%). For different PAH/PAA pH permutations, the relative amount of carboxylic acid (COOH) compared to the ionized carboxylate

(COO^-) groups on PAA were determined by Fourier transform infrared spectroscopy (FTIR). In the ISAM film with PAH and PAA at pH 7 and 3.5, respectively, PAA was found to have an 80-90% degree of ionization in the film after assembly. However, the degree of ionization of PAA sharply decreased in an acidic solution of pH 2.4 to 60% and substantially more in an acidic solution of pH 2.0 to ≤ 35%. Essentially, the carboxylate groups were protonated by the acid (converted to COOH) and the inter-chain ionic linkages between PAH and PAA were split, resulting in the microporous structure. It was found that the microporous structure returned to the original structure after immersion in neutral water overnight. Also it was found that the microporosity was prevented with the creation of amide covalent crosslinks (-NHCO) by heating the film to greater than 200 ^oC. The pK_a is defined as the pH that a polyelectrolyte had a 50% degree of ionization, and therefore, this report exposed that the pK_a of PAA in a PAH/PAA ISAM resided between pH 2.0 and 2.4. In a final report by Rubner's group, Choi *et al.* again utilized FTIR to fully reveal the degree of ionization dependence on pH for PAH and PAA (**Figure 2.8**).[27] In solution, PAH was found to be 100% ionized at pH ~2.0, 85% ionized at pH 7.0, 50% ionized (pK_a) at pH ~8.9, and 0% ionized at pH 12.0. PAA in solution was found to be 100% ionized at pH 9.5, 65% ionized at pH 7.0, 50% ionized (pK_a) at pH ~6.5, and 0% ionized at pH 2.0. In an ISAM film, the ionization shift of weak polyelectrolytes is more substantial with other weak polyelectrolytes compared to strong types. For instance, PAA at pH 4.0 is 7% ionized in solution, and dramatically shifts to 63% ionization in PAH/PAA ISAMs, but only shifts to 30% ionization in PDDA/PAA or PVTAC/PAA ISAMs. Therefore, the pK_a for PAA in PAH/PAA film and a PDDA/PAA was found be pH ~2.2 and pH ~3.0, respectively. The ionization shifts only occurred when the degree of ionization in solution for the not fully-charged polyelectrolyte was below the "trigger point", which for PAH and PAA was 89% and 70 – 80%, respectively. Earlier reports also

present the pK_a for PAA and PAH in the ISAM film to be approximately 2.5 to 4.5 and 9.9 to 10.9, respectively, depending on the solution pH and the film thickness.[35]

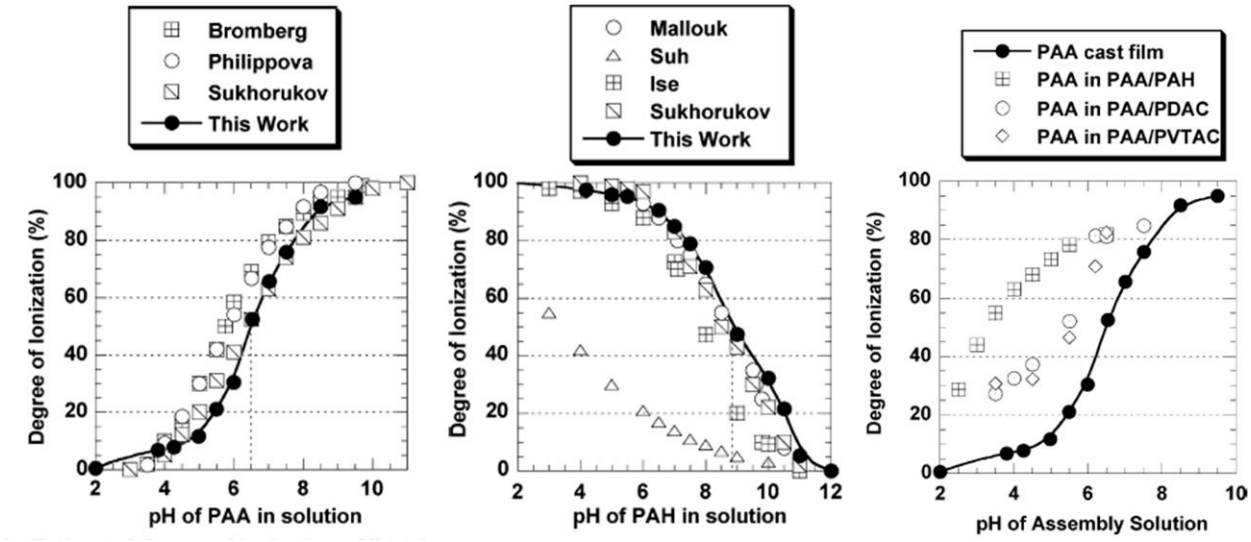

Figure 2.8. Degree of ionization of PAH and PAA in solution. Degree of ionization of PAA in ISAM films containing weak and strong polyelectrolytes. Reprinted (adapted) with permission from Choi, J.; Rubner, M. F. Influence of the Degree of Ionization on Weak Polyelectrolyte Multilayer Assembly. *Macromolecules* **2005**, *38* (1), 116-124.[27] Copyright 2005 American Chemical Society.

Although electrostatic attraction between ionized groups is the primary growth mechanism for polyelectrolyte-based ISAM films, weaker secondary interactions such as hydrogen bonding and hydrophobic interactions can become dominant forces for chains with low linear charge densities.[36-37] Clark *et al.* studied the pH-dependent growth selectivity of PAH/PAA and PEI/PAA ISAMs on carboxylic acid (COOH) and oligoethylene glycol (EG) terminated SAMs.[36] EG is a neutral polymer with low interfacial energy. At a low pH of 2.5, the lowly-charged PAA interpenetrated through the very thin PAH layers and developed hydrogen bonds with COOH and other PAA layers, which enhanced absorption. With increased pH, electrostatic repulsion from the

increasingly ionized PAA chains and the COOH-terminated SAMs diminished the hydrogen bonding effects. Since PAH and EG are strong hydrogen bonding donors and acceptors, respectively, PAH/PAA ISAMs thicknesses at the pH 4.8 were found to be greater on EG SAMs compared to the weakly ionized COOH SAMs. For the neutral pH 7.0, electrostatic attractive forces again became the dominant driving force for PAH/PAA ISAM growth, and the ISAMs preferred COOH over EG SAMs. Yang and Rubner developed PAA and polyacrylamide (PAAm) ISAMs at pH 3.0 entirely from hydrogen bonding.[37] PAA and PAAm both act as hydrogen bond donors and acceptors, and this hydrogen bonding was confirmed by FTIR. When immersed in water at pH 5.0 or higher, the ionization of PAA overwhelmed the hydrogen bonding, so the PAA/PAAm film was dissolved. The dissolution of the film in higher pH's was avoided by thermal crosslinking, which induced imide bonding, stabilized the film up to pH 7.0, and allowed for functional film patterning.

On fully-charged weak polyelectrolytes, counterions were reported to condense on ionized groups and screen charges with similar conformation changes to strong polyelectrolytes.[28] For highly-charged polyelectrolytes, greater solution ionic strength diminished the extended conformations and also caused a release of water from the chains nonpolar, hydrophobic moieties. Since divalent counterions (SO_4^{2-} from Na_2SO_4) could bind a greater number of ionized groups, they were found to have a stronger screening effect than monovalent counterions (ClO_3^- from $NaClO_3$). The addition of counterions to an uncharged weak polyelectrolyte had a vastly different outcome. At low ionic strength ($\leq$0.05 M), the counterions produced a "salting-out" effect, in which the chains became fully dehydrated and hydrophobic segmental interactions caused a complete collapse of the chain. However, at greater ionic strength (>0.05 M) for the uncharged polyelectrolytes, the nonelectrostatic van der Waals adsorption of the anionic counterions to

functional groups resulted in a rehydration and extension of the chains, known as a "salting-in" effect. The "salting-in" effect occurred with Na_2SO_4 and $NaClO_3$, but not with NaCl. Since weak polyelectrolytes contain a dynamic degree of ionization, their counterion interaction is profoundly different than strong polyelectrolytes.

2.1.4.4 Linear-growth. As initially established by Decher, ISAM films containing strong and highly-charged polyelectrolytes (e.g. PSS and PAH) generally exhibit linear-growth in ISAM films with interpenetration spanning two to three layers.[18, 22-23] Linear-growth was also demonstrated in PAH/PSS films with the addition of counterions.[31, 38] Ladam *et al.* provided clarity to the structure of linear-growing films with the introduction of a three domain model.[38] The model explained that in a "precursor" domain (zone I), film growth is dictated by substrate properties and thus has a different structure than the bulk of the film. Zone I was found to be composed of approximately three bilayers and the growth rate was markedly slower than later domains. As the film grows, an outer surface domain (zone III) forms with attributes of typical polyions that swell (extend) and collapse with the rinsing of water and salt, respectively. The surface domain drives the growth of the film by charge overcompensation, but its thickness remains relatively constant. Beyond this thickness, a central bulk domain (zone II) is conceived, which continues to grow with increased bilayers. Zone II is more characteristic of zwitterions that swell and deswell with an increase or decrease of the ionic strength of solution, respectively. Since counterions are primarily stored in the bulk of the film, represented by Zone II, an increase in their concentration partially breaks ionic bonds and induces swelling.

2.1.4.5 Exponential-growth. More recently, exponential-growth film growth has been extensively studied in ISAM films assemblies.[39-48] Exponential-growth generally involves a polyelectrolyte with a chemical structure that is conducive for diffusion. Exponential-growing

films were first reported in ISAMs with natural polyelectrolytes through the use of polyelectrolytes poly(L-lysine) (PLL) and alginate for modeling of tissue healing.[39] The film surfaces for exponential-growing films were less structured than linear-growing film and more characteristic of hydrogels. At that point in time, there was no established understanding for the mechanism of exponential-growth. Picart *et al.* later utilized optical waveguide lightmode spectroscopy (OWLS) in poly(L-lysine) and hyaluronic acid (PLL/HA) polyelectrolyte films.[41] During film growth, the refractive index near the substrate was reported to increase and decrease, related to the diffusion of free PLL chains "in" and "out" of a strongly bound multilayer film. Although a large portion of the PLL anchored strongly into the film, another portion was "free", diffusing chains that interacted weakly with the strongly bound HA chains. Since the number of free diffusing chains is proportional to the relative thickness, the thickness increases exponentially per bilayer. The exponential-growth occurred when HA was deposited, as the free PLL chains (which overall concentration increased per bilayer) diffused to the film surface to form polyelectrolyte complexes. During the growth of the film, free chains can be exchanged with other diffusing chains or anchored chains. Soon after this report, the free chain diffusion concept was confirmed on a molecular level through the use of dye-labeled versions of PLL/HA and confocal laser scanning microscopy (CLSM), by the same group.[42] The diffusion process was again established in poly(L-glutamic acid) and poly(L-lysine) (PGA/PLL) multilayer films.[40] Exponential-growing films were shown to contain substantially larger growth islands and roughness values in the initial bilayers when compared to linearly-growing films.

Hübsch *et al.* combined various ratios of diffusing (PGA) and non-diffusing (PSS) polyanions with the polycation PAH.[43] As expected, with a greater concentration of PGA, the growth became increasingly exponential. Free PGA chains were found to diffuse "in" and "out" when the film was

brought in contact with the PGA and PAH solution, respectively. Therefore, it was confirmed by QCM that the thickness was unaffected when the chains diffused "in" and increased when the chains diffused "out". However, a puzzling phenomenon arose when the exponential-growth abruptly transitioned over to linear-growth at a certain thickness. It was proposed that due to the diffusion coefficient (D_p) of the diffusing polyanion and the limited immersion time (t) of the film in the polycation solution, the surface domain or "Zone III" is restricted to a thickness equal to $(D_p t)^{1/2}$. Basically, only a limited number of free polyanions could diffuse to the surface and at the critical thickness, the thickness slope became constant. Since the surface domain remained a constant thickness, further growth essentially increased the size of the central zone. The linear regime after an exponential regime had a substantially larger slope, compared to a purely linear-growing film, and was also inherently different in character (diffusion-based). Thus, Hübsch *et al.* fundamentally applied the three-domain model from Ladam *et al.* to the diffusing polyelectrolytes. Salomäki *et al.* soon thereafter came out with a nearly identical theory for polyelectrolyte diffusion, based on the temperature of the polyelectrolyte solution.[44] They reported at a certain heightened temperature, the zone III can dominate the entire thickness of the film, related to the increased level of free chain diffusion. It was shown that even assemblies of PAH/PSS that contain the strong polyelectrolyte PSS can experience exponential-growth at a high enough temperature, primarily due to increased diffusion rates. Porcel *et al.* later proved a variation to the Hübsch and Salomäki theories (**Figure 2.9**).[45] Porcel showed that for a PLL/HA multilayer film that consisted of a large thickness (80 bilayers) and had already transitioned from the exponential-growth to the linear-growth regime, free chain diffusion still occurred to the bottom of the film. They deposited the last layer as a dye-labeled version of PLL, and found through CLSM that the chains diffused to the bottom of the film. Their explanation for the transition from linear to exponential-growth

was based on the saturation concentration of free chains within a film, even as the polyelectrolyte concentration was increased. It should be noted that the group utilized both a dipping and spraying self-assembly technique.

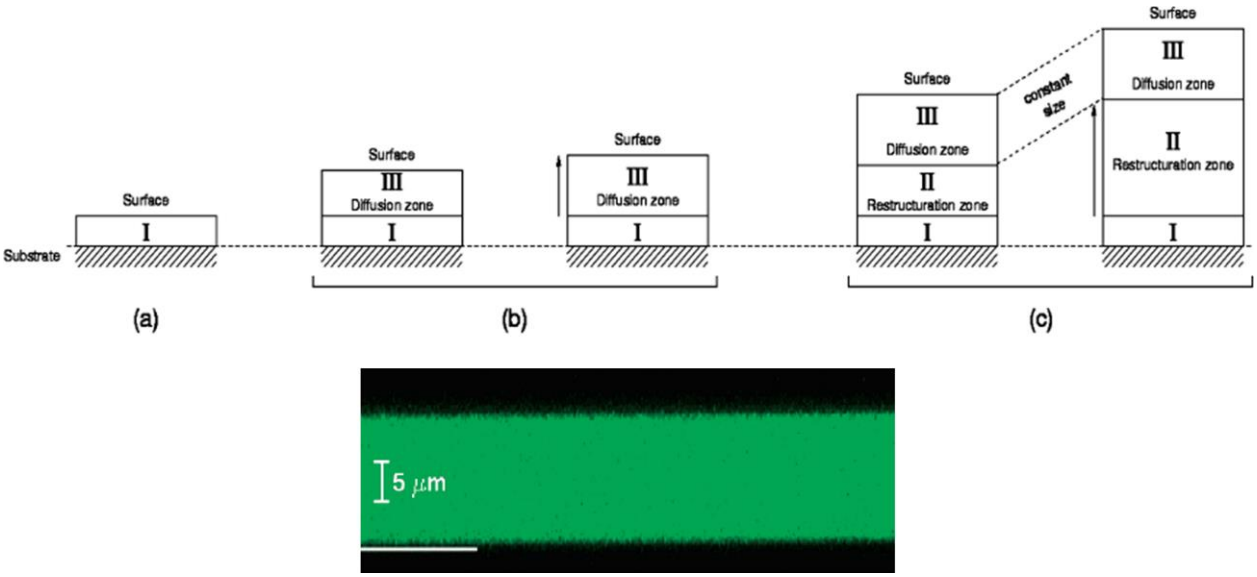

Figure 2.9. Schematic of the three zones model that constitutes exponential growth. A CLSM image of an 81 bilayer PLL/HA ISAM film with the last layer being PLL labeled with a fluorescent dye, fluorescein Isothiocyanate (FITC). As the bottom of the film is indicated by the white horizontal line, the CLSM image exemplifies a thorough diffusion of free PLL chains. Reprinted (adapted) with permission from Porcel, C.; Lavalle, P.; Ball, V.; Decher, G.; Senger, B.; Voegel, J.-C.; Schaaf, P. From Exponential to Linear Growth in Polyelectrolyte Multilayers. *Langmuir* **2006**, *22* (9), 4376-4383.[45] Copyright 2006 American Chemical Society.

PAA was later discovered to possess diffusing properties that resulted in exponential growth in PAH/PAA, especially augmented in lower molecular weight batches.[46] This finding was later applied to polyethylenimine (PEI)/PAA films, where free chains were found by CLSM to fully diffuse throughout the thickness of the film.[47] In a later study, the pH of PAH/PAA ISAMs was adjusted together, similar to the manner done by Rubner's group, to show that Regions I, III, and

V (pH 10 to 12) displayed linear-growth, whereas Regions II and IV exhibited exponential-growth.[48] Essentially, the linear charge density of the two polyelectrolytes correlated to the level of diffusion and the type of growth. They showed specific growth and viscoelastic properties that pertained uniquely to each pH regime.

2.1.4.6 Covalently-crosslinked polyelectrolyte ISAMs. The construction of polyelectrolyte-based ISAMs is only practical if the films possess the necessary mechanical and/or chemical stability required for longevity. After developing and characterizing the exponentially-growing PLL/HA hydrogel ISAMs, Picart and co-workers later showed that these films could be covalently crosslinked to vastly improve their mechanical robustness.[49] Crosslinking was accomplished by immersion of the films into a 1-ethyl-3-(3-dimethylamino-propyl)carbodiimide (EDC) and N-hydrosulfosuccinimide (sulfo-NHS) solution. The PLL amine and HA carboxylate groups allowed for the creation of covalent amide linkages between the polyelectrolyte chains, upon immersion in the EDC/sulfo-NHS solution. The crosslinked films showed a 4 to 10-fold enhancement in the Young's modulus over the uncrosslinked films, which was attributed to a stiffening of the film by the covalent bonds. Furthermore, crosslinking of the PLL/HA films, as well as later studied PLL/PGA, PLL/poly(alginic acid) (Palg), PLL/poly(galacturonic acid) (Pgal) films, also dramatically improved biological cell spreading and adhesive properties.[49-50]

Similar to the biological polyelectrolytes, the amine and carboxylate groups on PAH and PAA provide the necessary elements for the formation of covalent amide cross-linkages. Crosslinking of PAH/PAA ISAMs has proven to drastically enhance film stability and can be accomplished through thermal[26, 51-56] or chemical (EDC/sulfo-NHS)[57] means. Harris *et al.* were some of the first to examine the formation of covalent amide crosslinks between PAH and PAA using FTIR, following different thermal treatments at moderate (130 ^{o}C) and high (215 ^{o}C) temperatures.[51] Liu

et al. developed exponentially-growing PAH/PAA-$CaCO_3$ (PAA-complexed $CaCO_3$ NPs) ISAMs and thermally crosslinked the films after processing (180 ºC for 5 h).[52] The PAH/PAA-$CaCO_3$ films were examined with a Hysitron Triboindenter (nanoindentation), and it was discovered that thermal crosslinking increased the hardness and Young's modulus by 51% and 6%, respectively. The addition of $CaCO_3$ NPs into the films greatly enhanced the mechanical properties over pure PAH/PAA films. The thermally crosslinked PAH/PAA-$CaCO_3$ films withstood a thorough qualitative rubbing analysis and a tape pull test (ASTM D 3359 standard), which attested to the film adhesion. Pavoor *et al.* used nanoindentation to examine hardness and Young's modulus on ISAM films with PAH (pH = 7.5) / PAA (pH = 3.5), both PAH/PAA pH at 3.5, and both PAH/PAA pH at 6.5.[53] It was discovered that as-assembled PAH/PAA films with both pH set to 3.5 and 6.5 showed the highest Young's modulus and hardness, respectively. Thermal crosslinking at a moderate temperature (150 ºC 6 h) also slightly increased the mechanical properties of PAH (pH = 7.5) / PAA (pH = 3.5) ISAMs, although thermal crosslinking was not reported for the other pH conditions. Yang *et al.* created ISAMs containing different combinations of PAH, PAA, and positively-charged, aminopropyltrimethoxysilane-capped SiO_2 NPs (10-20 nm).[54] After thermal crosslinking (215 ºC for 2 h), composite films with all three components had greater mechanical stability than pure PAH/PAA and SiO_2/PAA films. The mechanical stability was assessed using a microtribometer, which had frictional wear and scratch-testing capabilities. Dai *et al.* used increasing normal forces from AFM contact mode to evaluate the mechanical properties on ISAM films of pure PAH/PAA and composite films with separate stacks of PAH/PAA and C_{60}-ethylenediamine adduct (C_{60}-EDA)/PAA.[55] After thermal crosslinking of the films, the mechanical and chemical stability increased, as uncrosslinked films were soluble in polar organic solvents (DMF), while crosslinked films were not. Pure PAH/PAA films showed higher mechanical

stability compared to composite films, which was attributed to the higher molecular weight of PAH over C_{60}-EDA. Thermal crosslinking of PAH/PAA has also been utilized for the cohesive strengthening of paper fibers.[56] PAH/PAA showed to drastically increase the tensile index of the fiber-to-fiber joints, as well as the overall sheet strength.

Besides PAH/PAA ISAMs, the polycation 4-diazodiphenylamine/formaldehyde condensate hydrogen sulfate (diazo-resin; DAR) has shown to be an attractive material for providing film stability by crosslinking.[58-61] DAR is typically photo-crosslinked by exposure to UV-irradiation and forms covalent linkages with polyanions bearing sulfonate groups (PSS) or carboxylic groups (PAA). More discussion on DAR can be found in **Chapter 4.**

2.1.4.7 Nanoparticle ISAMs. Along with polyelectrolytes, the growth processes of nanoparticle layers in ISAM films has also been thoroughly explored. Since the original work done by Iler,[20] ISAMs containing inorganic oxide nanoparticles such as silica (SiO_2 NPs) or titania (TiO_2 NPs) have received considerable attention. Lvov *et al.* studied the characteristics of 45 nm diameter SiO_2 NPs and PDDA layer adsorption using a quartz crystal microbalance (QCM).[62] It was discovered that the growth rate and the surface coverage increased with SiO_2 NP solution concentration. The introduction of 0.25 M NaCl into the SiO_2 NP solution increased the layer thickness by a factor of seven (layer thickness of 20 nm and 143 nm for 0 and 0.25 M NaCl, respectively), demonstrating that counterions have a substantially larger impact on SiO_2 NPs when compared to polyelectrolytes. Upon the inclusion of PDDA at different concentrations directly into the SiO_2 NP solution, maximum flocculation occurred at a SiO_2/PDDA mass ratio of 64, which represents the condition of charge neutrality or 1:1 stoichiometry. Since the SiO_2/PDDA mass ratio was only 13 to 31 (based on ionic strength) in the ISAM film, then charge neutrality was therefore not achieved, as excess PDDA chains were present in the film. The differences were attributed to

the greater charge density on the PDDA chains over the fixed charge distribution the SiO_2 NPs. Additionally, it was revealed through QCM that the PDDA chains only reached a 1-2 nm depth with each layer, elucidating the likelihood that polymer layers only formed on the top and bottom of SiO_2 NPs, as well as the existence of "long-range charge pairs" in the film. Hence, the analysis clarified that the polyelectrolyte-nanoparticle ISAM adsorption mechanisms was inherently different than only-polyelectrolyte films. In a subsequent study, Lvov *et al.* reported that adsorption layer saturation occurred very rapidly for PDDA and SiO_2 NPs at 20 s and 2 s, respectively, when every PDDA layer was dried.[63] Using the SiO_2/PDDA mass ratio of ~13, the films were found to contain 30% pore, 10% PDDA, and 60% SiO_2 NP (0.6 packing coefficient) by volume, which was very close to the theoretical 63% for closely packed spheres. As determined by ellipsometry, the porosity of the film contributed to an overall refractive index of 1.25 at 633 nm, which was lower value than pure silica at 1.46. The work done by Lvov *et al.* laid the groundwork for anti-reflection coatings, as to be discussed later.

2.1.5 Nanoparticle and Colloidal Stabilization.

The self-assembly of polymers onto nanoparticle surfaces in solution functions as a means of stabilization, functionalization, and/or encapsulation. Colloidal stabilization is necessary for resistance against particle aggregation, which can occur due to particle collisions from centrifugation or Brownian motion.[64-65] Stabilization is achieved in solution through electrostatic, steric, or electrosteric mechanisms.[64-67]

2.1.5.1 Electrostatic Stabilization. Electrostatic stabilization is described by DLVO theory (establishd by Derjaguin, Landau, Verwey and Overbeek), accounting for both attractive forces and repulsive electrostatic forces.[64-67] Attractive forces are comprised of London dispersion interactions and van der Waals forces.[64-67] Because of the large number of atoms in a nanoparticle,

the attractive forces are more extensive than single atoms in solution. The attractive potential energy for two identically sized spherical particles with small separation distance is[64-67]

$$V_A = \frac{-Aa}{12h} \quad (\mathbf{2.2})$$

where A is the Hamaker constant, a is the spherical radius, and h is the separation distance. The Hamaker constant encompasses the attractive interactions, as well as the material density. As the solvent medium itself also has an attractive force, its Hamaker constant must be subtracted out in calculating the overall Hamaker constant for the dispersion material (i.e. $A = (\sqrt{A_{particle}} - \sqrt{A_{medium}})^2$; A_{SiO2} = 6.5 x 10^{-20} J, A_{H2O} = 3.7 x 10^{-20} J so A = 0.39 x 10^{-20} J).[64] The attractive forces are counteracted by mutual electrostatic columbic repulsive forces that arise from neighboring nanoparticles of similar surface charge in solution. The surface charge is founded by the dissociation of surface ions upon transfer of an ionogenic material to an aqueous medium, such as silica,

$$-SiOH \leftrightarrow -SiO^- + H^+ \quad (\mathbf{2.3})$$

which holds a negative surface charge in solution. The surface charge for oxides is pH dependent, with a negative surface charge at high pH, positive surface charge at low pH, and zero surface charge at a moderate pH (point-of-zero charge; isoelectric point; PZC).[64, 66] The PZC is largely dependent on the material; the PZC for SiO_2 and Ag_2O is pH 2.0 and 11.2, respectively.[66] The lack of surface charge at the PZC eliminates the repulsive forces and aggregation inevitably follows. Whether or not aggregation is a desirable effect, maintenance of the surface charge is critical. An accurate depiction of the charged dispersion also includes some level of counterions in the solution. For negatively-charged particles, positive counterions are attracted and adsorb strongly onto the surface to form what is known as a "Stern layer" (**Figure 2.10**).[65, 67-68] The counterion

concentration continuously decreases with further distance from the particle. Negatively-charged "co-ions" are also repelled by the particle's surface charge and increase in concentration with increased distance.[65, 67-68] The surrounding counterions and co-ions form a "diffuse layer".[65, 67-68] Together, the Stern and diffuse layers are referred to as an "Electrical double layer", which can be portrayed as an electrical cloud surrounding the particle.[65, 67-68] The double layer thickness is inversely proportional to the counterion concentration and is also known as the Debye length (κ^{-1}).[64-65]

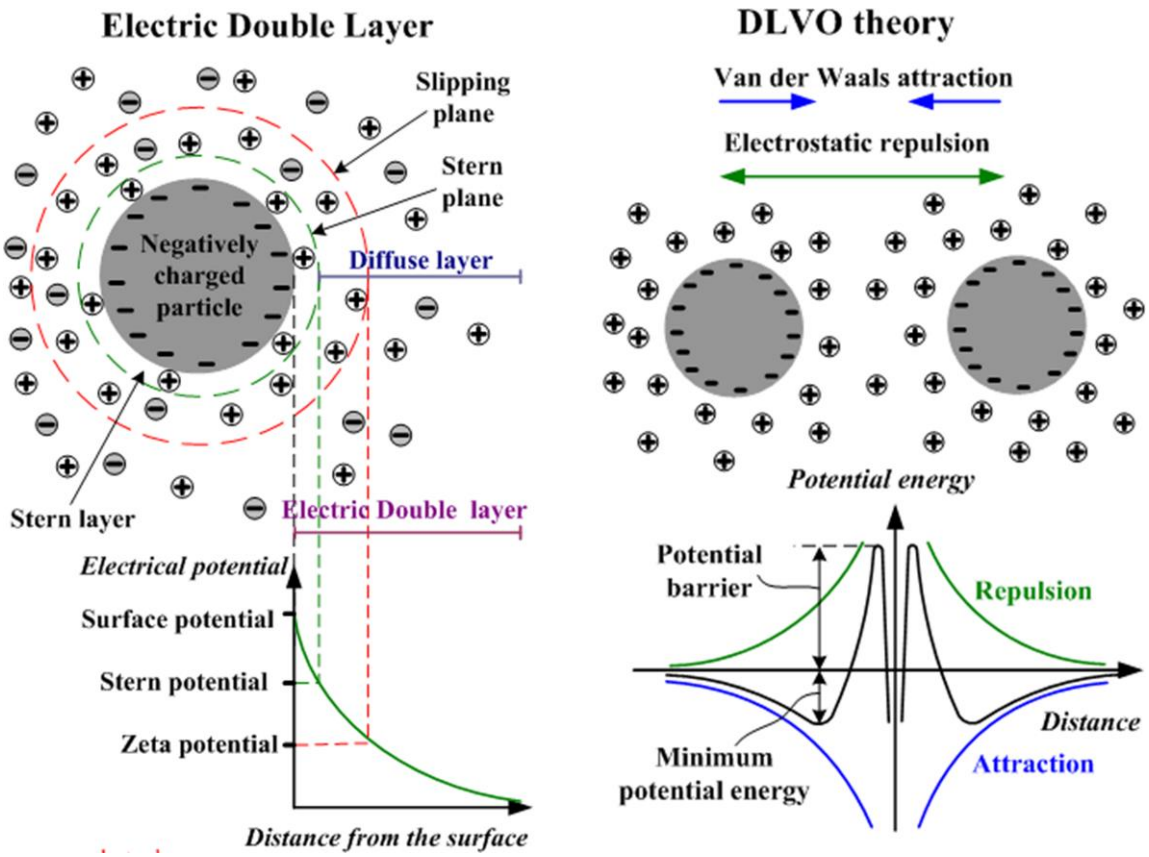

Figure 2.10. Schematic of the Electrical Double Layer surrounding a charge particle, along with the corresponding Surface potential, Stern potential, and ζ-potential. DLVO theory schematic related to van der Waals attractive forces and electrostatic repulsive forces. This figure found on

the webpage titled, “Stabilization of colloids”, by Dr. Dmitri Kopeliovich. The work on the page is licensed under the Creative Commons Attribution-Noncommercial-Share Alike 3.0 License.

The electrical potential is the highest at the surface of the particle, drops off linearly in the Stern layer, exponentially in the diffuse layer, and then reaches approximately zero at the outside of the double layer.[64-65] The overall charge of the double layer and the particle surface are equal, so that the entire aqueous system is effectively neutral.[65-68] With application of an external electrical field to the particle solution, a portion of the fluid that contains ions close to the particle surfaces continues to move with the particles, where another portion moves with the electric field.[65, 68] The separation of these two regions is called the “slipping plane” and the potential at this separation is known as the zeta potential (ζ-potential).[65, 68] Although the ζ-potential is not technically the same as the electrical surface potential or Stern layer potential, it is generally close in magnitude, easily measured, and therefore, quite useful for characterization.[64, 68] The electrical repulsive potential energy is represented as,[64, 67]

$$V_R = 2\pi\varepsilon a\zeta^2 e^{-\kappa h} \text{ for } \kappa a << 1 \qquad (\mathbf{2.4})$$

$$V_R = 2\pi\varepsilon a\zeta^2 \ln(1 + e^{-\kappa h}) \qquad \text{for } \kappa a >> 1 \qquad (\mathbf{2.5})$$

where ε is the permittivity of the solvent, a is the shared radius of two spheres, ζ is the ζ-potential, κ is the inverse Debye length, and h is the separation distance. As stated previously, the Debye length is largely dependent on the counterion concentration (for symmetrical electrolytes),[64, 67]

$$\kappa^2 = \frac{2n_0 e^2 z^2}{\varepsilon k T} \qquad (\mathbf{2.6})$$

where n_0 is the counterion concentration, e is the elementary charge of an electron, z is the counterion valency, k is Boltzmann's constant, and T is the absolute temperature. Essentially, spheres with a larger radius, greater surface charge, lower counterion concentration, and closer separation distance have increased repulsive energy. The repulsive energy becomes significant as the electrical double layers of two different particles overlap.[67] The combination of both the attractive and repulsive potential energies is equivalent to the overall potential energy as,

$$V_T = V_A + V_R \quad (\mathbf{2.7})$$

and is generally expressed in units of kT.[64-65, 67] Here, the repulsive energy opposes the attractive energy, given that **Equation 2.2** is negative and **Equations 2.4** and **2.5** are positive. The "Potential barrier" or "primary maximum" (V_{max}) represents the activation energy barrier that the particles must exceed for aggregation (**Figure 2.10**).[64-65] For kinetic stability, i.e. resistance against aggregation by Brownian collisions, V_{max} must exceed 1.5 kT.[64] However, for long-term stability, V_{max} must exceed ~15-20 kT with a ζ-potential of approximately -20 mV.[64, 67]

2.1.5.2 Steric Stabilization and Polymer Brushes. The attractive forces between particles can also be counteracted by steric stabilization, which involves the adsorption of polymers onto particle surfaces. The polymers strongly anchor onto the surface and create a dense coating, often extending loops and tails into the solution.[64, 66-67, 69-70] The polymer layer creates repulsive forces between the particles called steric repulsion.[64, 66, 69-70] As two particles approach one another with a separation distance of *d* and a polymer chain length of *δ*, there exists three domains for Steric interactions: The "noninteractional" ($d \geq 2\delta$), "interpenetration" ($\delta \leq d \leq 2\delta$), and the "interpenetration plus compressional" domain ($d < \delta$).[69-70] The noninteractional domain does not contain any substantial repulsive forces since the interactions between the chains is nonexistent.[69] In the interpenetration domain, the polymer chains are close enough for intermixing.[64, 66-67, 69-70] In

this domain, steric repulsion arises from "volume restriction effects" or the configurational entropy cost as a result of multiple polymer chains spatially coinciding. Additionally, as the solvent maintains strong interactions with the polymer chains, increased interpenetration leads to a buildup of osmotic pressure. As the particles and chains intermingle closer into the interpenetration plus compressional domain, opposing chains compress on one another and the polymer concentration increases significantly.[64, 69-70] As the chains compress, the steric repulsion gains an elastic contribution, cumulative with the mixing repulsions (volume restriction, osmotic pressure).[69-70] Therefore, the steric repulsion begins in the interpenetration domain and dramatically increases in the interpenetration plus compressional domain.

Steric stabilization is advantageous since unlike electrostatic stabilization, it is independent of counterion concentration and it is effective in nonaqueous solvents where electrostatic stabilization would be impossible.[64, 66, 70] In fact, the solvent stability of a polymer-coated particle is based on the solubility of the polymer, which can be defined by the Flory-Huggins interaction parameter χ.[64] When $\chi < 0.5$, the polymer is in a "good" solvent and the chains expand as a result of desirable interactions with the solvent's small molecules. At $\chi = 0.5$, the solvent is recognized as a "theta" solvent, in which case the polymer acts ideal. A "poor" solvent corresponds to $\chi > 0.5$, and here, the polymer collapses because of poor interactions with the solvent molecules. Above a certain polymer volume fraction in a poor solvent, the polymer becomes immiscible.[64] Miscibility is correlated with a negative change in free energy ($\Delta G < 0$).[64]

In the spontaneous adsorption of polymers onto particle surfaces, dewetting of the polymer chains and the particle surfaces is first necessary, which requires energy ($\Delta G < 0$) attributed to the attractive interactions between the material and the solvent.[66] The fixation of polymer chains onto the surface requires energy, due to the loss in configurational entropy. However, the dewetting and

spontaneous polymer adsorption processes also release energy back into the solvent ($\Delta G > 0$). Essentially, the combination of these energies impacts the capability for adsorption of the polymer on the surface.[66] Another representation is the Flory surface parameter χ_s, which must be greater than the critical value χ_{SC} for adsorption ($\chi_s > \chi_{SC}$).[64] For effective steric repulsion, the particle must have high surface polymer coverage, which requires a sufficient polymer concentration for adsorption.

Typically, polymers for steric stabilization either are composed of copolymers or a polymer with a functional group.[64, 66] In the example of copolymers, one type of monomer would adsorb strongly onto the surface and the other type would have favorable interactions with the solution molecules. For polymers with functional groups, either the functional group or the polymer would adsorb onto the surface and the other component would interact with the solvent.

Polymer brushes are attractive for steric stabilization, attributed to the high surface density of grafted polymer layers.[70-75] The tethering of polymer layers onto particles allows for dispersion and long-term stability in solvents that would otherwise be impossible for uncoated particles.[73, 76-77] For instance, poly(ethylene glycol) (PEG) and polystyrene (PS) brushes are utilized for stabilization in aqueous and organic solvents, respectively.[74, 76-78] Polymer brushes can also consist of more than one type of polymer chain, permitting the surface to "switch" wettability properties, among other applications.[73] The attachment of the polymer layers can either be achieved by "graft-from" or "graft-to".[73, 75] Grafting-from entails polymerization of brushes directly onto initiator groups, covalently bound to the surface.[73, 75] Brushes can be grown with high surface densities and controllable molecular weights, given that the monomers can easily diffuse through already-tethered chains.[73, 75] The grafting-to of polymer brushes is perhaps more straightforward, as it involves simply the tethering of previously-synthesized polymer chains onto surfaces.[73, 75] In both

the graft-from and graft-to techniques, the initiator groups or the polymer chain terminal head groups require a favorable interaction with the surface composition (or functionalization) for the formation of covalent bonds.[73, 75] Similar to SAMs, silane derivative groups are often used with hydroxylated surfaces, whereas organosulfur derivative groups, specifically thiols, are typically used for noble metals (gold, silver).[72-78] Without these critical functional groups, the adsorption of polymer brushes is improbable.[72, 74]

The adsorption kinetics for graft-to polymer brushes has been extensively investigated by *in-situ* and *ex-situ* analysis methods, including plasmonic nanoparticle sensing, atomic force microscopy (AFM), QCM, simulations, and solution concentrations changes.[72, 74] As confirmed by these analyses, the grafting of polymer brushes follows three growth regimes, and a thorough understanding of these processes is vital for their utilization in colloid or particle stabilization. The first regime is characterized by the rapid diffusion and tethering of chains to the surface.[72, 74] This regime is referred to as the "diluted regime" where the chains adsorb as an unstretched polymer coil. In a good solvent, the unstretched coils are commonly referred to as "mushrooms" or "blobs" (**Figure 2.11a**), and in a poor solvent, they are referred to as "pancakes", which represents the more favorable polymer interaction with the substrate over the solvent.[70, 72-74] The mushroom conformation is reported to have an equivalent radius (R_e) equal to or larger than the radius of gyration ($R_g = N^{1/2}a$), and the spacing between neighboring chains is greater than twice the Flory radius (R_F).[72, 74] Due to the relaxed conformation in this stage, each chain possesses a relatively high surface area, which limits the chain density.[72] Therefore, the rate of adsorption in the first regime is independent of the polymer concentration, as solution is always replete with excess polymer.[74]

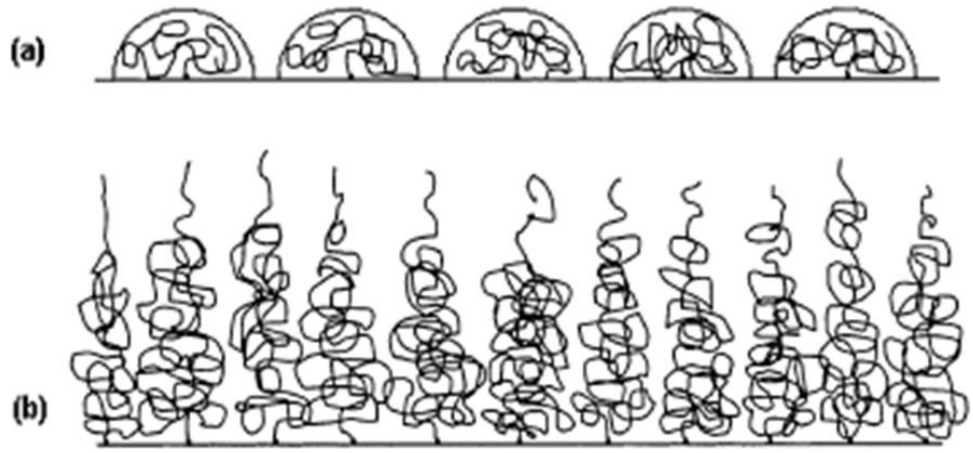

Figure 2.11. Polymer brushes with (**a**) mushroom and (**b**) and stretched conformations. Reprinted (adapted) with permission from Penn, L.; Huang, H.; Sindkhedkar, M.; Rankin, S.; Chittenden, K.; Quirk, R.; Mathers, R.; Lee, Y. Formation of Tethered Nanolayers: Three Regimes of Kinetics. *Macromolecules* **2002**, *35* (18), 7054-7066.[72] Copyright 2002 American Chemical Society.

In the second regime, the increasing energy barrier with greater chain crowding substantially slows the additional tethering of chains, and thus, this regime is also known as the "latent" regime with an adsorption rate proportional to a log(time) scale.[72, 74] During the second regime, the mushrooms begin to rearrange and extend perpendicular to the surface to regain the loss configurational entropy upon adsorption.[74] The rearrangement rate is greater at heightened temperatures and for lower molecular weights.[74]

The lateral contraction and vertical stretching of the chains initiates the third regime, and the newly available surface area leads to a drastically increased tethering rate that is proportional to the polymer concentration.[72, 74] The brush layer density increases to more than double that of the first regime, until saturation is achieved. At the third regime, $R_e < R_g$ and the neighboring chain spacing decreases to less than twice the R_F. In this regime, the chains stretch from the surface in a good solvent (**Figure 2.11b**), and form "pinned micelles" or "clusters" in a poor solvent.[73] The stretched chain conformation originates from the counterbalance of the osmotic pressure and the

stretching free energy.[71, 73] In a brush layer, the osmotic pressure φ is represented as $\varphi \approx (N\sigma/h)$, where N is the degree of polymerization, σ is the surface density, h is the thickness. The free energy related to osmotic pressure is $f_{osmo} \approx kTwN\varphi$, where w is represented as the "excluded volume parameter", which is correlated to the strength of repulsion between chain units. The osmotic pressure and the brush density profile have been represented as parabolic with a semi-dilute and dilute characteristic close to and far from the surface, respectively. The configurational entropy penalty upon stretching of chains associates with a free energy equal to $f_{stretch} \approx kT(3h^2/2Na^2)$.[71, 73] The total free energy of the brush is $\Delta f \approx f_{stretch} + f_{osmo}$, and minimization with respect to the thickness, h, leads to $h \approx N(w\sigma a^2)^{1/3}$. Where R_g (which approximately represents unstretched chains) grows with $N^{1/2}$, the stretched brush height increases directly proportional to N.

2.1.5.3 Electrosteric Stabilization. In the adsorption of polyelectrolytes onto surfaces for electrosteric stabilization, both electrostatic and steric stabilization methods are utilized, along with their associated repulsion energies. In this scenario, particles function as substrates for ISAM development and their surface charge provides the electrostatic driving force. Early electrosteric stabilization work used one polymer layer adsorbed onto colloidal particles. Cesarno *et al.* examined the adsorption of poly(methacrylic acid) (PMMA) onto alumina particles as a function of pH and added PMMA.[79] Adsorption was restricted above the PZC at pH 8.7, where both PMMA and alumina possess negative surface charge. Below the PZC, adsorption increased with decreased pH, until the sedimentation point occurred due to a substantial decrease in the degree of ionization of PMMA. Low concentrations of PMMA led to bridging flocculation as chains adsorbed onto multiple particles at once, which also associated with low ζ-potential magnitudes. At an optimum added amount of PMMA, alumina showed lower sedimentation levels and greater stability over bare alumina because of the electrosteric stabilization. In most likely the first report of particles

with polyelectrolyte multilayers, Keller *et al.* developed alternating layers of redox cationic polyelectrolytes and anionic zirconia phosphate sheets grown directly onto high surface area silica particles.[80] Gittins and Caruso later produced PDDA/PSS ISAMs directly onto gold nanoparticles (AuNPs).[81-82] The AuNPs were regarded as a necessary platform for monitoring the ISAM growth as their localized surface plasmon resonance (LSPR; more to be discussed on this below) wavelength is highly dependent on the surrounding dielectric medium (and refractive index). Because of this dependency, the LSPR extinction peak (λ_{LSPR}) was reported to redshift between 2 to 5 nm with a greater number of polyelectrolyte layers. Low salt concentrations (1 mM NaCl) were found to be necessary to partially screen the polyelectrolyte charge density, otherwise, the electrostatic repulsions would restrict wrapping of the particles, which was especially true for particles with diameters smaller than κ^{-1}. It was also found to be critical to use low molecular weight polyelectrolytes (M_w = 15 – 20k) at sufficient solution concentrations to avoid bridging flocculation. In other words, low polyelectrolyte concentrations and high molecular weight chains can cause attachment of more than one particle at once, leading to aggregation. Aggregation was associated with redshift of the λ_{LSPR} greater than 50 nm. It was noted that despite the negative surface provided by sodium citrate (small molecule capping layer), the attachment of anionic alkanethiol SAMs to the particles was a necessary step for their stability. After the successful creation of the polyelectrolytes ISAMs onto the AuNPs, the AuNPs were dissolved by a cyanide solution to leave a hollow nanocapsule, left intact and stable. Schneider and Decher more comprehensively expanded on the work and further explored electrosteric stability in PAH/PSS ISAMs on AuNPs for hollow nanocapsule production.[83-85] In the earliest report, it was highlighted that the attachment of thiols to the AuNP surfaces was unnecessary for stability (as done previously by Gittins and Caruso) with appropriate deposition procedures of the polyelectrolyte layers.[83] The

thickness per layer was methodically presented by the PSS UV absorption increases, along with the λ_{LSPR} redshifts, for a total shell thickness of 7.5 nm after 20 monolayers. With a removal of the excess citrate and a drop-by-drop deposition of the AuNPs into the polyelectrolyte solution, aggregation was avoided and nanocapsule stability was ensured for up to year. A similar processing method was used in a following report, but an organic fluorescent dye was covalently attached to PAH for the last ISAM layer.[84] Fluorescence quenching was substantially reduced following the cyanide dissolution of the AuNP core, as well as a greater number of polyelectrolyte layers before deposition of the last dye layer. Therefore, the fluorescence quenching was primarily attributed to a fluorescence radiative rate degradation with a close proximity of the dye to the core. The effects of polyelectrolyte bridging flocculation was deeply investigated in later paper by the same authors.[85] For a single-layer polyelectrolyte nanoparticle coating, the number of polyelectrolyte chains to AuNPs was separated into three regimes. The first regime related to an excess of colloids to polyelectrolyte chains (<10 chains/NP), in which the surfaces were not fully covered and the stabilization was weak. In the second regime, the polyelectrolyte and AuNPs charges were nearly in a 1:1 stoichiometry (10 – 20 chains/NP), causing a drastic rise in aggregates and sedimentation (**Figure 2.12**). For the third regime, the polyelectrolyte chains were in excess of AuNPs (>20 chains/NP), resulting in the greatest stability. However, it was found that below 10,000 chains/NP, there was an incomplete recovery of coated AuNPs after centrifugation (<60%), which correlated to an inadequate level of electrosteric stabilization. An optimum recovery was found at 60,000 chains/NP (~80%). Additionally, it was confirmed that both low polyelectrolyte molecular weights and counterion concentrations were critical for suppression of bridging flocculation.

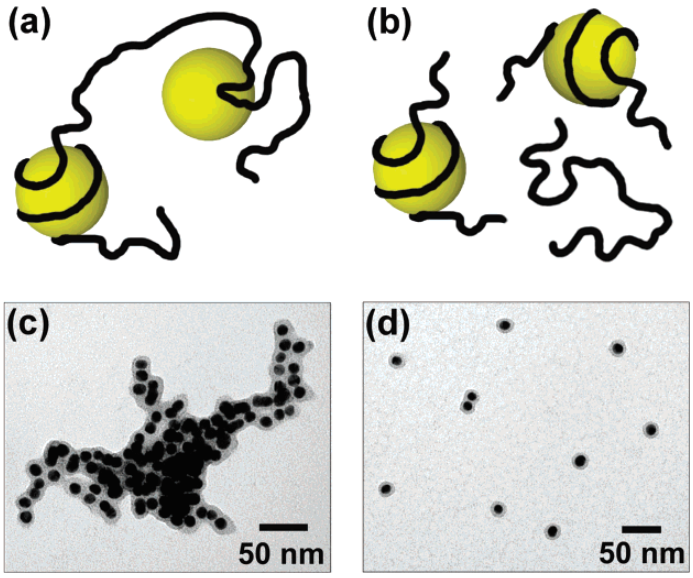

Figure 2.12. Bridging flocculation (**a**) schematic and (**c**) TEM image. Optimal chain concentration for electrosteric stabilization of individual AuNPs (**b**) schematic and (**d**) TEM image. Reprinted (adapted) with permission from Schneider, G.; Decher, G. Functional Core/Shell Nanoparticles Via Layer-by-Layer Assembly. Investigation of the Experimental Parameters for Controlling Particle Aggregation and for Enhancing Dispersion Stability. *Langmuir* **2008**, *24* (5), 1778-1789.[85] Copyright 2008 American Chemical Society.

2.2 ANTI-REFLECTION COATINGS

2.2.1 Theory.

As incident light travels through a medium of a certain refractive index (n_0) into the interface of another medium with a different refractive index (n_s), a portion of the light is transmitted and refracted, and another portion of the light is reflected. The optical behavior at the interface is eloquently conveyed by the Fresnel equations (these equations were adapted from the Optics textbook by Eugene Hecht).[86] Fresnel merged principles by Huygens on light refraction and Young on light interference into a cohesive wave theory of light.[86-87] Fresnel also determined that light beams polarized at right angles cannot interfere. Thus, the Fresnel equations are partitioned into

separate equations governing the transmitted and reflected amplitude coefficients for light with E-fields perpendicular (s-polarization) and parallel (p-polarization) to the incident plane. S-polarized light at the optical interface can be represented as[86]

$$r_s \equiv \frac{n_0\cos\theta_i - n_s\cos\theta_t}{n_0\cos\theta_i + n_s\cos\theta_t} \quad \textbf{(2.8)}$$

$$t_s \equiv \frac{2n_0\cos\theta_i}{n_0\cos\theta_i + n_s\cos\theta_t} \quad \textbf{(2.9)}$$

where r_s is the amplitude reflection coefficient, t_s is the amplitude transmission coefficient, θ_i is the angle of incidence, and θ_t is the angle of refraction. For p-polarized light the Fresnel equations are represented as[86]

$$r_p \equiv \frac{n_s\cos\theta_i - n_0\cos\theta_t}{n_0\cos\theta_t + n_s\cos\theta_i} \quad \textbf{(2.10)}$$

$$t_p \equiv \frac{2n_0\cos\theta_i}{n_0\cos\theta_t + n_s\cos\theta_i} \quad \textbf{(2.11)}$$

where r_p is the amplitude reflection coefficient, t_p is the amplitude transmission coefficient. The Fresnel equations above are fundamental to the field of thin-film optics. However, perhaps a more applicable variation to the amplitude reflection and transmission coefficients is reflectance and transmittance. Reflectance is the ratio of reflected to incident radiant flux (i.e. percent of the light reflected), whereas transmittance is the ratio of transmitted to incident radiant flux (i.e. percent of the light transmitted). The reflectance and transmittance for s-polarized and p-polarized light is represented by[86]

$$R_s = {r_s}^2 = \left(\frac{n_0\cos\theta_i - n_s\cos\theta_t}{n_0\cos\theta_i + n_s\cos\theta_t}\right)^2;\ \ R_p = {r_p}^2 = \left(\frac{n_s\cos\theta_i - n_0\cos\theta_t}{n_0\cos\theta_t + n_s\cos\theta_i}\right)^2 \quad \textbf{(2.12)}$$

$$T_s = \left(\frac{n_s\cos\theta_t}{n_0\cos\theta_i}\right){t_s}^2;\ \ T_p = \left(\frac{n_s\cos\theta_t}{n_0\cos\theta_i}\right){t_p}^2 \quad \textbf{(2.13)}$$

where R_s and R_p are the reflectance for s-polarized and p-polarized light, respectively, and T_s and T_p are the transmittance for s-polarized and p-polarized light, respectively. In the case of normal incidence, $\theta_i = \theta_t$, the reflectance and transmittance become,[86]

$$R = R_s = R_p = \left(\frac{n_s - n_0}{n_s + n_0}\right)^2 \quad \textbf{(2.14)}$$

$$T = T_s = T_p = \frac{4n_s n_0}{(n_s + n_0)^2} \quad \textbf{(2.15)}$$

$$R + T = 1 \quad \textbf{(2.16)}$$

where R is reflectance and T is transmittance, respectively. If light travels from air (n_0 = 1.0) to glass (n_1 = 1.5) at normal incidence, then using **Equations 2.14** and **2.15**, the total theoretical reflectance and transmittance is 4% and 96%, respectively. Since the Fresnel equations consider optical loss mechanisms such as absorption and scattering as negligible, the summation of reflectance and transmittance is unity.

Anti-reflection coatings (ARCs) reduce detrimental reflectance occurring from light incident on an optical interface. Incident light encompasses the propagation of electrical ($\vec{E}$) and magnetic ($\vec{H}$) fields, characterized as a plane wave traveling in the $\vec{k}$ direction.[86] Upon incidence with an ARC, the incoming light now encounters two interfaces: (I) the interface between air and the ARC and (II) the interface between the ARC and the substrate. At each of the two interfaces, a portion of the light is reflected and another portion is refracted. Here, we examine the optical interference behavior for a linearly polarized wave of wavelength λ, incident onto a single-layer ARC with a distinctive refractive index (n_1) and physical thickness (d) (**Figure 2.13**).

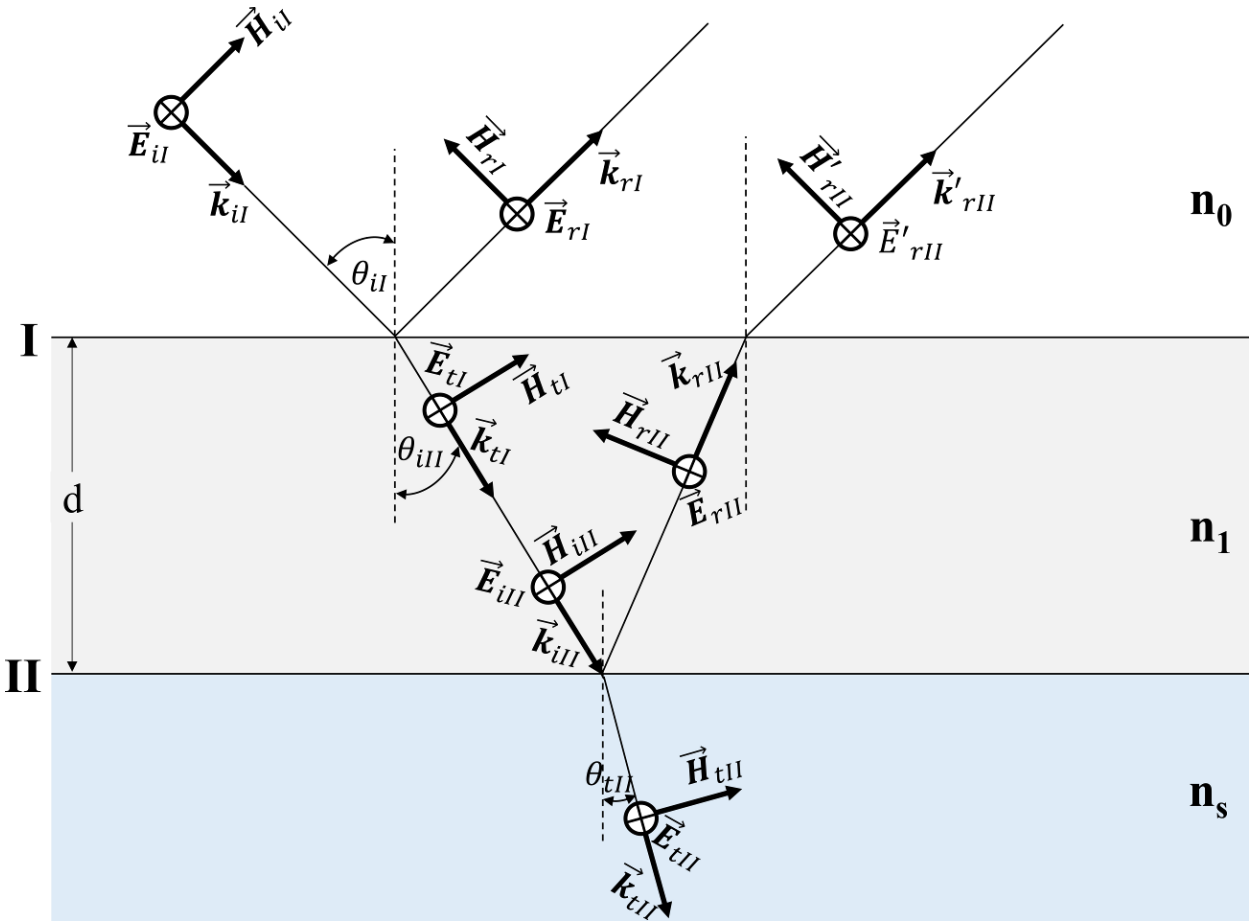

Figure 2.13. Propagation of electrical ($\vec{E}$) and magnetic ($\vec{H}$) fields, traveling in the $\vec{k}$ direction. The fields travel from air (n_0) into a film of a particular thickness (d), refractive index (n_1), and situated onto of a glass substrate (n_s). Light is reflected and refracted at both Interfaces I and II. This figure was recreated from Hecht, E. Optics, 4th. *International edition, Addison-Wesley, San Francisco* **2002**, *3* 2, Figure 9.49.[86]

The total amplitude reflection and transmission coefficient, for light incident onto the single-layer ARC system is (as adapted from the Optics textbook by Eugene Hecht)[86]

$$r = \frac{\Upsilon_0 \cos k_0 h + \frac{\Upsilon_0 \Upsilon_s i(\sin k_0 h)}{\Upsilon_1} - \Upsilon_1 i(\sin k_0 h) - \Upsilon_s \cos k_0 h}{\Upsilon_0 \cos k_0 h + \frac{\Upsilon_0 \Upsilon_s i(\sin k_0 h)}{\Upsilon_1} + \Upsilon_1 i(\sin k_0 h) + \Upsilon_s \cos k_0 h} \qquad (2.17)$$

$$t = \frac{2\Upsilon_0}{\Upsilon_0 \cos k_0 h + \frac{\Upsilon_0 \Upsilon_s i(\sin k_0 h)}{\Upsilon_1} + \Upsilon_1 i(\sin k_0 h) + \Upsilon_s \cos k_0 h} \quad \textbf{(2.18)}$$

where $\Upsilon_0 \equiv \sqrt{\frac{\epsilon_0}{\mu_0}} n_0 \cos\theta_{iI}$, $\Upsilon_1 \equiv \sqrt{\frac{\epsilon_0}{\mu_0}} n_1 \cos\theta_{iII}$ (for $\vec{E}$ not in the plane-of-incidence), $\Upsilon_1 \equiv \sqrt{\frac{\epsilon_0}{\mu_0}} n_1 / \cos\theta_{iII}$ (for $\vec{E}$ in the plane-of-incidence), $\Upsilon_s \equiv \sqrt{\frac{\epsilon_0}{\mu_0}} n_s \cos\theta_{tII}$, $k_0 = \frac{2\pi}{\lambda_0} \equiv$ wavenumber, and $h \equiv (n_1 d) cos\theta_{iI} \equiv$ optical thickness. For the special case of normal incidence where $\theta_{iI} = \theta_{iII} = \theta_{tII} = 0$, the amplitude reflection coefficient reduces to

$$r = \frac{n_1(n_0 - n_s)\cos k_0 h + i(n_0 n_s - n_1^2)\sin k_0 h}{n_1(n_0 + n_s)\cos k_0 h + i(n_0 n_s + n_1^2)\sin k_0 h} \quad \textbf{(2.19)}$$

and multiplying the amplitude reflection coefficient by its complex conjugate leads to the reflectance for the normal incidence condition as

$$R = \frac{n_1^2(n_0 - n_s)^2 \cos^2 k_0 h + (n_0 n_s - n_1^2)^2 \sin^2 k_0 h}{n_1^2(n_0 + n_s)^2 \cos^2 k_0 h + (n_0 n_s + n_1^2)^2 \sin^2 k_0 h} \quad \textbf{(2.20)}$$

For the condition of

$$k_0 h = \frac{\pi}{2} \quad \textbf{(2.21)}$$

$$h = \frac{\pi}{2}\left(\frac{1}{k_0}\right) = \frac{\pi}{2}\left(\frac{\lambda}{2\pi}\right) = \frac{\lambda_0}{4} \quad \textbf{(2.22)}$$

or when $h = n_1 d$ is an odd multiple of $\frac{\lambda_0}{4}$, such as,

$$2n_1 d = \left(m + \frac{1}{2}\right)\lambda_0 \quad (m = 0, \pm 1, \pm 2..) \quad \textbf{(2.23)}$$

the ARC is also known as a "quarter-wavelength coating" as it induces maximum destructive interference for the reflected light of wavelength λ_0.[86] Upon refraction of the incident light through

Interface I (air and ARC) of the coating at the maximum destructive interference condition, a quarter of the wavelength travels to the back of the coating and another quarter of a wavelength reflects off Interface II (ARC and substrate). Therefore, the beam reflected off the Interface II is π out-of-phase with the beam reflected off the Interface I, which results in maximum destructive interference for λ_0. Since physical thickness, d, is generally an easily adjusted parameter, h can be easily tuned for maximum destructive interference or anti-reflectivity at virtually any λ_0.

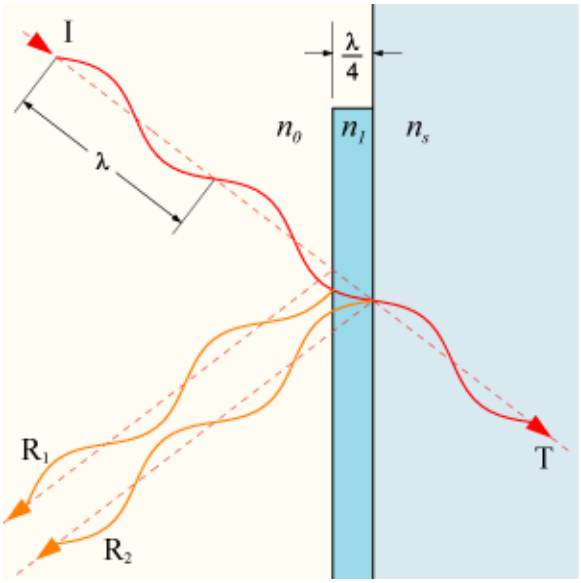

Figure 2.14. Destructive interference by a π-phase shift of the reflected beams off of Interfaces I and II on a quarter-wavelength ARCs. This figure was created by Bob Mellish "DrBob", an optics material editor on Wikipedia. The original title of this figure is, "Interference in a λ/4 coating" and it is licensed under the Creative Commons Attribution-Share Alike 3.0 Unported license.

Substitution of $k_0 h = \frac{\pi}{2}$ (**Equation 2.21**) into **Equation 2.20** provides the reflectance,[86]

$$R = \frac{(n_0 n_s - n_1^2)^2}{(n_0 n_s + n_1^2)^2} \qquad \textbf{(2.24)}$$

and when the reflectance is equal to zero,

$$n_1 = \sqrt{n_0 n_s} \quad (2.25)$$

which represents the ideal refractive index for an ARC. For the ARC in a medium of air ($n_0 = 1.0$) and on top of glass ($n_s = 1.5$), the ideal refractive index is $n_1 = 1.22$. When the ARC's actual refractive index is equal to the ideal, the reflected waves off of Interfaces I and II have equal amplitude, and the reflectance is zero for λ_0. Since the refractive index is an intrinsic material property, it is substantially more difficult to tune compared to the optical thickness. In summary, the two essential parameters in designing ARCs are as follows:

1) The optical thickness $h = \frac{\lambda_0}{4}$ is necessary for maximum anti-reflection at the wavelength λ_0

2) For zero reflectance, the refractive index of the ARC must be $n_1 = \sqrt{n_0 n_s}$

2.2.2 History.

The first ARCs were not coatings at all, but rather accidental surface conditions on glass. In 1817, Joseph Fraunhofer grinded and polished glass, then immersed the glass in sulfuric or nitric acid for 24 h.[87-88] It was discovered that the treated section of glass had a defined reflection loss, and the effect was augmented for glass that was more easily tarnished. The treated glass also exhibited pronounced interference colors, upon rotation under incident light. Nearly a century later, Lord Rayleigh independently found that the polishing of aged glass actually *increased* the reflectance of the glass from 3.5% to 4.8%.[89] Even though Rayleigh never deposited an actual coating, he realized the presence of a transparent layer with an "intermediate index" would result in anti-reflection. Despite these early occurrences of anti-reflection on glass, the first single-layer ARC was invented by Alexander Smakula in 1935, while working for the company Carl Zeiss in Germany.[90-91] These ARCs dramatically improved binocular transmittance to "over 80 per cent",

which was significant at the time.[91] Due to the advent of World War II, ARCs remained a military trade secret until 1940.

2.2.3 Porous ISAM ARCs.

ARCs can be produced by virtually any thin-film processing technique, including physical vapor deposition (PVD; e.g. thermal evaporation, e-beam evaporation, ion-beam sputtering),[92-95] plasma-enhanced chemical vapor deposition (PECVD)[96] sol-gel synthesis,[97-98] nano-imprint lithography,[98-99] spin-coating,[100] and chemical etching.[101] Despite the various advantages among these processing methods, large-scale production is expensive and especially difficult for non-planar or irregular surfaces. Furthermore, all of the listed techniques generally produce single, homogeneous materials with a refractive index far from the optimum value for zero reflectance. Magnesium fluoride (MgF_2) is commonly utilized as an ARC on glass, although with a refractive index of $n_{MgF2} = 1.38$, it provides a theoretical reflectance of only 1.4% (**Equation 2.24**). ISAM film deposition addresses the shortcomings inherent in other ARC processing methods, as the deposition is unrestricted by substrate geometry or size, in addition to the inexpensive nature. Most importantly for ARCs specifically, ISAMs allow for the processing of heterogeneous nanocomposites with controlled porosities and refractive indices close to ideal value for ARC films.

2.2.3.1 Polyelectrolyte-Nanoparticle ISAM ARCs. Hattori expanded on the previously discussed work by Lvov *et al.*[62-63] and applied the work to ARCs.[102] A *single-layer* of 110 nm diameter SiO_2 NPs were deposited onto one to ten bilayers of PDDA/PSS, resulting in a maximum transmittance and reflectance of 98.8% and 0.07%, respectively. The magnitude of anti-reflection was found to progressively increase with up to five polyelectrolyte bilayers (under the single SiO_2 NP layer). The refractive index of the films was approximately 1.25 with a calculated porosity of

50.3%. Heat treatment of the film at 75 ^{o}C caused a deformation of the SiO_2 NPs and further enhanced the anti-reflection. Sara Yancey, from our group, conducted a far more comprehensive study on PAH/SiO_2 ISAM ARCs, and constructed films with 15, 45, and 85 nm diameter SiO_2 NPs.[103] The pH of PAH and the SiO_2 NPs were separately adjusted to maximize the film quality. The optical thickness and the anti-reflection destructive interference peak λ_0 was easily manipulated by the number of bilayers from three to twenty. Maximum anti-reflectivity was displayed in films with the 45 nm SiO_2 NPs (pH = 9) / PAH (pH = 7) that provided transmittance at ≥98% and reflectance of <0.2%. The 15 nm SiO_2 NP (pH = 7) / PAH (pH = 7) and 85 nm SiO_2 NPs (pH = 9) / PAH (pH = 9) films were reported to have transmittances of ~97% and ≥97% (reflectance of 2.2% and 0.2 – 1.2%), respectively. As the film constituents had negligible absorption in the visible wavelength range, all extinction losses were attributed to optical scattering. Furthermore, extinction was linearly proportional to λ^{-4}, which suggests Rayleigh scattering at long wavelengths. The extinction magnitude and slope intensified with greater particle size, which was associated with elevated inhomogeneity and roughness levels. As confirmed by ellipsometry, the SiO_2 volume fractions and refractive indices of the films are interrelated and thus trend in a similar fashion. For the 15 nm SiO_2 NPs, the volume fraction remained consistently at 82% with a refractive index of 1.39. In films with 45 nm SiO_2 NPs, the volume fractions and refractive indices were 1) <100 nm thickness: ~55% and ~1.26, 2) 100 – 200 thickness: ~70% and ~1.34, and 3) >200 nm thickness: ~55% and ~1.26, respectively. Differently for films with 85 nm SiO_2 NPs, the volume fractions and refractive indices were 1) 100 – 200 thickness: ~75% and ~1.36, and 2) >200 nm thickness: a gradual decrease down to ~30% and ~1.14, respectively. Evidently, the anti-reflectivity of the films with 15 nm SiO_2 NPs was associated with the high SiO_2 volume fraction and refractive index values. Since the 45 and 85 nm SiO_2 NPs both had volume

fractions and refractive indices close to the ideal, their anti-reflectivity was limited by the increasing optical scattering magnitudes. Finally, due to the nature of ISAMs, the nanoparticle films were found to be non-crystalline, lacking of long-range order, and with a random close-packed (RCP) structure.

Rubner, Cohen, and associates (as previously discussed for PAH/PAA ISAMs) also released several reports related to porous polycation-SiO_2 ISAM ARCs with superhydrophilic (anti-fogging) and superhydrophobic (self-cleaning) properties.[104-105] Cebeci *et al.* created superhydrophilic ARC ISAMs using PAH and 7 nm diameter SiO_2 NPs.[104] The SiO_2 concentration was systematically examined from 0.005 to 0.1 wt%, and 0.03 wt% was reported as the optimum concentration for sufficient density and hydrophilicity. Optimum pH of SiO_2 NP solution was between 7.5 – 9, although quality was still present down to a pH of 4.0. Additionally, more than 8 bilayers were required for hydrophilicity, whereas, above 24 bilayers the films lost their transparency necessary for ARCs, due to optical scattering. For a 14-bilayer PAH (pH = 7.5) / SiO_2 NP (pH = 9.0), deposited on top of a 4-bilayer PAH/PSS adhesive stack, the transmittance was 99.7% with a refractive index of 1.25. After film processing, the films were calcined by thermal treatment up to 500 ^oC, which fused neighboring particles, induced siloxane bridges, and dramatically improved the mechanical properties (resistance to rubbing). Calcination of the films also decreased the thickness and the refractive index (as polymer was burned out, void volume increased), which therefore caused a slight blue-shift in the anti-reflection peak and increased the transmittance to 99.8%. The 14-bilayer films had superhydrophilic behavior with an advancing contact angle of less than 5^o in under 0.5 s, associated with the ability of the films to fully accommodate the extent of water on the film. The film porosity was considered the primary source of film wetting, as the pores allowed for rapid water penetration throughout the film called

"nanowicking". Bravo *et al.* from Rubner's group soon thereafter reported on superhydrophobic ISAM ARCs in effort to model a lotus plant.[105] Essentially, the goal was to intentionally produce film aggregates with high surface roughness, while maintaining transparency. These films were also composed of an adhesive stack (similar to the previously discussed report), a central stack with PAH / 50 nm *and* 20 nm SiO_2 NPs (0.03 wt%), and a top stack with PAH / 20 nm SiO_2 NPs. At 40 bilayers (of the central stack), the film had ideal superhydrophobic behavior with an advancing contact angle of 160°, although this film was far from transparent. The 20-bilayer film was the only film to exhibit both superhydrophobicity and mediocre anti-reflection with transmittance at 94.6%. Despite the near ideal refractive index, the heightened levels of optical scattering largely diminished the anti-reflectivity. Calcination of the films substantially improved the mechanical properties and also enhanced the superhydrophobicity.

Zhang *et al.* also produced superhydrophilic and superhydrophobic ISAM ARCs, but with slightly different materials and processes.[106-107] Superhydrophilicity films deposited onto quartz substrates consisted of PDDA complexed with sodium-silicate for a cationic material and the polyanion PAA.[106] Along with an augmentation of mechanical properties, calcination for these films were reported to significantly reduce the density and induce higher levels porosity. Because of these effects, calcination provided excellent anti-reflectivity, with maximum transmittance at 99.86%, and also enhanced superhydrophilic properties. Superhydrophobic films were formed with a 5-bilayer ISAM stack of PDDA/sodium silicate, on top of an 8-bilayer stack of PDDA/SiO_2 NPs (200 nm diameter), and had a broad-band anti-reflectivity with peak transmittance of 98.5% in the NIR range.[107] However, for superhydrophobic properties, the CVD deposition of fluoroalkylsilane on the top surface of the films was required, which slightly reduced the AR properties.

2.2.3.2 Nanoparticle-Nanoparticle ISAM ARCs. ISAM composed purely of nanoparticles have gained a considerable amount of attention for porous ARCs, as also extensively reported Rubner and Cohen's group.[108-111] Lee *et al.* created superhydrophilic ISAMs containing positively-charged 7 nm TiO_2 NPs and negatively-charged 7 nm or 22 nm SiO_2 NPs.[108] Due to the higher porosity in films consisted of 22 nm SiO_2 NPs compared to 7 nm SiO_2 NPs (45 and 35 vol%), the 22 nm SiO_2 NPs provided a more ideal refractive index (1.28 vs. 1.32) and had superior anti-reflection with >99% transmittance. The all-nanoparticle films were also calcined, which was reported to induce partial fusion of the NPs and enhanced film durability. Regardless of the SiO_2 NP size, the significantly higher TiO_2 surface charge attributed to a remarkably lower TiO_2 wt% than SiO_2 wt% in all films. The exposure of TiO_2 to UV-irradiation in the film also facilitated the elimination of organic contaminants, which was demonstrated as a key method to maintain superhydrophilicity. In a following study, Lee *et al.* systematically examined the effect of solution pH on TiO_2 (7 nm)/SiO_2 NP (22 nm) ISAM growth.[109] With a reduction in the SiO_2 NP pH and therefore the surface charge, the bilayer thickness continuously increased, until the SiO_2 PZC at pH 2.0, where a dramatic drop in bilayer thickness ensued. The opposite scenario was true for the TiO_2 NPs, where an increase in pH caused increased bilayer thickness, and at TiO_2 pH 4 and SiO_2 pH 3 the maximum bilayer thickness was achieved at 30 nm/bilayer. Additionally, it was found that the thickest films were also the most porous. The refractive indices for ISAMs at all pH's remained relatively consistent between 1.25-1.29, although anti-reflectivity was not specifically reported. Near the respective PZC's, SiO_2 NPs were reported to exhibit astonishing aggregation resistance, whereas TiO_2 NPs rapidly flocculated into large aggregates. Five bilayers of stable TiO_2 (pH=3)/SiO_2 (pH=3) ISAMs were deposited onto PS microspheres, which allowed for the development of robust hollow microcapsules upon calcination. Lee *et al.* again reported on all-

nanoparticle ISAMs using positively-charged 3-aminopropyl-functionalized SiO_2 NPs (AP-SiO2 NPs) with a 16.2 nm diameter, along with negatively-charged SiO_2 NPs with sizes of 8.6, 15.4, and 24.2 nm.[110] With a synchronized adjustment of both the AP-SiO_2 and SiO_2 NP pH, maximum thickness of the bilayers containing 8.6, 15.4, and 24.2 nm SiO_2 NPs was discovered at pH 5.0, 4.5, and 3.0, respectively. At these maximum thickness pH's, increased SiO_2 NP size showed increased porosity (8.6, 15.4, 24.2 nm = 42%, 45%, 49%, respectively) and decreased refractive indices (8.6, 15.4, 24.2 nm = 1.26, 1.25, 1.22 respectively). All SiO_2 NPs showed a negative ζ-potential slope with increased pH (i.e. increased ζ-potential magnitude with higher pH). The 8.6 and 15.4 nm SiO_2 NPs had similar slopes, while the 24.2 nm SiO_2 NPs had the greatest negative slope out of all three NP sizes. AP-SiO_2 NPs lacked ζ-potential dependency on pH with a steady magnitude of +23 mV (until beyond pH ≈ 6). The relationship of the normalized thickness ratio (h/h_0 = thickness relative to pH / maximum thickness) to the normalized ζ-potential ratio (z/z_0 = ζ-potential relative to pH / ζ-potential of AP-SiO_2 NPs) was surprisingly nearly identical for all the different SiO_2 NP sizes, with a peak h/h_0 between $0.6z_0$ and $1.2z_0$. Years later, Shimomura *et al.* synthesized the work from Lee *et al.* into broadband ARCs.[111] The ARCs consisted of alternating low-index and high-index stacks of AP-SiO_2/SiO_2 NPs (both 15 nm) and PVS/TiO_2 NPs (7 nm), respectively, with designed thicknesses for broadband anti-reflection. The final assembled film was of a 4-stack design with average reflectance less than 0.5% in the visible wavelength range and approximately 0.2% haze (ratio of diffuse to total transmittance; wide angle optical scattering). Large-scale roughness was reported to be the primary contributor to optical scattering and haze. Calcination densified the films and enhanced mechanical durability, represented by only a 0.3% reduction in transmittance after abrasion at 100 kPa.

As discussed thus far, calcination has been utilized as primary means of promoting mechanical robustness for nanoparticle-containing ISAMs, but calcination is incompatible with plastic substrates due to the high ~550 ºC temperatures. Gemici, who worked with Shimomura, Cohen, and Rubner, produced a comprehensive study comparing calcination to hydrothermal treatment (HT) methods.[112] HT involves autoclaving the samples to temperatures of 124 – 134 ºC. PDDA/SiO_2 NP (15 nm), AP-SiO_2 (15 nm)/SiO_2 (15 nm) NP or TiO_2 (5nm)/SiO_2 (15 nm) NP ISAM films were all examined for both calcination and HT methods. Qualitative (by rubbing) and quantitative (by 25 or 100 kPa by a metal polisher) testing was carried out for all films. As calcination densified the films and increased the refractive index, there were no noticeable changes to surface morphology under SEM (**Figure 2.15**). Differently for the HT, "particle necking" became visibly apparent, which entailed the dissolution and redeposition of soluble silicates between regions of neighboring particles. Furthermore, acceleration of the particle necking process for films on soda lime glass was attributed to the Na^+ ions within the substrates. XPS and FTIR revealed that HT had no effect on the PDDA in the films, whereas calcination completely eliminated the polycation. All films (as-assembled, calcined, HT) exhibited >99% transmittance for their peak anti-reflection wavelengths. However, PDDA/SiO_2 NP ISAMs showed significantly higher durability over all-nanoparticle films for both calcination and HT techniques. The HT technique was also reported to consistently provide greater robustness compared to calcination for all of the films. The different films were also processed on quartz, silicon, and polycarbonate substrates. Since quartz and silicon have high annealing temperatures (~1000 ºC) and do not contain Na^+, calcination and HT was ineffective on these substrates. On the other hand, the low glass transition temperature of polycarbonate (~140 ºC) allowed for an effective platform for the

HT durability film enhancement, despite the lack of Na^+ within the substrates. Essentially, the thermal and chemical properties are critical for thermally treated films.

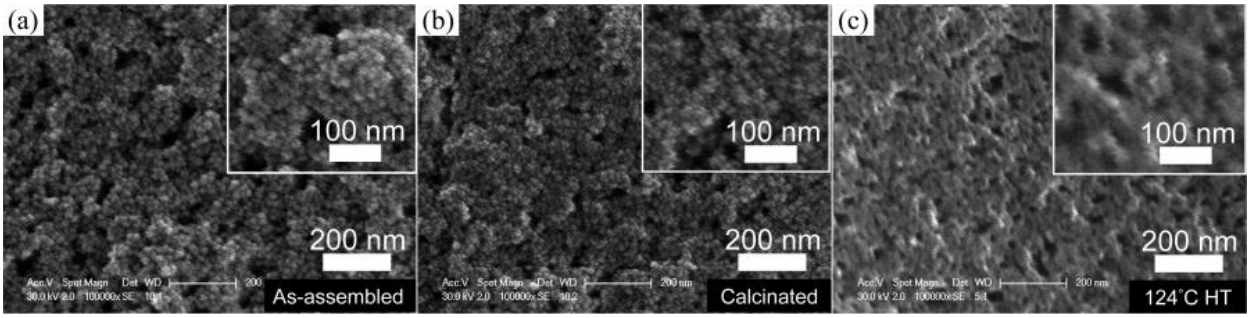

Figure 2.15. PDDA/SiO_2 NP ISAMs on soda lime glass. (**a**) as-assembled, (**b**) calcinated, (**c**) 124 ºC HT treatments. The particle necking is evident in the HT film. Reprinted (adapted) with permission from Gemici, Z.; Shimomura, H.; Cohen, R. E.; Rubner, M. F. Hydrothermal Treatment of Nanoparticle Thin Films for Enhanced Mechanical Durability. *Langmuir* **2008**, *24* (5), 2168-2177.[112] Copyright 2008 American Chemical Society.

2.2.3.3 Polyelectrolyte-Polyelectrolyte ISAM ARCs. ISAM films composed purely of polyelectrolytes can also be achieve the sufficient porosity necessary for anti-reflection. As discussed in **Section *2.1.4.3.***, Mendelsohn *et al.* processed PAH/PAA films that developed swelled microporous structures (with largely reduced refractive indices) upon immersion into acidic solutions, attributed to carboxylate group protonation and the splitting of inter-chain ionic linkages.[26] Years later, Hiller, Mendelsohn, and Rubner applied the methodology for nanoporous ISAM ARCs.[113] The pH-induced reversible swelling of PAH (pH = 8.5)/PAA (pH = 3.5) ISAMs allowed for switching between a nanoporous, swelled state (thickness ≈ 130 nm) with low refractive index (n ≈ 1.25 – 1.15) and a non-porous, collapsed state (thickness ≈ 85 nm) with high refractive index (n ≈ 1.52) (**Figure 2.16**). The pore penetration depth (~50 – 80 nm) increased and the refractive index decreased with increased immersion times and ionic strength (0.05 and 0.1 M $MgCl_2$) of the acidic solution. Upon achievement of the ideal refractive index on glass, the ARC

exhibited 99.99% transmittance. Thermal crosslinking of the films (heating to >200 ºC) formed covalent amide linkages between the two polyelectrolytes and substantially improved the mechanical robustness of the film. The crosslinking also secured the refractive index of the film, so that multiple PAH/PAA ISAM stacks with different refractive indices could be utilized together for an effective broadband ARC. This work was repeated almost identically by Fujita *et al.*, although CeO_2 NPs were instead used to produce the high index stack.[114] Fujita did present that the waterproofness of the PAH/PAA films after crosslinking, as also shown previously by Mendelsohn. Later, Fujita *et al.* reported that decreased dipping times (3 min instead of 15 min), and hence thinner PAH/PAA bilayers, showed improved anti-reflectivity because of lower optical scattering.[115]

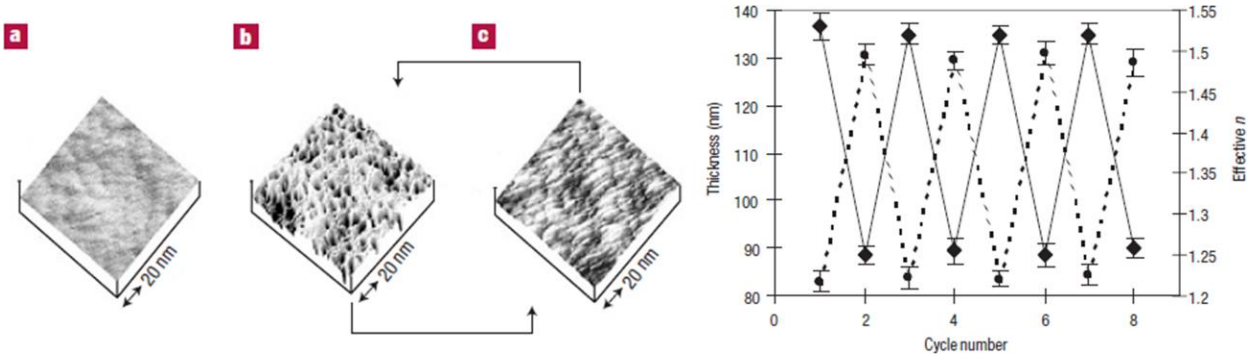

Figure 2.16. pH-induced switching for PAH/PAA films. 3-D AFM image of (**a**) the original film (**b**) the nanoporous, swelled film, and (**c**) the non-porous, collapsed film. The plot on the right represents the change in refractive index and thickness upon swelling and collapse. Reprinted by permission from Springer Nature: Hiller, J. A.; Mendelsohn, J. D.; Rubner, M. F. Reversibly Erasable Nanoporous Anti-Reflection Coatings from Polyelectrolyte Multilayers. *Nature Materials* **2002**, *1* (1), 59-63.[113] Copyright 2002.

2.3 ORGANIC PHOTOVOLTAICS

2.3.1 OPV Device Materials and Architecture.

2.3.1.1 Conjugated Polymers. Carbonaceous molecular materials represent the heart of all OPVs and other organic semiconductor devices. Among the different types of carbon-based materials, here we focus on polymers. Non-conjugated polymers, such polyethylene (PE), have saturated backbones primarily connected through single (σ) bonds between carbon atoms, and often with heteroatoms (N, O, S, etc.).[116-117] In these non-conjugated backbones, the four valence carbon electrons generally hybridize into four sp^3 orbitals (the 2s orbital overlaps with the $2p_x$, $2p_y$, and $2p_z$ orbitals), each containing one electron. Due to their very large band gaps ($E_{g,\,PE} \approx 8$ eV), non-conjugated polymers normally do not absorb visible light and are electrically insulating.[116-117]

Conjugated polymers instead are composed of unsaturated backbones with alternating single (σ) and double (one σ and π) bonds.[116-118] In this case, the valence electrons on carbon form three hybridized sp^2 orbitals (the 2s orbital overlaps with the $2p_x$ and $2p_y$ orbitals), leaving one remaining unhybridized $2p_z$ orbital. Bonding between two carbon atoms involves the overlap of two separate sp^2 orbitals to form rigid covalent σ bonds, as well as the overlap (conjugation) of two $2p_z$ orbitals to form π-bonds. The π-bonds contain weakly-bound, delocalized electrons located outside the plane of the carbon chain. A π bond itself is also composed of two separate molecular orbitals with lower and higher energy than the original $2p_z$ orbitals. The bonding (π) orbital has the lower energy of the two orbitals, and therefore two π-electrons favorably reside here at ground state.[116] The antibonding (π*) orbital has the higher energy and is unoccupied by electrons at ground state. The highest energy level in the bonding orbital is known as the highest occupied molecular orbital (HOMO), and the lowest energy level in the antibonding orbital is known as the lowest unoccupied molecular orbital (LUMO).[116, 118-119] The HOMO and LUMO are separated by the band gap (E_g),

which is analogous to the separation between the valence and conduction band in inorganic semiconductors.

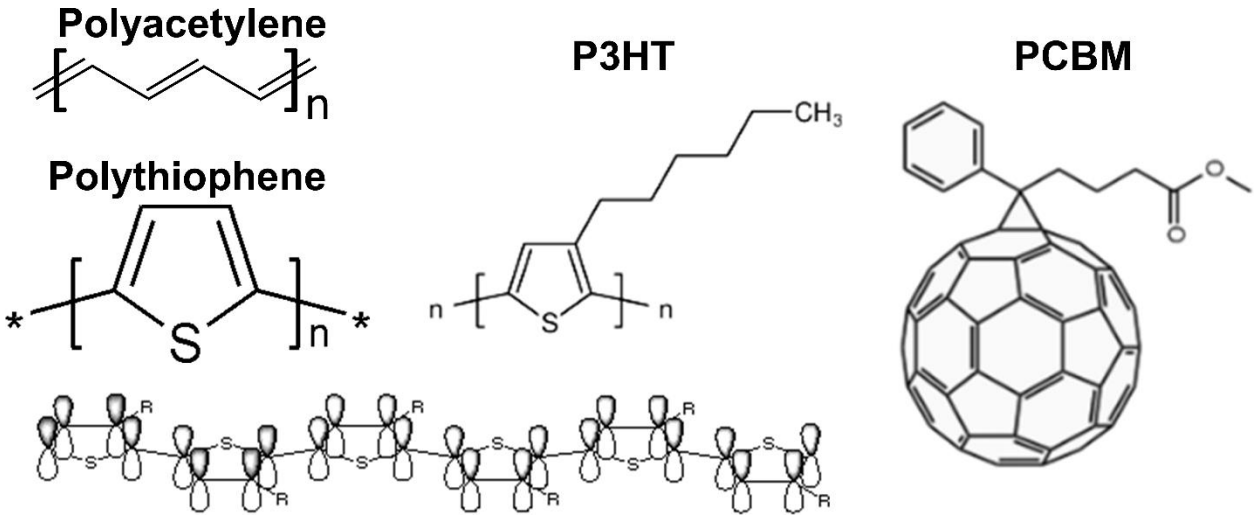

Figure 2.17. Conjugated polymer repeat units and the conjugated π-orbitals of polythiophene. Structure of PCBM. The P3HT figure was created by Sigma-Aldrich. These figures were created by Dr. David Flanagan, "Grimlock", and "Cubane" on Wikipedia. The original title of theses figure are "The monomer repeat unit of unsubstituted polythiophene.", "Conjugated π-orbitals of a coplanar and a twisted substituted PT" "Phenyl-C61-butyric acid methyl ester" and are licensed under the Creative Commons Attribution-Share Alike 3.0 Unported license.

The most fundamental conjugated polymer is polyacetylene (**Figure 2.17**), with a repeat unit consisting simply of alternating single and double bonds.[116-118] Increased stability and versatility can be realized in conjugated polymers containing aromatic rings. Aromatic rings often contain heteroatoms, such as sulfur in polythiophene, which ultimately affects the electronic properties. Polythiophenes usually have alkyl side chains (**Figure 2.17; P3HT**), which affects solubility, as well as ordering in films. A longer conjugation length in conjugated polymers (e.g. number of coplanar aromatic rings in polythiophene), relates to the energetic overlap of π-orbitals and the related to the density of the frontier (HOMO and LUMO) electronic levels, which also affects the

E_g (**Figure 2.18**).[116, 120] The conjugation length is broken at kinks and torsional defects found in all conjugated polymers. In this sense, the molecular orbital energetic overlap is less defined in conjugated polymers, and distinctive conduction and valence bands do not form as they do in inorganic materials.[119-120] The degree of π-orbital overlap also extends to electronic inter-chain effects, which correlates to charge carrier mobility properties.

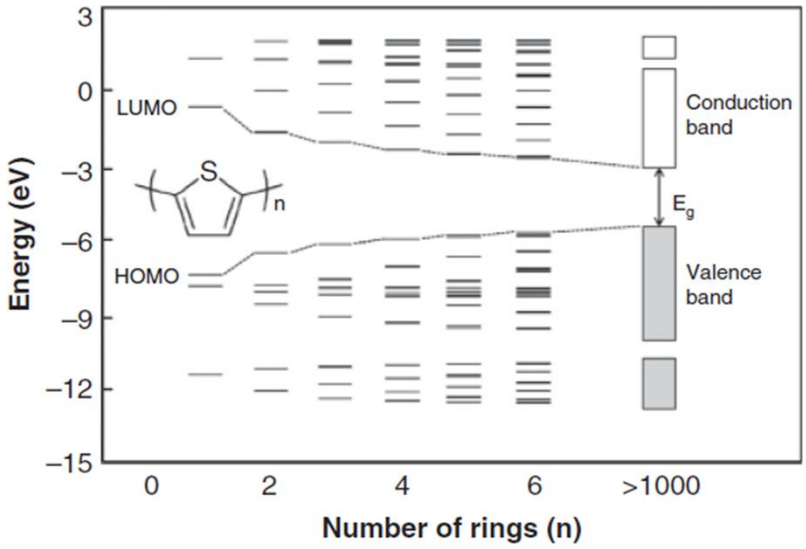

Figure 2.18. Conjugation length (number of continuous aromatic rings) in polythiophenes in relation to π-bond molecular orbital energy splitting. For a higher conjugated length, HOMO and LUMO are more densely packed. Reproduced with permission from Kar, P. Doping in Conjugated Polymers, *John Wiley & Sons*, **2013**.[116] Copyright 2013.

Besides molecular structure, doping is essential to the electrical and optical properties of conjugated polymers.[116-118] In the neutral, undoped form, conjugated polymers act as insulators with relatively high E_g's (3-6 eV) and low conductivities (10^{-7} – 10^{-11} S/cm).[116] Upon doping of the conjugated polymer chains, the E_g can be reduced to that of semiconductors or conductors (1 – 4 eV), along with drastically increased conductivities (10^{-5} – 10^{3} S/cm). Doping entails either a partial reduction (n-type) or oxidation (p-type) of the polymer chains, in which electrons are added

by an electron donor or removed by an electron acceptor, respectively. The majority of conjugated polymers are p-type semiconductors. P-type dopants for polythiophenes include BF_4^-, ClO_4^-, or $FeCl_4^-$.[116] Counterions are added with dopants to neutralize the dopant charge. As doping inorganic semiconductors is achieved by substitution of a lattice atom, doping in conjugated polymers often involves a charge transfer reaction. The doping concentration is related to the conductivity of the polymers with optimal levels between 0.1–0.5 mol %. P-type conjugated polymers are used as the electron donor (D) in this dissertation and the majority of work done on OPVs.

2.3.1.2 Electron Acceptors. Another commonly used conjugated structure is the buckminsterfullerene (C_{60}).[118] C_{60} contains 60 carbon atoms, with alternating single and double bonds. The high levels of conjugation in C_{60} allow for excellent electron acceptor capabilities and it can hold up to six electrons at once. The fullerene derivative, [6,6]-phenyl C_{61} butyric acid methyl ester (PCBM) (**Figure 2.17**) is often used due to its good solubility and stability in organic solvents.

Other fullerenes such as the non-symmetrical C_{70} or [6,6]-Phenyl-C71-butyric acid methyl ester ($PC_{71}BM$) have sparked interest recently, attributed to their optical absorption in the visible wavelengths, which allows for greater photogeneration.[121] Additionally, non-fullerene electron acceptors, including conjugated polymers or small molecules have been utilized for the same reason.[121-123] However, many of these new electron acceptors face the challenge of solution dispersion and homogeneity in thin films, which keeps traditional electron acceptors popular.

2.3.1.3 OPV Device Architectures. Original OPV devices were constructed from a single organic donor layer between two electrodes (**Figure 2.19**). An early report of a single layer OPV by Marks *et al.* was constructed by spin coating a conjugated polymer, poly(*p*-phenylene vinylene) (PPV), onto the transparent anode, indium tin oxide (ITO), and evaporating a metallic cathode on

top of PPV.[124] For the ITO-PPV-metal devices, metals of different work functions including Al (4.28 eV), Mg (3.66 eV), and Ca (2.87 eV) were examined, which resulted in different open-circuit voltages (V_{oc}) ranging from 1.2 to 1.7 V. The V_{oc} levels were attributed to the difference in the high work function ITO (4.8 eV) to the lower work function metals. Despite the high V_{oc} levels, the device photocurrents were very poor and external quantum efficiencies (EQE; ratio of number of photogenerated electrons to number of incident photons) were ~1%. The low photocurrents and EQE are a result of high bimolecular recombination levels in the single conjugated polymer layer.

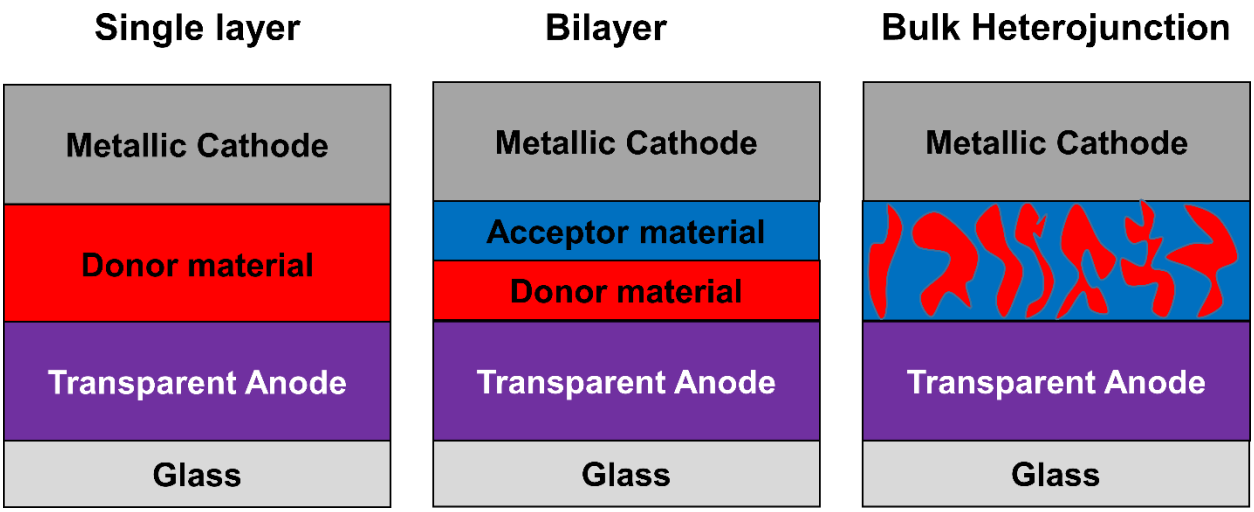

Figure 2.19. OPV device architectures including single layer, bilayer, and bulk heterojunction.

In 1986, Tang developed perhaps the first reported bilayer OPV device, which essentially represented the *p-n* junction from inorganic PVs (**Figure 2.19**).[125] The devices were fabricated using a p-type Copper phtalocyanine (CuPc) and a n-type perylene tetracarboxylic derivative (PV), vacuum evaporated onto ITO. The p- and n-type materials effectively transport holes to the ITO anode and electrons to the Ag cathode, respectively. After exciton dissociation (separation of the electron-hole pair from photoexcitation) occurred at the interface between the two materials, detrimental charge recombination effects found in single-layers were substantially reduced. This work revolutionized OPVs, as it introduced the importance of separate donor (D) and acceptor (A)

charge materials for efficient device operation. It is critical that the ionization potential (IP) and electron affinity (EA), analogous to the HOMO and LUMO, respectively, are offset in the two components for effective exciton dissociation. In the bilayer devices, the V_{oc} was dependent on the organic materials themselves rather than the difference in work functions between electrodes. The ITO/CuPc/PV/Ag bilayer OPV device showed a V_{oc} = 0.45 V, FF = 0.65, EQE of ~15% at λ = 620 nm, and an overall power conversion efficiency (PCE) of 0.95%. In 1993, Sariciftci *et al.* and Kraabel *et al.* from Wudl and Heeger's groups developed bilayer devices with using the conjugated polymers poly[2-methoxy,5-(2'-ethylhexyloxy)-1,4-phenylene-vinylene] (MEH-PPV) and poly(3-octylthiophene) (P3OT) as p-type donor materials and a buckminsterfullerene (C_{60}) as an electron acceptor.[126-127] The combination of the conjugated polymer with C_{60} allowed for ultra-fast charge transport under 1 picosecond, which strongly rivaled recombination effects present in pure conjugated polymer films. However, despite advancements made by bilayer OPV devices over single-layers, the inherent design in these devices are ultimately restricted by the disproportionality between optical absorption depths and short exciton diffusion lengths.[128-129] For instance, typical optical absorption depths ($1/\alpha$) in conjugated polymers is roughly 100 nm and the exciton diffusion length (L_d) is only ~10 nm. This means that either the active layer thickness must be unfavorably limited to only absorb a small fraction of light or a large percentage of photogenerated excitons will recombine, as they are unable to reach the D/A interface. This creates a situation referred to as a "exciton diffusion bottleneck", which caps the overall device efficiency.[128]

The introduction of the bulk heterojunction (BHJ) addressed the exciton diffusion length limitations by blending D/A components together into one layer of interpenetrated phases with high levels of interfacial area (**Figure 2.19**).[128-129] Therefore, exciton dissociation is independent of the active layer thickness, as the D/A interface is highly probable to be within the diffusion

length of photogenerated excitons. Additionally, the BHJ maintains bicontinuous pathways for percolating charge carriers to their respective electrodes. Yu *et al.* from Wudl and Heeger's groups presented the first report on the BHJ in OPVs with a blend of MEH-PPV and PCBM, sandwiched between ITO and Ca/Al electrodes.[130] The MEH-PPV:PCBM BHJ devices showed EQE of ~29% and PCE ~2.9%. Almost a decade later, poly(3-hexylthiophene) (P3HT) was utilized as a conjugated polymer in P3HT:PCBM BHJ devices, which displayed EQE of >70% and PCE of 3.5%, after annealing.[131] Given the numerous advantages, BHJ is the standard architecture employed universally for OPV devices.

2.3.2 OPV Device Operation.

The conversion of sunlight to electrical current in OPV devices is a six-step process involving: 1) optical absorption, 2) exciton generation, 3) exciton diffusion, 4) exciton dissociation, 5) charge transport, and 6) charge collection (**Figure 2.20**). In the following sections, the charge photogeneration steps are discussed in detail.

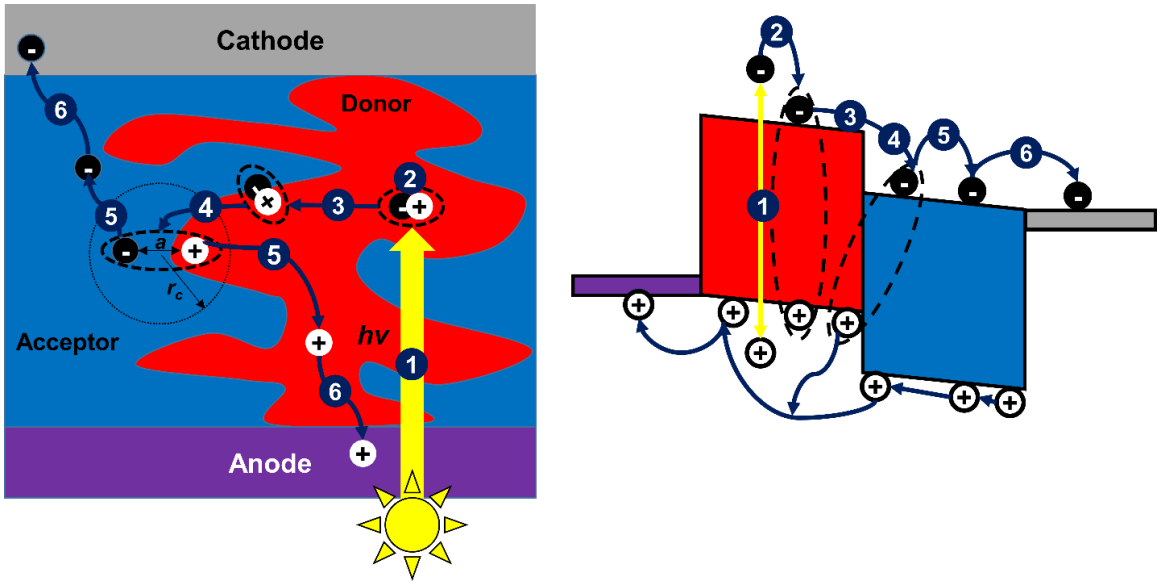

Figure 2.20. Charge photogeneration process schematic for the BHJ OPV device and material energy levels. The Onsager radius and thermalization length are represented by "r_c" and "a",

respectively. The numbers in the blue dots represent the six steps for charge photogeneration process including: 1) optical absorption, 2) exciton generation, 3) exciton diffusion, 4) exciton dissociation, 5) charge transport, and 6) charge collection. In the energy level schematic, the colors correspond to the same materials in the device schematic.

2.3.2.1 Optical Absorption. The sun is classified as a blackbody emitter, which corresponds to a radiation spectrum based on the surface temperature (T_{sun} = 5762 K).[119] Emission of light from the sun arrives to the earth in the form of photons. The incident photons vary in energy based on their wavelength such as,[119]

$$E_{ph} = \frac{hc}{\lambda} \quad (\mathbf{2.26})$$

where h is the Planck's constant, c is the speed of light, and λ is the wavelength of light. In the discussion of photon energy, typically units of electron-volts (eV) are utilized. Additionally, the quantity of photons delivered per time and unit area are represented by the photon flux,[132]

$$\phi = \frac{N_{ph}}{m^2 s} \quad (\mathbf{2.27})$$

where N_{ph} is the number of photons. From the photon energy and flux, spectral irradiance can then be calculated for each wavelength as,[132]

$$F(\lambda) = \phi E \frac{1}{\lambda} \quad (\mathbf{2.28})$$

Spectral irradiance is important for characterization of the radiation spectrum from a blackbody emitter. As sunlight is irradiated into the Earth's atmosphere, the interaction with gas molecules (O_3, O_2, H_2O, CO_2, etc.) and particles result in optical loss including such as reflection, absorption, or scattering.[133] These optical effects alter the spectral irradiance intensity onto the Earth compared to levels outside the atmosphere in the extraterrestrial regimes. Air mass is commonly used to

describe the radiation spectrum, which is the ratio of the sunlight's path length at angle to the normal compared to the path length at the normal, or related to the light angle as,[119]

$$AM = \frac{1}{cos\theta} \tag{2.29}$$

where θ is the angle from the Earth's surface normal (θ = 0°). The solar radiation spectrum outside the earth's atmosphere is represented as "Air Mass 0" (AM0), which translates to zero atmospheres with a total intensity of 1.35 kW/m^2 (**Figure 2.21**).[119] The standard radiation spectrum for the characterization of PV devices is the "Air Mass 1.5 Global" (AM1.5G) or the equivalence of 1.5 atmospheric thicknesses (**Figure 2.21**). The AM1.5G is embodies the radiation spectrum at θ = 48.2, an annual average angle for mid-latitudes, and at a total power density of 1 kW/m^2 (100 mW/cm^2). "Global" in AM1.5G associates with direct radiation, but also the indirect radiation components from the atmosphere and surrounding topography, including scattering and reflection. "Air Mass 1.5 Direct" (AM1.5D) only accounts for the direct radiation component (**Figure 2.21**).

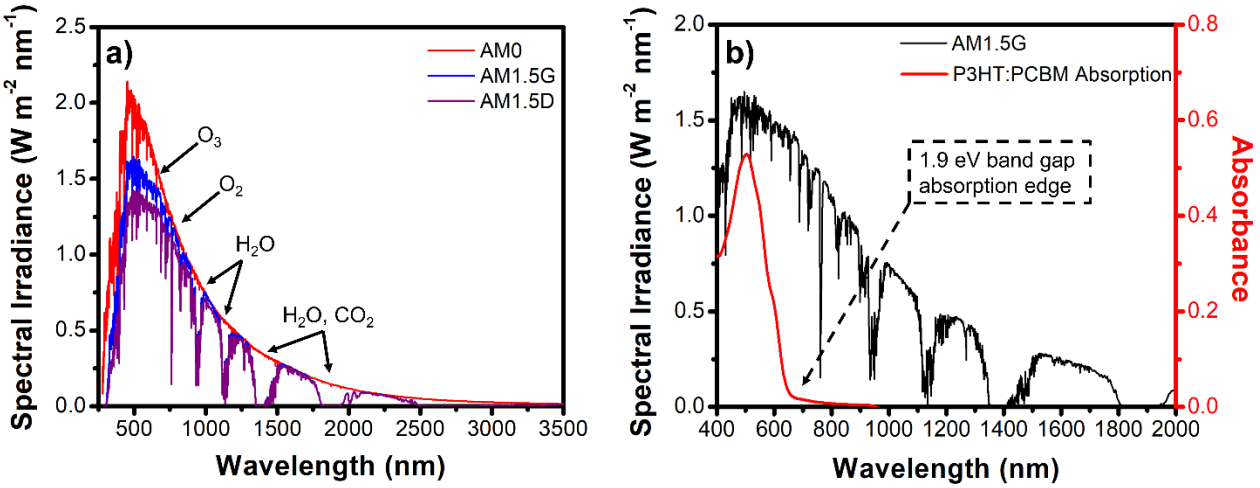

Figure 2.21. (**a**) Spectral Irradiance for the AM0, AM1.5G, and AM1.5D solar radiation spectra. The optical loss by the atmospheres gas molecules (O_3, O_2, H_2O, CO_2) gas molecules are shown.[133]

(**b**) Comparison of the AM1.5G to P3HT:PCBM optical absorption spectra (for a 100 nm thickness from our own work). The solar radiation spectra were recreated from NREL data.[132]

Incident light is absorbed into a semiconductor based on its E_g in relation the photon energy. Photons will be absorbed with energy equal to or greater than the E_g, whereas photons with energy less than the E_g will simply transmit through. In order to absorb a majority of the AM1.5G spectrum, optimal E_g values range from 1.3 to 1.8 eV or if considering all optical losses, then 1.1 to 1.5 eV.[119, 134] Basically, a narrower E_g means that the PV's absorption onset will be shifted to longer wavelengths and cover a greater percentage of the AM1.5G spectrum. Traditional OPV conjugated polymers, such as polythiophenes have E_g's ≈ 1.8 to 2.0 eV, although significant effort has been carried out to produce polymers with more narrow E_g's such as PTB7-Th (E_g ≈ 1.59 eV) or ITIC-Th1 (E_g ≈ 1.55 eV).[119, 123, 134] The conjugated polymer used in this dissertation, poly(3-hexylthiophene (P3HT), has an E_g ≈ 1.9 eV or an absorption onset of λ ≈ 650 nm. In general, conjugated polymers exhibit broad absorption spectra over 1 eV in width, attributed to wave function overlaps between ground and excited states, as well as structural deformation/relaxations in excited states.[120, 135] Even if the E_g of the absorbing material is not completely desirable, the absorption width compensates for it. Furthermore, conjugated polymers are known for their high absorption coefficients ($\alpha = 4\pi k/\lambda$; k is the extinction coefficient) in the range of $\alpha = 1 - 2 \times 10^5$ cm^{-1}, which allows for significant light absorption from relatively low thicknesses.[119-120, 135] For instance, a 100 nm thick film of P3HT:PCBM has an absorbance (also referred to as absorption efficiency; $\eta_A = (1 - e^{-\alpha d})$ where d = thickness) ranging from ~0.3 – 0.6 (single pass) from λ = 400 – 600 nm or ~0.6 – 1.2, if accounted for a double pass of the light after being reflected by the metallic cathode. The absorption depth, equal to the inverse of the absorption coefficient (1/α),

corresponds to path length in which 63% ($d = 1/\alpha$, so $\eta_A = 1\text{-}e^{-1}$) of light has been absorbed.[132] In conjugated polymers, the absorption depth is typically ~100 nm.

Thermal annealing of BHJ OPV films has a significant effect on the optical absorption. Annealing involves heating above the glass transition temperature (T_g) of the D/A components in the film (e.g. $T_{g,\,P3HT}$ = 9.3 ºC and $T_{g,PCBM}$ = 118.3 ºC), which induces greater phase separation, reordering, and crystallization of the of the constituents.[136-138] Following annealing of P3HT:PCBM, the absorption peak redshifts to longer wavelengths (~473 to 505 nm), and the extinction coefficient increases (~0.4 to 0.5) significantly. Hence, annealing can improve the optical absorption without changing the film thickness.

2.3.2.2 Exciton Generation. The optical absorption of photons with sufficient energy to surmount the E_g of a conjugated polymer leads to electron excitation called photoexcitation.[118-119, 135, 139] This excitation forms a fundamental quasi-particle consisting of an electron-hole bound pair called an exciton (**Figure 2.22**). In the exciton, the electron and hole reside nearly at the LUMO and HOMO of the donor polymer, respectively. Two types of excitons exist: singlet and triplet. Singlet excitons are formed by photoexcitation (ground state to singlet state; $S_0 \rightarrow S_1$), in which the hole and the electron have opposite spins. Triplet excitons can then form from singlet excitons from intersystem crossing and have identical ground and excited state electron spins, but are lower in energy by ~0.1 eV.[118, 135, 139]

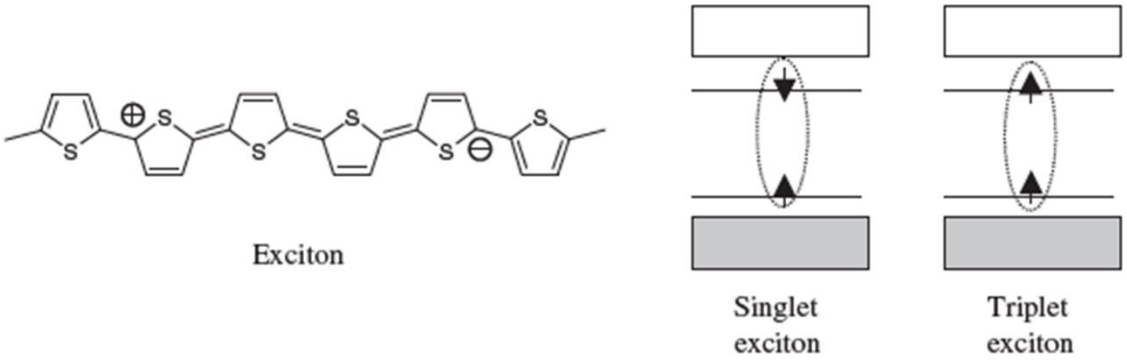

Figure 2.22. Representation of an exciton on a polythiophene molecule. Energy diagram for spin states of a singlet and triplet exciton. Reprinted by permission from Springer: Brabec, C. J.; Dyakonov, V.; Parisi, J.; Sariciftci, N. S. Organic Photovoltaics: Concepts and Realization, *Springer Science & Business Media*, **2003**; Vol. 60.[118] Copyright 2003.

Exciton formation induces a structural relaxation of the polymer chain, i.e. a reversal of the C-C bond alternation or a temporary semiquinoidal domain.[118, 135, 139] Compared to singlet excitons, triplet excitons have a smaller degree of structural deformation/relaxation, but are also more localized (deformation/relaxation only extending 1-2 repeat units). The binding energy of an exciton attributed to coulomb attraction forces is,[119, 139]

$$E_b = \frac{e^2}{4\pi\varepsilon_r\varepsilon_0 R} \quad (\mathbf{2.30})$$

where e is the charge of an electron, ε_r is the dielectric constant of the surrounding medium, ε_0 is the permittivity of free space, and R is the separation distance between the electron and hole. Because of the high dielectric constants in inorganic semiconductors, such as Si ($\varepsilon_r \approx 12$), more-screened coulomb attractive forces lead to a relatively small exciton binding energy of less than 0.02 eV.[119, 121, 139] Also, the electron-hole separation distance is larger, delocalized over many lattices. On the other hand, the lower dielectric constants in organic semiconductors ($\varepsilon_r \approx 3.5$) lead to larger binding energies ranging from ~0.1 to 1 eV, and also smaller separation distances ranging

from ~0.5 – 1 nm (e.g. localized to a single molecule or only over several monomer units on a single polymer chain). The high exciton binding energy in organics is attributed to both coulombic forces and structural relaxation effects.[120, 139] Because of the inherent exciton differences, excitons in inorganic and organic semiconductors are generally classified as Mott-Wannier and Frenkel excitons, respectively.[118-119] The lifetime of an exciton on an organic molecule varies from 100 ps to 1 ns, and if electron-hole pair does not dissociate in this time, then the exciton will recombine either radiatively (photon emission; photoluminescence) or non-radiatively back to ground-state.[118, 139]

2.3.2.3 Exciton Diffusion. Upon the photogeneration of excitons in organic materials, the electron-hole pair together is a neutral entity, which allows for random diffusion through the donor material.[120, 135, 139] As previously discussed, the D/A interface must be within the exciton diffusion length $L_D = \sqrt{D\tau} \sim 10\, nm$ (where D is the diffusion coefficient and τ is the lifetime) or recombination will occur.[120-121, 135] Therefore, the optimal domain size in a BHJ is <20 nm. Singlet excitons are known to diffuse faster (higher D) with faster decay times than triplet excitons (ps or ns vs μs or ms scale for singlet and triplet, respectively). Excitons diffuse by intramolecular or intermolecular movement, in which "hopping" occurs through adjacent molecules or polymer chains. The diffusion can be characterized by either a Förster resonant energy transfer (FRET) or Dexter energy transfer process (**Figure 2.23**).[120, 135, 140] Singlet excitons typically follow FRET mechanisms, which involve long-range transfer (up to 10 nm) by dipole-dipole electrostatic interactions and spin conservation ($^1D^* + {}^1A \rightarrow {}^1D + {}^1A^*$; D is a donor molecule, A is another molecule that acts as an acceptor for the exciton, 1 corresponds to the singlet spin state). Alternatively, triplet excitons are transferred purely by Dexter mechanisms, associated with short-range transfers (up to 2 nm) and molecular orbital overlaps. In Dexter energy transfers, there is

spin conservation for the system, but not of the individual D/A molecules ($^3D^* + {}^1A \rightarrow {}^1D + {}^3A^*$; 3 corresponds to triplet spin state).

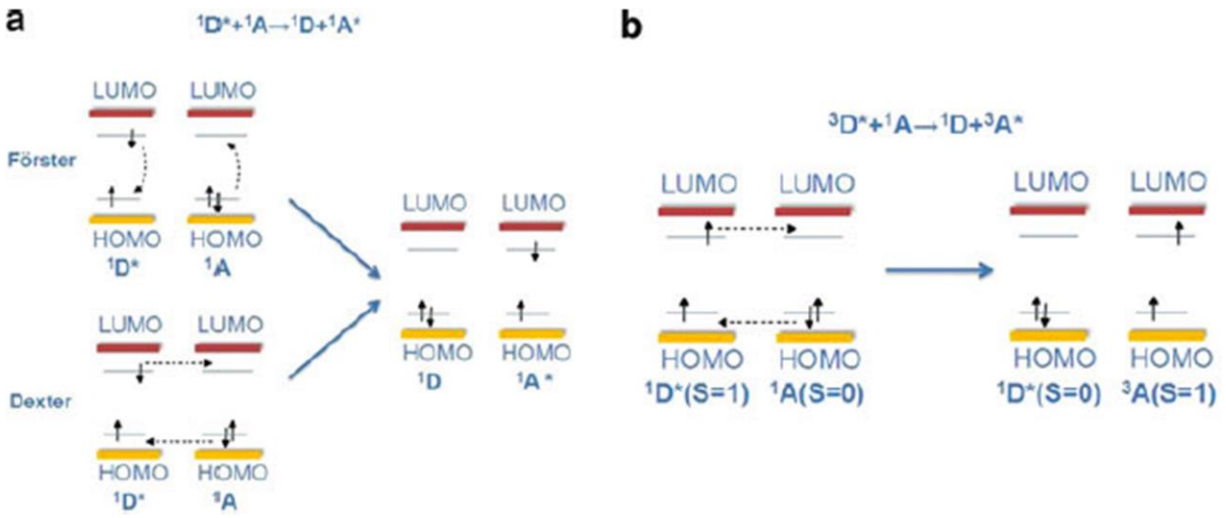

Figure 2.23. (**a**) Singlet exciton diffusion by both Förster and Dexter energy transfer mechanisms. (**b**) Exciton diffusion by the Dexter energy transfer process between singlet (S = 0) and triplet states (S = 1). Reprinted by permission from Springer: Giulianini, M.; Motta, N. Polymer Self-Assembly on Carbon Nanotubes. In Self-Assembly of Nanostructures; *Springer*: **2012**; pp 1-72.[140] Copyright 2012.

As energy transfers causes a decrease of the exciton energy, charge trapping (and eventually non-radiative recombination) can occasionally occur during the process for materials with especially broad density of states or high levels of disorder.[139, 141] Charge trapping can also occur when excitons encounter defects or aggregates. The exciton diffusion efficiency (η_{ED}) represents the ratio of the excitons that diffuse to the D/A interface to the amount of generated excitons.[121]

2.3.2.4 Exciton Dissociation. If the exciton diffuses to the D/A interface, excitons do not directly dissociate into free charge carries, but first partially separate into an intermediate, charge-transfer (CT) state (hole on donor HOMO, electron on acceptor LUMO) (**Figure 2.23**).[118, 120-121, 135, 139] In order to reach the CT state, the exciton must overcome the binding energy, requiring the energy

offset between the D to A to be ~0.3 – 0.5 eV (greater than or equal to the binding energy).[120] This offset causes a "hot charge transfer" (CT*) state with an surplus of thermal energy and will eventually relax into the CT state with an electron-hole pair separated at a thermalization length (a) (**Figure 2.24**).[120, 139] In this relaxed CT state, the electron-hole pair remain strongly coulombically-bound and form a different quasi-particle called a polaron pair (two oppositely-charged polarons), associated with a structural deformation.[118, 139] The polaron pair is geminate (monomolecular) when both oppositely-charge polarons are formed from same photoexcitation. In the CT state, the polaron pair can switch between singlet or triplet spin states with four possible spin permutations. Polarons can also exist as two carriers with the same charge on one molecule, referred to a bipolaron.

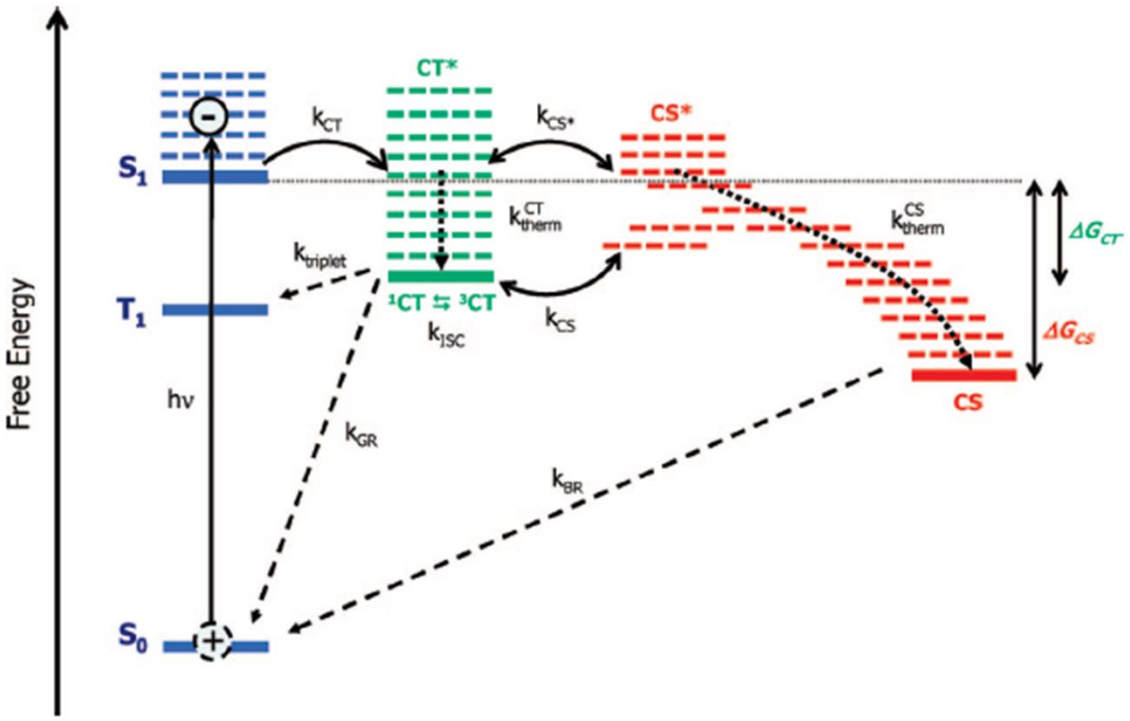

Figure 2.24. Energy level diagram for the photogeneration process. S_0 is the ground state, T_1 is the triplet exciton energy, S_1 is the singlet exciton energy, k_{CT} is the exciton dissociation to the CT state, $k_{triplet}$ is the geminate recombination of the CT state back to the triplet energy state, k_{GR} is

the geminate recombination back to ground state, CT* is the thermalized CT state, k_{ISC} is spin mixing between singlet and triplet states, k_{CS*} is the hot transfer from the CT* state to the CS state, k_{therm}^{CT} is the thermal relaxation of the CT state, k_{CS} is the transfer of the CT state to the CS, CS* is the thermalized CS state, k_{therm}^{CS} is the thermal relaxation of the CS state, and k_{BR} is the bimolecular recombination. Reprinted (adapted) with permission from Clarke, T. M.; Durrant, J. R. Charge Photogeneration in Organic Solar Cells. *Chemical reviews* **2010**, *110* (11), 6736-6767.[139] Copyright 2010 American Chemical Society.

Similar to excitons, the CT state also has a limited lifetime related to a competition between dissociation and geminate recombination (electron decays from the acceptor LUMO back to donor ground state).[118, 120, 139] Polarons in the CT state can also decay back to triplet excitons (**Figure 2.24**).[139] The strong coulombic attractions, low charge mobilities, and low dielectric constants all play a counteracting role to polaron pair dissociation. Although dissociation from the CT state is still under debate, the Onsager model predicts dissociation by comparing the thermalization length (a) to the capture or Onsager radius (r_c) (**Figure 2.20**).[139] This Onsager radius is equal to the separation distance between the polaron pairs where the coulomb forces are equal to the thermal energy (k_BT). If r_c is greater than a, then the Onsager model predicts that dissociation will occur at certain escape probability,[139]

$$P(T,E) = e^{-\frac{r_c}{a}}\left(1 + \frac{er_c}{2k_BT}E\right) \quad (\mathbf{2.31})$$

where E is the applied electric field strength. As is implied, by the Equation **2.31**, the probability of dissociation is strongly contingent upon both electric field and temperature. The dissociation probability can also be related to,[139]

$$P(T,E) = \frac{k_d(E)}{k_f + k_d(E)} = k_d(E)\tau(E) \quad (\mathbf{2.32})$$

where k_f is the geminate recombination rate, $k_d(E)$ is electric field related dissociation rate into charge carriers, and $\tau(E)$ is the lifetime of polaron pairs in the CT state. The dissociation rate (k_d) depends on the charge carrier mobilities and the coulomb attraction components.[139]

Full exciton dissociation means a transfer from the CT state to the charge-separated state (CS) (**Figure 2.24**).[120, 135, 139] In the CS state, the electron and hole no longer are coulombically-bound and are free to move by polaron hopping. Similar to the CT state, initially the CS state is "hot" with an excess of thermal energy (CS*) (**Figure 2.24**). Eventually, the CS* state thermally relaxes to the CS state, with a final energy equal to the difference between the acceptor's electron affinity (LUMO) and the donor's ionization potential (HOMO) (E_{final} = IP(D) – EA(A)). This energy is correlated to the E_g of BHJ and is associated with the theoretical maximum for the open-circuit voltage, as discussed later. Transition from the thermally "hot" CT* to CS* state ensues at a very fast rate due to ultrafast polaron hopping and transfer (~100 fs) with a greater efficiency compared to thermally relaxed states.[135] Additionally, charge mobility is stated to be two several orders of magnitude larger while states are thermally "hot". The charge separation efficiency (η_{CS}) represents the ratio of for amount of excitons that have been fully dissociated to the amount of excitons that have diffused to the D/A interface.[121]

2.3.2.5 Charge Transport. After the polaron pair is fully separated into free electron and hole charge carriers, they drift or diffuse towards their respective electrodes by intermolecular polaron hopping.[119-120, 135] Holes travel in the donor material phase towards the anode (high work function electrode) and electrons move in the acceptor phase towards the cathode (low work function electrode). The work function difference between the two electrodes creates a built-in electric field, which drives charge carrier migration to the appropriate electrodes. Essentially, the difference in work functions causes a chemical potential difference and charges are "pushed" from the D/A

interface by high to low density gradients. The efficiency of charge transport is quantified by charge carrier mobilities. Charge mobility is hindered in organic materials due to strong electron-phonon couplings, weak intermolecular electronic couplings, and disorder effects.[120, 135] Organic materials can feature charge mobilities either many orders of magnitude lower or equal to inorganics (organics: 10^{-10}-10^{-2} $m^2/(Vs)$, inorganics: 10^{-2} to 10^{-1} $m^2/(Vs)$) depending on the ordering of the film, as well as crystallinity, molecular weight, or regioregularity of the conjugated polymers.[120, 135, 142-144] For instance, annealing of the film allows significant enhancements to the charge mobility due to greater crystallinity and intermolecular ordering.[137] In P3HT:PCBM, μ_n and μ_p (electron and hole mobility) are 1.7 x 10^{-8} and 1.0 x 10^{-10} $m^2/(Vs)$ before annealing, respectively, and μ_n and μ_p are 1.8 x 10^{-7} and 4.0 x 10^{-8} $m^2/(Vs)$ after annealing, respectively.[142]

Charge transport competes directly with charge recombination by either monomolecular (geminate), trap-assisted (also referred to as Shockley-Read-Hall (SRH)), or bimolecular (also known as Langevin or non-geminate recombination) processes.[119-120, 139, 142, 145-146] Monomolecular recombination occurs between two opposite charges of the same photoexcitation either in or directly after the CT state. In trap-assisted recombination, charge carriers are immobilized by defects, aggregates or interfacial trap states. Traps introduce energy states within the material's energy gap, and immobilization charge carrier eventually leads to recombination. Bimolecular recombination refers to recombination of two charges from different photoexcitations, in which charge diffuse within the Onsager radius. Additionally, bimolecular recombination follows second-order kinetics, meaning that the rate increases with photoexcitation density or light intensity.[139] Since most OPV materials are considered mostly trap-free, bimolecular recombination is recognized as the dominant recombination process in the BHJ architecture.[142, 146] The bimolecular recombination rate is,[145-146]

$$R = \gamma(np - n_i p_i) \quad (\mathbf{2.33})$$

where n and p are the free charge carrier densities, n_i and p_i are the intrinsic charge carrier densities, and γ is the recombination rate given by,[145-146]

$$\gamma = \frac{e}{\varepsilon_r \varepsilon_0}(\mu_n + \mu_p) \quad (\mathbf{2.34})$$

where μ_n and μ_p are the electron and hole mobilities, respectively. Annealing of the film reduces bimolecular recombination rates due to greater phase separation between D/A components.[137] In P3HT:PCBM, the recombination rates (γ) before and after annealing are 1.1 x 10^{-17} and 1.1 x 10^{-18} m^3/s.[142] Since both charge transport and recombination depend on charge carrier mobilities, there is an optimal trade-off point.[145] It has been reported that the highest device efficiencies are achieved for charge mobilites from 10^{-6} to 10^{-4} $m^2/(Vs)$, and higher values result in a charge extraction reduction.

2.3.2.6 Charge Collection. Once a charge carrier arrives at an electrode, charge extraction is influenced by several factors. Electrodes can either form ohmic or Schottky contacts, associated band bending of the work function of the electrode in relation to the HOMO or LUMO level of the donor (hole collection) or acceptor (electron collection), respectively.[119, 147] For an ohmic contact, the work function must be equal to or higher than the HOMO level of the donor, or equal to or lower than the LUMO level of the acceptor. The opposite is true for a Schottky contact. Ohmic contacts pose no significant potential barrier on charge extraction, whereas a Schottky contact does. Tunneling through a Schottky contact can occur with barrier thinning, making it more ohmic. The charge collection efficiency (η_{CC}) is the ratio of the collected charge carriers by the electrodes to the number of fully dissociated charge carriers.[121]

Carrier (hole or electron) transport layers are used between the OPV BHJ and the separate electrodes to more closely match energy levels for improved η_{CC} (associated with reduced

recombination rates). A commonly used hole-transport layer is poly(3,4-ethylenedioxythiophene)-poly(styrenesulfonate) (PEDOT:PSS), which has a closely matched work function with the HOMO level of P3HT (~5.2 eV for both), allowing for effective hole transport to ITO.

In reality, the η_{CC} is more convoluted than energy diagrams illustrate. For instance, a mismatch between hole and electron charge carrier mobility can cause charge accumulation at the electrodes, associated with space-charge.[148] Furthermore, deposition of metallic layers onto organic layers may induce chemical reactions and structural changes, which ultimately affect the energy band alignment.[120, 135, 148] Specifically, low deposition rates of the metallic layers onto the organic layers provides increased uniformity, which is well-known to be critical for the η_{CC}.

2.3.3 OPV Device Electrical Characterization.

2.3.3.1 Current-Density to Voltage Characteristics. PV devices are a type of photodiode optimized to convert light into usable electrical power. Since power is the product of voltage and DC current (P = V x I), current-voltage (I-V) characterization is fundamental to the electrical properties of PV devices. The current-density (J) is calculated from the ratio of current to the area, (J = I/A; in this case, the area is the device active area), which is often utilized over simply current as active area sizes may vary. Therefore, J-V curves are presented primarily in this dissertation.

Without illumination (dark J-V curve), the PV device acts a conventional diode that allows the flow of current in the forward-bias and a small current in reverse-bias (ideal devices have zero current in reverse-bias) (**Figure 2.25**). The dark current-density (J_D) in reverse-bias is known as dark saturation current density (J_0) or often referred to as leakage current density (leakage current flowing over the diode in reverse bias), which is an important parameter for comparing device recombination levels (more recombination means higher leakage current).[132, 149-150] The Shockley diode equation for the PV device without illumination is,[119, 132]

$$J_D = J_0 \left[\exp\left(\frac{Ve}{nkT}\right) - 1\right] \quad \textbf{(2.35)}$$

where J_0 is the dark saturation current-density, e is charge of an electron, and n is the ideality factor. Together, kT/e is the thermal voltage (V_T), and at 25°C, $V_T \approx 0.0259$ V. The ideality factor represents of the degree of similarity to an ideal diode (n = 1).

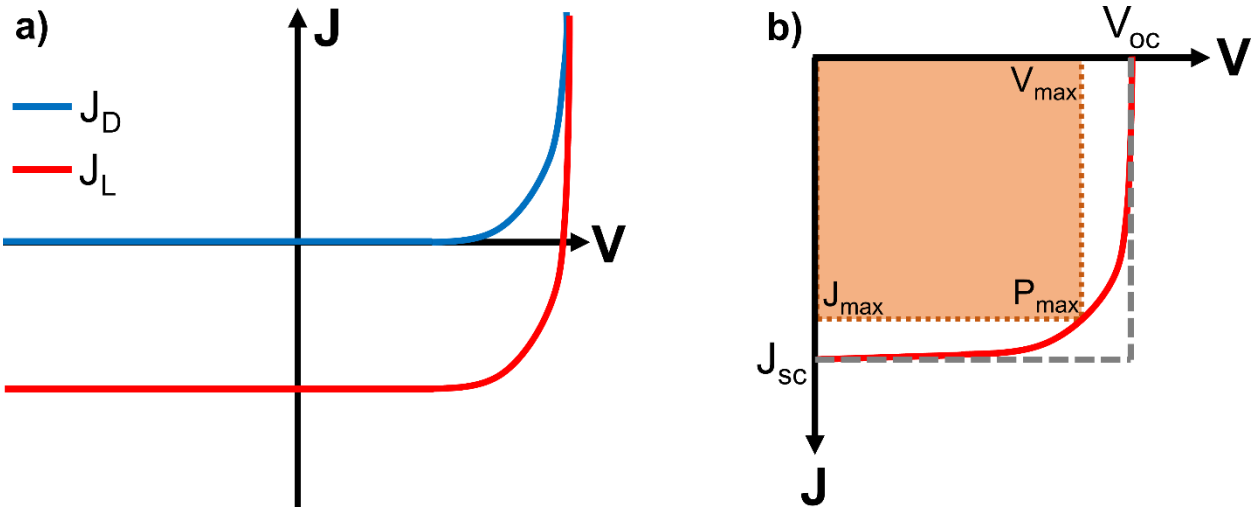

Figure 2.25. Current-density to voltage (J-V) curves for (**a**) both dark and light current-density. (**b**) Fourth-quadrant representation of the light J-V curve. J_{sc} is short-circuit current density, V_{oc} is open-circuit voltage, and P_{max} is the maximum product of current and voltage.

As discussed in the previous sections, illumination of the device causes a photogeneration of charge carriers. Generated charge carriers constitute the device's photocurrent (J_{ph}). The photocurrent shifts the J-V curve below the x-axis (voltage axis) (**Figure 2.25**), and the light current-density (J_L) represented by the Shockley equation (without parasitic resistances) is,[119, 132]

$$J_L = J_D - J_{ph} = J_0 \left[\exp\left(\frac{Ve}{nkT}\right) - 1\right] - J_{ph} \quad \textbf{(2.36)}$$

For standard comparison of the PV devices, J_L is measured for devices under AM1.5G (100 mW/cm^2) illumination. The flow of generated current together with the diode's operation in forward-bias places the generated power from the PV device in the fourth-quadrant (**Figure 2.25**). Here, the current-density at zero voltage is known as the short-circuit current-density ($J_{V=0} = J_{sc}$). For negligible parasitic resistances or leakage current, J_{sc} is approximately equal to photocurrent ($J_{sc} \approx J_{ph}$), as the J_D is roughly zero for zero voltage.[132] J_{sc} scales with the device's optical absorption and charge carrier mobilities, and is degraded with an increase in series resistance.[148, 151-154]

The voltage at J = 0 is referred to as the open-circuit voltage ($V_{J=0} = V_{oc}$). At V_{oc}, the J_{ph} equals the J_D. The theoretical maximum V_{oc} is correlated to the E_g of a D/A BHJ OPV device by,

$$V_{oc} \approx \frac{E_g}{e} - V_{loss} \quad \textbf{(2.37)}$$

where (E_g = IP(D) – EA(A)) and V_{loss} is voltage losses and is primarily associated with band bending at the electrode ohmic contacts, which can vary in the vicinity of 0.4 V (~0.2 V per contact) due to thermal fluctuations or illumination power densities. The voltage losses in the V_{oc} are also related to device recombination levels, as discussed later.[132]

The maximum power produced from the PV device is equal to the maximum product of voltage and current-density in the fourth-quadrant as,

$$P_{max} = V_{max}J_{max} \quad \textbf{(2.38)}$$

and the product of the P_{max} is represented by the shaded square in **Figure 2.25.** The fill factor (FF) quantifies the "squareness" of the J-V curve and the quality of the device as,[119, 132]

$$FF = \frac{V_{max}J_{max}}{V_{oc}J_{sc}} = \frac{P_{max}}{V_{oc}J_{sc}} \quad \textbf{(2.39)}$$

The FF is graphically shown in the ratio of the shaded square to the dotted square in **Figure 2.25**. The power conversion efficiency (PCE) or efficiency (η) is the fundamental value for the comparison of PV devices represented as,

$$PCE = \frac{FFV_{oc}J_{sc}}{P_{in}} = \frac{P_{max}}{P_{in}} \quad \textbf{(2.40)}$$

where P_{in} is the incident power density from the illumination source onto the PV device.

2.3.3.2 Equivalent Circuit and Parasitic Resistance. The photodiode design of the PV device can be characterized by an equivalent circuit with previously discussed parameters including a photocurrent source (J_{ph}) and a diode with a dark current-density (**Figure 2.26**). The two parasitic resistances, shunt (R_{sh}) and series (R_s) are also added to the equivalent circuit. These parasitic resistances directly influence the FF, so R_{sh} and R_s should be as high and low as possible, respectively.

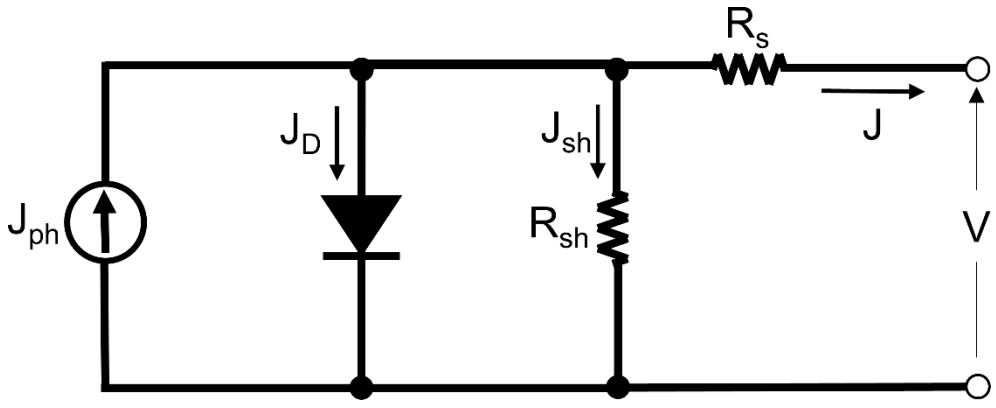

Figure 2.26. Equivalent circuit for the OPV device with parasitic resistances.

Ideally, the R_{sh} should be as high as possible, which correlates to limited linear ohmic shunts (short circuits) and nonlinear local shunts (caused by localized recombination centers; i.e. interfacial/crystal defects, impurities and nanoparticle aggregations).[120, 155-159] In the equivalent

circuit, the shunt current-density (J_{sh}) flows over the R_{sh}, which associates with current lost to shunts.[149] The R_{sh} can be determined by the reciprocal J-V slope at zero voltage by,[149]

$$R_{sh} = \left(\frac{dV}{dJ}\right)_{V \to 0} \tag{2.41}$$

R_{sh} degradations cause the J-V curve to lose its diode characteristics and become more ohmic with a drop in the FF. Decreases in the R_{sh} are associated with deteriorations of the V_{oc} (**Figure 2.27a**), since both are related to charge recombination, which becomes more significant at low light intensities.[119, 155] A reduction of the R_{sh} to very low levels causes the V_{oc} to approach 0 V.[132] Generally, the R_{sh} is not influential on the J_{sc}.

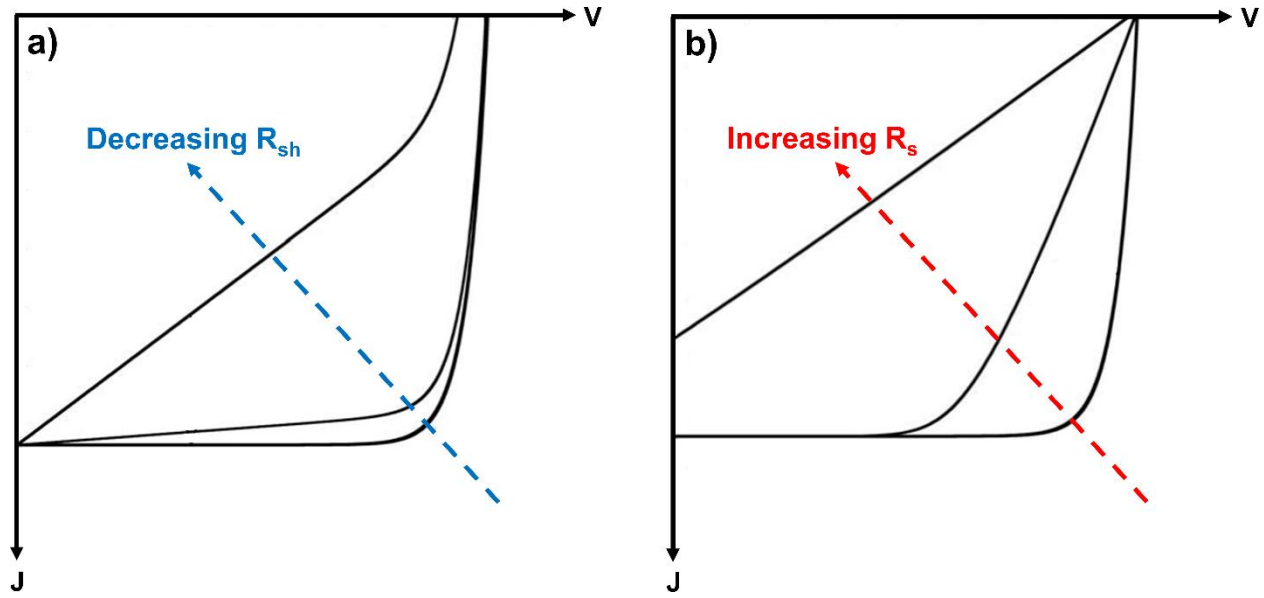

Figure 2.27. Effect of parasitic resistances on a J-V curve, such as (**a**) decreasing R_{sh} for $R_s = 0$, and (**b**) increasing R_s for $R_{sh} \approx \infty$. This figure was adapted from Luque, A.; Hegedus, S. Handbook of Photovoltaic Science and Engineering, *John Wiley & Sons*, **2011**.[119] Copyright 2011.

The R_s is associated with the resistance of the bulk heterojunction, electrodes, and interfacial contacts.[154] Ideally, the R_s should be as low as possible. Increased R_s leads to a reduction in the J_{sc}, and very high R_s causes the J_{sc} to approach zero (**Figure 2.27b**). Typically, the R_s does not

affect the V_{oc} levels. The R_s can be calculated from the reciprocal slope at voltages much larger than V_{oc} as,[149]

$$R_S = \left(\frac{dV}{dJ}\right)_{V\to\infty} \quad \textbf{(2.42)}$$

Translating the equivalent circuit with parasitic resistances into the Shockley diode equation is shown in,[132, 149, 154]

$$J_L = J_D + J_{sh} - J_{ph} \quad \textbf{(2.43)}$$

$$J = J_0\left\{\exp\left(\frac{V+JR_S}{n\frac{kT}{e}}\right) - 1\right\} + \frac{V+JR_S}{R_{sh}} - J_{ph} \quad \textbf{(2.44)}$$

and the V_{oc} by R_{sh} is represented by,[120, 132]

$$V_{OC} = n\frac{kT}{e} ln\left\{1 + \frac{J_{ph}}{J_0}\left(1 - \frac{V_{oc}}{J_{ph}R_{sh}}\right)\right\} \approx n\frac{kT}{e} ln\left\{1 + \frac{J_{ph}}{J_0}\right\} \quad \textbf{(2.45)}$$

Equation **2.45** represents that J_0 is inversely proportional to V_{oc}, meaning that a decrease in J_0 is critical maximize V_{oc} levels.

2.3.3.3 External Quantum Efficiency. Measurement of the generated current per wavelength of light provides a more complete understanding of the electrical characteristics in a PV device. The current to wavelength spectrum is established in the photoresponsivity (PR; or the spectral response) spectrum by,

$$PR(\lambda) = \frac{I_{SC}(\lambda)}{P_{source}(\lambda)} \quad \textbf{(2.46)}$$

where $P_{source}(\lambda)$ is the illumination power from light source per wavelength and $I_{sc}(\lambda)$ is the short-circuit current at each wavelength. Typically, the $P_{source}(\lambda)$ is calculated by measuring the $I_{sc}(\lambda)$

from a calibrated photodiode with an issued PR spectrum from its manufacturer. This can then be used to calculate the PR spectrum for a PV device. Therefore, PR is an essential property to photodiodes or PV devices. Units for PR are amps per watt (A/W). Similar to the PR is the external quantum efficiency (η_{EQE}) equal to,

$$\eta_{EQE}(\lambda) = \frac{N_e}{N_{ph}}\, x\, 100\% \qquad (\mathbf{2.47})$$

where N_e is the number of electrons and N_{ph} is the number of photons, specific to a distinctive wavelength λ. The η_{EQE} is calculated directly from the PR by,

$$\eta_{EQE}(\lambda) = E_{ph}\frac{PR(\lambda)}{e} = \frac{hcPR(\lambda)}{e\lambda}\, x\, 100\% \qquad (\mathbf{2.48})$$

The EQE takes account for all of the photons incident on a device. The η_{EQE} can also be represented as,[121, 128]

$$\eta_{EQE}(\lambda) = \eta_A(\lambda)\eta_{ED}(\lambda)\eta_{CT}(\lambda)\eta_{CC}(\lambda) \qquad (\mathbf{2.49})$$

Essentially, the quantum efficiency corresponds to the efficiency for the entire charge carrier photogeneration process per wavelength. The internal quantum efficiency (η_{IQE}) is also often reported since it isolates only the photons *absorbed* by the device,[120, 128]

$$\eta_{IQE}(\lambda) = \frac{\eta_{EQE}(\lambda)}{(1-R)} \qquad (\mathbf{2.50})$$

2.3.4 OPV Device Degradation Pathways and Stability.

The introduction of new, high-performance conjugated polymers has allowed OPVs to reach PCE's above 10%, making them increasingly competitive to their inorganic counterparts. However, since the advent OPVs, degradation and limited lifetimes has remained a principal barrier to their commercialization viability. While inorganic PVs can last upwards of 25 years,

OPVs are limited to 7 – 10 years.[160] The three primary degradation pathways are photo-oxidation, temperature, and photo-induced "burn-in".

Photo-oxidation is the result of oxygen or water diffusion into the device, coupled with illumination.[160-161] UV-irradiation on the conjugated polymers drives an oxidative free radical reaction on the alkyl side chains and the polymer backbone. This reaction leads to a disruption of the chain conjugation, by either a scission of the chain or the growth of carbonyl, ester, alkoxy, or sulfoxide bonds. The end result is a loss in absorption, called "bleaching", and the reduction of the operational active area by propagation of "dead zones". The addition of PCBM to P3HT has been stated to slow photo-oxidation as electron transfer directly competes with oxygen radicals.[160] Additionally, low work function metallic electrodes are known to oxidize leading to performance degradations. Although photo-oxidation can cause rapid device failure within seconds to hours, it can be prevented by encapsulation, such as glass-on-glass (preferable) or flexible plastic.

Thermal degradation is a large area of concern for OPVs, due to the substantially lower T_g's in polymers compared to inorganics.[160] PV operating temperatures range from room temperature to 60 ºC (140 ºF), which is especially problematic for traditional conjugated polymers blends, such as P3HT:PCBM with $T_g \approx 56$ ºC. Heating the device above the materials T_g essentially causes unintentional annealing, leading to large scale phase separation between the D/A components, and reduction in the exciton dissociation or charge extraction efficiencies. For traditional polymers, crosslinking between components can promote thermal stability, but at the cost of performance. Fortunately, the high-performance conjugated polymer blends PCDTBT:$PC_{71}BM$ and PBT7-Th:$PC_{71}BM$ have significantly greater T_g's ranging from 120 ºC to 150 ºC, and thus show superior thermal stability to traditional polymers.[160, 162-163]

Photo-induced burn-in has recently been identified as the leading cause in reduced device performance over photo-oxidation and temperature, although a full understanding of this degradation pathway is still incomplete.[160, 164-165] In the first hundred to thousand hours, burn-in causes a 10 – 50% performance decrease, then transitions to either a ceased or very gradual degradation for the remaining lifetime of the device. Burn-in has been found to cause photo-dimerization in fullerenes, specifically C_{60} (or PCBM), leading to significant J_{sc} losses.[160, 164] Fullerene photo-dimerization is not currently understood, but it can be prevented by either using $PC_{71}BM$ or a non-fullerene acceptor. Burn-in also causes V_{oc} deteriorations, attributed to heightened disorder levels, density of states broadening, and recombination losses. Recently, burn-in in PTB7-Th:$PC_{71}BM$ devices has been correlated to the absorption of high energy UV photons, which cause a spin-flip at the D/A interface and the formation of long-lived triplet anions (in the CT state of $PC_{71}BM$).[164] However, without the additive, 1,8 diiodooctane (DIO), and with the the utilization of UV filters, these devices exhibited an initial 8.87% PCE and a projected T_{80} lifetime (lifetime for the device to maintain 80% PCE) for 7 years.

2.3.5 Plasmonics Nanoparticles in OPV Devices.

Even with the possibility of future stability enhancements and the advancement of high-performance conjugated polymers to reach higher PCE's, low dielectric constants are still inherent to organic semiconductors. Compared to inorganics, these low dielectric constants create large exciton binding energies, short exciton diffusion lengths, limited charge mobility, and hence significant charge recombination. These properties conspire together in limiting the optimal active layer thickness and the overall absorption efficiency.

2.3.5.1 Localized Surface Plasmon Resonance. Plasmonic metallic nanoparticles can effectively address the issues of OPVs by inducing substantial absorption efficiency increases

without modification of the active layer thickness. As incident light is irradiated onto the nanoparticles, a resultant coherent oscillation of the conduction electrons occurs within the metallic core (**Figure 2.28**).[166-172] The light's electric field exerts force on the electrons, which creates an electron displacement and dipole within the nanoparticle. The greater the displacement, the greater the subsequent restoring force. Similar to a damped linear oscillator, the largest displacement amplitude occurs at the nanoparticle's plasmonic resonant frequency,[169]

$$\omega_p = \frac{ne^2}{\varepsilon_0 m^*} \tag{2.51}$$

where n is the conduction electron density and m* is the optical mass of the conduction electrons.

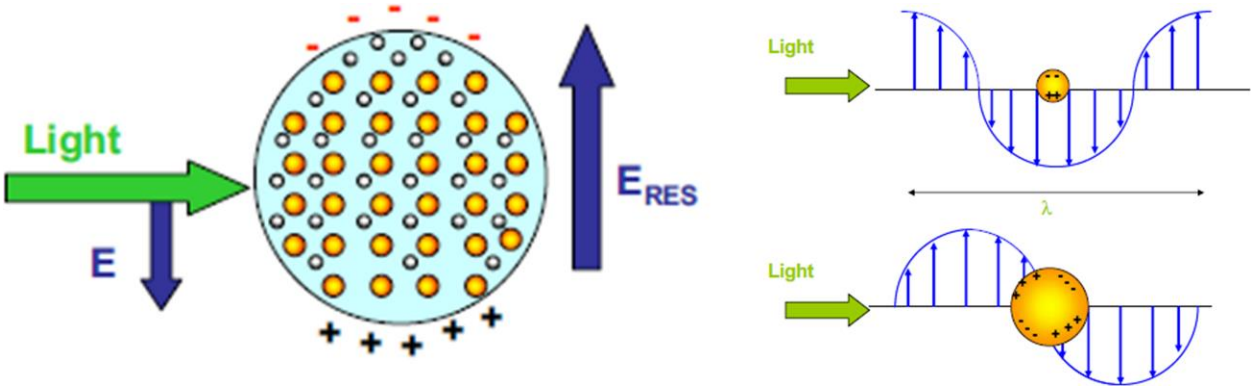

Figure 2.28. Coherent oscillation of conduction electrons within the metallic core of a nanoparticle and the electric field enhancements around two different sized nanoparticles. Reproduced with permission from García, M. A. Surface Plasmons in Metallic Nanoparticles: Fundamentals and Applications. *Journal of Physics D: Applied Physics* **2011**, *44* (28), 283001.[168]

The electron oscillations develop large electric field enhancements at the nanoparticle surface by a mode of extinction called localized surface plasmon resonance (LSPR).[166-175] The peak LSPR wavelength (λ_{LSPR}) is dependent on the nanoparticle shape, size, aspect ratio (ratio of the lateral dimension to thickness), and the dielectric constant of the surrounding medium. Essentially, the

nanoparticle LSPR is effective at concentrating the incident light and increasing the overall absorption of the organic semiconducting layer. Surface plasmons (SPs) also exist at the interface between bulk metals with a negative permittivity and a dielectric medium with a positive permittivity, creating an electronic oscillation.[168, 174] However, LSPR is unique to nanoparticles where electrons are three-dimensionally confined and have a less than <200 nm diameter, which is below the wavelength of light. LSPR can increase the electric field near the nanoparticle surface up by ~50 to 10,000 times that of the incident light, with a spatial range of 10 to 50 nm, depending on the nanoparticle properties.[173] The spatial range is provided by the LSPR extinction cross-section, which consists of a non-radiative absorption and a radiative scattering (transformation of plasmons into photons) component.[166-170, 172] The absorption component is more substantial in smaller nanoparticles (5 to 20 nm in diameter), which act as subwavelength light "antennas" due to LSPR-induced local field enhancements (**Figure 2.29a**).[166-167] Differently, larger nanoparticles (>50 nm diameter) have a more dominant scattering component, and therefore act as subwavelength light "scattering elements" (**Figure 2.29b**). In this sense, scattering elements cause "light trapping", where light scattered beyond the critical angle for reflection will be contained within a semiconducting layer given the presence of a reflective metallic electrode. The scattering mechanism allows for an increase in the optical path length. Light trapping can also be achieved by surface plasmon polaritons (SPPs), created by metal corrugation or nanostructures, in which light is guided laterally (**Figure 2.29c**).[166, 173]

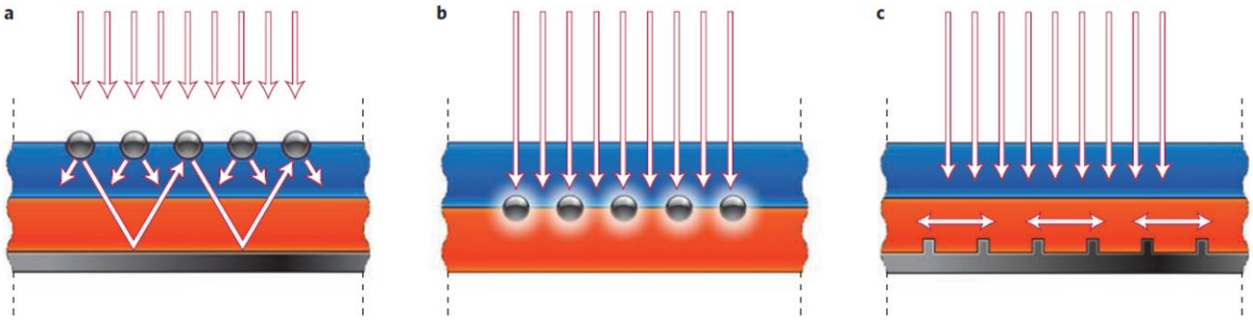

Figure 2.29. Plasmonic nanoparticles in PVs enhancement mechanisms. (**a**) Light trapping by scattering elements, (**b**) electric-field enhancements by LSPR, and (**c**) lateral light guiding by SPPs. Reprinted by permission from Springer Nature: Atwater, H. A.; Polman, A. Plasmonics for Improved Photovoltaic Devices. *Nature Materials* **2010**, *9* (3), 205.[166] Copyright 2010.

The absorption (σ_{abs}) and scattering (σ_{sc}) cross-section are given by,[167]

$$\sigma_{abs} = (k)Im\left[3V\left(\frac{\left(\frac{\varepsilon_p}{\varepsilon_m}\right)+1}{\left(\frac{\varepsilon_p}{\varepsilon_m}\right)+2}\right)\right] \quad (\mathbf{2.52})$$

$$\sigma_{sc} = \frac{1}{6\pi}k^2\left[3V\left(\frac{\left(\frac{\varepsilon_p}{\varepsilon_m}\right)+1}{\left(\frac{\varepsilon_p}{\varepsilon_m}\right)+2}\right)\right]^2 \quad (\mathbf{2.53})$$

where k is the wavenumber, ε_p is the dielectric constant of the nanoparticle's metal, ε_m is the dielectric constant of the surrounding medium, and V is the nanoparticle volume. The absorption and scattering cross-section can also be interpreted as an efficiency, i.e. the ratio of absorbed or scattered photons on actual particle to the number of absorbed or scattered photons on an opaque particle (that fully absorbs or scatters all photons).[167-168] The LSPR extinction cross-section is sum of the two components ($\sigma_{ext} = \sigma_{abs} + \sigma_{sc}$). Near the λ_{LSPR}, the extinction cross-section can be greater than 10 times the geometrical cross-section of the nanoparticle.

2.3.5.2 Plasmonics Metals. Plasmonic materials are often composed of noble metals (such as Ag, Au, Cu, Pt) since they have large absorption in the visible wavelengths, higher conductivity,

larger plasma frequencies, and lower loss compared to conventional metals.[167, 169, 171] Losses occur from electron-electron or electron-phonon interactions, scattering within lattice defects, or interband electronic transition losses. Interband losses are attributed to a broad density of states between the valence and conduction band, leading to electron transitions and an onset frequency. Losses can be described by the Drude theory related to the permittivity of a metal as,[169, 171]

$$\varepsilon(\omega) = \varepsilon(\omega)' + i\varepsilon(\omega)'' = \varepsilon_{int} - \frac{\omega_p^2}{\omega(\omega + i\Gamma)} \quad (\mathbf{2.54})$$

where $\varepsilon(\omega)'$ is the real part of the dielectric function (strength of e-field polarization), $\varepsilon(\omega)''$ is the imaginary portion related to the losses in the material (low loss means low $\varepsilon(\omega)''$), ε_{int} is permittivity portion related to interband transitions and Γ is the damping rate. Γ correlates to damping of the plasmons (analogous to a linear oscillator) and is defined as,[168-169, 172]

$$\Gamma = \Gamma_\infty + \frac{A v_F}{R} = \frac{1}{\tau} = \frac{2\hbar}{T_2} \quad (\mathbf{2.55})$$

where Γ_∞ is the relaxation constant for the bulk, A is a material dependent constant, v_F is the fermi velocity, R is the particle radius, τ is the relaxation time for conduction electrons, $\hbar$ is the reduced Planck's constant, and T_2 is the dephasing time. Since the T_2 is proportional to the field enhancement factor ($T_2 \propto |f|$) and inversely proportional to Γ, a smaller Γ associates with a greater field enhancement.[172] The damping constant combines both radiative (scattering) and non-radiative (absorption) portions of the LSPR extinction ($\Gamma = \Gamma_{rad} + \Gamma_{non\text{-}rad}$). Γ is also considered the homogeneous line width or the full-width half maximum (FWHM) for a monodisperse nanoparticle solution λ_{LSPR}. Therefore, a narrower line width in an extinction spectrum corresponds to a greater field enhancement. However, since other solution factors can also result in an increased FWHM, such as a broad nanoparticle size distribution (polydispersity), extensive analysis is required in examination of these properties.[172]

Among noble metals, Ag and Au are most common for plasmonic applications due to their lower losses in the optical wavelengths, however, Ag is optically superior for plasmonics.[169, 171] For instance, the Γ of Ag is 0.02 eV, substantially smaller than Au at 0.07 eV.[171] Furthermore, the interband onset frequency (ω_{int}) of Ag is located outside of visible wavelength range at 3.9 eV (318 nm), whereas it is within the visible range for Au at 2.3 eV (539 nm), making Au unfavorable for various functions. Ag also has higher conductivity at 6.21 x 10^7 S/m compared to Au at 4.55 x 10^7 S/m.[171] Besides the optical and electrical intrinsic properties, the price difference between the two metals is tremendously significant with Ag at $964/kg and Au at $52,019/kg. Despite all of the advantages in using Ag, it lacks the high-end chemical stability found in Au.[169, 171] This makes either metal attractive, depending on the application requirements.

2.3.5.3 Anisotropic Silver Nanoprisms. Traditionally, nanoparticles are spherical or isotropic in nature. More recently, anistropic particles, including nanoplates, nanoprisms, nanorods, and many other shapes have received considerable recent attention, especially for plasmonics.[172-173, 175-176] Anisotropic particles allow for large tunability of the λ_{LSPR} across the visible wavelengths into the NIR range, due to the facile control over the aspect ratio and hence, the anisotropy. The λ_{LSPR} can be dramatically different for nanoparticles with identical volume, but different anisotropy and shape (**Figure 2.29**). Since isotropic nanoparticles have a fixed aspect ratio at 1 their λ_{LSPR} range is limited, whereas the aspect ratio in anistropic particles can range from ~1 to over 40.[176-177] In the synthesis of anistropic nanoparticles, the adjustment of the lateral dimension is typically more common in comparison to the thickness, which stays relatively constant for each type of particle.[172, 175, 177] Along with tunability, anisotropic nanoparticles possess substantially higher LSPR extinction efficiencies and local electric-field enhancements over isotropic nanoparticles. Although these properties are not easily measured, they can be readily predicted using simulation

models including discrete dipole approximation (DDA), in which a modeled particle is partitioned into polarizable fragments. The model produces an electric-field contour for a specific geometry (**Figure 2.30**). For a sphere, cube, and pyramid, DDA predicts peak electric field contour ($|\mathbf{E}|^2$) values of 54, 745, and 9770, respectively, which shows the apparent differences in enhancements.

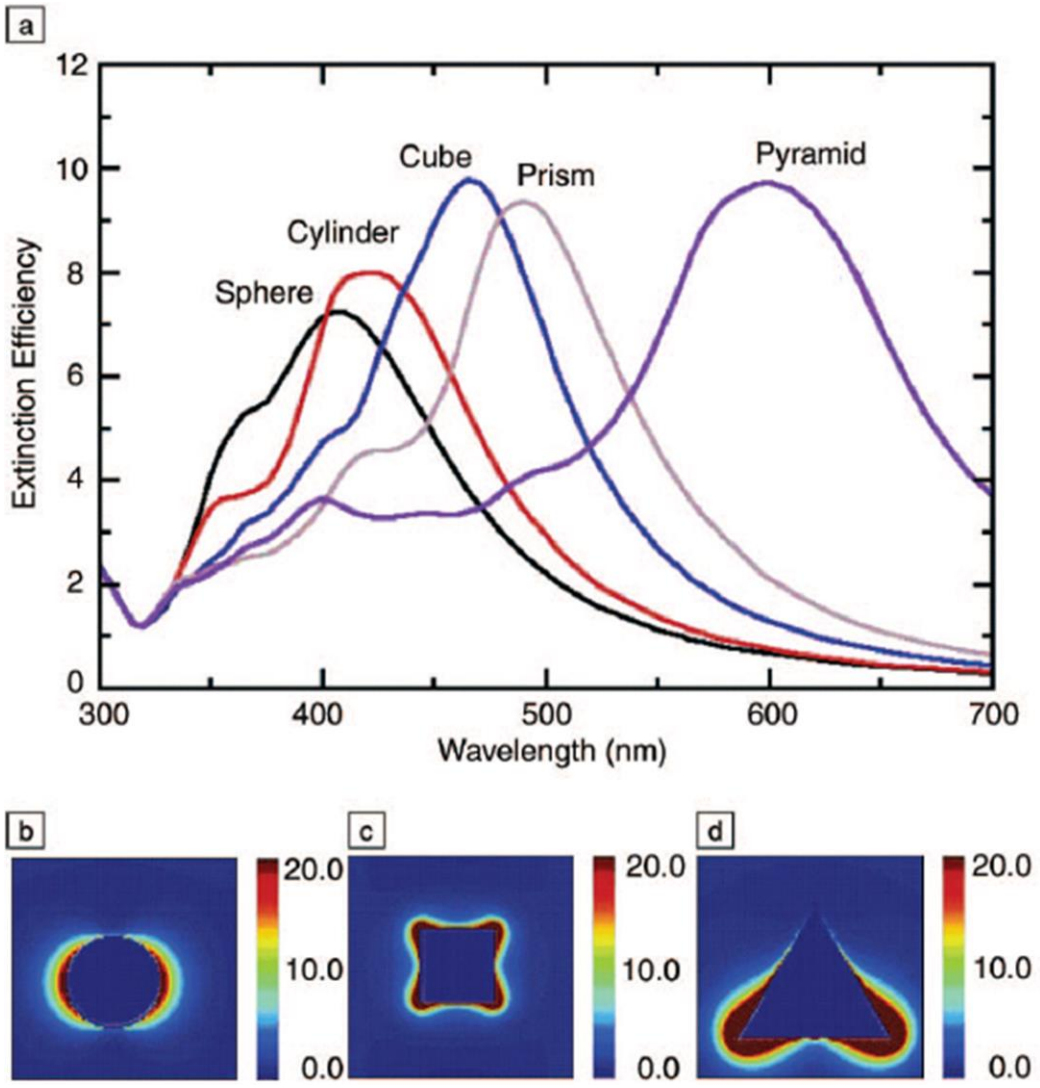

Figure 2.30. (**a**) Extinction efficiencies for different particle geometries all identical volume to a sphere with a 50 nm radius. Electric field contours ($|\mathbf{E}|^2$) of a (**b**) sphere, (**c**) cube, and (**d**) pyramid. Reproduced with permission from Haes, A. J.; Haynes, C. L.; McFarland, A. D.; Schatz, G. C.;

Van Duyne, R. P.; Zou, S. Plasmonic Materials for Surface-Enhanced Sensing and Spectroscopy. *MRS bulletin* **2005**, *30* (5), 368-375.[173]

Silver nanoprisms or nanoplates (AgNPs) are attractive since they often contain sharp tips, which contribute to significant optical properties.[172, 176] AgNPs can be synthesized through photochemical or thermal means. Photochemical synthesis requires excitation illumination beams, which can produce high quality, monodisperse solutions, but require days to complete. In thermal synthesis, AgNPs grow at specific temperature (often room temperature) and pH, which develops nanoparticle solutions in hours, but often with increased polydispersity. However, recent thermal methods show largely monodisperse, high-quality solutions (>95% yield) solutions using stability and capping agents, such as PSSS and sodium citrate.[172] Furthermore, these methods produce AgNPs at room temperature, using a seed-mediated method, and anisotropic growth is driven by defects in the seeds. Growth onto the seeds develops a hexagonal FCC crystal with a large flat {111} face (with lattice constant of 2.50 Å), edges composed of combinations of {111} and {100} FCC faces, and a 1.5 nm thick defect-rich HCP layer sandwiched between the two faces (**Figure 2.31**). Every other edge has alternating larger {100} or {111} FCC faces. Due to the instability of the HCP layer (unnatural crystal for Ag) and relatively lower stability in the {100} face compared to the {111} face, AgNP growth is purely driven at the edges with larger {100} faces. That way, AgNPs begin as hexagonal nanoplates, and then develop into large-area triangular nanoprisms. Since the amount of added silver nitrate ($AgNO_3$) is kept constant, the size of the prisms is inversely proportional to the concentration of Ag seeds. Larger AgNPs have λ_{LSPR}'s at longer wavelengths. In this method, AgNPs are developed with λ_{LSPR}'s spanning the entire visible range, with lateral dimensions ranging from ~20 to 70 nm, and thicknesses in the range of 5 to 6 nm (**Figure 2.31**). This method was utilized in this dissertation with slight modifications.

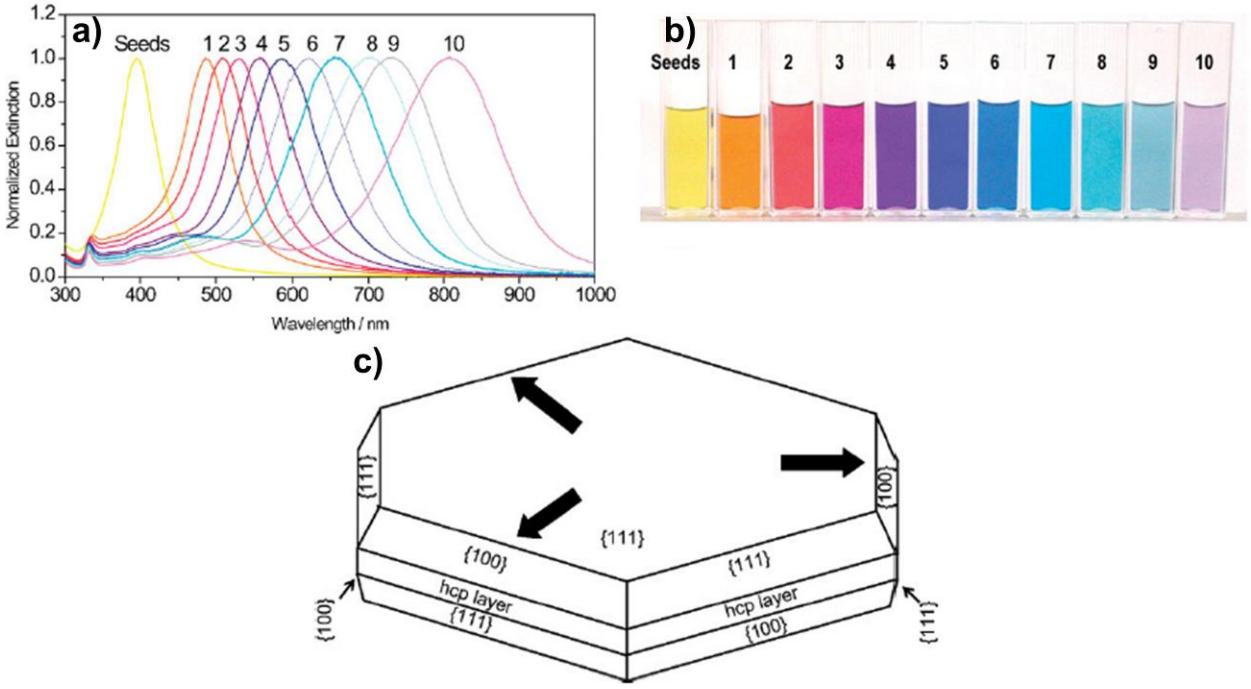

Figure 2.31. Room temperature seed-mediated growth of AgNPs. (**a**) LSPR extinction spectra and (**b**) solutions for a range of AgNP sizes (1 being the smallest, 10 being the largest) with seed concentrations of 1) 650 µL, 2) 500 µL, 3) 400 µL, 4) 260 µL, 5) 200 µL, 6) 120 µL, 7) 90 µL, 8) 60 µL, 9) 40 µL, and 10) 20 µL. (**c**) FCC crystal and growth mechanism for AgNPs. Reproduced with permission from Aherne, D.; Ledwith, D. M.; Gara, M.; Kelly, J. M. Optical Properties and Growth Aspects of Silver Nanoprisms Produced by a Highly Reproducible and Rapid Synthesis at Room Temperature. *Advanced Functional Materials* **2008**, *18* (14), 2005-2016.[172]

The use of NPs in OPV devices is outlined thoroughly in the introductions of **Chapters 6** and **7**. Please refer there for more information.

REFERENCES

(1) Whitesides, G. M.; Grzybowski, B. Self-Assembly at All Scales. *Science* **2002,** *295* (5564), 2418-2421.
(2) Pelesko, J. A. Self Assembly: The Science of Things That Put Themselves Together, *CRC Press*, **2007**.
(3) Philp, D.; Stoddart, J. F. Self-Assembly in Natural and Unnatural Systems. *Angewandte Chemie International Edition* **1996,** *35* (11), 1154-1196.

(4) Hermanson, K. D.; Lumsdon, S. O.; Williams, J. P.; Kaler, E. W.; Velev, O. D. Dielectrophoretic Assembly of Electrically Functional Microwires from Nanoparticle Suspensions. *Science* **2001,** *294* (5544), 1082-1086.
(5) Lee, W.; Amini, H.; Stone, H. A.; Di Carlo, D. Dynamic Self-Assembly and Control of Microfluidic Particle Crystals. *Proceedings of the National Academy of Sciences* **2010,** *107* (52), 22413-22418.
(6) Bowden, N.; Terfort, A.; Carbeck, J.; Whitesides, G. M. Self-Assembly of Mesoscale Objects into Ordered Two-Dimensional Arrays. *Science* **1997,** *276* (5310), 233-235.
(7) Gracias, D. H.; Tien, J.; Breen, T. L.; Hsu, C.; Whitesides, G. M. Forming Electrical Networks in Three Dimensions by Self-Assembly. *Science* **2000,** *289* (5482), 1170-1172.
(8) Roberts, G. Langmuir-Blodgett Films, *Springer Science & Business Media,* **2013**.
(9) Ulman, A. An Introduction to Ultrathin Organic Films: From Langmuir--Blodgett to Self--Assembly, *Academic press,* **2013**.
(10) Zasadzinski, J.; Viswanathan, R.; Madsen, L.; Garnaes, J.; Schwartz, D. Langmuir-Blodgett Films. *Science* **1994,** *263* (5154), 1726-1733.
(11) Paul, S.; Pearson, C.; Molloy, A.; Cousins, M.; Green, M.; Kolliopoulou, S.; Dimitrakis, P.; Normand, P.; Tsoukalas, D.; Petty, M. Langmuir− Blodgett Film Deposition of Metallic Nanoparticles and Their Application to Electronic Memory Structures. *Nano Letters* **2003,** *3* (4), 533-536.
(12) Zhu, J.; Yu, Z.; Burkhard, G. F.; Hsu, C.-M.; Connor, S. T.; Xu, Y.; Wang, Q.; McGehee, M.; Fan, S.; Cui, Y. Optical Absorption Enhancement in Amorphous Silicon Nanowire and Nanocone Arrays. *Nano letters* **2008,** *9* (1), 279-282.
(13) Ulman, A. Formation and Structure of Self-Assembled Monolayers. *Chemical reviews* **1996,** *96* (4), 1533-1554.
(14) Love, J. C.; Estroff, L. A.; Kriebel, J. K.; Nuzzo, R. G.; Whitesides, G. M. Self-Assembled Monolayers of Thiolates on Metals as a Form of Nanotechnology. *Chemical reviews* **2005,** *105* (4), 1103-1170.
(15) Madou, M. J. Fundamentals of Microfabrication: The Science of Miniaturization, *CRC press,* **2002**.
(16) Samant, M. G.; Brown, C. A.; Gordon, J. G. An Epitaxial Organic Film. The Self-Assembled Monolayer of Docosanoic Acid on Silver (111). *Langmuir* **1993,** *9* (4), 1082-1085.
(17) Tillman, N.; Ulman, A.; Penner, T. L. Formation of Multilayers by Self-Assembly. *Langmuir* **1989,** *5* (1), 101-111.
(18) Decher, G. Fuzzy Nanoassemblies: Toward Layered Polymeric Multicomposites. *Science* **1997,** *277* (5330), 1232-1237.
(19) De Villiers, M. M.; Otto, D. P.; Strydom, S. J.; Lvov, Y. M. Introduction to Nanocoatings Produced by Layer-by-Layer (Lbl) Self-Assembly. *Advanced drug delivery reviews* **2011,** *63* (9), 701-715.
(20) Iler, R. Multilayers of Colloidal Particles. *Journal of Colloid and Interface Science* **1966,** *21* (6), 569-594.
(21) Decher, G.; Hong, J. D. In *Buildup of Ultrathin Multilayer Films by a Self-Assembly Process, 1 Consecutive Adsorption of Anionic and Cationic Bipolar Amphiphiles on Charged Surfaces*, Makromolekulare Chemie. Macromolecular Symposia, Wiley Online Library: 1991; pp 321-327.
(22) Decher, G.; Hong, J.; Schmitt, J. Buildup of Ultrathin Multilayer Films by a Self-Assembly Process: Iii. Consecutively Alternating Adsorption of Anionic and Cationic Polyelectrolytes on Charged Surfaces. *Thin solid films* **1992,** *210* 831-835.

(23) Decher, G.; Lvov, Y.; Schmitt, J. Proof of Multilayer Structural Organization in Self-Assembled Polycation-Polyanion Molecular Films. *Thin Solid Films* **1994,** *244* (1), 772-777.
(24) Yoo, D.; Shiratori, S. S.; Rubner, M. F. Controlling Bilayer Composition and Surface Wettability of Sequentially Adsorbed Multilayers of Weak Polyelectrolytes. *Macromolecules* **1998,** *31* (13), 4309-4318.
(25) Shiratori, S. S.; Rubner, M. F. Ph-Dependent Thickness Behavior of Sequentially Adsorbed Layers of Weak Polyelectrolytes. *Macromolecules* **2000,** *33* (11), 4213-4219.
(26) Mendelsohn, J.; Barrett, C. J.; Chan, V.; Pal, A.; Mayes, A.; Rubner, M. Fabrication of Microporous Thin Films from Polyelectrolyte Multilayers. *Langmuir* **2000,** *16* (11), 5017-5023.
(27) Choi, J.; Rubner, M. F. Influence of the Degree of Ionization on Weak Polyelectrolyte Multilayer Assembly. *Macromolecules* **2005,** *38* (1), 116-124.
(28) Wang, X.; Liu, G.; Zhang, G. Conformational Behavior of Grafted Weak Polyelectrolyte Chains: Effects of Counterion Condensation and Nonelectrostatic Anion Adsorption. *Langmuir* **2011,** *27* (16), 9895-9901.
(29) Elzbieciak, M.; Zapotoczny, S.; Nowak, P.; Krastev, R.; Nowakowska, M.; Warszynski, P. Influence of Ph on the Structure of Multilayer Films Composed of Strong and Weak Polyelectrolytes. *Langmuir* **2009,** *25* (5), 3255-3259.
(30) Wang, S.; Granick, S.; Zhao, J., Charge on a Weak Polyelectrolyte. AIP: 2008.
(31) Decher, G.; Schmitt, J. Fine-Tuning of the Film Thickness of Ultrathin Multilayer Films Composed of Consecutively Alternating Layers of Anionic and Cationic Polyelectrolytes. *Progr. Colloid Polym. Sci.* **1992,** 160-164.
(32) Steitz, R.; Jaeger, W.; Klitzing, R. v. Influence of Charge Density and Ionic Strength on the Multilayer Formation of Strong Polyelectrolytes. *Langmuir* **2001,** *17* (15), 4471-4474.
(33) Steitz, R.; Leiner, V.; Siebrecht, R.; Klitzing, R. v. Influence of the Ionic Strength on the Structure of Polyelectrolyte Films at the Solid/Liquid Interface. *Colloids and Surfaces A: physicochemical and engineering aspects* **2000,** *163* (1), 63-70.
(34) Lourenço, J. M.; Ribeiro, P. A.; Botelho do Rego, A. M.; Braz Fernandes, F. M.; Moutinho, A. M.; Raposo, M. Counterions in Poly (Allylamine Hydrochloride) and Poly (Styrene Sulfonate) Layer-by-Layer Films. *Langmuir* **2004,** *20* (19), 8103-8109.
(35) Burke, S. E.; Barrett, C. J. Acid− Base Equilibria of Weak Polyelectrolytes in Multilayer Thin Films. *Langmuir* **2003,** *19* (8), 3297-3303.
(36) Clark, S. L.; Hammond, P. T. The Role of Secondary Interactions in Selective Electrostatic Multilayer Deposition. *Langmuir* **2000,** *16* (26), 10206-10214.
(37) Yang, S. Y.; Rubner, M. F. Micropatterning of Polymer Thin Films with Ph-Sensitive and Cross-Linkable Hydrogen-Bonded Polyelectrolyte Multilayers. *Journal of the American Chemical Society* **2002,** *124* (10), 2100-2101.
(38) Ladam, G.; Schaad, P.; Voegel, J.; Schaaf, P.; Decher, G.; Cuisinier, F. In Situ Determination of the Structural Properties of Initially Deposited Polyelectrolyte Multilayers. *Langmuir* **2000,** *16* (3), 1249-1255.
(39) Elbert, D. L.; Herbert, C. B.; Hubbell, J. A. Thin Polymer Layers Formed by Polyelectrolyte Multilayer Techniques on Biological Surfaces. *Langmuir* **1999,** *15* (16), 5355-5362.
(40) Lavalle, P.; Gergely, C.; Cuisinier, F.; Decher, G.; Schaaf, P.; Voegel, J.; Picart, C. Comparison of the Structure of Polyelectrolyte Multilayer Films Exhibiting a Linear and an Exponential Growth Regime: An in Situ Atomic Force Microscopy Study. *Macromolecules* **2002,** *35* (11), 4458-4465.

(41) Picart, C.; Lavalle, P.; Hubert, P.; Cuisinier, F.; Decher, G.; Schaaf, P.; Voegel, J.-C. Buildup Mechanism for Poly (L-Lysine)/Hyaluronic Acid Films onto a Solid Surface. *Langmuir* **2001,** *17* (23), 7414-7424.
(42) Picart, C.; Mutterer, J.; Richert, L.; Luo, Y.; Prestwich, G.; Schaaf, P.; Voegel, J.-C.; Lavalle, P. Molecular Basis for the Explanation of the Exponential Growth of Polyelectrolyte Multilayers. *Proceedings of the National Academy of Sciences* **2002,** *99* (20), 12531-12535.
(43) Hübsch, E.; Ball, V.; Senger, B.; Decher, G.; Voegel, J.-C.; Schaaf, P. Controlling the Growth Regime of Polyelectrolyte Multilayer Films: Changing from Exponential to Linear Growth by Adjusting the Composition of Polyelectrolyte Mixtures. *Langmuir* **2004,** *20* (5), 1980-1985.
(44) Salomäki, M.; Vinokurov, I. A.; Kankare, J. Effect of Temperature on the Buildup of Polyelectrolyte Multilayers. *Langmuir* **2005,** *21* (24), 11232-11240.
(45) Porcel, C.; Lavalle, P.; Ball, V.; Decher, G.; Senger, B.; Voegel, J.-C.; Schaaf, P. From Exponential to Linear Growth in Polyelectrolyte Multilayers. *Langmuir* **2006,** *22* (9), 4376-4383.
(46) Sun, B.; Jewell, C. M.; Fredin, N. J.; Lynn, D. M. Assembly of Multilayered Films Using Well-Defined, End-Labeled Poly (Acrylic Acid): Influence of Molecular Weight on Exponential Growth in a Synthetic Weak Polyelectrolyte System. *Langmuir* **2007,** *23* (16), 8452-8459.
(47) Fu, J.; Ji, J.; Shen, L.; Küller, A.; Rosenhahn, A.; Shen, J.; Grunze, M. Ph-Amplified Exponential Growth Multilayers: A Facile Method to Develop Hierarchical Micro-and Nanostructured Surfaces. *Langmuir* **2008,** *25* (2), 672-675.
(48) Bieker, P.; Schönhoff, M. Linear and Exponential Growth Regimes of Multilayers of Weak Polyelectrolytes in Dependence on Ph. *Macromolecules* **2010,** *43* (11), 5052-5059.
(49) Richert, L.; Engler, A. J.; Discher, D. E.; Picart, C. Elasticity of Native and Cross-Linked Polyelectrolyte Multilayer Films. *Biomacromolecules* **2004,** *5* (5), 1908-1916.
(50) Picart, C.; Elkaim, R.; Richert, L.; Audoin, F.; Arntz, Y.; Da Silva Cardoso, M.; Schaaf, P.; Voegel, J. C.; Frisch, B. Primary Cell Adhesion on Rgd-Functionalized and Covalently Crosslinked Thin Polyelectrolyte Multilayer Films. *Advanced Functional Materials* **2005,** *15* (1), 83-94.
(51) Harris, J. J.; DeRose, P. M.; Bruening, M. L. Synthesis of Passivating, Nylon-Like Coatings through Cross-Linking of Ultrathin Polyelectrolyte Films. *Journal of the American Chemical Society* **1999,** *121* (9), 1978-1979.
(52) Liu, X.; Zhou, L.; Liu, F.; Ji, M.; Tang, W.; Pang, M.; Sun, J. Exponential Growth of Layer-by-Layer Assembled Coatings with Well-Dispersed Ultrafine Nanofillers: A Facile Route to Scratch-Resistant and Transparent Hybrid Coatings. *Journal of Materials Chemistry* **2010,** *20* (36), 7721-7727.
(53) Pavoor, P. V.; Bellare, A.; Strom, A.; Yang, D.; Cohen, R. E. Mechanical Characterization of Polyelectrolyte Multilayers Using Quasi-Static Nanoindentation. *Macromolecules* **2004,** *37* (13), 4865-4871.
(54) Yang, G.; Ma, H.; Yu, L.; Zhang, P. Preparation and Characterization of Layer-by-Layer Self-Assembled Polyelectrolyte Multilayer Films Doped with Surface-Capped Sio 2 Nanoparticles. *Journal of colloid and interface science* **2009,** *333* (2), 776-781.
(55) Dai, X.; Zhang, Y.; Guan, Y.; Yang, S.; Xu, J. Mechanical Properties of Polyelectrolyte Multilayer Self-Assembled Films. *Thin Solid Films* **2005,** *474* (1), 159-164.
(56) Eriksson, M.; Torgnysdotter, A.; Wågberg, L. Surface Modification of Wood Fibers Using the Polyelectrolyte Multilayer Technique: Effects on Fiber Joint and Paper Strength Properties. *Industrial & engineering chemistry research* **2006,** *45* (15), 5279-5286.

(57) Zhang, C.; Hirt, D. E. Layer-by-Layer Self-Assembly of Polyelectrolyte Multilayers on Cross-Section Surfaces of Multilayer Polymer Films: A Step toward Nano-Patterning Flexible Substrates. *Polymer* **2007,** *48* (23), 6748-6754.
(58) W. X. Cao, S. J. Y., S. G. Cao, C. Zhao. Novel Polyelectrolyte Complexes Based on Diazo-Resins. *Macromol. Rapid Commun.* **1997,** *18* 983-989.
(59) J. Sun, T. W., Y. Sun, Z. Wang, X. Zhang, J. Shena, W. Caob. Fabrication of a Covalently Attached Multilayer Via Photolysis of Layer-by-Layer Self-Assembled Films Containing Diazo-Resins. *Chem. Commun.* **1998,** *17* 1853-1854.
(60) J. Sun, Z. W., Y. Sun, X. Zhang, J. Shen. Covalently Attached Multilayer Assemblies of Diazo-Resins and Porphyrins. *Chem. Commun.* **1999,** *8* 693-694.
(61) J. Sun, T. W., F. Liu, Z. Wang, X. Zhang, J. Shen. Covalently Attached Multilayer Assemblies by Sequential Adsorption of Polycationic Diazo-Resins and Polyanionic Poly(Acrylic Acid). *Langmuir* **2000,** *16* (10), 4620-4624.
(62) Lvov, Y.; Ariga, K.; Onda, M.; Ichinose, I.; Kunitake, T. Alternate Assembly of Ordered Multilayers of Sio2 and Other Nanoparticles and Polyions. *Langmuir* **1997,** *13* (23), 6195-6203.
(63) Lvov, Y. M.; Rusling, J. F.; Thomsen, D. L.; Papadimitrakopoulos, F.; Kawakami, T.; Kunitake, T. High-Speed Multilayer Film Assembly by Alternate Adsorption of Silica Nanoparticles and Linear Polycation. *Chemical Communications* **1998,** (11), 1229-1230.
(64) Cosgrove, T. Colloid Science: Principles, Methods and Applications, *John Wiley & Sons,* **2010**.
(65) Kopeliovich, D. Stabilization of Colloids. http://www.substech.com/dokuwiki/doku.php?id=stabilization_of_colloids.
(66) Morrison, I. D.; Ross, S. Colloidal Dispersions: Suspensions, Emulsions, and Foams, *Wiley-Interscience New York,* **2002**.
(67) Barnes, G.; Gentle, I. Interfacial Science: An Introduction, *Oxford University Press,* **2011**.
(68) A Complete Course in 5 Minutes. *Zeta-Meter Inc* **2012**.
(69) Napper, D. H. Polymeric Stabilization of Colloidal Dispersions, *Academic Pr,* **1983**; Vol. 3.
(70) Lin, S.; Wiesner, M. R. Theoretical Investigation on the Steric Interaction in Colloidal Deposition. *Langmuir* **2012,** *28* (43), 15233-15245.
(71) Milner, S. Polymer Brushes. *Science* **1991,** *251* (4996), 905-914.
(72) Penn, L.; Huang, H.; Sindkhedkar, M.; Rankin, S.; Chittenden, K.; Quirk, R.; Mathers, R.; Lee, Y. Formation of Tethered Nanolayers: Three Regimes of Kinetics. *Macromolecules* **2002,** *35* (18), 7054-7066.
(73) Stamm, M. Polymer Surfaces and Interfaces. *Polymer Surfaces and Interfaces: Characterization, Modification and Applications, ISBN 978-3-540-73864-0. Springer Berlin Heidelberg* **2008,** *1*.
(74) Khan, A. U.; Scruggs, C.; Hicks, D.; Liu, G. Two-Dimensional Plasmonic Nanoparticle as a Nanoscale Sensor to Probe Polymer Brush Formation. *Analytical Chemistry* **2017,** *89* (14), 7541-7548.
(75) Li, D.; He, Q.; Li, J. Smart Core/Shell Nanocomposites: Intelligent Polymers Modified Gold Nanoparticles. *Advances in colloid and interface science* **2009,** *149* (1-2), 28-38.
(76) Pletsch, H.; Peng, L.; Mitschang, F.; Schaper, A.; Hellwig, M.; Nette, D.; Seubert, A.; Greiner, A.; Agarwal, S. Ultrasound–Mediated Synthesis of High–Molecular Weight Polystyrene–Grafted Silver Nanoparticles by Facile Ligand Exchange Reactions in Suspension. *Small* **2014,** *10* (1), 201-208.

(77) Lombardo, M. T.; Pozzo, L. D. Clusters and Inverse Emulsions from Nanoparticle Surfactants in Organic Solvents. *Langmuir* **2015,** *31* (4), 1344-1352.
(78) Bokern, S.; Getze, J.; Agarwal, S.; Greiner, A. Polymer Grafted Silver and Copper Nanoparticles with Exceptional Stability against Aggregation by a High Yield One-Pot Synthesis. *Polymer* **2011,** *52* (4), 912-920.
(79) CESARANO III, J.; Aksay, I. A.; Bleier, A. Stability of Aqueous A-Al2o3 Suspensions with Poly (Methacrylic Acid) Polyelectrolyte. *Journal of the American Ceramic Society* **1988,** *71* (4), 250-255.
(80) Keller, S. W.; Johnson, S. A.; Brigham, E. S.; Yonemoto, E. H.; Mallouk, T. E. Photoinduced Charge Separation in Multilayer Thin Films Grown by Sequential Adsorption of Polyelectrolytes. *Journal of the American Chemical Society* **1995,** *117* (51), 12879-12880.
(81) Gittins, D. I.; Caruso, F. Multilayered Polymer Nanocapsules Derived from Gold Nanoparticle Templates. *Advanced Materials* **2000,** *12* (24), 1947-1949.
(82) Gittins, D. I.; Caruso, F. Tailoring the Polyelectrolyte Coating of Metal Nanoparticles. *The Journal of Physical Chemistry B* **2001,** *105* (29), 6846-6852.
(83) Schneider, G.; Decher, G. From Functional Core/Shell Nanoparticles Prepared Via Layer-by-Layer Deposition to Empty Nanospheres. *Nano Letters* **2004,** *4* (10), 1833-1839.
(84) Schneider, G.; Decher, G.; Nerambourg, N.; Praho, R.; Werts, M. H.; Blanchard-Desce, M. Distance-Dependent Fluorescence Quenching on Gold Nanoparticles Ensheathed with Layer-by-Layer Assembled Polyelectrolytes. *Nano letters* **2006,** *6* (3), 530-536.
(85) Schneider, G.; Decher, G. Functional Core/Shell Nanoparticles Via Layer-by-Layer Assembly. Investigation of the Experimental Parameters for Controlling Particle Aggregation and for Enhancing Dispersion Stability. *Langmuir* **2008,** *24* (5), 1778-1789.
(86) Hecht, E. Optics, 4th. *International edition, Addison-Wesley, San Francisco* **2002,** *3* 2.
(87) Macleod, H. A.; Macleod, H. A. Thin-Film Optical Filters, *CRC press,* **2010**.
(88) Fraunhofer, J. Bestimmung Des Brechungs-Und Des Farbenzerstreungs-Vermögens Verschiedener Glasarten, in Bezug Auf Die Vervollkommnung Achromatischer Fernröhre. *Annalen der Physik* **1817,** *56* (7), 264-313.
(89) Strutt, J. W. Iv. On the Intensity of Light Reflected from Certain Surfaces at Nearly Perpendicular Incidence. *Proceedings of the Royal Society of London* **1887,** *41* (246-250), 275-294.
(90) Smakula, A. Verfahren Zur Erhöhung Der Lichtdurchlässigkeit Optischer Teile Durch Erniedrigung Des Brechungsexponenten an Den Grenzflächen Dieser Optischen Teile. *German patent* **1935**.
(91) Cohen, M. C. Carl Zeiss - a History of a Most Respected Name in Optics. http://www.smecc.org/ziess.htm.
(92) Zhang, G.; Zhao, J.; Green, M. A. Effect of Substrate Heating on the Adhesion and Humidity Resistance of Evaporated Mgf2/Zns Antireflection Coatings and on the Performance of High-Efficiency Silicon Solar Cells. *Solar energy materials and solar cells* **1998,** *51* (3-4), 393-400.
(93) Li, M.; Shen, H.; Zhuang, L.; Chen, D.; Liang, X. Sio2 Antireflection Coatings Fabricated by Electron-Beam Evaporation for Black Monocrystalline Silicon Solar Cells. *International Journal of Photoenergy* **2014,** *2014*.
(94) Jacob, D.; Peiro, F.; Quesnel, E.; Ristau, D. Microstructure and Composition of Mgf2 Optical Coatings Grown on Si Substrate by Pvd and Ibs Processes. *Thin Solid Films* **2000,** *360* (1-2), 133-138.

(95) Kim, K.; Kim, S.; An, S.; Lee, G.-H.; Kim, D.; Han, S. Anti-Reflection Porous Sio2 Thin Film Deposited Using Reactive High-Power Impulse Magnetron Sputtering at High Working Pressure for Use in a-Si: H Solar Cells. *Solar Energy Materials and Solar Cells* **2014,** *130* 582-586.
(96) Shi, J.; Geng, Z.; Zhang, J.; Wang, C. Study on the Anti-Reflection and Structure Evolution of Hydrogenated Amorphous Carbon Grown by Plasma Chemical Vapor Deposition. *Surface and Interface Analysis* **2014,** *46* (8), 530-534.
(97) Makableh, Y.; Vasan, R.; Sarker, J.; Nusir, A.; Seal, S.; Manasreh, M. Enhancement of Gaas Solar Cell Performance by Using a Zno Sol–Gel Anti-Reflection Coating. *Solar Energy Materials and Solar Cells* **2014,** *123* 178-182.
(98) van de Groep, J.; Spinelli, P.; Polman, A. Single-Step Soft-Imprinted Large-Area Nanopatterned Anti-Reflection Coating. *Nano Lett.* **2015**.
(99) Han, K.-S.; Shin, J.-H.; Yoon, W.-Y.; Lee, H. Enhanced Performance of Solar Cells with Anti-Reflection Layer Fabricated by Nano-Imprint Lithography. *Solar Energy Materials and Solar Cells* **2011,** *95* (1), 288-291.
(100) Lee, Y.-Y.; Ho, W.-J.; Yeh, C.-W. Fabrication of Silicon Solar Cell with> 18% Efficiency Using Spin-on-Film Processing for Phosphorus Diffusion and Sio2/Graded Index Tio2 Anti-Reflective Coating. *Applied Surface Science* **2015,** *354* 20-24.
(101) Lu, Y.-T.; Barron, A. R. Anti-Reflection Layers Fabricated by a One-Step Copper-Assisted Chemical Etching with Inverted Pyramidal Structures Intermediate between Texturing and Nanopore-Type Black Silicon. *Journal of Materials Chemistry A* **2014,** *2* (30), 12043-12052.
(102) Hattori, H. Anti-Reflection Surface with Particle Coating Deposited by Electrostatic Attraction. *Advanced Materials* **2001,** *13* (1), 51-54.
(103) Yancey, S.; Zhong, W.; Heflin, J. R.; Ritter, A. L. The Influence of Void Space on Antireflection Coatings of Silica Nanoparticle Self-Assembled Films. *Journal of applied physics* **2006,** *99* (3), 034313.
(104) Cebeci, F. Ç.; Wu, Z.; Zhai, L.; Cohen, R. E.; Rubner, M. F. Nanoporosity-Driven Superhydrophilicity: A Means to Create Multifunctional Antifogging Coatings. *Langmuir* **2006,** *22* (6), 2856-2862.
(105) Bravo, J.; Zhai, L.; Wu, Z.; Cohen, R. E.; Rubner, M. F. Transparent Superhydrophobic Films Based on Silica Nanoparticles. *Langmuir* **2007,** *23* (13), 7293-7298.
(106) Zhang, L.; Li, Y.; Sun, J.; Shen, J. Mechanically Stable Antireflection and Antifogging Coatings Fabricated by the Layer-by-Layer Deposition Process and Postcalcination. *Langmuir* **2008,** *24* (19), 10851-10857.
(107) Zhang, L.; Li, Y.; Sun, J.; Shen, J. Layer-by-Layer Fabrication of Broad-Band Superhydrophobic Antireflection Coatings in near-Infrared Region. *Journal of colloid and interface science* **2008,** *319* (1), 302-308.
(108) Lee, D.; Rubner, M. F.; Cohen, R. E. All-Nanoparticle Thin-Film Coatings. *Nano letters* **2006,** *6* (10), 2305-2312.
(109) Lee, D.; Omolade, D.; Cohen, R. E.; Rubner, M. F. Ph-Dependent Structure and Properties of Tio2/Sio2 Nanoparticle Multilayer Thin Films. *Chemistry of materials* **2007,** *19* (6), 1427-1433.
(110) Lee, D.; Gemici, Z.; Rubner, M. F.; Cohen, R. E. Multilayers of Oppositely Charged Sio2 Nanoparticles: Effect of Surface Charge on Multilayer Assembly. *Langmuir* **2007,** *23* (17), 8833-8837.

(111) Shimomura, H.; Gemici, Z.; Cohen, R. E.; Rubner, M. F. Layer-by-Layer-Assembled High-Performance Broadband Antireflection Coatings. *ACS applied materials & interfaces* **2010,** *2* (3), 813-820.
(112) Gemici, Z.; Shimomura, H.; Cohen, R. E.; Rubner, M. F. Hydrothermal Treatment of Nanoparticle Thin Films for Enhanced Mechanical Durability. *Langmuir* **2008,** *24* (5), 2168-2177.
(113) Hiller, J. A.; Mendelsohn, J. D.; Rubner, M. F. Reversibly Erasable Nanoporous Anti-Reflection Coatings from Polyelectrolyte Multilayers. *Nature materials* **2002,** *1* (1), 59-63.
(114) Fujita, S.; Shiratori, S. Waterproof Anti Reflection Films Fabricated by Layer-by-Layer Adsorption Process. *Japanese journal of applied physics* **2004,** *43* (4S), 2346.
(115) Fujita, S.; Shiratori, S. The Optical Properties of Ultra-Thin Films Fabricated by Layer-by-Layer Adsorption Process Depending on Dipping Time. *Thin Solid Films* **2006,** *499* (1-2), 54-60.
(116) Kar, P. Doping in Conjugated Polymers, *John Wiley & Sons*, **2013**.
(117) Salaneck, W. R.; Friend, R. H.; Brédas, J. L. Electronic Structure of Conjugated Polymers: Consequences of Electron–Lattice Coupling. *Physics Reports* **1999,** *319* (6), 231-251.
(118) Brabec, C. J.; Dyakonov, V.; Parisi, J.; Sariciftci, N. S. Organic Photovoltaics: Concepts and Realization, *Springer Science & Business Media*, **2003**; Vol. 60.
(119) Luque, A.; Hegedus, S. Handbook of Photovoltaic Science and Engineering, *John Wiley & Sons*, **2011**.
(120) Kippelen, B.; Brédas, J.-L. Organic Photovoltaics. *Energy & Environmental Science* **2009,** *2* (3), 251-261.
(121) Su, Y.-W.; Lan, S.-C.; Wei, K.-H. Organic Photovoltaics. *Materials Today* **2012,** *15* (12), 554-562.
(122) Schwenn, P. E.; Gui, K.; Nardes, A. M.; Krueger, K. B.; Lee, K. H.; Mutkins, K.; Rubinstein-Dunlop, H.; Shaw, P. E.; Kopidakis, N.; Burn, P. L. A Small Molecule Non-Fullerene Electron Acceptor for Organic Solar Cells. *Advanced Energy Materials* **2011,** *1* (1), 73-81.
(123) Zhao, F.; Dai, S.; Wu, Y.; Zhang, Q.; Wang, J.; Jiang, L.; Ling, Q.; Wei, Z.; Ma, W.; You, W. Single-Junction Binary-Blend Nonfullerene Polymer Solar Cells with 12.1% Efficiency. *Advanced Materials* **2017,** *29* (18), 1700144.
(124) Marks, R.; Halls, J.; Bradley, D.; Friend, R.; Holmes, A. The Photovoltaic Response in Poly (P-Phenylene Vinylene) Thin-Film Devices. *Journal of Physics: Condensed Matter* **1994,** *6* (7), 1379.
(125) Tang, C. W. Two-Layer Organic Photovoltaic Cell. *Applied Physics Letters* **1986,** *48* (2), 183-185.
(126) Sariciftci, N.; Braun, D.; Zhang, C.; Srdanov, V.; Heeger, A.; Stucky, G.; Wudl, F. Semiconducting Polymer-Buckminsterfullerene Heterojunctions: Diodes, Photodiodes, and Photovoltaic Cells. *Applied physics letters* **1993,** *62* (6), 585-587.
(127) Kraabel, B.; Lee, C.; McBranch, D.; Moses, D.; Sariciftci, N.; Heeger, A. Ultrafast Photoinduced Electron Transfer in Conducting Polymer—Buckminsterfullerene Composites. *Chemical physics letters* **1993,** *213* (3-4), 389-394.
(128) Forrest, S. R. The Limits to Organic Photovoltaic Cell Efficiency. *MRS bulletin* **2005,** *30* (1), 28-32.
(129) Coakley, K. M.; McGehee, M. D. Conjugated Polymer Photovoltaic Cells. *Chemistry of materials* **2004,** *16* (23), 4533-4542.
(130) Yu, G.; Gao, J.; Hummelen, J. C.; Wudl, F.; Heeger, A. J. Polymer Photovoltaic Cells: Enhanced Efficiencies Via a Network of Internal Donor-Acceptor Heterojunctions. *Science* **1995,** *270* (5243), 1789-1791.

(131) Padinger, F.; Rittberger, R. S.; Sariciftci, N. S. Effects of Postproduction Treatment on Plastic Solar Cells. *Advanced Functional Materials* **2003,** *13* (1), 85-88.
(132) Christiana Honsberg, S. B. https://www.pveducation.org/.
(133) The Sun and Its Radiation. http://energyprofessionalsymposium.com/?p=21472.
(134) He, Z.; Xiao, B.; Liu, F.; Wu, H.; Yang, Y.; Xiao, S.; Wang, C.; Russell, T. P.; Cao, Y. Single-Junction Polymer Solar Cells with High Efficiency and Photovoltage. *Nature Photonics* **2015,** *9* (3), 174.
(135) Brédas, J.-L.; Norton, J. E.; Cornil, J.; Coropceanu, V. Molecular Understanding of Organic Solar Cells: The Challenges. *Accounts of chemical research* **2009,** *42* (11), 1691-1699.
(136) Ngo, T. T.; Nguyen, D. N.; Nguyen, V. T. Glass Transition of Pcbm, P3ht and Their Blends in Quenched State. *Advances in Natural Sciences: Nanoscience and Nanotechnology* **2012,** *3* (4), 045001.
(137) Marsh, R. A.; Hodgkiss, J. M.; Albert-Seifried, S.; Friend, R. H. Effect of Annealing on P3ht: Pcbm Charge Transfer and Nanoscale Morphology Probed by Ultrafast Spectroscopy. *Nano letters* **2010,** *10* (3), 923-930.
(138) Ng, A.; Liu, X.; To, C. H.; Djurišić, A. B.; Zapien, J. A.; Chan, W. K. Annealing of P3ht: Pcbm Blend Film the Effect on Its Optical Properties. *ACS applied materials & interfaces* **2013,** *5* (10), 4247-4259.
(139) Clarke, T. M.; Durrant, J. R. Charge Photogeneration in Organic Solar Cells. *Chemical reviews* **2010,** *110* (11), 6736-6767.
(140) Giulianini, M.; Motta, N. Polymer Self-Assembly on Carbon Nanotubes. In *Self-Assembly of Nanostructures*; Springer: 2012; pp 1-72.
(141) Shao, Y.; Yuan, Y.; Huang, J. Correlation of Energy Disorder and Open-Circuit Voltage in Hybrid Perovskite Solar Cells. *Nature Energy* **2016,** *1* (1), 15001.
(142) Bartesaghi, D.; del Carmen Pérez, I.; Kniepert, J.; Roland, S.; Turbiez, M.; Neher, D.; Koster, L. J. A. Competition between Recombination and Extraction of Free Charges Determines the Fill Factor of Organic Solar Cells. *Nature communications* **2015,** *6* 7083.
(143) Kline, R. J.; McGehee, M. D.; Kadnikova, E. N.; Liu, J.; Fréchet, J. M.; Toney, M. F. Dependence of Regioregular Poly (3-Hexylthiophene) Film Morphology and Field-Effect Mobility on Molecular Weight. *Macromolecules* **2005,** *38* (8), 3312-3319.
(144) Mauer, R.; Kastler, M.; Laquai, F. The Impact of Polymer Regioregularity on Charge Transport and Efficiency of P3ht: Pcbm Photovoltaic Devices. *Advanced Functional Materials* **2010,** *20* (13), 2085-2092.
(145) Mandoc, M.; Koster, L.; Blom, P. Optimum Charge Carrier Mobility in Organic Solar Cells. *Applied physics letters* **2007,** *90* (13), 133504.
(146) Mandoc, M. M.; Veurman, W.; Koster, L. J. A.; de Boer, B.; Blom, P. W. Origin of the Reduced Fill Factor and Photocurrent in Mdmo-Ppv: Pcnepv All-Polymer Solar Cells. *Advanced Functional Materials* **2007,** *17* (13), 2167-2173.
(147) Würfel, P.; Würfel, U. Physics of Solar Cells: From Basic Principles to Advanced Concepts, *John Wiley & Sons,* **2009**.
(148) Gupta, D.; Bag, M.; Narayan, K. Correlating Reduced Fill Factor in Polymer Solar Cells to Contact Effects. *Applied Physics Letters* **2008,** *92* (9), 70.
(149) Proctor, C. M.; Nguyen, T.-Q. Effect of Leakage Current and Shunt Resistance on the Light Intensity Dependence of Organic Solar Cells. *Applied Physics Letters* **2015,** *106* (8), 23_1.

(150) Wu, B.; Wu, X.; Guan, C.; Tai, K. F.; Yeow, E. K. L.; Fan, H. J.; Mathews, N.; Sum, T. C. Uncovering Loss Mechanisms in Silver Nanoparticle-Blended Plasmonic Organic Solar Cells. *Nature communications* **2013,** *4* 2004.
(151) Lu, L.; Zheng, T.; Wu, Q.; Schneider, A. M.; Zhao, D.; Yu, L. Recent Advances in Bulk Heterojunction Polymer Solar Cells. *Chemical reviews* **2015,** *115* (23), 12666-12731.
(152) Li, G.; Shrotriya, V.; Huang, J.; Yao, Y.; Moriarty, T.; Emery, K.; Yang, Y. High-Efficiency Solution Processable Polymer Photovoltaic Cells by Self-Organization of Polymer Blends. *Nature materials* **2005,** *4* (11), 864-868.
(153) Li, G.; Zhu, R.; Yang, Y. Polymer Solar Cells. *Nature photonics* **2012,** *6* (3), 153.
(154) Servaites, J. D.; Yeganeh, S.; Marks, T. J.; Ratner, M. A. Efficiency Enhancement in Organic Photovoltaic Cells: Consequences of Optimizing Series Resistance. *Advanced Functional Materials* **2010,** *20* (1), 97-104.
(155) Li, P.; Jiu, T.; Tang, G.; Wang, G.; Li, J.; Li, X.; Fang, J. Solvents Induced Zno Nanoparticles Aggregation Associated with Their Interfacial Effect on Organic Solar Cells. *ACS applied materials & interfaces* **2014,** *6* (20), 18172-18179.
(156) Li, Y. Three Dimensional Solar Cells Based on Optical Confinement Geometries, *Springer Science & Business Media,* **2012**.
(157) Xue, M.; Li, L.; Tremolet de Villers, B. J.; Shen, H.; Zhu, J.; Yu, Z.; Stieg, A. Z.; Pei, Q.; Schwartz, B. J.; Wang, K. L. Charge-Carrier Dynamics in Hybrid Plasmonic Organic Solar Cells with Ag Nanoparticles. *Applied Physics Letters* **2011,** *98* (25), 119.
(158) Topp, K.; Borchert, H.; Johnen, F.; Tunc, A. V.; Knipper, M.; Von Hauff, E.; Parisi, J.; Al-Shamery, K. Impact of the Incorporation of Au Nanoparticles into Polymer/Fullerene Solar Cells. *The Journal of Physical Chemistry A* **2009,** *114* (11), 3981-3989.
(159) Breitenstein, O.; Rakotoniaina, J.; Al Rifai, M. H.; Werner, M.; Applications. Shunt Types in Crystalline Silicon Solar Cells. *Progress in Photovoltaics: Research* **2004,** *12* (7), 529-538.
(160) Mateker, W. R.; McGehee, M. D. Progress in Understanding Degradation Mechanisms and Improving Stability in Organic Photovoltaics. *Advanced Materials* **2017,** *29* (10), 1603940.
(161) Sai, N.; Leung, K.; Zádor, J.; Henkelman, G. First Principles Study of Photo-Oxidation Degradation Mechanisms in P3ht for Organic Solar Cells. *Physical Chemistry Chemical Physics* **2014,** *16* (17), 8092-8099.
(162) Yin, J.; Zhou, W.; Zhang, L.; Xie, Y.; Yu, Z.; Shao, J.; Ma, W.; Zeng, J.; Chen, Y. Improved Glass Transition Temperature Towards Thermal Stability Via Thiols Solvent Additive Versus Dio in Polymer Solar Cells. *Macromolecular rapid communications* **2017,** *38* (20), 1700428.
(163) Wang, T.; Pearson, A. J.; Dunbar, A. D.; Staniec, P. A.; Watters, D. C.; Yi, H.; Ryan, A. J.; Jones, R. A.; Iraqi, A.; Lidzey, D. G. Correlating Structure with Function in Thermally Annealed Pcdtbt: Pc70bm Photovoltaic Blends. *Advanced Functional Materials* **2012,** *22* (7), 1399-1408.
(164) Liu, Q.; Toudert, J.; Liu, F.; Mantilla-Perez, P.; Bajo, M. M.; Russell, T. P.; Martorell, J. Circumventing Uv Light Induced Nanomorphology Disorder to Achieve Long Lifetime Ptb7-Th: Pcbm Based Solar Cells. *Advanced Energy Materials* **2017,** *7* (21), 1701201.
(165) Peters, C. H.; Sachs-Quintana, I.; Mateker, W. R.; Heumueller, T.; Rivnay, J.; Noriega, R.; Beiley, Z. M.; Hoke, E. T.; Salleo, A.; McGehee, M. D. The Mechanism of Burn-in Loss in a High Efficiency Polymer Solar Cell. *Advanced Materials* **2012,** *24* (5), 663-668.
(166) Atwater, H. A.; Polman, A. Plasmonics for Improved Photovoltaic Devices. *Nature Materials* **2010,** *9* (3), 205.
(167) Stratakis, E.; Kymakis, E. Nanoparticle-Based Plasmonic Organic Photovoltaic Devices. *Materials Today* **2013,** *16* (4), 133-146.

(168) García, M. A. Surface Plasmons in Metallic Nanoparticles: Fundamentals and Applications. *Journal of Physics D: Applied Physics* **2011,** *44* (28), 283001.
(169) West, P. R.; Ishii, S.; Naik, G. V.; Emani, N. K.; Shalaev, V. M.; Boltasseva, A. Searching for Better Plasmonic Materials. *Laser & Photonics Reviews* **2010,** *4* (6), 795-808.
(170) Kelly, K. L.; Coronado, E.; Zhao, L. L.; Schatz, G. C. The Optical Properties of Metal Nanoparticles: The Influence of Size, Shape, and Dielectric Environment. *J. Phys. Chem. B* **2003**.
(171) Lindquist, N. C.; Nagpal, P.; McPeak, K. M.; Norris, D. J.; Oh, S.-H. Engineering Metallic Nanostructures for Plasmonics and Nanophotonics. *Reports on Progress in Physics* **2012,** *75* (3), 036501.
(172) Aherne, D.; Ledwith, D. M.; Gara, M.; Kelly, J. M. Optical Properties and Growth Aspects of Silver Nanoprisms Produced by a Highly Reproducible and Rapid Synthesis at Room Temperature. *Advanced Functional Materials* **2008,** *18* (14), 2005-2016.
(173) Haes, A. J.; Haynes, C. L.; McFarland, A. D.; Schatz, G. C.; Van Duyne, R. P.; Zou, S. Plasmonic Materials for Surface-Enhanced Sensing and Spectroscopy. *MRS bulletin* **2005,** *30* (5), 368-375.
(174) Sarid, D.; Challener, W. A. Modern Introduction to Surface Plasmons: Theory, Mathematica Modeling, and Applications, *Cambridge University Press*, **2010**.
(175) Pastoriza-Santos, I.; Liz-Marzán, L. M. Colloidal Silver Nanoplates. State of the Art and Future Challenges. *Journal of Materials Chemistry* **2008,** *18* (15), 1724-1737.
(176) Millstone, J. E.; Hurst, S. J.; Métraux, G. S.; Cutler, J. I.; Mirkin, C. A. Colloidal Gold and Silver Triangular Nanoprisms. *Small* **2009,** *5* (6), 646-664.
(177) Khan, A. U.; Zhao, S.; Liu, G. Key Parameter Controlling the Sensitivity of Plasmonic Metal Nanoparticles: Aspect Ratio. *The Journal of Physical Chemistry C* **2016,** *120* (34), 19353-19364.

Chapter 3

Experimental Methods and Materials

3.1 ANTI-REFLECTION COATINGS

3.1.1 Materials. Fisherbrand™ Premium Plain Glass Microscope Slides (75 mm x 25 mm) were purchased from Fisher Scientific. Hydrochloric acid (HCl; ACS Reagent; 12.1 M), sulfuric acid (H_2SO_4; ACS Reagent), acetic acid (CH_3COOH; Certified ACS), ammonium hydroxide (NH_4OH; Certified ACS Plus) methanol (MeOH; Certified ACS), N,N-dimethylformamide (DMF; Certified ACS), sodium hydroxide (NaOH; Pellets/Certified ACS), and laboratory cleaning tissues (Kimwipes Delicate Task Wipers; Kimberly-Clark Professional Kimtech Science™; 1-Ply) were purchased from Fisher Scientific. Hydrogen peroxide (H_2O_2; 30 wt%), 95% (3-mercaptopropyl)trimethoxysilane (MPTS) solution, and zinc chloride (ZnCl; powder; Purity >= 98%) were purchased from Sigma-Aldrich.

Colloidal SiO_2 nanoparticles were used as the primary building block for all ionic self-assembled multilayer (ISAM) ARCs in this dissertation. The SiO_2 NP solution was purchased from Nissan Chemical (SNOWTEX ST-20L). The SiO_2 NPs are amorphous nanospheres with an average diameter of 45 nm.[1] The SiO_2 NP solution has a 20 wt% (3.76 M) concentration in solution with a opalescent, milky color. The hydroxyl functional groups (-OH) on the SiO_2 NPs contributes a negative surface charge and facilitates their dispersion in aqueous medium. The SiO_2 NPs pH is important for aggregation resistance, and the stable pH range is 9.5 to 11.0 (as stated by the manufacturer), however, we found the optimum pH for high-quality ISAM ARC fabrication to be 9.0.[1-2] The glass transition temperature (T_g) and melting temperature (T_m) of the SiO_2 NPs are approximately 800 ºC and 1700 ºC, respectively.[1]

The following two polyelectrolytes were used together for the work done in **Chapter 4**. Poly(sodium-p-styrenesulfonate) (PSS) powder was purchased from Fisher Scientific ($M_w \approx$ 70,000; ACROS Organics™; Stock # AC222271000). The sulfonic acid functional groups on the PSS polymer chains provide a negative charge surface (**Figure 3.1**). The PSS solution pH was always maintained at 7.0. 4-Diazodiphenylamine/formaldehyde condensate hydrogen sulfate (diazo-resin; DAR; M_w = 2,800) powder was graciously donated by Secant Chemicals (**Figure 3.1**). The diazonium groups ($R\text{-}N_2^+$) on DAR provide a positive surface charge, but are also very light sensitive and decompose with UV exposure. Due to DAR's photosensitivity, the handling of the material was always done in the dark, until it was fully incorporated into ISAM films. For the work outlined in this dissertation, DAR was never made into an individual solution and was only used for the self-assembled encapsulation of SiO_2 NPs in solution.

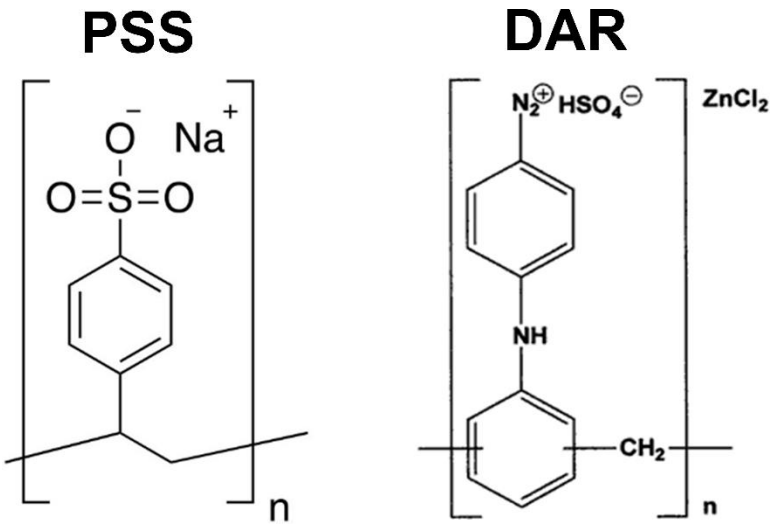

Figure 3.1. Chemical structure of PSS and DAR. Reprinted from Polysciences Inc. and Secant Chemicals.

The following two polyelectrolytes were used for work done in **Chapter 5**. Poly(allylamine hydrochloride) (PAH) powder was purchased from Sigma-Aldrich ($M_w \approx$ 17,500; Stock # 283215) and Alfa Aesar ($M_w \approx$ 120,000 to 200,00; Stock # 43092-09). The amine functional group ($R\text{-}NH_2$)

contributes the positive charge to the PAH polymer chains and is responsible for the repulsion of individual chains in the aqueous solution (**Figure 3.2**). The pH of the PAH solution was typically adjusted to 7.0, unless otherwise noted. The pK_a of PAH is reported to be between 8.0 to 9.0 in solution, without the addition of salt.[3] Poly(acrylic acid) (PAA) powder was purchased from Sigma-Aldrich (M_v ~450,000; Stock # 181285). PAA's negative charge is due to the carboxylic acid group (R-COOH) (**Figure 3.2**). The PAA pK_a is reported to be located in range of 4.5 – 6.5 while in solution and without the addition of salt.[3-4] The PAA solution pH was the primary variable for the methods in **Chapter 5**. For PAH and PAA, a vacuum filtration assembly with 3.0 μm filter was used to remove large aggregates from the solution. This filtration method vastly improved film homogeneity and clarity. The glass transition temperatures (T_g) for pure PAH and PAA are reported to be 223 ºC and 128 ºC, respectively.[5]

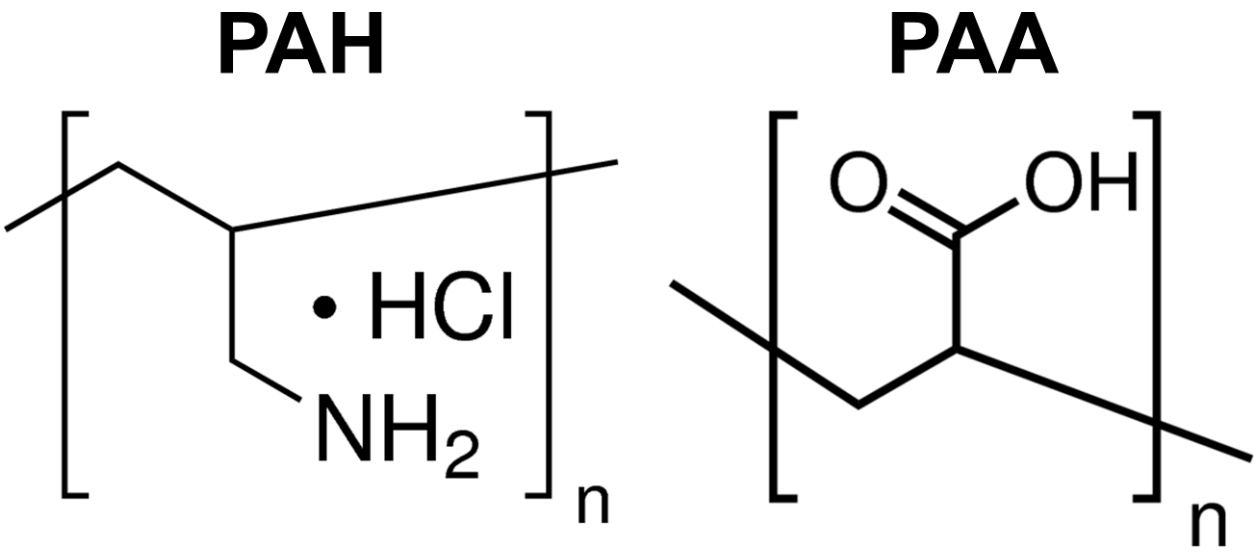

Figure 3.2. Chemical structure of PAH and PAA. Reprinted from Sigma-Aldrich.

The polyelectrolyte powders were added at a 10 mM concentration to ultrapure de-ionized water (18 MΩ cm resistivity) (DI water) and stirred overnight. The pH of polyelectrolyte solutions was adjusted with 1.0 M HCl and 1.0 M NaOH solutions.

3.1.2 Substrate Preparation. For the work done in **Chapter 4**, silanes were grafted to glass substrates, and then functionalized with sulfonate groups (more details in the chapter). The silane grafting method was similar to previous procedures with slight modifications.[6]

The experimental methods in **Chapter 5** followed a standard RCA cleaning method[7] with various modifications. First, glass microscope slide substrates were vigorously cleaned with acetone and laboratory cleaning tissues, then thoroughly dried with N_2 gas. The substrates were placed in a glass staining jar, immersed in a RCA base solution ($H_2O/H_2O_2/NH_4OH$, 72%/14%/14%, v/v/v; i.e. 100 mL H_2O/20 mL H_2O_2/20 mL NH_4OH), and heated to 75 - 85 ^oC for 30 min. The substrates were then copiously rinsed with DI water while remaining in the glass staining jar. Afterwards, the substrates were immersed in a RCA acid solution (H_2O/H_2O_2/HCl, 75% /12.5% /12.5%, v/v/v; i.e. 120 mL H_2O/20 mL H_2O_2/20 mL HCl) for 30 min. The substrates were again thoroughly rinsed with DI water and placed into a vacuum oven at ~100 ^oC for ~2-6 h. The RCA cleaned substrates were mostly free of organic contaminants, had an abundance of negative hydroxyl groups (-OH) on their surface, and were therefore suitable for ISAM film growth.

3.1.3 ISAM Film Growth. ISAM films were fabricated by the operation of a programmable automated immersion machine (nanoStrata Inc.). The immersion machine features a pneumatic platform that has the capacity for eight different solutions (**Figure 3.3**). The immersion machine is programmed using software (StratoSmart), which includes control over the number of bilayers, dipping times, solution refill step (for rinsing DI water solutions), spinning of substrates, drying, and more. The machine's substrate holder can secure up to four substrates simultaneously, which is useful for the processing of films with identical conditions and for maintaining uniform solution

current flow. The substrate holder can be programmed to spin for a range of speeds (600 – 3,000 rpm) while immersed in a solution.

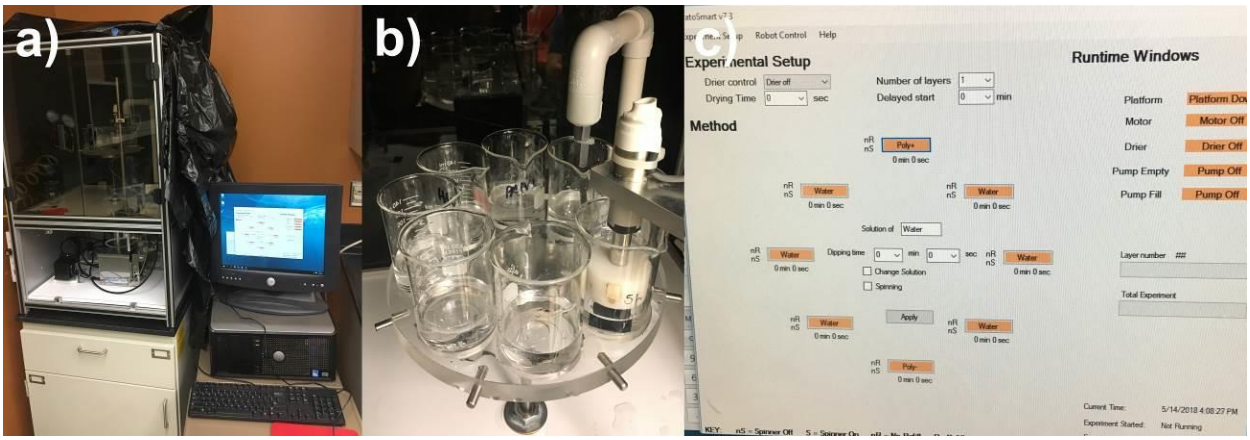

Figure 3.3. (**a**) Immersion machine setup, (**b**) pneumatic solution platform, (**c**) and the StratoSmart program.

ISAM film growth procedures either involved a standard bilayer design (two repeating individual layers) or a quadlayer design (four repeating layers). For the bilayer design, the substrates were first immersed into the polycation solution. Following the polycation solution, the substrates were immersed and spun in three aqueous rinsing solutions for 45 seconds each, which were refilled with fresh DI water after each bilayer. Next, the substrates were immersed into the polyanion solution, and then rinsed again by three rinsing solutions. The polycation and polyanion immersion times could vary from three minutes to five hours based on the solution, although five-minute immersion times were used for typical polyelectrolyte solutions. For the quadlayer design, the procedure consisted of: **(1)** polycation solution 1 **(2)** 135 second rinse (spin) **(3)** polyanion solution 1 **(4)** 135 second rinse (spin) **(5)** polycation solution 2 **(6)** 135 second rinse (spin) **(7)** polyanion solution 2 **(8)** 135 second rinse (spin). Following ISAM film growth, the films were dried with a stream of air, and stored in a microscope slide holder. Specific immersion schedules are included in **Chapters 4** – **7**.

3.1.4 Covalent Crosslinking of ISAM Films. The crosslinking of ISAM films was accomplished through UV-irradiation (**Chapter 4**) and thermally (**Chapter 5**). For crosslinking by UV-irradiation, films were placed into a Kinsten KVB-30 exposure unit, which had six 20 W UV fluorescent bulbs with peak wavelength $\lambda \approx 350 - 400$ nm. Prior to UV-irradiation crosslinking, photosensitive films were kept in the dark. A UV-irradiation time of 15 min was effective for crosslinking of films with DAR. A Thermo Scientific Lindberg/Blue M™ Vacuum Oven was used for the thermal crosslinking of ISAM films. The films were first placed into a glass staining jar and then into the oven chamber. The oven chamber was pumped down to ~20 in. Hg vacuum using the laboratory house vacuum, and then heated to a desired temperature. Once the films were thermally crosslinked for a desired amount of time, the oven was cooled, and then vented using N_2 gas.

3.1.5 Characterization Instrumentation. A Zetasizer nanoZS (Malvern Instruments) operating at a fixed angle of 173° and 633 nm wavelength was utilized for dynamic light scattering (DLS) measurements and ζ-potential. For all ζ-potential and DLS measurements, at least three measurements were recorded per sample.

Optical spectroscopy was performed using UV-vis-IR and FTIR spectrometers. The optical transmission (T) and reflection (R) spectra were recorded by Perkin Elmer Lambda 950 UV/VIS and Filmetrics F10-VC-EXR spectrometers with wavelength ranges of $\lambda \approx 300$ to 1100 nm and $\lambda \approx 380$ nm to 1700 nm, respectively. Fourier transform infrared (FTIR) spectroscopy measurements were acquired using a Bruker IFS 66v/S, type I18174. The unit collected spectra in reflectance mode using OPUS for 100 scans per spectrum at a scan speed of 20 kHz with a MIR-Source and a KBr beam splitter. The FTIR samples were pressurized at ~24 mbar.

A J.A. Woollam VB-400 ellipsometer with a HS-190 monochromatic system was used to measure thickness values, especially those less than 20 nm. All ellipsometry measurements were recorded from ISAM films deposited onto silicon substrates to increase the signal-to-noise ratio. The ellipsometry measurements were recorded in a range of λ = 400 to 1000 nm (with 5 nm increments), angles 55 to 75 degrees (by 10 degree increments), with 50 revolutions per measurement, and dynamic averaging. Initially, a bare silicon substrate was modeled and found to have a native oxide layer of 1.81 nm. A model was then built which involved three sections, a Cauchy layer, the silicon oxide layer, and the silicon substrate. Since the Cauchy layer is assumed as a transparent material, a zero extinction coefficient was used for the entire measured wavelength spectrum. The Cauchy layer dispersion model for the film was represented by **Equation 3.1**:

$$n(\lambda) = A + \frac{B}{\lambda^2} + \frac{C}{\lambda^4} \quad (\mathbf{3.1})$$

where A, B, and C are fit parameters, determined by the software. For work done in **Chapter 5**, several relatively thick films of ten to twenty PAH/PAA bilayers in the pH range of 4-6 were measured and analyzed by the modeling software. Thicker films were used to improve the accuracy of the model, due to the higher signal-to-noise ratio, when compared to thinner films. The model determined optical constants of A = 1.5373 and B = 0.0053271 while C = 0 was kept constant. These optical constants were applied to the experimental polarization data for the rest of the films to determine the thickness. Mean squared error (MSE) values were consistently below 5, which signified that the data fit well to the model. All of the reported quantitative values involved averaging three to five measurements per sample.

The thickness and RMS roughness measurements were recorded using a Veeco DekTak 150 Stylus Profilometer with a 2.5 μm tip radius stylus. At least four measurements were averaged for each sample. For step thickness measurements, the samples were first scored down to the substrate

using plastic tweezers, and the thickness was recorded as the height difference from the sample to the substrate.

A field-emission scanning electron microscope (SEM; LEO (Zeiss) 1550) with an accelerating voltage of 5 kV was used to image the film surfaces. Samples were cut into small squares (~ 1 x 1 cm) and attached to a SEM sample stub using carbon tape. The samples were sputter-coated (Leica EM ACE600) with ~2.5 nm of high resolution iridium before use. Atomic force microscopy (AFM; Dimension Icon) was also used to image the surface of the films at scan rate of 1 Hz.

The micro-scale scratch test results were obtained with a Hysitron TriboIndenter, using a 1 μm radius conical diamond tip. The instrument's scanning probe microscope (SPM) scanned the scratched section *in-situ,* directly after scratching. The scratch test procedure involved a linear ramp of the normal force from near zero force to a specified peak force, over a lateral distance of 10 to 20 μm. Based on the nature of each specific film set, the peak force was varied from 50 to 300 μN to maximize the resolution of the scratch. SPM was then used to image the scratch *in-situ,* centered on the 10 to 20 μm^2 scratched area of the film. The initiation of the scratch was identified as by a continuous decrease in the SPM height profile over the scratch, in relation the overall film roughness. Qualitative analysis of the SPM image was used to confirm the scratch's initiation location. The normal force applied at the initiation location of the scratch was designated as the critical load value (L_{c1}). The L_{c1} was specific to the TriboIndenter setup parameters (tip geometry, tip size, calibration, etc.).

The macro-scale scratch test was performed by sliding the end of a stainless steel rod over the samples (**Figure 3.4**). The rod had a circular profile of 1.29 cm^2 and a total mass of 451 grams. The rod was fixed in the x-y plane and was free to move in the z-direction, by an open clamp attached to a shelf above. The end of the rod was wrapped tightly with three laboratory cleaning

tissues and attached with tape. New cleaning tissues were installed after each sample for consistency. The samples were secured to a motorized translational stage (MLS203; Thorlabs). Three single passes at approximately 0.4 cm/s were made down the length of the sample to cover the entire area of the film. Four samples were abraded from each sample set, corresponding to the PAA pH and whether the films were crosslinked or uncrosslinked. A haze meter (BYK Gardner) was used to measure the haze of each sample before and after the scratch, at three different spots per sample. The results were averaged for each sample set. The percent difference for each sample set was calculated by dividing the difference of the haze before and after the scratch by the haze before the scratch.

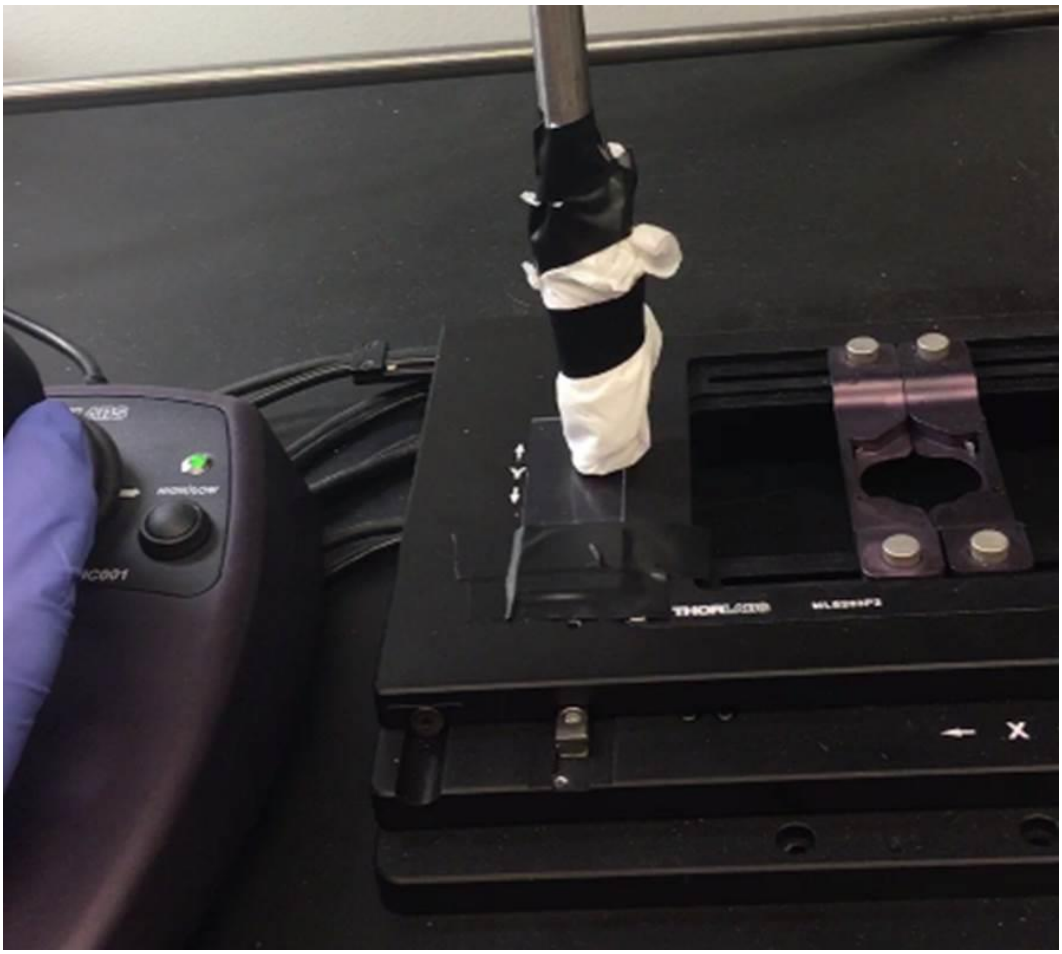

Figure 3.4. Motorized abrasive rod setup for macro-scale scratch testing of films.

3.2 ORGANIC PHOTOVOLTAICS

3.2.1 Materials. Sodium citrate tribasic dihydrate (ACS Reagent; Purity ≥99.0%; Stock # S4641), sodium borohydride ($NaBH_4$; granular; Purity ≥99.99%; Stock # 480886), silver nitrate ($AgNO_3$; Purity ≥99.9999%; Stock # 204390), poly(sodium 4-styrenesulfonate) (PSS; powder; M_w ~1,000,000; Stock# 434574), ascorbic acid (crystalline; Purity ≥99.0%; Stock # A5960), gold(III) chloride trihydrate (Purity ≥99.9%; Stock # 520918), styrene (ReagentPlus®; Purity ≥99%; Stock # S4972); 2-Phenyl-2-propyl benzodithioate (CDB; Purity ≥99%; Stock # 731269), chlorobenzene (CB; anhydrous; Purity ≥99.8%; Stock # 284513), hydrogen peroxide (H_2O_2; 30 wt%), and PAH (M_w ≈ 17,500; Stock # 283215) were all purchased from Sigma-Aldrich. Fisherbrand™ Premium Plain Glass Microscope Slides (75 mm x 25 mm), hydrochloric acid (HCl; Certified ACS Plus; 36.5 to 38.0 wt%), sulfuric acid (H_2SO_4; Technical Grade; Purity = 93 to 98%), N,N-dimethylformamide (DMF; Spectranalyzed; Purity ≥99.8%), sodium hydroxide (NaOH; Pellets/Certified ACS), isopropyl alcohol (IPA; HPLC Grade; Purity ≥99.5%), toluene (Certified ACS; Purity ≥99.5%), and pyridine (Certified ACS; Purity ≥99%) were purchased from Fisher Scientific. Ammonium hydroxide (NH_4OH; ACS Reagent) and methanol (MeOH; HPLC Grade) were purchased from Spectrum Chemical. Ethanol (EtOH; ACS reagent; absolute; 200 proof; Purity ≈100%;) was purchased from Decon Laboratories. Dichloromethane (ACS, Stabilized; Purity ≥99.5%;) was purchased from VWR.

Float glass slides passivated with indium tin oxide (ITO) on one side and an anti-reflection coating (ARC) on the other side were purchased from Delta Technologies Limited (25 × 75 × 0.9 mm; CH-50IN-S109). The ITO's thickness is reported to be 1500 to 2000 Å with a sheet resistance of 8 to 15 ohms per square. ITO is a transparent, conductive coating with a work function of approximately 4.7 eV.[8] The substrate's ARC has a reflectance minimum of ≤0.5% at wavelength

$\lambda \approx 500$ to 550 nm. For all for OPV device processing in **Chapters 6** and **7**, ITO was used as the anode and the base layer.

Aluminum (Al) pellets were purchased from Kurt J. Lesker (1/8" Dia. x 1/8" Length; Purity = 99.999%; Stock # EVMAL50EXEA). Tungsten wire baskets were purchased from RD Mathis Company (1 ⅞ in. x ½ in.; ½ in inner diameter; 4.57 Volts; 40 Amps; 183 Watts; 1800º C Temp; Stock # ME17-3X.025W). Al was evaporated onto devices as the cathode for all OPV work done in **Chapters 6** and **7**. The work function of Al in OPV devices is reported to be 4.3 eV, which is consistent with the work function of FCC (111) Al at 4.26 eV.[9-10]

Poly(3,4-ethylenedioxythiophene)-poly(styrenesulfonate) (PEDOT:PSS) was purchased from Heraeus (CLEVIOS™ P VP AI 4083) with a PEDOT to PSS ratio of 1:6, mean particle size of 75 nm, a resistivity of 750 Ω-cm, and a work function of 5.2 eV.[11] PEDOT:PSS was used as the primary hole-transport layer (HTL) for OPV devices in **Chapters 6** and **7**. PEDOT:PSS is made up of globular dispersion nanoparticles that are comprised of encapsulated PEDOT (hydrophobic) by PSS (hydrophilic) in an aqueous liquid phase (**Figure 3.5**).[11-13] The PEDOT:PSS nanoparticles have a negative charge, since the negatively-charged PSS lines their outside. The PEDOT:PSS dispersion is highly acidic, which is a necessary feature for their work function and conductivity.[14] PEDOT:PSS was refrigerated in the dark to increase the shelf-life and filtered through a 0.45 μm PVDF syringe filter before use.

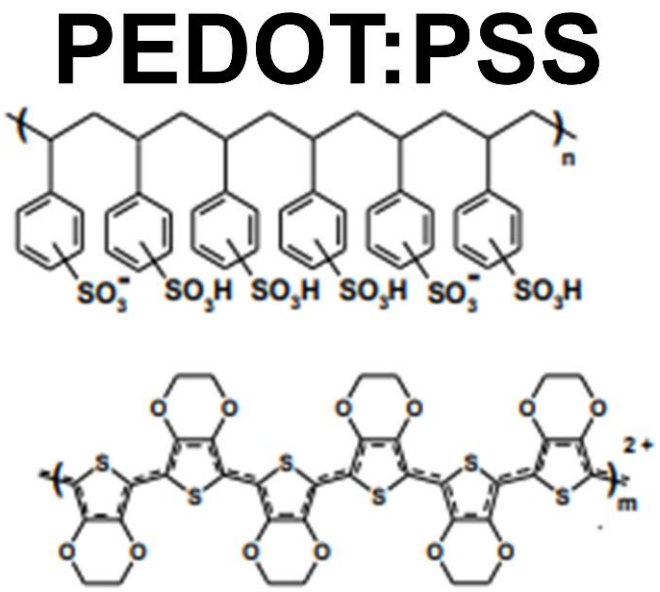

Figure 3.5. PEDOT:PSS chemical structure. Reprinted from Heraeus.

For all OPV device work done in this thesis, the bulk heterojunction active layer was composed of a blend of the electron donor poly(3-hexylthiophene-2,5-diyl) (P3HT) and the electron acceptor [6,6]-phenyl C_{61} butyric acid methyl ester (PCBM).

P3HT was purchased from Rieke Metals (4002-E; M_w ~50,000 – 70,000; Regioregularity = 91-94%) and is composed of a stiff π-conjugated backbone and short alkyl side chains (hexyls) (**Figure 3.6**), which allow for good solubility in organic solvents.[15] In relation to other poly(3-alkylthiophenes) (P3ATs), P3HT's shorter alkyl side chains allow for better π-stacking and interchain coupling.[16] P3HT films have been shown to be composed of ordered crystalline lamellae.[15, 17] Low M_w P3HT conforms to highly crystalline nanorod structures, and high M_w P3HT creates isotropic, nodule structures with relatively lower crystallinity.[15, 17] However, charge mobility has been reported to increase drastically with P3HT M_w, ranging from a 1 x 10^{-7} cm^2/Vs (very low M_w) to 1 x 10^{-2} cm^2/Vs (high M_w).[17] Additionally, higher regioregularity of P3HT and annealing have also been reported to increase charge carrier mobility.[17-18] Using cyclic voltammetry (CV), P3HT is reported to have HOMO and LUMO levels of -5.20 eV and -3.53 eV,

respectively.[16] The HOMO level of P3HT have also been reported as -4.90 eV using ultraviolet photoelectron spectroscopy (UPS), from which the LUMO levels were calculated as -3.00 eV using the optical absorption bandgap (E_g^{opt}).[19] Therefore, P3HT bandgap determined by CV (E_g^{CV}) is reported as ~1.67 eV and the E_g^{opt} is ~1.90 eV, although the discrepancy between the two values has not yet been resolved in the literature.[16] The peak absorption coefficient (α) for P3HT is reported to be ~1.75 x 10^5 cm^{-1} at 2.48 eV (500 nm).[16] The glass transition temperature (T_g) for P3HT has been reported to be 9.3 °C.[20] P3HT's melting temperature (T_m) is reported to increase logarithmically with the molecular weight, ranging from 300 to 545 K (27 to 272 °C).[20-21] At 420 °C, P3HT is shown to thermally degrade.[20]

PCBM was purchased from Nano-C (Nano-C-PCBM-BF). PCBM is a C_{60} fullerene derivative with enhanced solubility, stability and homogeneity in organic solvents (**Figure 3.6**).[22] At high film concentrations and annealing temperatures, PCBM forms large crystalline needle structures with lengths of 10 to 30 μm and heights of 20 to 180 nm.[22] PCBM has a HOMO level of -6.10 to -5.90 eV (depending on the source) and LUMO level of -3.73 eV, and an E_g of 2.17 to 2.37 eV.[9, 16] Peak absorptivity α of PCBM is reported to be 1.95 x 10^5 cm^{-1} at 3.64 eV (340 nm).[16] The T_g, T_m, and thermal degradation temperature for P3HT are reported to be 118.3, 279.5, and 398 °C, respectively.[20]

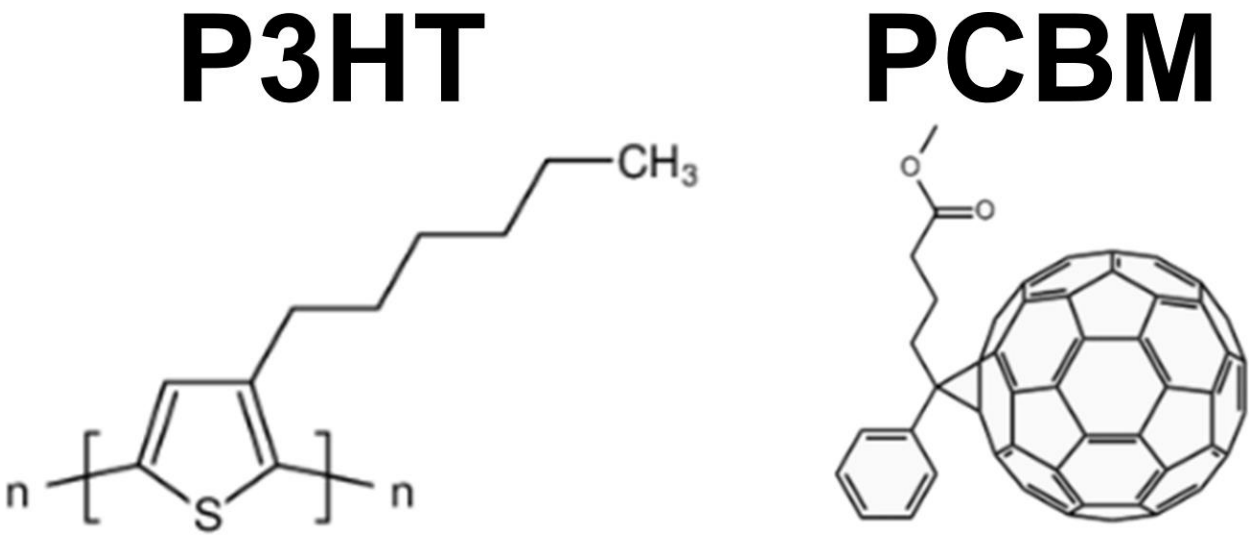

Figure 3.6. Chemical structure of P3HT and PCBM. Reprinted from Rieke Metals and Nano-C.

Detailed procedures on the synthesis of silver nanoplates (AgNPs) and thiol-terminated polystyrene (PS-SH) powder (**Figure 3.7**) are overviewed in **Chapters 6** and **7**. Poly(ethylene glycol) methyl ether thiol (PEG-SH) powder (**Figure 3.7**) was purchased from Sigma-Aldrich (M_n ≈ 6,000; Stock # 729159) and from Creative PEGWorks (M_w ≈ 10,000; Stock # PLS-603).

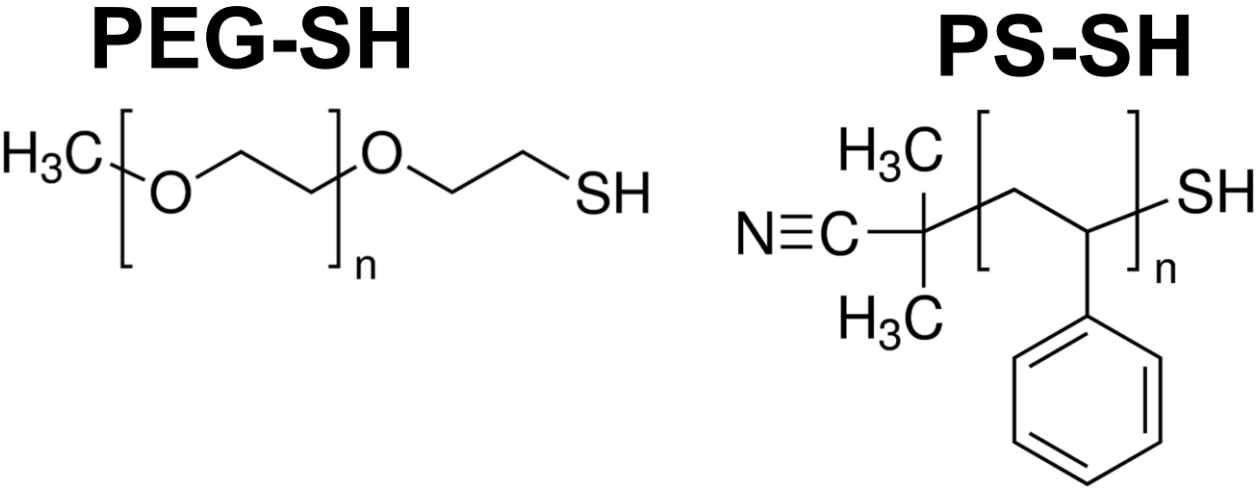

Figure 3.7. Chemical structure of PEG-SH and PS-SH. Image courtesy of Sigma-Aldrich.

3.2.2 Solution Formation. For standard OPV devices, PEDOT:PSS was filtered through a 0.45 μm PVDF syringe filter and vortex-mixed with IPA (PEDOT:PSS/IPA, 3/1, v/v). The addition of

IPA to the solution increased the overall vapor pressure of the solvent, which dramatically improved the uniformity on ITO. Separate solutions of P3HT and PCBM were made with a final concentration of 3 wt.% (30 mg/mL) each in CB and stirred overnight at 70 °C. After cooling down to room temperature, the two solutions were mixed at a volume ratio of P3HT:PCBM = 1:0.8 and then stirred at 70 °C in the dark. Before use of P3HT:PCBM, the solution was cooled down to room temperature, while stirring in the dark.

The formation of ISAM solutions for OPV devices is detailed in **Chapter 6.**

3.2.3 Substrate Preparation. ITO/ARC glass slides were vigorously cleaned with acetone before use. Two electrical tape strips (12.7 mm wide) were applied in the middle of the glass slides along the longitudinal direction to protect the center of the ITO on one side and the entire ARC on the other from etching. The glass slides were then immersed in a mixture of base solution (HCl/H_2O, 50%:50%, v/v) for 1 h to etch the exposed ITO and ARC. The slides were then copiously rinsed with DI water, and the electrical tape was removed to uncover the ITO and ARC (**Figure 3.11,** blue stripe). The slides were further cleaned by sonicating in a mixture of base solution ($H_2O_2/NH_4OH/H_2O$, 9%/14%/77%, v/v/v; i.e. 11 mL of H_2O_2, 18 mL of NH_4OH, and 97 mL of DI water). The ITO slides were then cut into small substrates (25 × 25 mm), cleaned with acetone and IPA, and then dried in a stream of nitrogen gas.

3.2.4 ISAM Film Growth. ISAM film processing on ITO/glass/ARC substrates involved using the substrates after the etching and cleaning procedure above without further modifications. For ISAM film growth with the ISAM immersion machine, the ARC side of the substrates was first covered with electrical tape to avoid deposition on that side. The substrates then were attached to microscope slides (ITO side facing out) with electrical tape.

For all other ISAM film processing on glass, glass microscope slides were RCA cleaned, as detailed in **Section 3.1.2**.

The operation of the immersion machine for ISAM film growth is outlined above in section ***3.1.3.*** The programming of the immersion machine for different ISAM films is described in **Chapter 6.**

3.2.5 Fabrication Instrumentation. A Chemat Scientific KW-4A Spin Coater was used to spin-coat thin-film layers for OPV device processing. After securing the substrate by a vacuum chuck inside the spin-coater, speeds of 250 to 8,000 rpm can be reached for a total of 78 seconds (using both timers). In spin-coating, either static or dynamic dispense can be used. Static dispense involves drop casting the solution onto the center of substrate, and starting the substrate rotation shortly thereafter. Dynamic dispense implies that the substrate is first accelerated and maintained at specific angular velocity, and then the solution is dispensed at the center of the substrate. Although static dispensing may increase surface coverage at lower spin speeds (<700 rpm), the homogeneity is typically compromised, as discovered by our own trials and from previous reports.[23] Therefore, dynamic dispensing was used all spin-coating related work in **Chapters 6** and **7**.

For the work done here, the thickness of a spin-coated film was primarily based on the spin-coating speed, the solution concentration, the vapor pressure (or boiling point) of the solvent, and the surface energy of the substrate (or previous film). After the surface is wetted by the solution, the rotation causes a majority of the solution (≥90%) to be casted off the substrate, and then airflow dries the remaining solution into a film.[23] A heightened spin-coating speed results in a greater quantity of solution to leave the substrate, and therefore a lower thickness of the resultant film. It has been reported that thickness is proportional to spin speed by **Equation 3.2**:

$$t \propto \frac{1}{\sqrt{\omega}} \quad (\mathbf{3.2})$$

where t is thickness and ω is angular velocity.[23] With the formation of each new P3HT:PCBM solution batch, the thickness was first evaluated empirically, before films were incorporated into OPV devices. Along with spin speed, the film thickness is highly dependent on the solution concentration, and therefore care was taken to maintain a P3HT:PCBM solution concentration of 3 wt% for consistency among films. Additionally, the primary variable in **Chapter 7** was the concentration of the AgNP solution, which directly affected the surface density of the spin-coated AgNPs. The vapor pressure of the solvent is also a critical factor in the thickness and morphology of the film. Since a lower vapor pressure solvent also has a higher boiling point, the effective result is less solvent evaporating during the spin-coating rotation process. With more solvent present, more solution will be flung from the substrate, and the film thickness will be relatively lower. However, a slower evaporation time can be beneficial for polymer films to induce increased self-organization of π-π stacking of polymer chains.[23] For spin-coating of nanoparticle solutions, a higher vapor pressure solvent was found to be essential for sufficient film coverage and uniformity, as discussed in **Chapter 7**. For PEDOT:PSS, a binary solvent (H_2O:IPA, 3:1, v/v) was utilized to make use of the higher vapor pressure of IPA, as discussed above. The surface energy of the film was also found to be essential for film wetting, which is directly correlated to thickness and morphology. Higher surface energy promotes greater hydrophilic wettability, whereas lower surface energy decreases hydrophilic wettability.[23-24] The formation of hydroxyl groups (-OH) on the surface increases surface energy, which is critical for spin-coating wettability.[23] Hydroxyl groups can be formed by UV/ozone cleaning, RCA cleaning (**Section 3.1.2.**), and sonication in the base cleaning solution used for the ITO substrates, as discussed above in **Section 3.2.3**.

A copper hot plate heated by two cartridge heaters (¼" diameter; 50 W; Omega Engineering Inc.) was used to anneal thin-films (**Figure 3.8**). The hot plate was powered by a temperature controller (CNi1622-C24; Omega Engineering Inc.), and temperature readings were sent to the temperature controller by self-adhesive thermocouples (SA1XL-K; Omega Engineering Inc.). The temperature controller was controlled by a LabVIEW computer program, and the communication between the temperature controller and computer was established by a USB GPIB controller (GPIB-USB-B; National Instruments Inc.). The LabVIEW program allowed for full programming of the heating ramp rate, peak temperature, and dwell time, which was essential for precise annealing operation. All annealing by the hot plate was done in a plexiglass box filled with argon gas, which maintained a positive pressure compared to the ambient laboratory environment (**Figure 3.8**). All sides of the plexiglass box were blacked-out for the dark annealing of films.

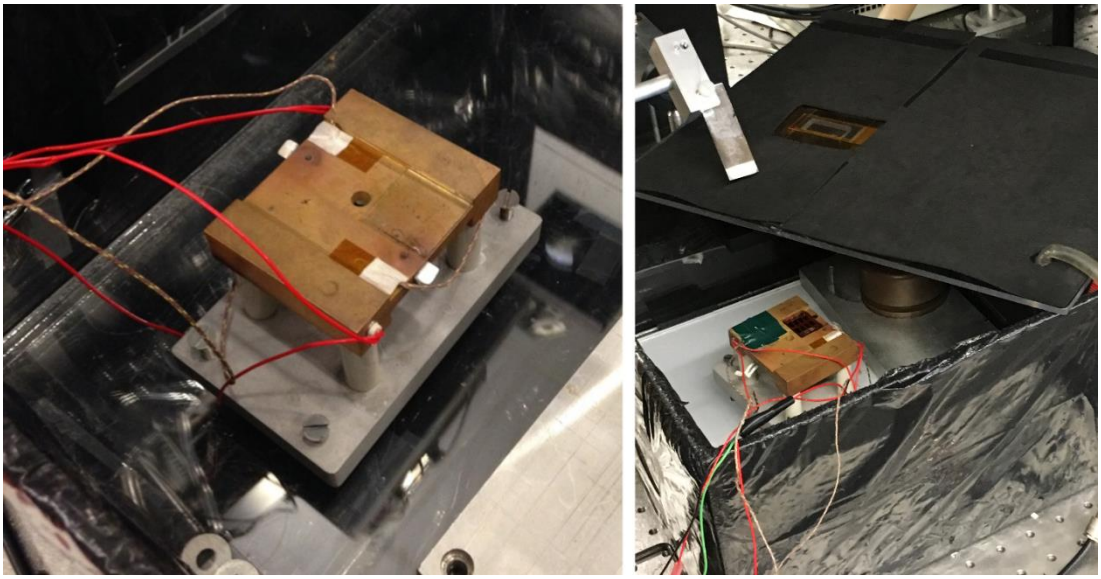

Figure 3.8. Copper hot plate in plexiglass box. For annealing, the plexiglass lid was installed and with a flow of argon gas.

A thermal evaporator (Classic Floor Model LADD Vacuum Evaporator; Ladd Research Industries) was used to evaporate metals onto devices (**Figure 3.9a-f**). The evaporator was

equipped with an aftermarket turbo pump (Alcatel 5400; Flow rate ≈ 400 l/s; Ultimate pressure ≤ 1 x 10^{-9} torr), which was controlled by a turbo molecular pump controller (Alcatel CFF 450). The turbo pump allowed for maximum vacuum levels (minimum pressures) in the magnitude of 10^{-7} torr, as measured by a glass ionization gauge tube (I-075-K; Iridium Filament; 0.75" Diameter Kovar Port; Duniway Stockroom Corp.) connected to vacuum ionization gauge controller (Varian 843). The turbo pump and bell jar chamber of the evaporator was pumped by a dual stage rotary vane vacuum pump (Alcatel 2021; Peak pumping speeding ≈ 14.6 cfm; Ultimate pressure ≈ 1.5 x 10^{-3} torr). The rotary vane vacuum pump was equipped with an oil mist eliminator (Varian OME 25 HP) and a foreline trap (Edwards FL20K) to reduce backstreaming into the turbo pump and chamber.

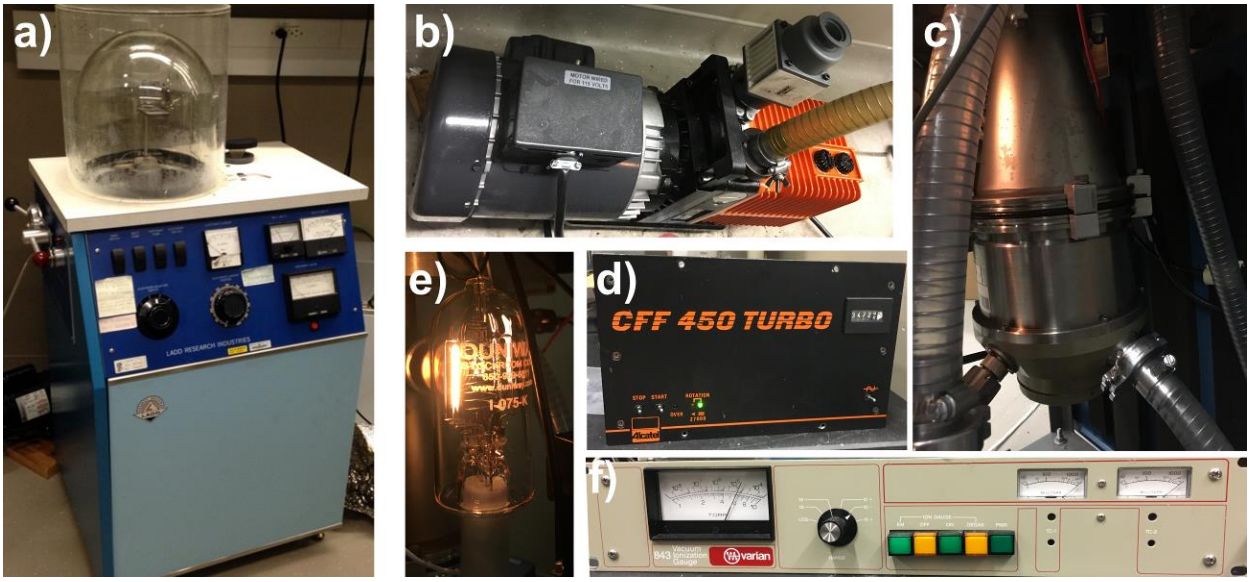

Figure 3.9. Thermal evaporator setup. (**a**) Thermal evaporator, (**b**) rotary vane vacuum pump, (**c**) turbo pump, (**d**) turbo pump controller, (**e**) ionization gauge tube, (**f**) ionization gauge controller.

Inside the thermal evaporator chamber, samples were placed film-side face down on a sample holder. Up to four samples could be placed on the sample holder and each sample location had identical shadow masks (**Figure 3.10a-e**). The shadow masks exposed the device so that eight

separate Al strips were deposited with identical areas. After a tungsten basket was installed into a tungsten basket holder inside the evaporator chamber, Al pellets were placed the basket. Prior to installing the tungsten basket into the basket holder, it was critical to stretch the basket with pliers to avoid shorting of the basket by Al during the evaporation process. If the basket was shorted, very large currents were required to maintain Al deposition, which generated heat from the basket holder's terminals, and this led to device degradations. The power supply within the evaporator supplied current to the tungsten basket by electrode feedthroughs, and the current was controlled by the user.

For standard procedure involving deposition of Al at 100 nm onto the sample, five pellets were placed into basket, and two samples were placed face-down in the holder. Aluminum foil was placed into the bell jar to avoid deposition onto the bell jar glass. The bell jar was then installed, and the chamber was pumped down to ~60 x 10^{-3} torr by the roughing (rotary vane) vacuum pump. The chamber was then opened to the turbo pump and pumped to at least 4 x 10^{-6} torr. A higher vacuum (lower pressure) correlated to a lower temperature for evaporation and a longer mean free path, so it was a crucial parameter for a clean and effective deposition. The Al evaporation temperature for 10^{-8}, 10^{-6}, and 10^{-4} torr is 677, 821, and 1,010 ^{o}C, respectively.[25] A thickness monitor (STM-100/MF; INFICON) was linked to a quartz crystal microbalance (QCM) inside the chamber, and the QCM was installed close to the samples. At the appropriate vacuum, the thickness monitor was turned on, and its shutter button was depressed. Current to the tungsten basket was then ramped up to ~30 amps, where it was stabilized until the deposition started. After initiation of the deposition, the current was manipulated between 30 to 40 amps to achieve the desired rate. The deposition rate was maintained at ~1.0 Å/s for first 10 nm of Al, and then capped at ~2.5 Å/s for the final 90 nm. Upon completion of the deposition, the current and thickness

monitor were turned off, and the chamber was allowed to cool to room temperature (>30 minutes). Cooling to room temperature is critical to avoid adsorption of gases within the chamber's components during venting. Regular cleaning of the chamber was also essential to lessen gas adsorption locations, which led to cleaner depositions and shorter pumping times.

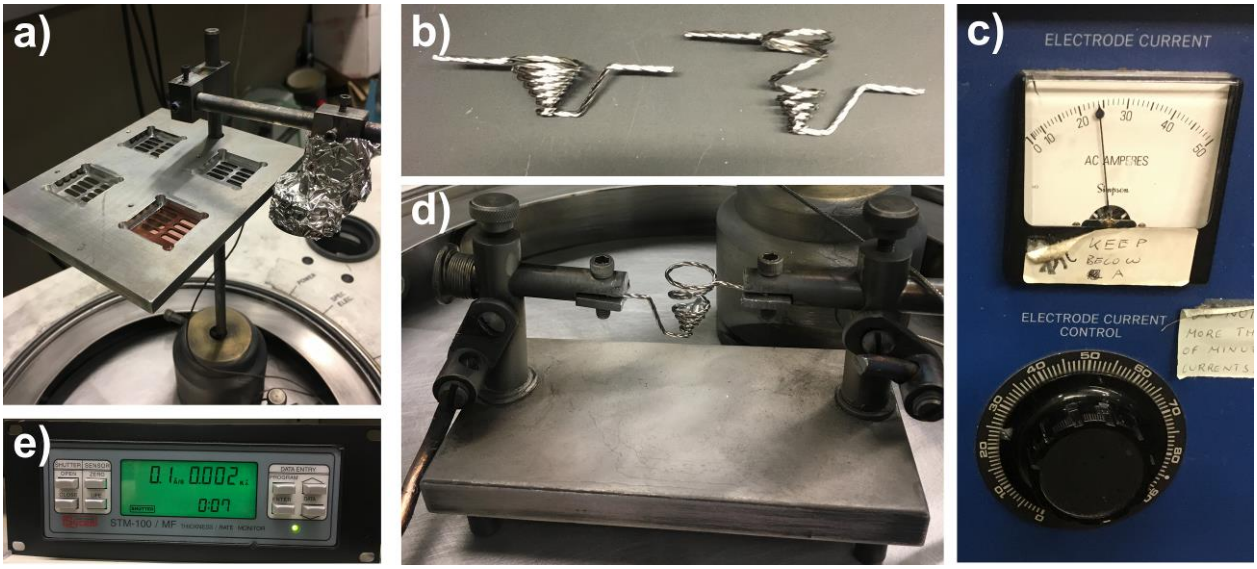

Figure 3.10. Thermal evaporator deposition setup. (**a**) The sample holder with four sample locations and a shadow mask for each sample. In the figure, the item covered with aluminum foil is the quartz crystal microbalance (QCM). (**b**) One tungsten basket from the factory (left) and after stretching with pilers to avoid shorting (right). (**c**) Power supply current knob and current meter. (**d**) Tungsten basket holder with tungsten basket and aluminum pellets. (**e**) QCM thickness monitor.

3.2.6 Fabrication of photovoltaic devices. The PEDOT:PSS solution was spin-coated onto an ITO substrate at 4000 rpm for 60 s to obtain a thickness of ~30 nm (as measured by profilometry). The top fifth (~5 mm) of the film was removed using a wetted laboratory cleaning tissue, in order to expose the ITO electrode. The PEDOT:PSS film was then annealed at 140 °C for 20 min in air to remove the solvent. To obtain an active layer of ~100 nm in thickness, the P3HT:PCBM solution

was cooled down to room temperature and then spin-coated on top of the PEDOT:PSS film at 1500 rpm for 30 s. The top fifth (~5 mm) of the film was again removed with a laboratory cleaning tissue soaked in CS_2 or CB solvent. After annealing, the sample was loaded into a thermal evaporator to deposit ~100 nm of Al at an ultra-high vacuum of 2 x 10^{-6} torr. The sample holder in the thermal evaporator featured an Al shadow mask to create an active area of 0.12 cm^2. After evaporating Al, the samples were annealed at 130 °C for 15 min under argon. Copper tape was attached to the ITO and individual Al electrodes to increase electrical contact. The schematic of the device processing and a pictorial image are represented in **Figure 3.11.**

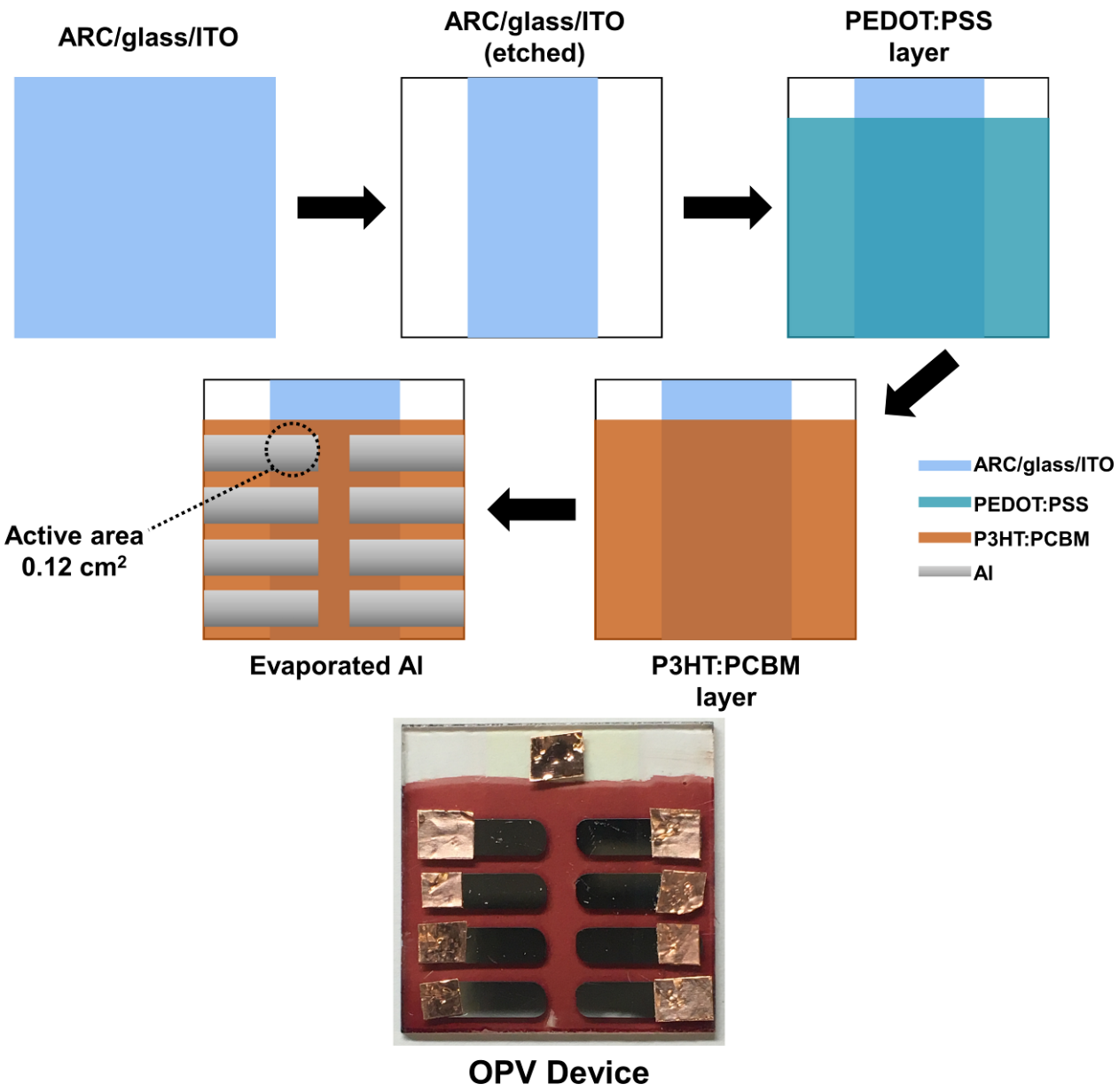

Figure 3.11. Graphical and pictorial representation of OPV devices. Each sample contains eight devices (one for each Al strip) that can be individually tested. The exposed ITO anode and the non-overlapping Al cathode are used as electrode contact in J-V and EQE measurements.

3.2.7 Characterization Instrumentation. The transmittance (T) and reflectance (R) spectra were recorded by a Filmetrics F10-UV-EXR spectrometer. Since optical loss in the P3HT:PCBM film was attributed to both significant absorption and reflectance, modifications were made to the

traditional Beer-Lambert's law. Along with the total light transmitted (T), the light transmitted as it enters the film (T_0) is also considered as

$$T = \frac{I}{I_0} \quad \textbf{(3.3)}$$

$$T_0 = \frac{I_1}{I_0} \quad \textbf{(3.4)}$$

where I is the transmitted light intensity, I_0 is the light intensity before entering the film (and before reflectance), and I_1 is the transmitted light intensity upon entering the film (and after reflectance). Therefore, as the light enters the film, it is split into two components, T_0 and R, that add to 1

$$1 = T_0 + R \quad \textbf{(3.5)}$$

and substituting **Equation 3.4** into **3.5**,

$$1 - R = \frac{I_1}{I_0} \quad \textbf{(3.6)}$$

where R is the total light reflectance. I_1 is then reduced to I according to Beer-Lambert's law as

$$\frac{I}{I_1} = 10^{-A} = e^{-\alpha l} \quad \textbf{(3.7)}$$

where A is the light absorption of the film, α is the absorption (attenuation) coefficient in cm^{-1}, and l is the thickness of the film. By multiplying the left side of **Equation 3.7** by I_0/I_0 and substituting in **Equations 3.3** and **3.6**,

$$\frac{I/I_0}{I_1/I_0} = \frac{T}{(1-R)} \quad \textbf{(3.8)}$$

and finally substituting **Equation 3.7** into **3.8**, the modified Beer-Lambert's law can be used to calculate the absorption (A) spectra:

$$A = -\log\left(\frac{T}{1-R}\right) \quad \textbf{(3.9)}$$

where T and R are the transmittance and reflectance at a given wavelength. The absorption spectrum of P3HT:PCBM was obtained by subtracting the absorption spectrum of

glass/ITO/PEDOT:PSS from that of glass/ITO/PEDOT:PSS/P3HT:PCBM. This is exemplified for a sample in **Figure 3.12**.

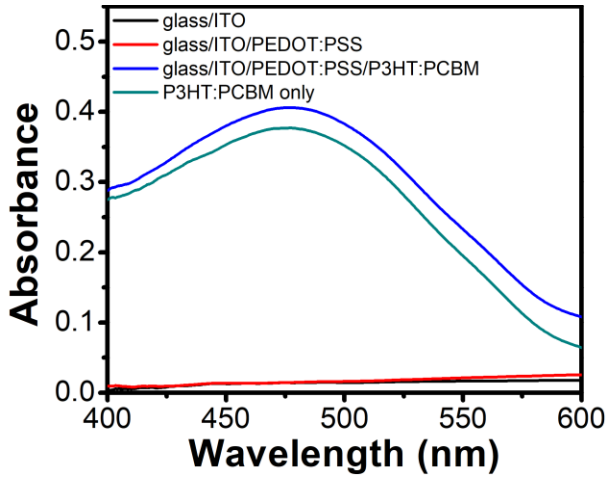

Figure 3.12. Optical absorption of glass/ITO, glass/ITO/PEDOT:PSS, glass/ITO/PEDOT:PSS/P3HT:PCBM, and P3HT:PCBM subtracted spectra.

As shown, the visible wavelength absorption of glass/ITO and PEDOT:PSS were both small in order to limit unnecessary light blocking from P3HT:PCBM. The absorption of these initial layers was not negligible, however, and therefore their subtraction was critical for an accurate representation of the P3HT:PCBM absorption spectrum.

A Veeco DekTak 150 Stylus Profilometer was used to measure the thickness of PEDOT:PSS and P3HT:PCBM films. The right side of **Equation 3.7** was manipulated to determine the the absorption coefficient (α) of P3HT:PCBM as:

$$\alpha = \frac{\ln(10) * A}{l} \qquad \textbf{(3.10)}$$

The absorption coefficient is dependent on wavelength (**Figure 3.13**). With the calculation of the absorption coefficient, the thickness of the P3HT:PCBM films without the profilometer could be calculated by a manipulating **Equation 3.10** to:

$$l = \frac{\ln(10) * A}{\alpha} \qquad \textbf{(3.11)}$$

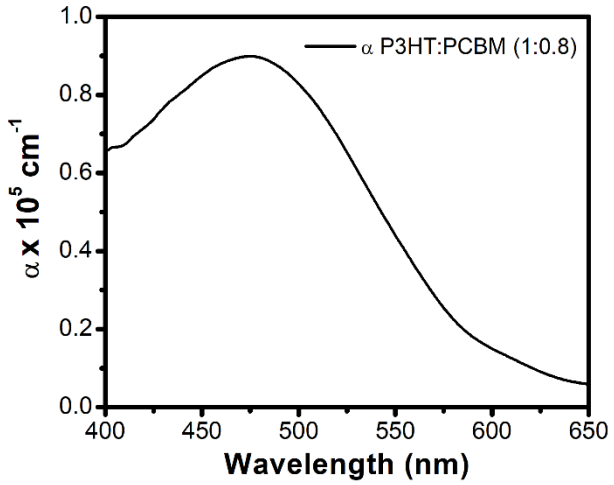

Figure 3.13. Absorption coefficient (α) of P3HT:PCBM (1:0.8) as a function of wavelength.

Photovoltaic devices were illuminated with an air mass 1.5 global standard spectrum (AM1.5G) created by a 300 W Xe lamp (Oriel Instruments). The lamp's beam passed through a AM0 and AM1.5G filter, and then was reflected down with a mirror to a sample in a covered plexiglass box. The lamp's beam intensity was adjusted to 100 mW/cm^2 (1 sun), which corresponded to a calibrated Si photodiode current of 0.118 mA (after placing the lid onto the plexiglass box). The current (I) – voltage (V) characteristics were evaluated on a sourcemeter (Keithley 236). Current (I) was divided by the active area (0.12 cm^2) to calculate the current-density (J) with units of mA/cm^2. All J-V characteristics for OPV devices was measured with the plexiglass box lid installed and with a positive pressure flow of argon.

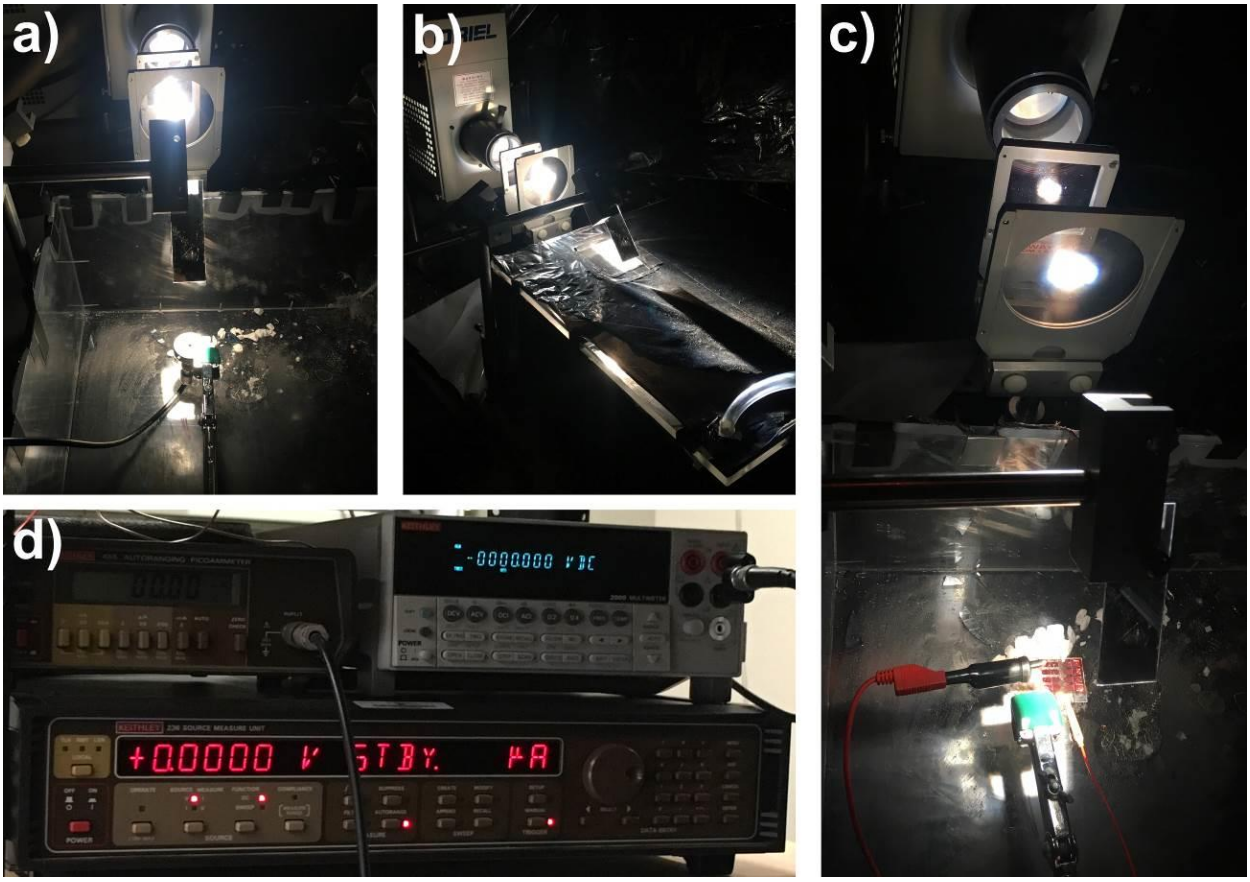

Figure 3.14. AM1.5G J-V testing setup. (**a**) Si photodiode in the plexiglass box for lamp calibration. For the AM1.5G calibration, the Si photodiode had its cap on with a pinhole light opening. (**b**) All calibration and J-V measurements were done with the plexiglass lid installed with argon gas flow. (**c**) An OPV device under the lamp source in the plexiglass box. (**d**) Keithley 236 sourcemeter and Keithley 485 picoammeter.

To measure the external quantum efficiency (EQE), a monochromator (CVI CM 110; Spectral Products) with 2400 grooves/nm grating filtered the light from a separate, identical 300 W Xe lamp (Oriel Instruments). The monochromator was operated by a controller (AB300-Series; Spectral Products), which was controlled by a LabVIEW program. The LabVIEW program cycled through a range of wavelengths in the range of λ = 300 to 700 nm. The light from the lamp was condensed into the monochromator by a lens, then light from the monochromator passed through

a lens to a mirror, and the reflected light from the mirror was condensed into a circular spot on the sample. The height of the OPV devices was adjusted so that the circular spot filled the entire active area. At an identical height, the short-circuit current of the Si photodiode was measured at each wavelength by a picoammeter (Keithley 485). The short-circuit current of the Si photodiode (with the pinhole cap removed) was used to measure the input optical power and the number of photons irradiated at each wavelength. For the OPV devices, the short-circuit current was measured and the number of electrons was calculated at each wavelength. The EQE spectra were obtained by dividing the number of electrons by the number of photons. All silicon photodiode and OPV device short-circuit currents were measured with the plexiglass box lid installed and with a positive pressure of argon gas (for the devices).

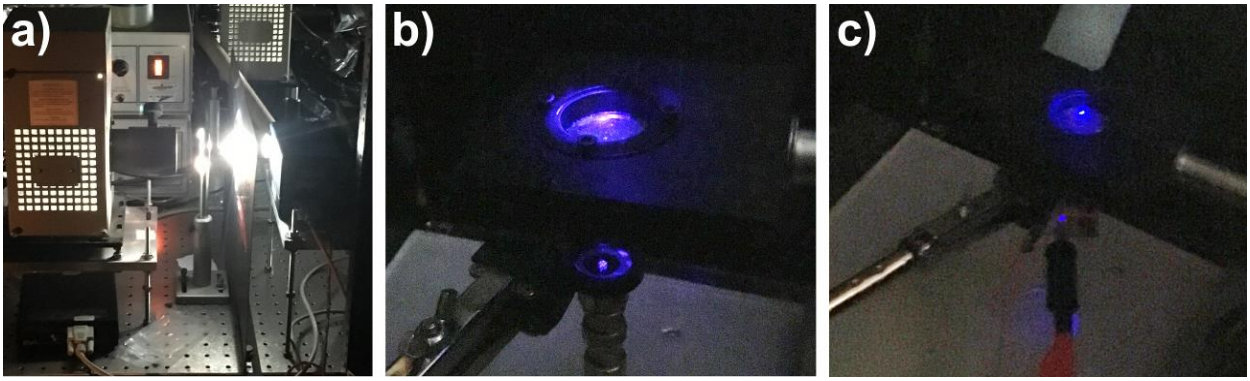

Figure 3.15. Monochromator lamp testing setup. (**a**) Lamp (left), lens (middle), monochromator (right), monochromator controller (bottom left). (**b**) Si photodiode with the same circular spot size as on the device with use of a lens. The pinhole cap was removed from the Si photodiode for this calibration. (**c**) OPV device under monochromator source in plexiglass box. The plexiglass lid was installed for Si photodiode calibration and OPV device testing.

A field-emission scanning electron microscope (SEM, LEO 1550) with an accelerating voltage of 5 kV was used to image the films. The samples were sputter-coated (Leica EM ACE600) with

~2.5 nm of high resolution iridium before use. An atomic force microscope (AFM, Veeco SPI 3100) with a scan rate of 1 Hz was used to determine the surface roughness of the films after annealing. Transmission electron microscopy (TEM) images were collected on a Phillips EM420 with an accelerating voltage of 120 kV. For examination of AgNPs, at least 100 AgNPs were surveyed using ImageJ to gain an estimate of the edge length and thickness.

Sheet resistance of films was measured using cylindrical four-point probe Jandel Multi Height Probe; Bridge Technology) coupled with a resistivity test unit (Jandel RM3; Bridge Technology). The four-point probe had an electrode radius of 500 μm with a spacing of 1 mm, and an adjustable load of 10 to 30 grams. The test unit supplied a constant current source from 10 nA to ~100 mA through the outer two probes, while measuring the voltage drop through the center two probes. The test unit calculated the sheet resistance as:

$$R_s = \frac{\pi}{\ln(2)} \frac{\nabla V}{I} = 4.5324 \frac{\nabla V}{I} = \frac{\rho}{l} \qquad (\mathbf{3.12})$$

where R_s is sheet resistance in ohms per square, ∇V is the change in voltage in volts, I is the current in amps, ρ is resistivity in ohms · cm, and l is the film thickness in cm.

Photoluminescence (PL) was excited by a continuous wave laser at 488 nm (Coherent Sapphire 488-20). The laser power was 28 mW supplied by Coherent Sapphire LP/SF Driver Unit. The PL was delivered to a 0.55 m focal length spectrometer (HORIBA Jobin Yvon iHR550) with a 0.1 mm slit width and a 600 grooves/mm, 500 nm blaze grating. The PL was recorded by a liquid nitrogen cooled, charge-coupled device (HORIBA Jobin Yvon Symphony II).

REFERENCES

(1) Snowtex ®. http://www.nissanchem-usa.com/products/snowtex/.
(2) Yancey, S.; Zhong, W.; Heflin, J. R.; Ritter, A. L. The Influence of Void Space on Antireflection Coatings of Silica Nanoparticle Self-Assembled Films. *Journal of applied physics* **2006,** *99* (3), 034313.

(3) Choi, J.; Rubner, M. F. Influence of the Degree of Ionization on Weak Polyelectrolyte Multilayer Assembly. *Macromolecules* **2005,** *38* (1), 116-124.
(4) Yoo, D.; Shiratori, S. S.; Rubner, M. F. Controlling Bilayer Composition and Surface Wettability of Sequentially Adsorbed Multilayers of Weak Polyelectrolytes. *Macromolecules* **1998,** *31* (13), 4309-4318.
(5) Shao, L.; Lutkenhaus, J. L. Thermochemical Properties of Free-Standing Electrostatic Layer-by-Layer Assemblies Containing Poly (Allylamine Hydrochloride) and Poly (Acrylic Acid). *Soft Matter* **2010,** *6* (14), 3363-3369.
(6) Chun-Guey Wu, L.-F. T., Yen-Ting Kuo, Chung Hsien Shu. Enhancement of the Photocatalytic Activity of Tio2 Film Via Surface Modification of the Substrate. *Appl. Catal., A* **2002,** *226* (1-2), 199-211.
(7) Kern, W.; Puotinen, D. The Rca-Clean. *RCA Review* **1970,** *31* 197.
(8) Park, Y.; Choong, V.; Gao, Y.; Hsieh, B. R.; Tang, C. W. Work Function of Indium Tin Oxide Transparent Conductor Measured by Photoelectron Spectroscopy. *Applied Physics Letters* **1996,** *68* (19), 2699-2701.
(9) Das, S.; Alford, T. Improved Efficiency of P3ht: Pcbm Solar Cells by Incorporation of Silver Oxide Interfacial Layer. *Journal of Applied Physics* **2014,** *116* (4), 044905.
(10) Eastment, R.; Mee, C. Work Function Measurements on (100),(110) and (111) Surfaces of Aluminium. *Journal of Physics F: Metal Physics* **1973,** *3* (9), 1738.
(11) Simpson, J. Advances and Applications of Baytron® Conductive Polymer Technologies https://www.aimcal.org/uploads/4/6/6/9/46695933/simpson_presentation.pdf.
(12) Alemu, D.; Wei, H.-Y.; Ho, K.-C.; Chu, C.-W. Highly Conductive Pedot: Pss Electrode by Simple Film Treatment with Methanol for Ito-Free Polymer Solar Cells. *Energy & environmental science* **2012,** *5* (11), 9662-9671.
(13) Valtakari, D.; Bollström, R.; Toivakka, M.; Saarinen, J. J. Influence of Anionic and Cationic Polyelectrolytes on the Conductivity and Morphology of Poly (3, 4-Ethylenedioxythiophene): Poly (Styrenesulfonate) Films. *Thin Solid Films* **2015,** *590* 170-176.
(14) Kim, H.; Nam, S.; Lee, H.; Woo, S.; Ha, C.-S.; Ree, M.; Kim, Y. Influence of Controlled Acidity of Hole-Collecting Buffer Layers on the Performance and Lifetime of Polymer: Fullerene Solar Cells. *J. Phys. Chem. C* **2011,** *115* (27), 13502-13510.
(15) Brinkmann, M.; Rannou, P. Effect of Molecular Weight on the Structure and Morphology of Oriented Thin Films of Regioregular Poly (3-Hexylthiophene) Grown by Directional Epitaxial Solidification. *Advanced Functional Materials* **2007,** *17* (1), 101-108.
(16) Al-Ibrahim, M.; Roth, H.-K.; Schroedner, M.; Konkin, A.; Zhokhavets, U.; Gobsch, G.; Scharff, P.; Sensfuss, S. The Influence of the Optoelectronic Properties of Poly (3-Alkylthiophenes) on the Device Parameters in Flexible Polymer Solar Cells. *Organic Electronics* **2005,** *6* (2), 65-77.
(17) Kline, R. J.; McGehee, M. D.; Kadnikova, E. N.; Liu, J.; Fréchet, J. M.; Toney, M. F. Dependence of Regioregular Poly (3-Hexylthiophene) Film Morphology and Field-Effect Mobility on Molecular Weight. *Macromolecules* **2005,** *38* (8), 3312-3319.
(18) Mauer, R.; Kastler, M.; Laquai, F. The Impact of Polymer Regioregularity on Charge Transport and Efficiency of P3ht: Pcbm Photovoltaic Devices. *Advanced Functional Materials* **2010,** *20* (13), 2085-2092.
(19) Gong, X.; Tong, M.; Brunetti, F. G.; Seo, J.; Sun, Y.; Moses, D.; Wudl, F.; Heeger, A. J. Bulk Heterojunction Solar Cells with Large Open-Circuit Voltage: Electron Transfer with Small Donor-Acceptor Energy Offset. *Advanced Materials* **2011,** *23* (20), 2272-2277.

(20) Ngo, T. T.; Nguyen, D. N.; Nguyen, V. T. Glass Transition of Pcbm, P3ht and Their Blends in Quenched State. *Advances in Natural Sciences: Nanoscience and Nanotechnology* **2012,** *3* (4), 045001.
(21) Snyder, C. R.; Nieuwendaal, R. C.; DeLongchamp, D. M.; Luscombe, C. K.; Sista, P.; Boyd, S. D. Quantifying Crystallinity in High Molar Mass Poly (3-Hexylthiophene). *Macromolecules* **2014,** *47* (12), 3942-3950.
(22) Swinnen, A.; Haeldermans, I.; vande Ven, M.; D'Haen, J.; Vanhoyland, G.; Aresu, S.; D'Olieslaeger, M.; Manca, J. Tuning the Dimensions of C60-Based Needlelike Crystals in Blended Thin Films. *Advanced Functional Materials* **2006,** *16* (6), 760-765.
(23) Picart, C.; Lavalle, P.; Hubert, P.; Cuisinier, F.; Decher, G.; Schaaf, P.; Voegel, J.-C. Buildup Mechanism for Poly (L-Lysine)/Hyaluronic Acid Films onto a Solid Surface. *Langmuir* **2001,** *17* (23), 7414-7424.
(24) Feng, X.; Feng, L.; Jin, M.; Zhai, J.; Jiang, L.; Zhu, D. Reversible Super-Hydrophobicity to Super-Hydrophilicity Transition of Aligned Zno Nanorod Films. *Journal of the American Chemical Society* **2004,** *126* (1), 62-63.
(25) Aluminum (Al) Pellets Evaporation Materials. https://www.lesker.com/newweb/deposition_materials/depositionmaterials_evaporationmaterials_1.cfm?pgid=al1.

Chapter 4

Stability of Anti-Reflection Coatings via the Self-Assembly Encapsulation of Silica Nanoparticles by Diazo-Resins

The majority of this chapter is from a manuscript published in Journal of Physics and Chemistry of Solids,[1] with slight modifications.

4.1 INTRODUCTION

Previously, our group fabricated highly-transparent anti-reflection coatings (ARCs) by ISAM film growth of poly(allylamine hydrochloride) (PAH) and silica nanoparticles (SiO_2 NPs). The self-assembled SiO_2 NPs formed a nano-porous randomly closed packed (RCP) film structure with an overall refractive index largely dependent on the porosity. ARCs constructed with 45 nm SiO_2 NPs yielded the greatest anti-reflection with a refractive index that resided in the range of 1.25 to 1.35 and a porosity ranging from 30% to 45%.[2] Since the refractive indices of the films were close to the ideal value ($n \approx 1.22$), the light transmittance and reflectance levels were >98% and <0.2%, respectively. Although the films had excellent anti-reflection, their mechanical stability was insufficient for commercial application.

The incorporation of the photo-curable, polycation 4-diazodiphenylamine/formaldehyde condensate hydrogen sulfate (diazo-resin; DAR) into ionic self-assembled multilayers (ISAMs) is a promising approach for increasing film stability. The exposure of DAR to UV irradiation causes decomposition of its diazonium group, which facilitates covalent crosslinking between DAR and

polyanionic sulfonate or carboxylic functional groups (PSS, PAA, porphyrins, etc.).[3-6] Without the presence of covalent linkages, ionically bonded polyelectrolytes are susceptible to being dissociated and dissolved by polar solvents (methanol, DMF, dimethyl sulfoxide, etc.), as well as strong electrolyte solutions containing LiCl, NaSCN, or $ZnCl_2$.[3-6] Ionically bonded polyelectrolyte films are especially prone to dissolution in ternary solvents featuring polar solvents and strong electrolytes combined, such as H_2O-DMF-LiCl, H_2O-DMF-NaSCN or H_2O-DMF-ZnCl.[3] However, after the addition of DAR and its UV irradiation crosslinking in ISAM films, the films have been reported to be entirely insoluble and unaffected when immersed in ternary solvents, including H_2O-DMF-$ZnCl_2$.[3-6] Film stability can be additionally enhanced through the development of covalent linkages between DAR and sulfonated functionalized silanes, grafted to the substrate surface before ISAM growth.[5, 7] Stability has also been reported for ISAM films containing DAR and nanoparticles functionalized with sulfonate or carboxylic acid groups.[7-8] Furthermore, DAR/PSS ISAMs were reported to be grown directly onto polystyrene (PS) particles *in solution* to form nanocomposites.[9] After intentional dissolving of PS particles to leave hollow DAR/PSS capsules, the capsules showed dramatic solvent and mechanical stability enhancements after crosslinking by UV irradiation. However, to our knowledge, detailed NP encapsulation analysis by DAR for improved ARC ISAM film stability has not been previously reported in the literature.

Here, we demonstrate induced film stability by the introduction of DAR-encapsulated SiO_2 NPs (modified SiO_2 NPs; MSNPs) into ISAM films. The crosslinking behavior of DAR was first analyzed through the inspection of DAR/PSS ISAM films without SiO_2 NPs. Next, the concentration of DAR in polycation MSNP solution was optimized by ζ-potential and dynamic light scattering (DLS). To produce ARCs, ISAM films were grown with alternating charged

solutions of MSNPs and poly(styrene sulfonate) (PSS) on silylated glass substrates. The MSNP/PSS ARCs were UV-irradiated, and then characterized using scanning electron microscopy (SEM) and UV-vis-IR spectrometry. The solvent stability of the ARCs before and after UV irradiation was thoroughly examined using UV-vis-IR spectrometry and atomic force microscopy (AFM).

4.2 EXPERIMENTAL

4.2.1 Materials. 4-Diazodiphenylamine/formaldehyde condensate hydrogen sulfate (DAR; $M_w \approx 2{,}800$) was graciously donated by Secant Chemicals. SNOWTEX ST-20L SiO_2 NP solution was purchased from Nissan Chemical, composed of 45 nm average diameter particles and a concentration of 20 wt%. Poly(styrene sulfonic acid) (PSS; $M_w \approx 70{,}000$) was purchased from Polysciences Inc. The aqueous solutions were developed and diluted with ultrapure de-ionized water (18 MΩ cm resistivity) (DI water). Hydrochloric acid (HCl; ACS Reagent), sulfuric acid (H_2SO_4; ACS Reagent), acetic acid (CH_3COOH; Certified ACS), methanol (MeOH; Certified ACS), N,N-dimethylformamide (DMF; Certified ACS), and sodium hydroxide (NaOH; Pellets/Certified ACS) were purchased from Fisher Scientific. Hydrogen peroxide (H_2O_2; 30 wt%), 95% (3-mercaptopropyl)trimethoxysilane (MPTS) solution and zinc chloride (ZnCl; powder; Purity >= 98%) were purchased from Sigma-Aldrich.

4.2.2 Solution Formation. The SiO_2 NP solution was first diluted by a factor of 100 to reduce the concentration from 3.76 to 0.0376 M. After dilution, a range of DAR concentrations were added to the SiO_2 NP solution and stirred for 12 h in the dark. The solutions were stirred in darkness for up to a week and sonicated for 80 min before use. The encapsulated SiO_2 NPs were denoted as modified silica nanoparticles (MSNPs). PSS solution was created by dissolving 10 mM PSS

powder into DI water at a pH of 7.0. The pH of the PSS solutions was adjusted with the addition of 1.0 M HCl and 1.0 NaOH solutions.

MPTS solution was added to MeOH at 7mM and stirred for 1 h before use. A ternary solvent was formed by mixing DI water, DMF, and ZnCl together (H_2O:DMF:ZnCl, 3:5:2, w/w/w) and stirred overnight.

4.2.3 Sulfonated Silane Slide Preparation. The grafting of silane molecules onto glass microscope slide substrates and their sulfonate group functionalization was performed according to a procedure from previous reports with slight modifications.[10] Glass microscope slides were first vigorously cleaned with IPA, air dried, and put into glass staining jars. The slides were then submerged in a piranha solution (H_2SO_4:H_2O_2 7:3) and heated to 90 ºC for 30 min. Afterwards, the slides were copiously washed with DI water, and then immersed into the MPTS in MeOH mixture for 18 h. The slides were then washed thoroughly with MeOH, then submerged into an acetic acid mixture (CH_3COOH:H_2O_2 5:1), and heated 70 ºC for 50 min. Finally, the slides were washed with DI water, dried, and stored for ISAM use.

4.2.4 Film Fabrication. The ISAM films were processed with an programmable immersion machine, which consisted of eight solution positions (one solution at every 45°). The immersion machine can be programmed to spin substrates in solutions at a range of frequencies (600-3,000 rpm). For ISAM film growth, the substrates were 1) immersed in the polycation MSNP solution for ten minutes while spinning in the solution at 3,000 rpm. Afterwards, the substrates were 2) rinsed in three buffer solutions (refilled with DI water after each bilayer) for 45 s each while spinning at 3,000 rpm. After rinsing, the substrates were 3) immediately dipped into the polyanion PSS solution for three minutes without spinning. Following the immersion into the PSS solution, the substrates were 4) again rinsed in three buffer solutions. For the ISAM film growth process,

steps 1 to 4 represented one complete bilayer. The substrate platform was kept full (four substrates) during the entire growth to promote uniform current flow as the substrates were spun in the solutions. The fabrication process was maintained in complete darkness to avoid premature decomposition of the DAR in the MSNP solution. Upon termination of ISAM film fabrication, the slides were dried by a stream of N_2 gas and then exposed to UV irradiation for fifteen minutes.

4.3 RESULTS

4.3.1 DAR/PSS Multilayers. An understanding of the crosslinking reaction between the DAR diazonium ($R\text{-}N_2^+$) and PSS sulfonate (SO_3^-) functional groups was established through examination of pure DAR/PSS multilayers. SiO_2 NPs were excluded from these preliminary DAR/PSS films to distinguish the optical absorption change after crosslinking, without the SiO_2 NPs optical interference effects. The optical absorption spectra were measured on five to eight bilayer DAR/PSS films before and after exposure to UV irradiation (**Figure 4.1a**). The absorption at the wavelength $\lambda = 380$ nm is a signature of the π-π^* transition in DAR's diazonium group, and the relative intensity is proportional to the multilayer film thickness.[4] Before exposure to UV, the absorption intensity at $\lambda = 380$ nm increased linearly with the number of bilayers of DAR/PSS, which signified linear-growth of the multilayer film (**Figure 4.1b**). After the DAR/PSS multilayer films were exposed to UV irradiation for fifteen min, a complete flattening of the absorption peak at $\lambda = 380$ nm indicated that a substantial decomposition of the diazonium groups occurred. It was expected that the decomposition of the diazonium groups facilitated the formation of covalent linkages between the diazonium and sulfonate groups functional groups, due to their close proximity in the DAR/PSS films (**Figure 4.2**).[4, 9]

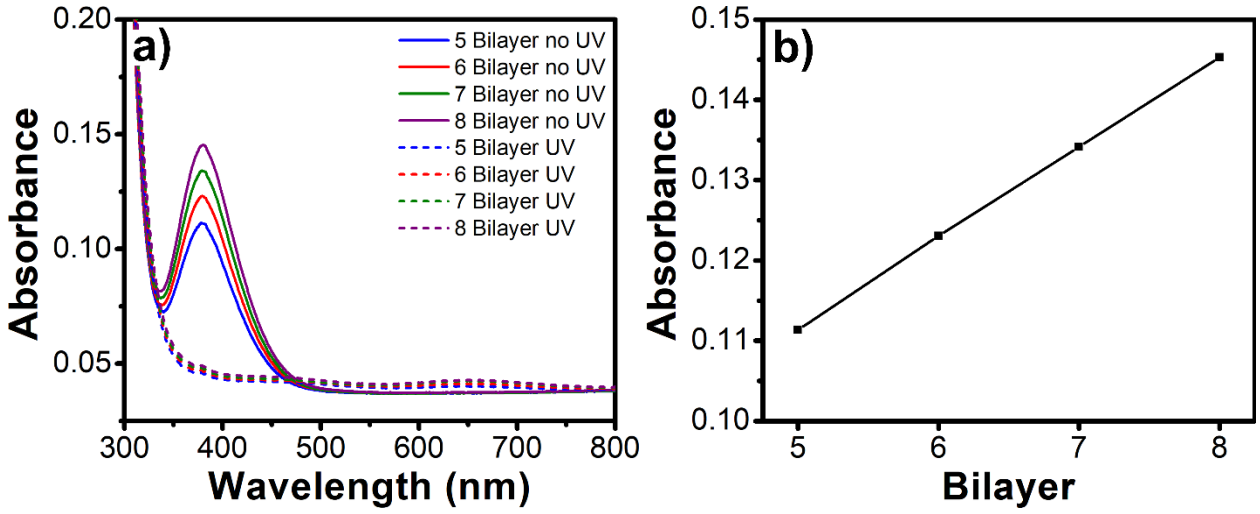

Figure 4.1. (**a**) Absorption spectra of five to eight bilayer DAR/PSS films before and after UV irradiation. (**b**) The absorption intensity at λ = 380 nm prior to UV exposure in relation to the number of DAR/PSS bilayers.

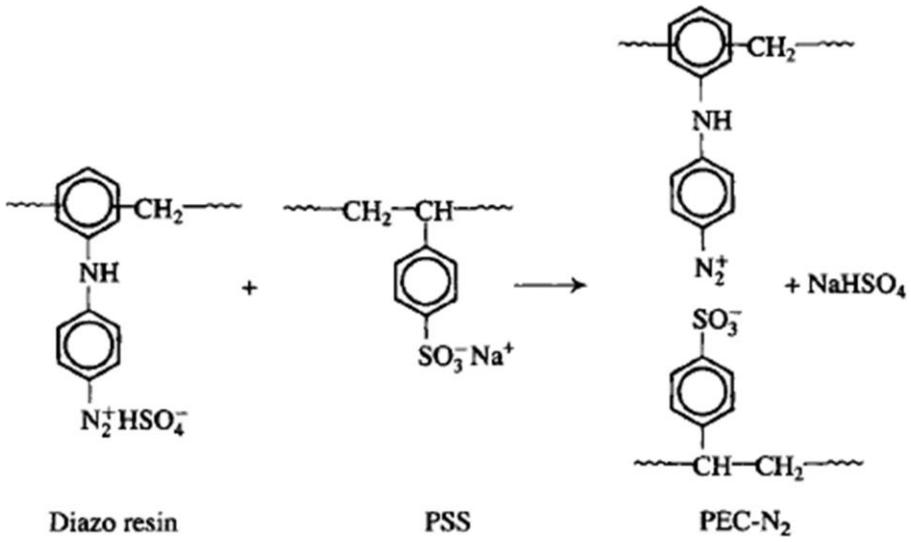

Figure 4.2. Chemical schematic of UV irradiation covalent crosslinking reaction between DAR and PSS. Reprinted (adapted) with permission from W. X. Cao, S. J. Y., S. G. Cao, C. Zhao. Novel Polyelectrolyte Complexes Based on Diazo-Resins. *Macromol. Rapid Commun.* **1997,** *18* 983-989.[3] The work from this journal is licensed under the Creative Commons Attribution License (CC-BY) License.

4.3.2 Modified Silica Nanoparticle Solution Formation. The encapsulation of the SiO_2 NPs by the self-assembly of DAR in solution to make modified silica nanoparticles (MSNPs) satisfied two conditions. First, the anionic SiO_2 NPs were converted to cationic, which allowed for ISAM growth of the MSNPs and the polyanionic PSS. Second, covalent crosslinking was made possible between the DAR functional groups on MSNPs and the sulfonic functional groups on PSS and grafted silanes on the substrates (**Figure 4.3**). The abundance of covalent bonds within the film and to the substrate would potentially lead to significant stability enhancements.

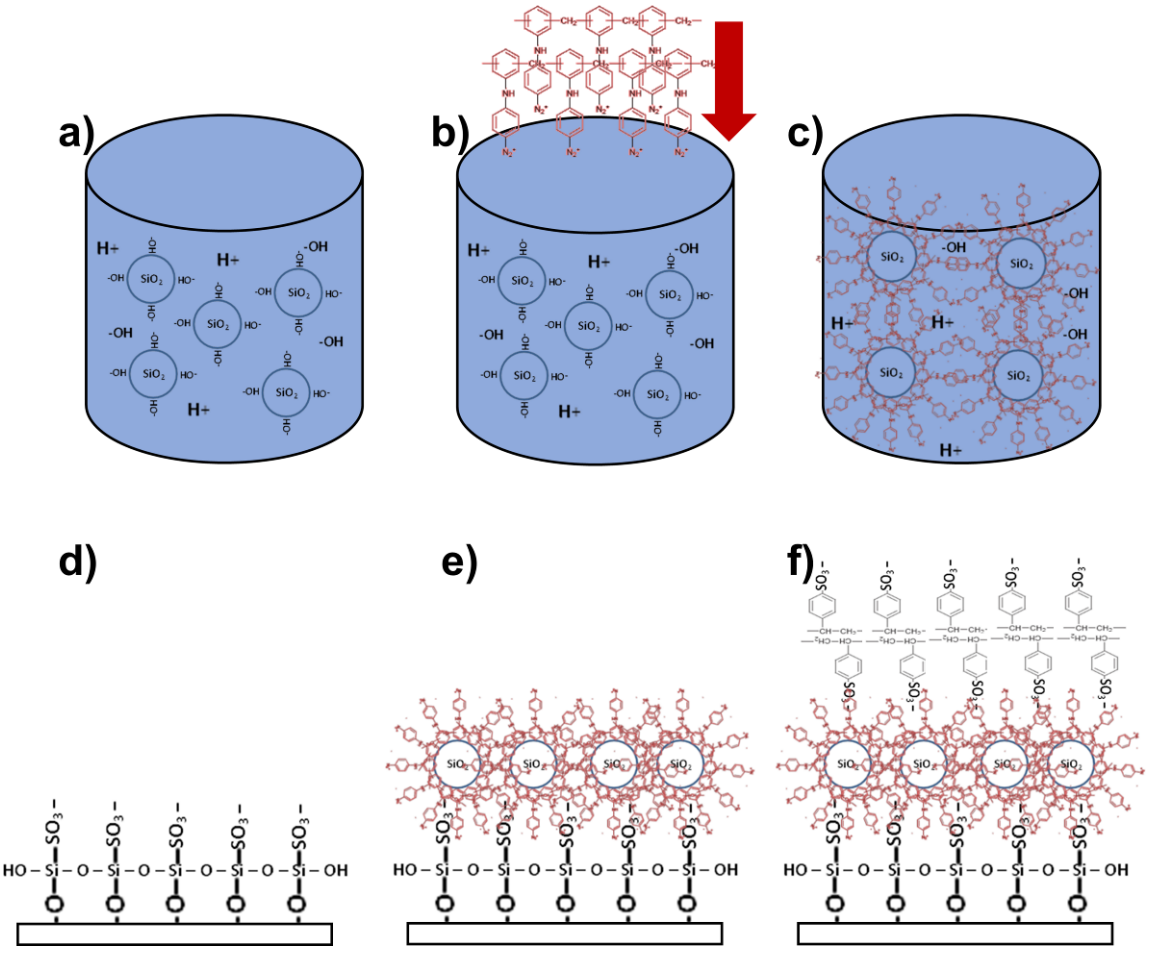

Figure 4.3. Schematic of MSNP solution formation: (**a**) diluted SiO_2 NP solution (0.0376 M), (**b**) deposition of the diazo-resin into the diluted SiO_2 NP solution, (**c**) encapsulation of the SiO_2 NP's

by the DAR to make MSNPs. Schematic of ISAM film formation: (**d**) silylation of glass substrates, (**e**) growth of the first MSNP polycation layer, (**f**) assembly of the second layer, PSS.

Despite the relatively low molecular weight of the DAR (M_w = 2,800) chains, their deposition into an undiluted solution of SiO_2 NPs (3.76 M) resulted in individual chains bridging multiple NPs together and the formation of large agglomerated particles in the solution. After the growth of MSNP/PSS ISAM films, the presence of the agglomerated particles on the film surface was clear in SEM images (**Figure 4.4**). Since the agglomerated particle size was comparable to the wavelength of light (>1 μm), the anti-reflection of the films deteriorated substantially as a result of significant Mie light scattering.

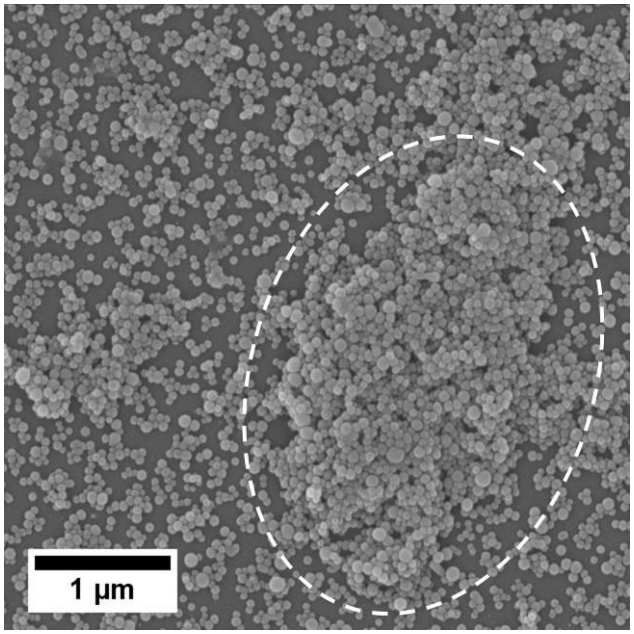

Figure 4.4. SEM characterization of a MSNP/PSS film produced from a solution with large agglomerates. A particularly large agglomerate is circled in the figure.

Dilution of the original SiO_2 NP solution concentration by a factor of 100 to 0.0376 M decreased particle proximity in the colloidal suspension, and thus lowered the probability of particle agglomeration by the encapsulating DAR chains. A complete conversion of the SiO_2 NPs to

MSNPs required a switch from a negative to a stable, positive surface charge. Therefore, the ζ-potential and dynamic light scattering (DLS) of the MSNP solutions were measured after the addition of DAR at final concentrations in the range of 0 to 0.45 mM (all in the dark) (**Figure 4.5a-b**). For the DAR concentration of 0 to 0.10 mM, the ζ-potential was negative from -53 to -46 mV, which indicated an incomplete encapsulation of the SiO_2 NPs. For an increased DAR concentration of 0.15 mM, the ζ-potential was still negative and the MSNPs were unstable (particle precipitation). Although the ζ-potential became positive for a DAR concentration of 0.20 mM, this concentration was only temporarily stable, and precipitation was evident after a short period of time. A DAR concentration in the range of 0.25 to 0.40 mM resulted in a stable, positively charged MSNP solution with a ζ-potential from 18.6 to 27.1 mV. As discovered through the DLS measurements, the addition a 0.05 mM DAR concentration resulted in an increase in the average particle size from 64.6 to 80.0 nm. For the stable DAR concentrations in the range of 0.1 to 0.4 mM, the average particle size remained relatively consistent in the approximate range of 90 to 100 nm. The unstable DAR concentration 0.15 mM was omitted from **Figure 4.5b**, as the precipitates in the solution caused the average particle size to drastically rise to 3531.5 nm. Since the DAR concentration of 0.25 mM was the lowest, stable DAR concentration for the MSNP solution, it was chosen for incorporation into ISAM films.

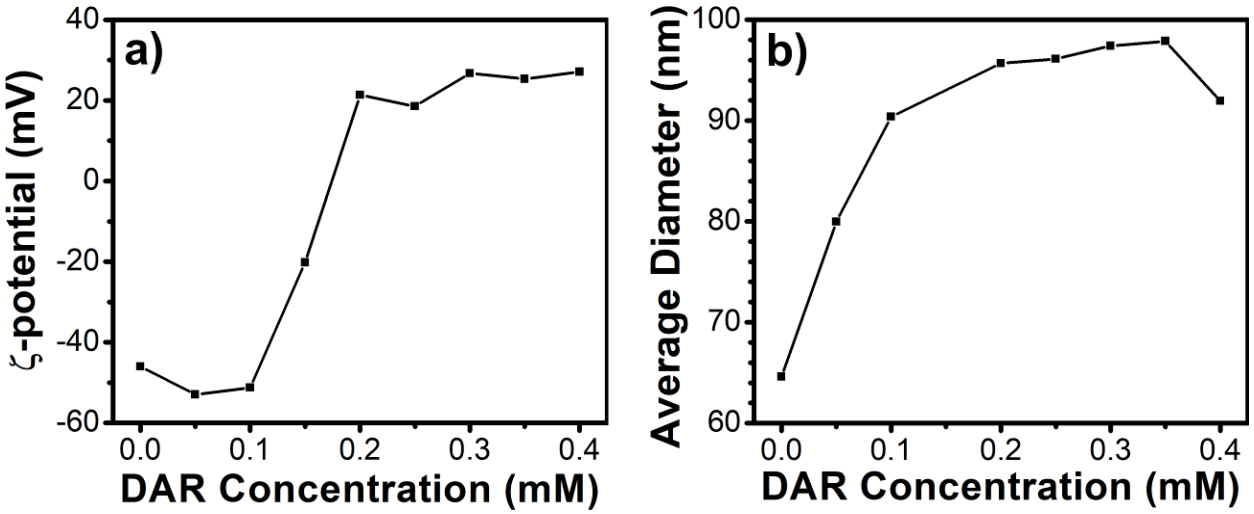

Figure 4.5. ζ-potential and average particle size by DLS vs. DAR concentration for the MSNP solution.

4.3.3 MSNP/PSS ARC Morphology. With the successful formation of the MSNP solution, ISAM films were constructed with MSNP and PSS as the catonic and anionic solutions, respectively to produce MSNP/PSS ARCs. After the processing of two, four, six, and eight bilayer MSNP/PSS ARCs, the films were subsequently exposed to UV irradiation for crosslinking of the DAR and PSS functional groups. The films were highly transparent and absent of the characteristic cloudiness from optical light scattering. Analysis by SEM revealed a dense nano-porous film matrix with excellent homogeneity for all of the bilayers (**Figure 4.6a-d**). The high transparency of the films was associated with the lack of large agglomerates on the surface. The coverage on the surface became increasingly thick with a progressive number of bilayers, and the morphology was nearly identical to the PAH/SiO_2 NP ARCs made previously in our group.[2]

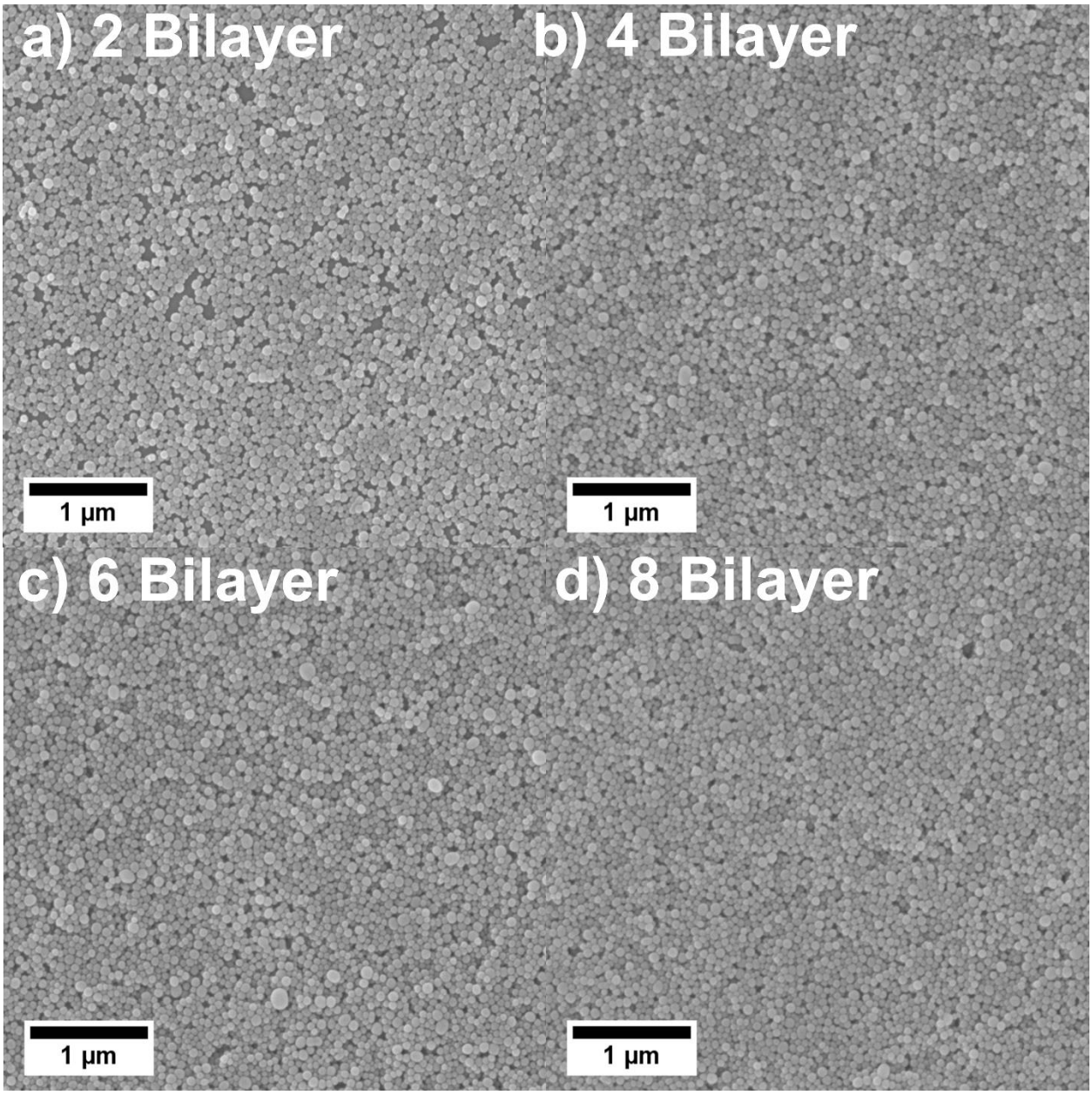

Figure 4.6. SEM characterization of MSNP/PSS films after UV irradiation. Images are shown for films of (**a**) two, (**b**) four, (**c**) six, and (**d**) eight bilayers.

4.3.4 MSNP/PSS ARC UV-vis-IR Spectrometry. Fundamentally, ARCs implement optical destructive interference in the reflected beams in order to increase the amount of the transmitted light. The peak positions of the transmittance maxima and minima are proportional to the physical thickness of the film, corresponding to **Equations 4.1** and **4.2**, respectively:

$$(m - 0.5)\lambda = 2nd \quad (\mathbf{4.1})$$

$$m\lambda = 2nd \quad (\mathbf{4.2})$$

where m is the interference order, λ is the wavelength, n is the refractive index, and d is the physical thickness. MSNP/PSS ARCs were processed for a range of bilayers (thicknesses) onto sulfonated substrates and exposed to UV irradiation directly after ISAM growth. As discovered through transmittance and reflectance UV-vis-IR spectrometry measurements, MSNP/PSS ARCs with one, two, three, and four bilayers had excellent anti-reflection with first order peaks in the visible wavelength range (**Figure 4.7a-b** and **Table 4.1**). The transmittance and reflectance spectra for all films were compared to bare glass. The film homogeneity found by SEM, as discussed earlier, was confirmed by the consistency of the transmittance and thickness measurements at four different film locations, as well as relatively low surface roughness values (**Table 4.1**). With a greater number of MSNP/PSS bilayers, the transmittance values increased and the peak positions red-shifted to longer wavelengths.

The absorption due to scattering (A_s) spectra was calculated for a quantifiable characterization of the optical scattering, as follows:

$$A_s(\lambda) = -\log(\frac{T(\lambda)}{1-R(\lambda)}) \quad (\mathbf{4.3})$$

where T is the transmission percentage and R is the reflection percentage at a specific wavelength λ. Given the non-absorbing nature in this wavelength range for all of the film constituents, A_s was attributed purely to optical scattering. Therefore, A_s is proportional to the scattering cross-section in

$$A_s(\lambda) = Cl\sigma_s(\lambda) \quad (\mathbf{4.4})$$

where C is the concentration, l is the path length, and σ_s is the scattering cross-section. The A_s spectra was calculated for all MSNP/PSS ARCs (**Figure 4.7c**), and the corresponding A_s slope

magnitude was also calculated (**Table 4.1**). The increased magnitude of the A_s slope with a greater number of bilayers correlated to an overall Rayleigh scattering increase. Since the roughness values remained invariable for all films, the A_s slope was attributed purely to the film thickness. As light traveled through films with larger thicknesses, the incident photons interacted with a greater number of particles and caused elevated levels of scattering. Rayleigh scattering naturally occurs more strongly at higher wavenumbers (shorter wavelengths), due to the $1/\lambda^4$ dependence. Since Rayleigh scattering is smaller for longer wavelengths, the transmittance peaks at longer wavelengths exhibited higher transmittances than those at shorter wavelengths.

The physical thickness and roughness values were found through profilometry for an average of five measurements (**Table 4.1** and **Table 4.2**). The optical thickness is the product of the refractive index and the physical thickness (**Table 4.2**).

The refractive index *n* was also calculated for all MSNP/PSS ARCs using **Equation 4.1** from the physical thickness *d* and the destructive interference (transmittance maxima or reflectance minima) peak wavelength (λ) (**Table 4.2**). The refractive indices were quite consistent for all MSNP/PSS ARCs in the range of 1.25 to 1.26, which confirmed uniformity for a different number of bilayers. Since refractive indices for the MSNP/PSS ARCs were close to the ideal anti-reflection refractive index for glass substrates in air ($n \approx 1.22$), the films displayed excellent peak transmittance levels and reflectance values.

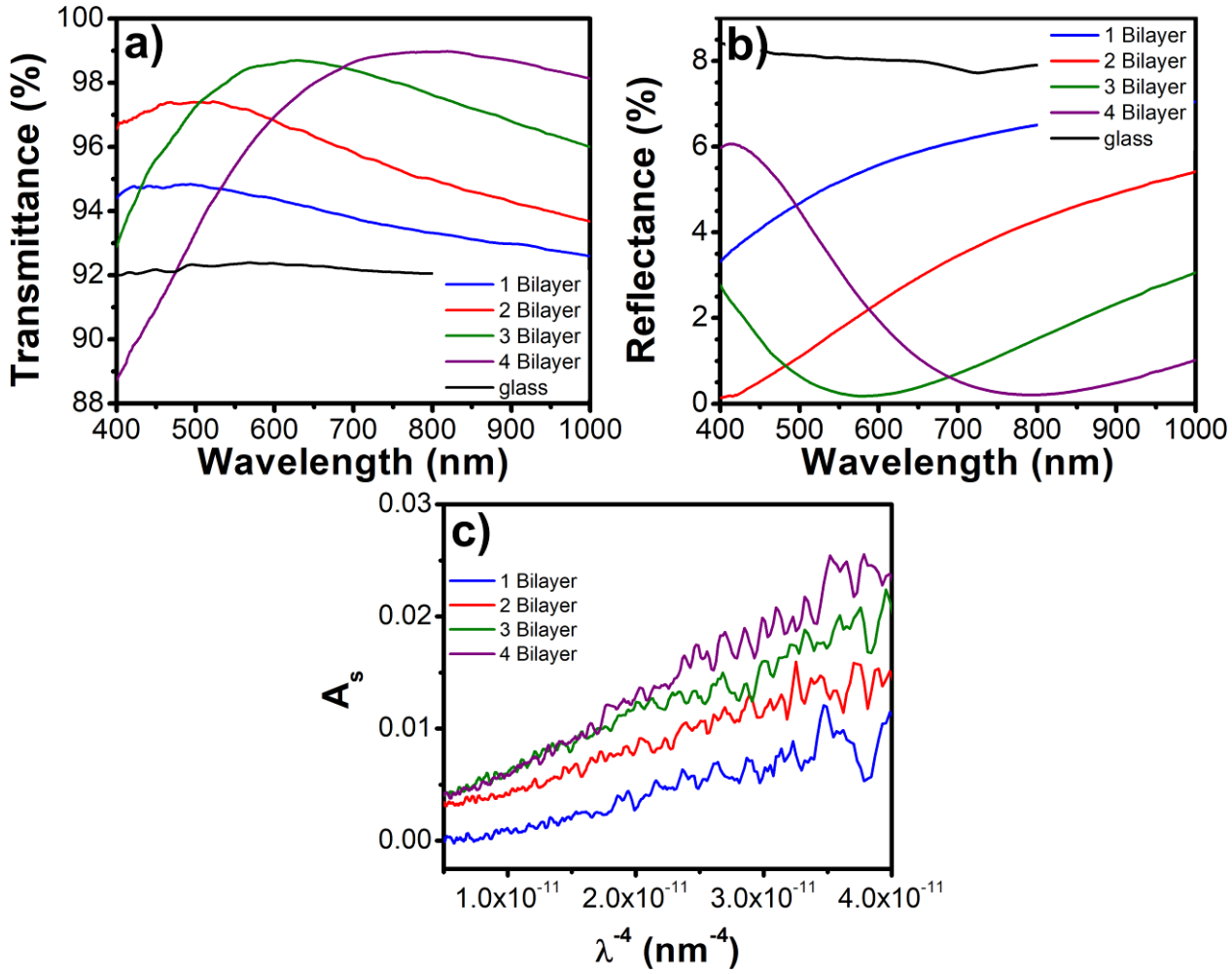

Figure 4.7. UV-vis-IR spectrometry characterization of one to four bilayer MSNP/PSS ARCs including (**a**) transmittance, (**b**) reflectance, and (**c**) absorbance due to scattering (A_s) spectra.

Table 4.1. Optical characteristics for one to four bilayer MSNP/PSS ARCs.

Bilayers	Transmittance Max (%)	Reflectance Min (%)	Wavelength peak (nm)	A_s slope	Roughness (nm)
1	-	-	-	2.95 x 10^8	5.75
2	97.59	0.015%	484	3.78 x 10^8	4.20
3	98.73	0.17%	620	4.60 x 10^8	5.78
4	99.02	0.20%	797	6.32 x 10^8	5.27

Table 4.2. Additional optical characteristics for one to four bilayer MSNP/PSS ARCs.

Bilayers	Wavelength peak (nm)	Thickness (nm)		Refractive index, n
		Optical	Physical	
1	-	-	62.52	-
2	484	121	95.70	**1.26**
3	620	155	124.0	**1.25**
4	797	199	158.8	**1.25**

4.3.5 Solvent Stability. The UV crosslinking reaction between the polyelectrolytes DAR and PSS forms covalent linkages and resistance to solubility for wide range of solvents.[3-4] After a set of ten-bilayer MSNP/PSS ARCs were fabricated, half of the films were left UV unirradiated, while the other half were UV-irradiated. All of the MSNP/PSS films were then sonicated in a ternary solvent solution (H2O:DMF:ZnCl2, 3:5:2, w/w/w) from one to ten minutes, in the dark. H_2O:DMF:$ZnCl_2$ was specifically chosen for the assessment of film stability due to the high solubility of ionic complexes in this ternary solvent. After the films were thoroughly rinsed to remove the ternary solvent residue, the transmittance spectra were recorded after each time period for both UV-irradiated and non-irradiated films (**Figure 4.8a-b**).

The UV-irradiated and non-irradiated MSNP/PSS ARCs had remarkably different resistances to the ternary solvent. The transmittance features for the non-irradiated MSNP/PSS ARCs spectra degraded rapidly from one to ten minute immersion times in the ternary solvent, which was associated with dissolving of the film. Specifically, the degraded transmittance features at $\lambda = 380$ nm and $\lambda = 566$ nm corresponded to the strong absorption from the diazonium group and the destructive interference of the reflected waves, respectively. After ten minutes of immersion in the

ternary solvent, the non-iraddiated films had completely dissolved and transmittance spectra appeared similar to glass. For the UV-irradiated MSNP/PSS ARCs, the transmittance spectra remained unchanged with increased ternary solvent exposure times, which confirmed that these films had gained stability and resistance to the ternary solvent due to the formation of covalent linkages. After ten minutes of the ternary solvent exposure, visual inspection of the non-iraddiated films showed very little of the original films present, whereas the UV-iraddiated films showed no observable changes.

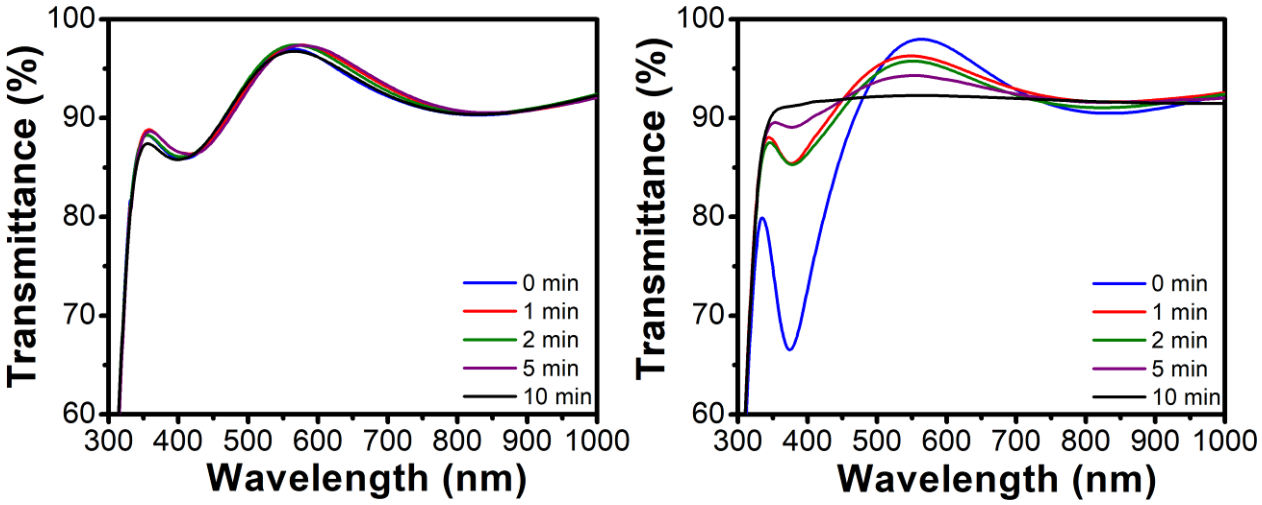

Figure 4.8. Transmittance spectra for two ten-bilayer MSNP/PSS films after being sonicated in a ternary solvent solution (H2O:DMF:ZnCl2, 3:5:2, w/w/w) for various periods of time. (**a**) UV-irradiated films (**b**) non-irradiated films.

AFM imaging was conducted on the UV-irradiated and non-irradiated ten-bilayer MSNP/PSS ARCs after ten minutes of ternary solvent immersion. The AFM images confirmed that the UV-irradiated films remained intact, while the non-iraddiated films were completely dissolved by the ternary solvent (**Figure 4.9a-b**).

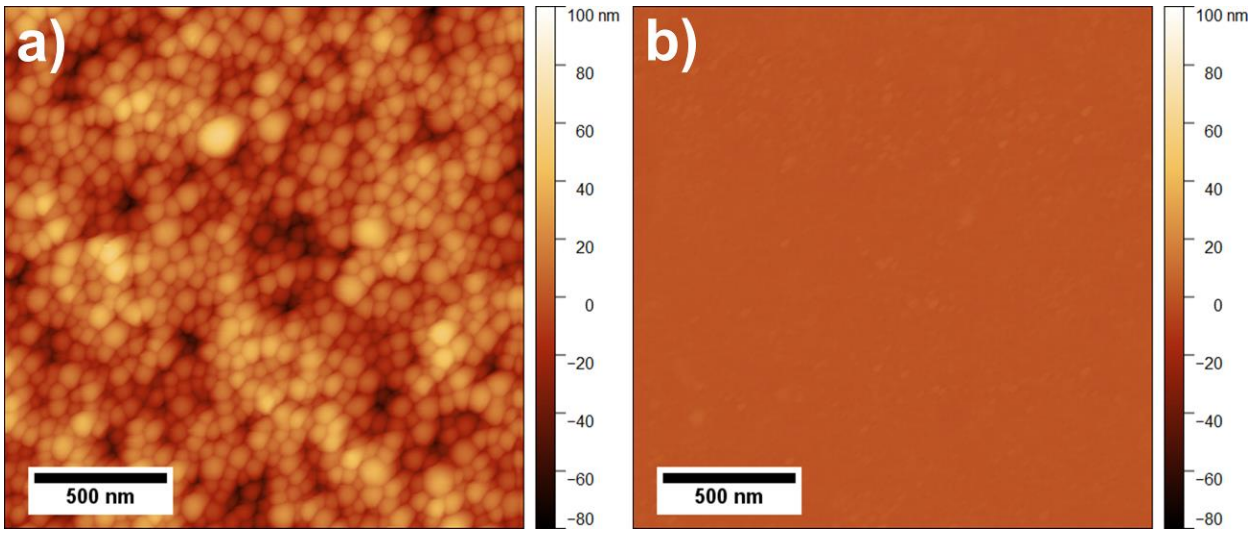

Figure 4.9. AFM characterization for two ten-bilayer MSNP/PSS films after being sonicated in a ternary solvent solution (H2O:DMF:ZnCl2, 3:5:2, w/w/w) for ten minutes. (**a**) UV-irradiated films (**b**) non-irradiated films.

4.4. CONCLUSIONS

The introduction of a diazo-resin (DAR) into ISAM ARC films successfully induced solvent stability of films after UV irradiation crosslinking. First, DAR/PSS ISAM films were examined, and it was found that UV irradiation caused a flattening of the diazonium absorption peak, associated with the formation of covalent bonds. SiO_2 NPs were encapsulated by DAR in solution (MSNPs) to form cationic NPs with functional groups that eventually covalently crosslink with the sulfonate groups on PSS after the processing of ISAM films. The MSNPs were created after dilution of the SiO_2 NP solution concentration by a factor of 100 and were optimized with a 0.25 mM DAR concentration added to the SiO_2 NPs for a stable, non-agglomerated solution. For the 0.25 mM DAR concentration MSNP solution, the ζ-potential and average particle size (found by DLS) were 19 mV and 96 nm, respectively. Anti-reflection coatings (ARCs) were grown by ISAM film processing with the polycation MSNP solution and the polyanionic PSS solution for up to ten

bilayers. Two to four bilayer MSNP/PSS ARCs had anti-reflection in the visible wavelength range with transmittance and reflectance levels >98% and <0.2%, respectively. SEM confirmed the high homogeneity of the MSNP/PSS ARCs. The UV-irradiated MSNP/PSS films displayed resilience against ternary solvents, which confirmed their solvent stability by the formation of covalent linkages between DAR/PSS.

This work highlights important methodologies for the encapsulation of NPs in solution for the addition of specific functional groups and key techniques to avoid agglomerations. These encapsulation methods are transferrable to many different applications. We show how the encapsulated NPs can be used process homogeneous thin films with strong solvent stability.

REFERENCES

(1) Metzman, J. S.; Ridley, J. I.; Khalifa, M. B.; Heflin, J. R. Stability of Anti-Reflection Coatings Via the Self-Assembly Encapsulation of Silica Nanoparticles by Diazo-Resins. *Journal of Physics and Chemistry of Solids* **2015,** *87* 271-277.
(2) S. E. Yancey, W. Z., J. R. Heflin, A. L. Ritter. The Influence of Void Space on Antireflection Coatings of Silica Nanoparticle Self-Assembled Films. *JOURNAL OF APPLIED PHYSICS* **2006,** *99* 034313.
(3) W. X. Cao, S. J. Y., S. G. Cao, C. Zhao. Novel Polyelectrolyte Complexes Based on Diazo-Resins. *Macromol. Rapid Commun.* **1997,** *18* 983-989.
(4) J. Sun, T. W., Y. Sun, Z. Wang, X. Zhang, J. Shena, W. Caob. Fabrication of a Covalently Attached Multilayer Via Photolysis of Layer-by-Layer Self-Assembled Films Containing Diazo-Resins. *Chem. Commun.* **1998,** *17* 1853-1854.
(5) J. Sun, Z. W., Y. Sun, X. Zhang, J. Shen. Covalently Attached Multilayer Assemblies of Diazo-Resins and Porphyrins. *Chem. Commun.* **1999,** *8* 693-694.
(6) J. Sun, T. W., F. Liu, Z. Wang, X. Zhang, J. Shen. Covalently Attached Multilayer Assemblies by Sequential Adsorption of Polycationic Diazo-Resins and Polyanionic Poly(Acrylic Acid). *Langmuir* **2000,** *16* (10), 4620-4624.
(7) Y. Fu, H. X., S. Bai, D. Qiu, J. Sun, Z. Wang, X. Zhang. Fabrication of a Stable Polyelectrolyte/Au Nanoparticles Multilayer Film. *Macromolecular Rapid Communications* **2002,** *23* (4), 256–259.
(8) H. Zhang, R. W., G. Zhang, B. Yang. A Covalently Attached Film Based on Poly(Methacrylic Acid)-Capped Fe3o4 Nanoparticles. *Thin Solid Films* **2003,** *429* (1-2), 167–173.
(9) I. Pastoriza-Santos, B. S., F. Caruso. Core–Shell Colloids and Hollow Polyelectrolyte Capsules Based on Diazoresins. *Adv. Funct. Mater.* **2001,** *11* (2), 122–128.
(10) Chun-Guey Wu, L.-F. T., Yen-Ting Kuo, Chung Hsien Shu. Enhancement of the Photocatalytic Activity of Tio2 Film Via Surface Modification of the Substrate. *Appl. Catal., A* **2002,** *226* (1-2), 199-211.

Chapter 5

Enhanced Scratch Resistance of Self-Assembled Silica Nanoparticle Anti-Reflection Coatings Using Crosslinked Polyelectrolyte Interlayers

The majority of this chapter is from a manuscript published in Journal of Materials Chemistry C,[1] *with slight modifications.*

5.1 INTRODUCTION

Anti-reflection coatings (ARCs) serve as a critical component in many optical systems by the means of destructive interference of the reflected incident light to reduce optical loss. Ionic self-assembled multilayers (ISAMs) are an attractive route for ARC production, as the method is inexpensive, simple, and versatile. Previously, we used the ISAM fabrication method to construct ARCs with poly(allylamine hydrochloride) (PAH) and 45 nm silica nanoparticles (SiO_2 NPs) to achieve a random closed-packed (RCP) porosity of 36% with an average refractive index (combining the SiO_2 NPs and pores) between 1.25 and 1.34.[2] As the refractive index of the ARC was close to the ideal value on glass (n = 1.22), the optical transmittance increased from ~92% to greater than 98%, and the reflectance decreased from ~8% to less than 0.2% in the visible wavelength range. Despite these dramatic improvements to the optical properties, the mechanical robustness of the films was insufficient, which hindered their commercial viability.

The thermal crosslinking reaction of poly(allylamine hydrochloride) (PAH) and poly(acrylic acid) (PAA) is effective for the stabilization of ISAM films through the formation of covalent

amide bond linkages between the cationic functional amine groups ($–NH_3^+$) of PAH and the anionic carboxylate functional groups ($–COO^-$) of PAA.[3-13] Since PAH and PAA are considered weak polyelectrolytes, their degree of ionization, charge density, and resultant multilayer thickness are highly sensitive to pH variation.[14-15] The pK_a value, also known as the acid dissociation constant, is the pH at which the average ionization of the polyelectrolyte chains is 50%. The PAA pK_a has been reported to be located in range of 4.5 – 6.5 while in solution and without the addition of salt.[14, 16] Adjustment of a weak polyelectrolyte's pH from a high to low degree of ionization can lead to dramatic variations in layer thicknesses from 4 Å to 80 Å.[15] The rise in thickness is partially attributed to an increased layer roughness, caused by decreased intra-chain repulsion and a larger population of loops and tails.[14] At pH values far from pK_a, the bilayer thickness is lower, since the polymer chains have a higher degree of ionization and fewer are required for charge reversal of the previous monolayer. It has been shown experimentally that the pK_a of PAA in a PAH/PAA multilayer film shifted to approximately 2.2, which is vastly different from in solution or a single layer casted film.[14, 17] Additionally, it has been previously reported that adjustment of PAH and PAA's pH close to their pK_a results in exponential-growth due to the diffusion of weakly-charged polyelectrolyte chains.[18] As the film thickness, roughness, and interpenetration are strongly dependent on the polyelectrolyte solution pH, it is necessary to determine how these properties influence the optical and mechanical properties. Although there has been exploration into the effect of PAH/PAA pH on the multilayer hardness and modulus,[5] information is lacking on dependence of polyelectrolyte pH on the multilayer film's scratch resistance, especially when applied to a composite ARC film.

Here, we present a method for incorporating PAH and PAA polyelectrolyte interlayers with silica nanoparticles to form stably crosslinked ARCs with improved anti-scratch properties. The

films' design was similar to the previous method used by our group,[2] but with an extra bilayer of PAA/PAH added between PAH and the SiO_2 NP's. To our knowledge, this is the first report to apply the beneficial properties of pure PAH/PAA multilayers into composite films that includes SiO_2 NP's for ISAM ARCs. These additional polyelectrolytes provide additional mechanical robustness to the film, especially after thermal crosslinking. Prior to incorporation into interlayer ISAM ARCs, the diffusive properties of PAA in PAH/PAA multilayers (without SiO_2 NP's) were examined through a variation of polyelectrolyte pH. We applied those findings to interlayer ISAM ARCs, where the diffusion and thickness of PAA was discovered to drastically affect the films' properties. These dramatic changes were further understood with respect to the films' surface morphology, through scanning electron microscopy (SEM). We show the correlation between the crossover from linear to exponential-growth in PAH/PAA multilayers and the observable rise in scratch resistance of the interlayer ISAM ARCs. The essential goal for the study was an optimization of both the anti-reflection and scratch resistance in the thermally-crosslinked interlayer ISAM ARCs through the variation of the pH of PAA.

5.2 EXPERIMENTAL

5.2.1 Materials. Poly(allylamine hydrochloride) (M_v = 120,000 – 200,000) was purchased from Alfa Aesar. Poly(acrylic acid) (M_v = 450,000) was purchased from Sigma Aldrich. SiO_2 solution (SNOWTEX ST-20L, 45 nm average particle diameter, 3.76 M) was purchased from Nissan Chemical. Hydrochloric acid (HCl, Certified ACS Plus) and Sodium Hydroxide (NaOH, Certified ACS, Pellets, ≥97.0 %) were purchased from Fisher Scientific. The polyelectrolyte solutions and ISAM rinsing buffers used 18 MΩ deionized (DI) water. Glass microscope slides were purchased from Fisher Scientific with 76.2 x 25.4 mm dimensions. Polished silicon wafers of 4" diameter, 500 micron thickness, and <111> orientation were purchased from University Wafer. The wafers

were cut to analogous microscope slide dimensions to be compatible with our programmable immersion machine. The same wafers were coated with 200 nm of Au and cut into 1" x 1" squares to be used for FTIR.

5.2.2 Solution Formation. The PAH and PAA solutions were formed by mixing the polymer powders into DI water at a concentration of 10 mM. The solutions were adjusted to a neutral pH value and then sonicated for 3 hours. The pH of the solutions was adjusted by the addition of 1.0 M HCl and 1.0 M NaOH solutions. A vacuum filtration assembly with 3.0 μm filter was then used to remove large aggregates from the solution. This filtration method vastly improved film homogeneity and clarity. The SiO_2 NP solution's concentration was left unaltered at 20 wt%, but its pH value was adjusted to 9. The nomenclature here for a polyelectrolyte with a specific pH is denoted as PAA_x, where PAA is the polyelectrolyte and x is the pH value.

5.2.3 Interlayer film Architecture and Fabrication. The interlayer stack order consisted of consecutive PAH, PAA, PAH, and SiO_2 NPs monolayers. Completion of one repeat is denoted as a "quadlayer", represented by $[PAH_{7.0}/PAA_x/PAH_{7.0}/SiO_{2\ 9.0}]_y$, where x and y correspond to the PAA pH and the number of quadlayers, respectively. Only the pH of PAA was varied for this study, whereas the pH of PAH and the SiO_2 NPs remained constant throughout the entire study at 7.0 ($PAH_{7.0}$) and 9.0 ($SiO_{2\ 9.0}$), respectively. All interlayer ISAM ARCs ended with a "sealant" stack that consisted of a single bilayer of PAH/PAA, which was deposited on top to further promote the mechanical integrity of the film by ensuring that the topmost SiO_2 NP layer had PAH/PAA layers above and below. Therefore, the variable y is denoted with the number of complete quadlayers plus 0.5. For instance, y = 4.5 means four quadlayers with an additional PAH/PAA bilayer.

The programmable immersion instrument used to fabricate the ISAM films allowed for fine-tuned control over the specific fabrication conditions. This included dipping time and substrate spinning speed. After an extensive period of experimentation, specific dipping conditions were established to maximize film homogeneity and reproducibility. The substrate was dipped into the polyelectrolyte (PAH, PAA, and then PAH again) solutions for 5 min each without any spinning. The substrate was dipped into the SiO_2 NP solution for 15 min, while spinning at 3,000 rpm. In between each solution, the substrates were rinsed by spinning at 3,000 rpm in neutral pH water for 135 s. The programmable immersion machine contained eight dipping solutions, which conveniently translated to four monolayer dipping steps, each followed by one neutral deionized water rinse step.

5.3 RESULTS

5.3.1 FTIR characterization of PAH/PAA multilayers. Thermal crosslinking to induce covalent amide bonding and stability in PAH/PAA multilayers has been reported with the use of elevated temperatures in the range of 150 – 250 ºC.[3, 5, 9, 11-12, 19-20] The confirmation of the crosslinking reaction was investigated through Fourier transform infrared spectroscopy (FTIR) on four identical two-bilayer $PAH_{7.5}/PAA_{4.5}$ films that were grown onto gold-coated substrates. The FTIR studies were carried out on an instrument in the labs of Dr. John Morris in the Department of Chemistry. Based on previous reports, the polyelectrolytes have a degree of ionization greater than 50% in the multilayer film at these pH values, which provides adequate IR absorption intensity for the ionized and unionized species.[14-15] The FTIR spectra revealed a systematic variation for PAH/PAA films thermally treated at 75, 150, 200, and 250 ºC for 1 h (under 20 in. Hg vacuum) (**Figure 5.1**).

In the 75 and 150 ºC films, the prominent peaks at 1560 and 1403 cm^{-1} are assigned to the carboxylate ($-COO^-$) asymmetric and symmetric stretching, corresponding to the ionized

(unprotonated) portions of the PAA polyelectrolyte. The peak located at 1720 cm^{-1} is assigned to the carbonyl absorption of the carboxylic acid (-COOH) groups, characteristic of the unionized (protonated) PAA polyelectrolyte segments.[3, 10, 13-14, 19]

In the 200 ºC film, the relative protonated –COOH peak intensity decreased and shifted from 1720 cm^{-1} to 1733 cm^{-1}. This is typical for amide formation and indicates a change of the hydrogen bonding.[3, 7, 10] The unprotonated $–COO^-$ peaks at 1560 cm^{-1} and 1403 cm^{-1} completely disappeared in the 200 ºC film spectrum, and were replaced by peaks at 1660 cm^{-1} and 1535 cm^{-1} that represent amide I and amide II peaks, respectively.[3, 7, 10, 13] The amide I peak is assigned to the primary and secondary vibrations that corresponded to the carbonyl (C=O) stretch (70-85%) and the amide (C-N) stretch (10-20%), respectively.[21] Similarly, the amide II is peak also composed of primary and secondary vibrations, which correspond to the amino (N-H) bending (40-60%) and the amide (C-N) stretch (18-40%), respectively.[21-22] The amide bonding chemical schematic is represented in **Figure 5.2**. These results provide confirmation of the covalent amide bond formation by thermal crosslinking between the two polyelectrolytes at this specific temperature and pH range.

The 250 ºC film showed the same general features as the 200 ºC film, although the amide peaks are far weaker. We suspect that at this temperature, the decomposition process of the polyelectrolyte film has begun. This may be specific to the film formation conditions used here, given that other reports show that this temperature is suitable for crosslinking and amide formation.[10-11]

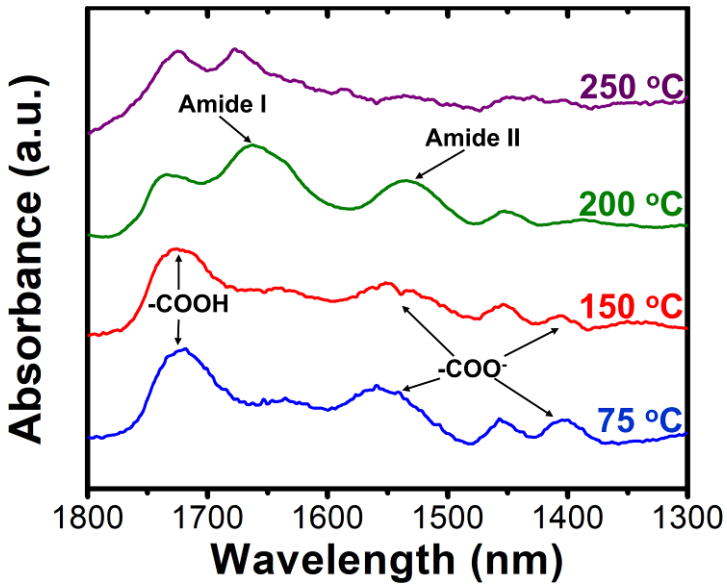

Figure 5.1. FTIR spectra for two-bilayer $PAH_{7.5}/PAA_{4.5}$ films on Au substrates.

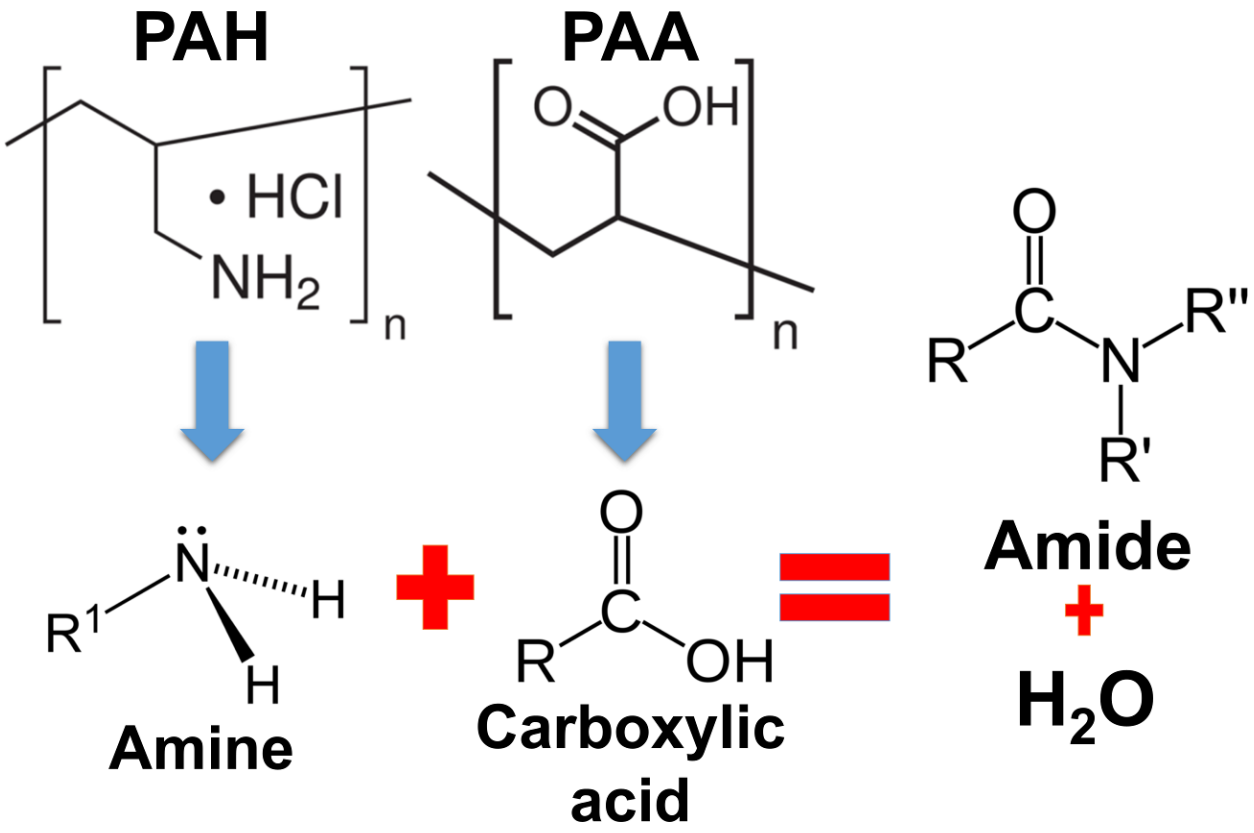

Figure 5.2. Amide bonding chemical schematic.

5.3.2 PAH/PAA Diffusion and Exponential-growth. Exponential-growth in polyelectrolyte films relies on the diffusion of lowly-charged, free polymer chains.[18-19, 23-27] The exponential-growth was evaluated for PAH/PAA multilayers, by a variation of the PAA pH. The pH of PAH was maintained at a value of 7.0, identical to the conditions for the interlayer ISAM ARCs. $PAH_{7.0}$ is reported as approximately 80% and 92% ionized in solution and in a multilayer film, respectively.[14] The PAH chains at this pH are virtually absent of free diffusing chains with a tight, rigid conformation to the previous layer.[5, 15, 18, 27] The determination of the PAH/PAA multilayer film thicknesses at various PAA pH's was achieved through ellipsometry using a Cauchy dispersion model. The model took into account the transparent Cauchy layer, the thin native silicon oxide layer, and the silicon substrate. The Cauchy dispersion model was represented as

$$n\,(\lambda) = A + \frac{B}{\lambda^2} + \frac{C}{\lambda^4} \qquad \textbf{(5.1)}$$

where A, B, and C are fit parameters, determined by the software. The model determined optical constants of A = 1.5373 and B = 0.0053271 while a value C = 0 was kept constant in the fit. The model thus provided a relationship between the refractive index and wavelength (**Figure 5.3**). More details about ellipsometry methods can be found in the **Chapter 3**. The range of $PAA_{3.0}$ to $PAA_{6.0}$ was specifically examined to understand growth at a low and high PAA charge density. The PAA pH was varied coarsely from $PAA_{3.0}$ to $PAA_{6.0}$ and finely from $PAA_{5.0}$ to $PAA_{6.0}$, each with a set of one through five PAH/PAA bilayers for thickness measurements (**Figure 5.4a** and **5.4b**). Along with the thickness, the PAH/PAA multilayer RMS surface roughness was measured through profilometry for the same films (**Figure 5.4c** and **5.4d**). All of the exponential-growth thickness curves were modeled (with Origin Pro software) by a single-term exponential function as

$$y = y_0 + ae^{bx} \qquad \textbf{(5.2)}$$

where a is the growth factor, b is the growth constant, and x is the number of bilayers (**Table 5.1**). A coefficient of determination (R^2) was also reported with the model parameters, which signified how well the growth characteristics fit a single exponential. From $PAA_{6.0}$ to $PAA_{3.0}$, the PAH/PAA multilayer growth shifted from linear to exponential. The primary crossover from linear to exponential-growth occurred near $PAA_{5.4}$. At $PAA_{5.2}$, the exponential-growth became even more pronounced and continued to increase to $PAA_{4.0}$. As the exponential-growth characteristics increased, the multilayers became more interpenetrated, but the high levels of ionic crosslinking were diminished due to the protonation of PAA.[15, 18] The overall increased exponential slope with a decreased PAA pH confirmed a reduction in the charge density of the PAA chains, along with an increase in the concentration of free, diffusing chains. At a higher number of bilayers (10-20) for the range of $PAA_{5.0}$ to $PAA_{6.0}$ (**Figure 5.5**), the growth eventually shifted from exponential to linear, which has been previously reported to occur at increased film thicknesses due to a saturation in the concentration of free diffusing chains necessary for exponential-growth.[23, 26]

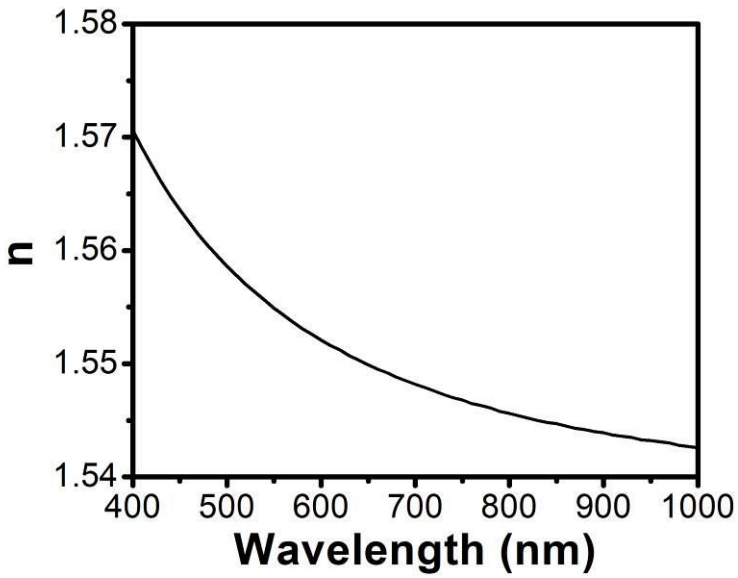

Figure 5.3. PAH/PAA refractive index vs. wavelength. Based on Cauchy dispersion model with A = 1.5373, B = 0.0053271, and C = 0.

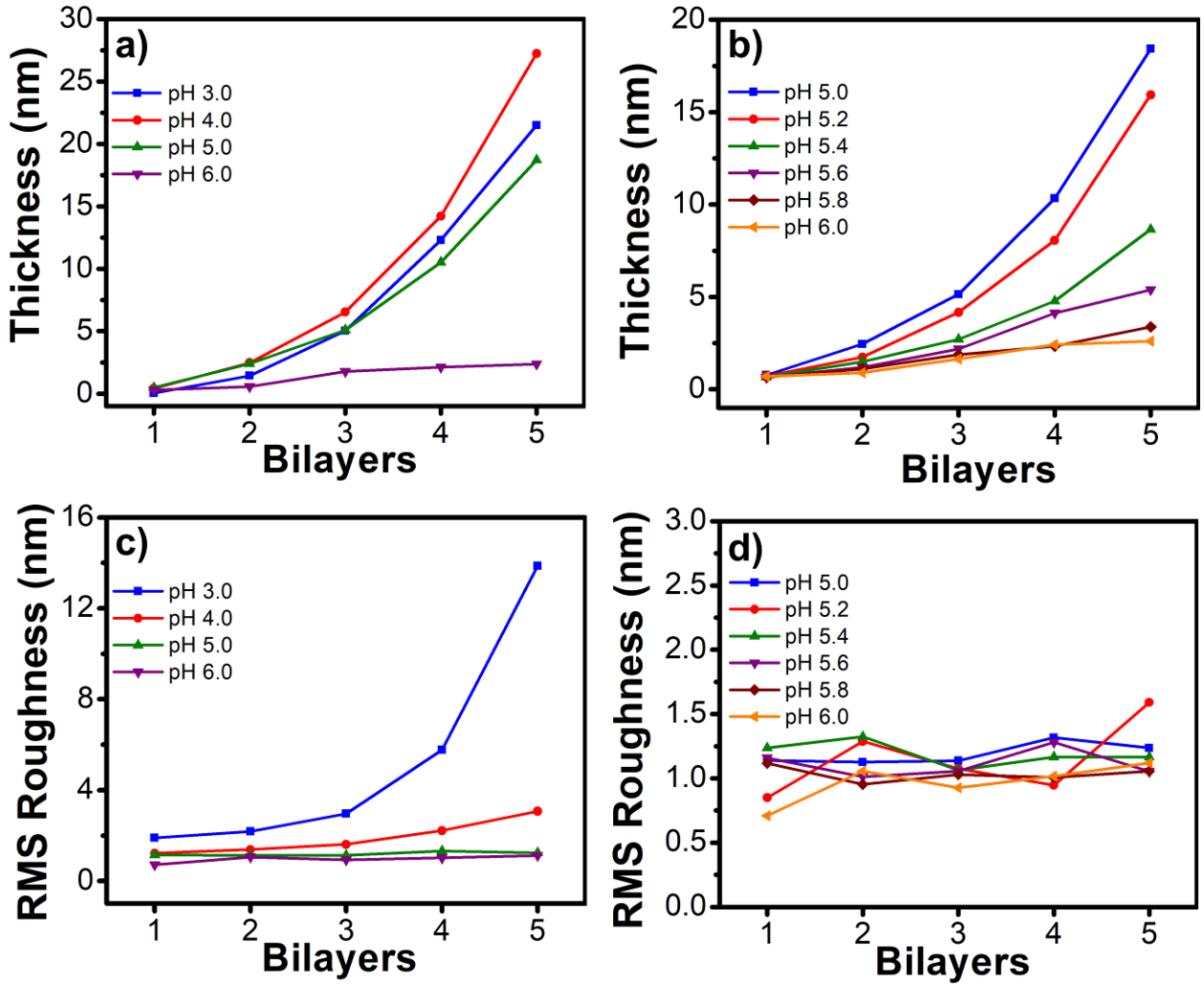

Figure 5.4. Thickness measurements for one to five bilayers of $PAH_{7.0}/PAA_x$ films with (**a**) $PAA_{3.0}$ to $PAA_{6.0}$ and (**b**) $PAA_{5.0}$ to $PAA_{6.0}$. RMS surface roughness measurements for one to five bilayers of $PAH_{7.0}/PAA_x$ films for (**c**) $PAA_{3.0}$ to $PAA_{6.0}$ and (**d**) $PAA_{5.0}$ to $PAA_{6.0}$.

Table 5.1. Exponential-growth constants of **Equation 5.2** for $PAH_{7.0}/PAA_x$ films with the PAA pH (x) range from 3.0 to 6.0.

PAA pH	y_0	a	b	R^2
3.0	-3.80	2.07	**0.50**	**0.993**
4.0	-2.56	1.59	**0.59**	**0.999**
5.0	-2.24	1.63	**0.51**	**0.999**
5.2	-1.17	0.78	**0.62**	**0.999**
5.4	-1.04	0.89	**0.47**	**0.998**
5.6	-3.87	3.17	**0.22**	**0.977**
5.8	-3.04	2.93	**0.15**	**0.975**
6.0	4.33	-5.10	**-0.20**	**0.878**

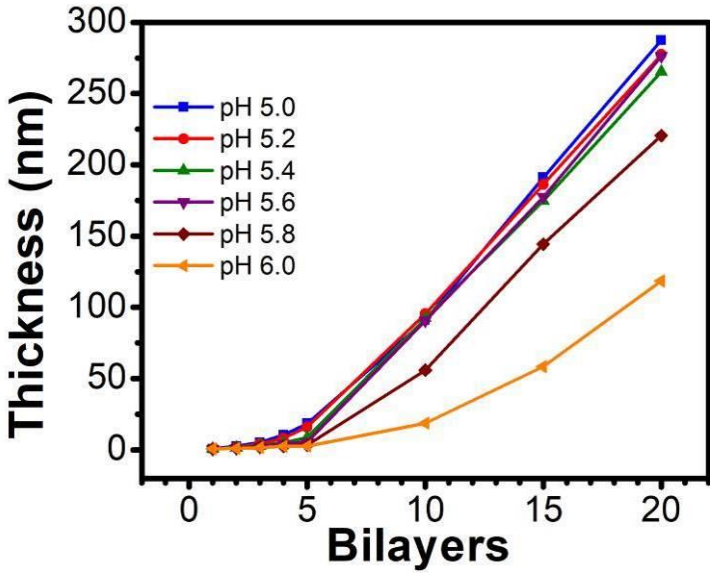

Figure 5.5. Thickness measurements for one to twenty bilayers of $PAH_{7.0}/PAA_x$ films with $PAA_{5.0}$ to $PAA_{6.0}$.

5.3.3 Interlayer SEM Characterization. Interlayer ISAM ARCs were formed with the repeating configuration of PAH/PAA/PAH/SiO_2 NPs quadlayers. The architecture of the films was designed to incorporate the anti-reflection effects from the porous silica nanoparticle matrix, while combining the mechanical stabilization effects of the crosslinking polymers. It is well established that polyelectrolyte multilayer assemblies are initially structured as islands for small numbers of bilayers rather than uniform lattices, due to material charge repulsion.[24-26] Here, the interlayer ISAM ARCs were composed of SiO_2 NP islands, encapsulated by PAH/PAA polyelectrolyte chains as schematically illustrated in **Figure 5.6**.

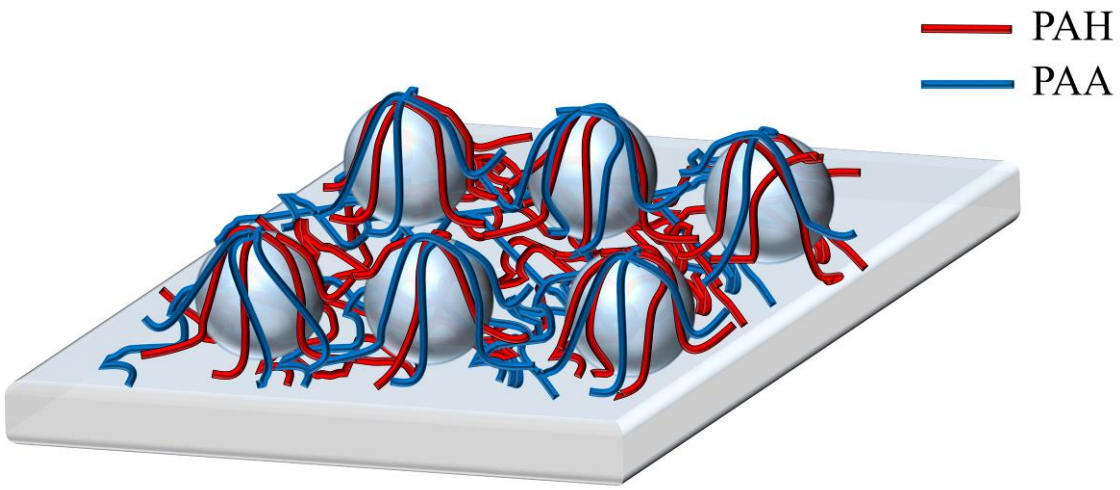

Figure 5.6. Interlayer ISAM ARC architectural schematic.

Interlayer ISAM ARCs of four quadlayers or $[PAH_{7.0}/PAA_x/PAH_{7.0}/SiO_{2\ 9.0}]_{n=4.5}$ (PAA as the last layer) were constructed for $PAA_{3.0}$, $PAA_{4.0}$, $PAA_{5.0}$, and $PAA_{6.0}$ and examined under SEM (**Figure 5.7a-d**).

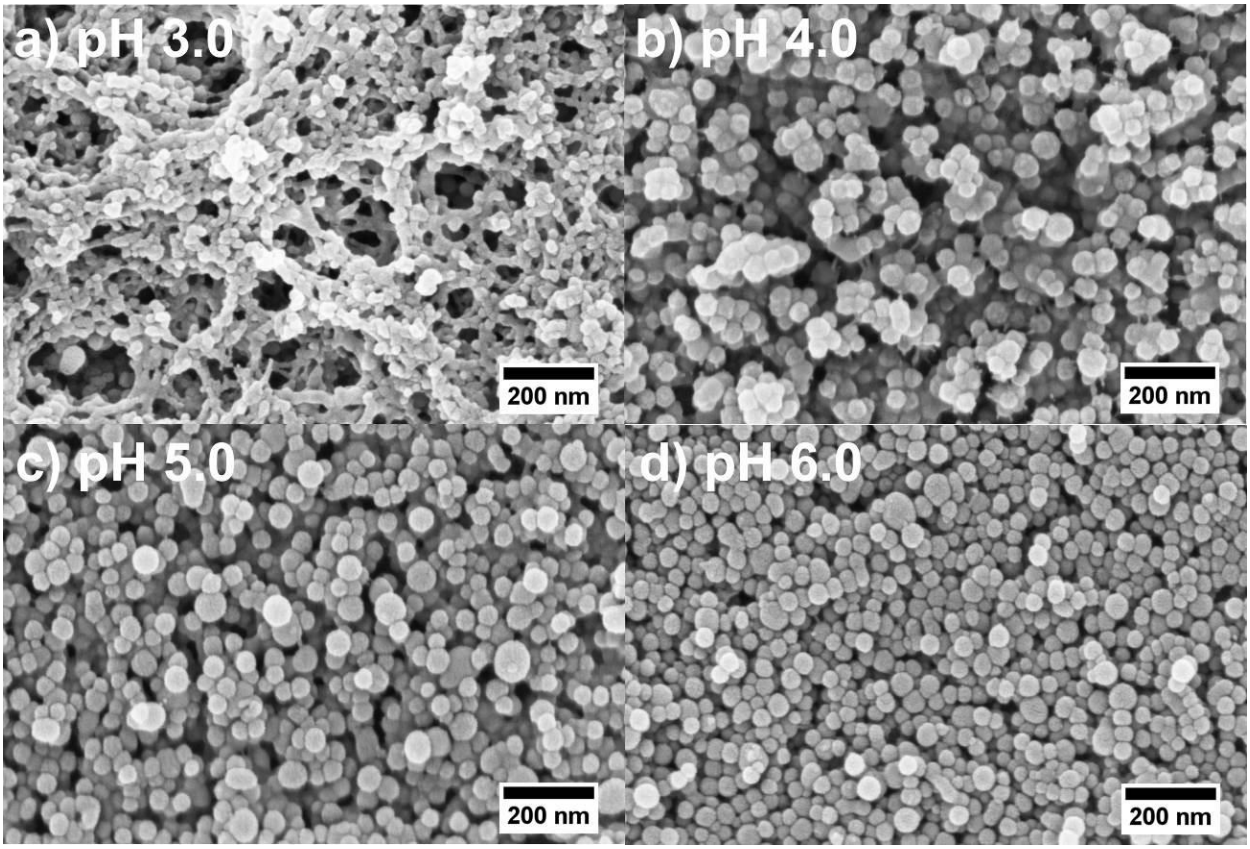

Figure 5.7. SEM characterization at 200 kX magnification for four-quadlayer interlayer ISAM ARCs of the architecture $[PAH_7/PAA_x/PAH_7/SiO_{2\ 9}]_{n=4.5}$, where PAA pH was varied from (**a**) $PAA_{3.0}$, (**b**) $PAA_{4.0}$, (**c**) $PAA_{5.0}$, and (**d**) $PAA_{6.0}$. All films were thermally crosslinked at 200 ºC for 2 h under 20 in. Hg vacuum.

For interlayer ISAM ARCs with $PAA_{6.0}$, the surface looks nearly identical to PAH/SiO_2 NP films created previously by our group, and the MSNP/PSS films in **Chapter 4**.[2, 28] Due to the tightly-bound, highly-charged nature of the encapsulating polyelectrolytes, their small thickness rendered them invisible by SEM, and the RCP structured SiO_2 NPs dominated the composition of the film. The minimal polyelectrolyte thickness correlated with the PAH/PAA multilayers at $PAA_{6.0}$ (**Figure 5.4a**). Furthermore, the SiO_2 NPs structure was highly homogeneous with a lack of agglomeration. While the SiO_2 NPs network was contiguous in the four-quadlayer interlayer

ISAM ARCs for the $PAA_{6.0}$, examination of the first quadlayer (**Figure 5.8**) showed segregated island formations, characteristic of ISAM growth.

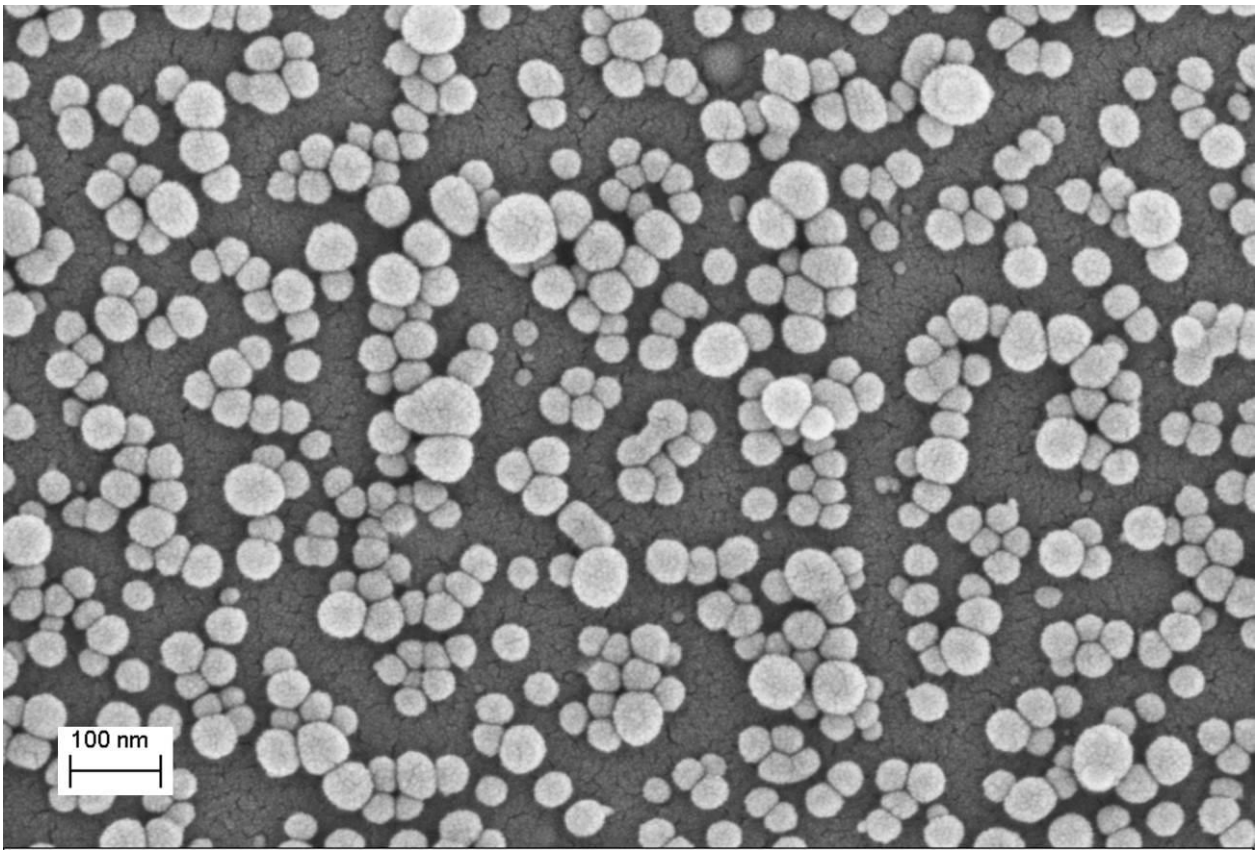

Figure 5.8. SEM characterization for a 1-quadlayer $[PAH_7/PAA_6/PAH_7/SiO_{2\ 9}]_{n=1.5}$ film at a magnification of 200 kX. This film was thermally crosslinked at 200 ºC for 2 h under 20 in. Hg vacuum.

For interlayer ISAM ARCs with $PAA_{5.0}$, the observed morphology was fairly similar to that for $PAA_{6.0}$, however, increased encapsulating polyelectrolyte thickness became apparent. The larger polyelectrolyte thickness can be distinguished by a slight globular background, and the presence of a few polyelectrolyte branches that connect some encapsulated NPs. Additionally, the SiO_2 matrix was clearly less contiguous and visibly more rough, which was attributed to the larger repulsions between neighboring polyelectrolyte encapsulations. Since $PAA_{5.0}$ showed

exponential-growth in the PAH/PAA multilayers (**Figure 5.4a**), the increased polyelectrolyte thickness was associated with a greater concentration of free, diffusing polymer chains during ISAM growth. A similar study provided strong evidence of PAA diffusion through montmorillonite layers in PEI/PAA/PEI/ Na+-montmorillonite (MTM) self-assembled interlayers. [29] Therefore, we are confident that the SiO_2 NP matrix allowed for free PAA chain diffusion within the interlayer ISAM ARCs.

Due to a greater level of free chains for $PAA_{4.0}$ in interlayer ISAM ARCs, the encapsulating polyelectrolyte thickness increased, and the number of polyelectrolyte branches became more prominent. The encapsulated SiO_2 NPs developed into more defined clusters and agglomerates. The SiO_2 NP agglomerations were again attributed to increased repulsion between larger polyelectrolyte encapsulations, but also due to increased roughness of $PAA_{4.0}$ in PAH/PAA multilayers (**Figure 5.4c**).

For interlayer ISAM ARCs with $PAA_{3.0}$, the resultant surface morphology was quite striking, as a web-like polyelectrolyte network morphology covered the film. The morphology for the $PAA_{3.0}$ films was characteristic of microporous formations, which are reported extensively in the literature.[4, 6, 17, 19, 30] Here, the formations only partially covered the film surface area (**Figure 5.9a** and **5.9d**), and many areas of the $PAA_{3.0}$ films appeared similar to the $PAA_{4.0}$ films. We associated the large microporous formations with 1) a substantial increase in polyelectrolyte thickness, due to heightened level of free, diffusing chains, and 2) the agglomeration of polyelectrolytes attributed to the severing of PAH/PAA ionic linkages in the film. This a result of the PAA pH being far below the pK_a in solution. Opposed to the relatively small agglomerates found in films with $PAA_{4.0}$, the microporous formations act as large-scale agglomerates, which clearly increased the roughness, also shown in the PAH/PAA multilayers (**Figure 5.4c**).

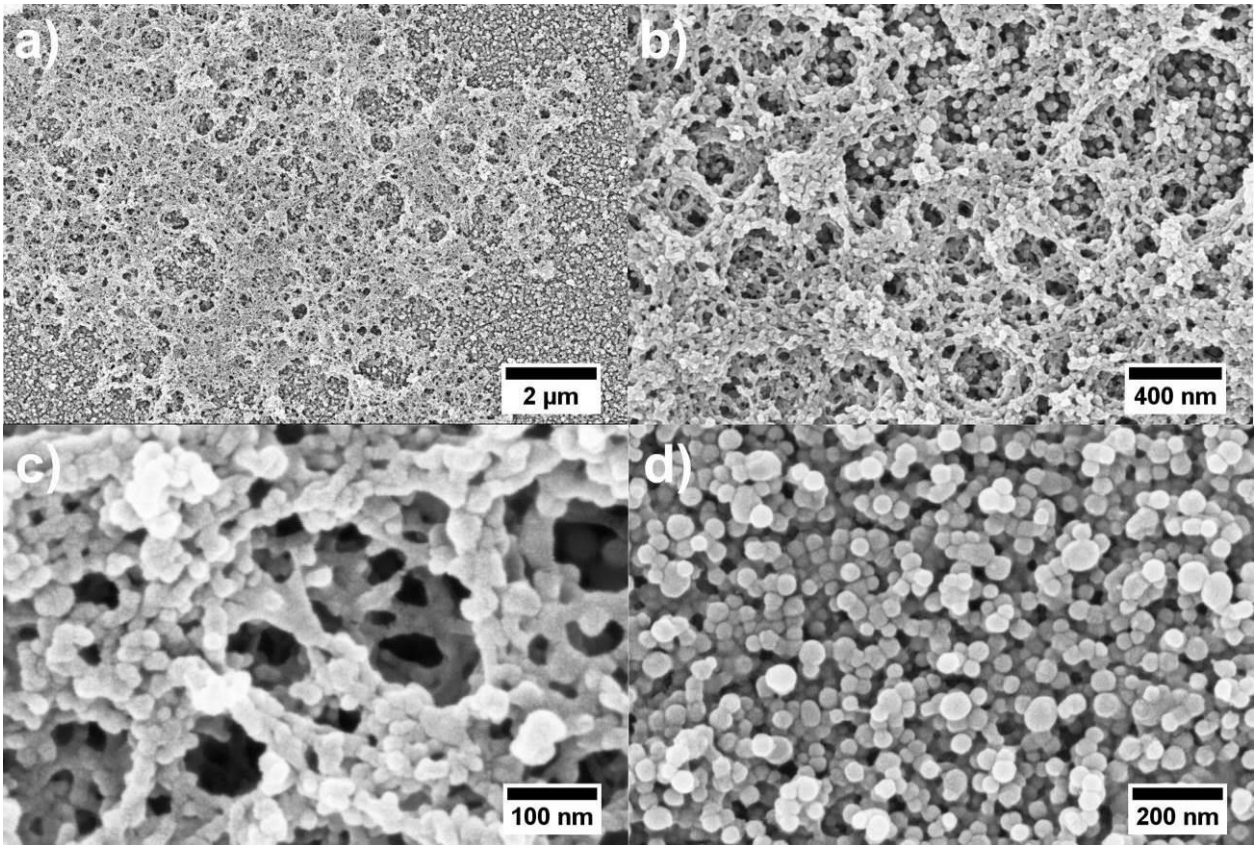

Figure 5.9. SEM characterization for four quadlayer interlayer ISAM ARCs with $PAA_{3.0}$, focused on the microporous formation for magnifications of (**a**) 20 kX, (**b**) 100 kX, (**c**) 400 kX. Images were also taken on regions without the microporous formations in the film at (**d**) 200 kX. All films were thermally crosslinked at 200 ºC for 2 h under 20 in. Hg vacuum.

5.3.4 Interlayer UV-vis-IR Spectra. The establishment of optical destructive interference fringes of the reflected incident light is the fundamental property of the ARCs. The wavelength maxima for destructive interference are proportional to the thickness of the nanoparticle-containing films, as discussed in **Chapter 4**. The film thickness is a simple parameter to adjust, due to its proportionality to the number of deposited layers. In this study, interlayer films of four quadlayers or $[PAH_{7.0}/PAA_x/PAH_{7.0}/SiO_{2\ 9.0}]_{n=4.5}$ (PAA as the last layer) were used, as those films provided anti-reflection in the visible wavelength range. The pH was varied from $PAA_{3.0}$ to $PAA_{6.0}$

(incremented by 1.0) for the four-quadlayer films to examine the effects of low and high polyelectrolyte charge density, respectively. After the four-quadlayer films were thermally crosslinked at 200 ºC for 2 h, the transmittance and reflectance were measured (**Figure 5.10a-b**). The transmittance and reflectance spectra were also compared to bare glass. The absorption due to scattering (A_s) spectra was calculated according to

$$A_s(\lambda) = -\log(\frac{T(\lambda)}{1-R(\lambda)}) \quad (\mathbf{5.3})$$

where T is the transmission percentage and R is the reflectance percentage at a specific wavelength. Since both the polyelectrolytes and SiO_2 NPs are non-absorbing in the wavelength range considered, the optical loss and the A_s slope was attributed purely to scattering. Therefore, A_s is proportional to the scattering cross-section through

$$A_s(\lambda) = Cl\sigma_s(\lambda) \quad (\mathbf{5.4})$$

where C is the concentration, l is the path length, and σ_s is the scattering cross-section. The A_s slope of the interlayer ISAM ARCs displayed a linear dependence on the inverse wavelength to the fourth power (λ^{-4}), characteristic of Rayleigh scattering. The A_s spectra were calculated as a function of the PAA pH for the four-quadlayer interlayer ISAM ARCs (**Figure 5.10c**) (**Table 5.2**).

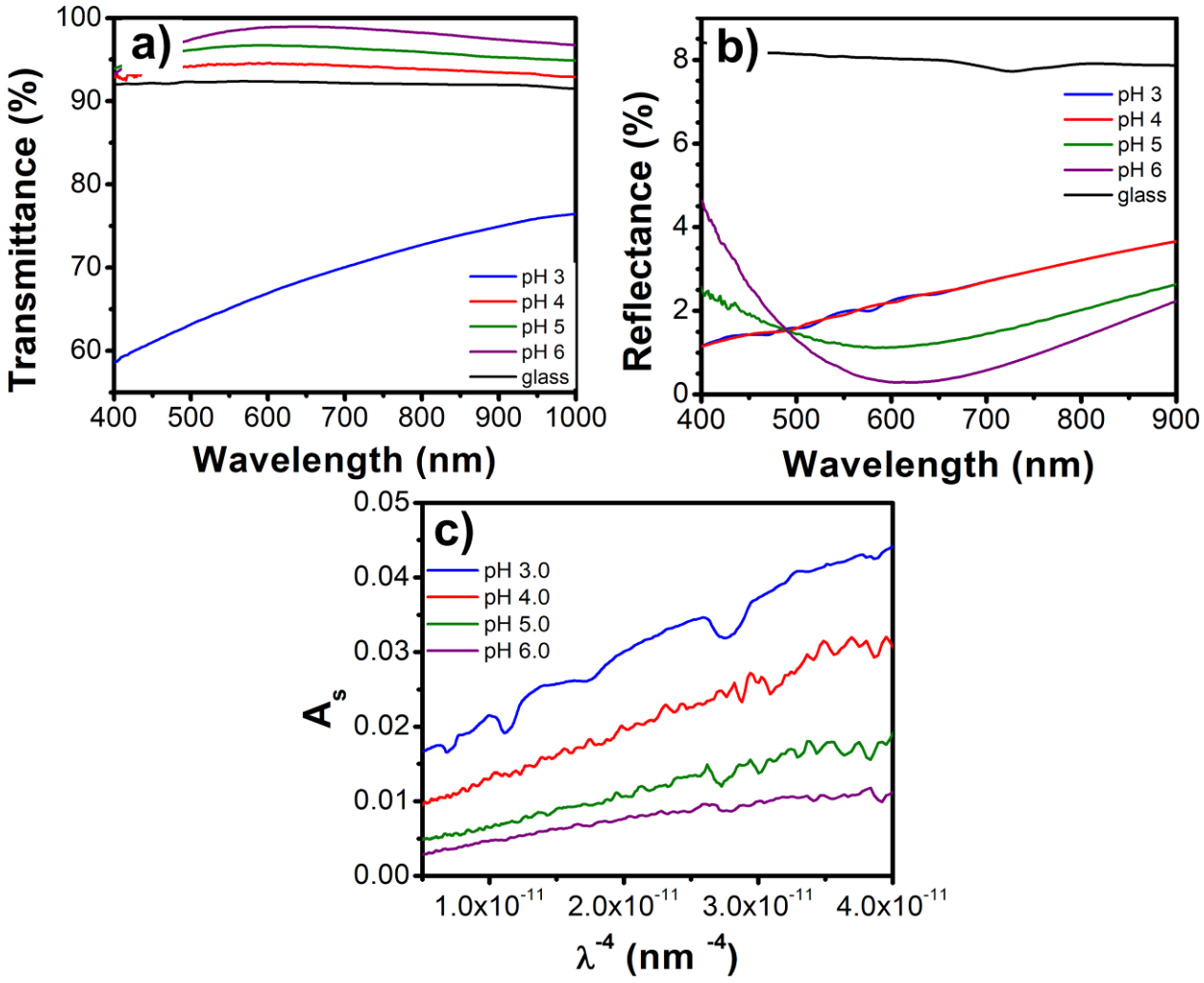

Figure 5.10. Measurements of (**a**) transmittance, (**b**) reflectance, (**c**) absorption due to scattering (A_s) for four-quadlayer interlayer ISAM ARCs with PAA pH varied from $PAA_{3.0}$ to $PAA_{6.0}$ by increments of 1.0. All of the films were thermally crosslinked at 200 ^{o}C for 2 h under 20 in. Hg vacuum.

Table 5.2. Optical and physical properties for the four-quadlayer interlayer ISAM ARCs. All values are averaged for at least 3 samples. Refractive indices are represented for three- and four-quadlayers, averaged for at least 3 samples.

Interlayer PAA pH	Transmittance Maxima (%)	Reflectance Minima (%)	n	A_s Slope	RMS Roughness (nm)
Glass	92.62 ± 0.17	8.40 ± 0.48	-	-	-
3.0	83.88 ± 9.61	0.95 ± 0.44	1.42 ± 0.21	(2.36 ± 1.18) x 10^9	73.22 ± 18.56
4.0	95.39 ± 0.80	1.22 ± 0.94	1.19 ± 0.07	(6.07 ± 0.32) x 10^8	11.05 ± 1.28
5.0	96.95 ± 0.09	1.09 ± 0.02	1.17 ± 0.13	(4.31 ± 0.65) x 10^8	5.28 ± 0.37
5.2	99.22 ± 0.29	0.06 ± 0.01	1.18 ± 0.06	(3.83 ± 1.13) x 10^8	5.74 ± 0.18
5.4	99.08 ± 0.28	0.03 ± 0.01	1.22 ± 0.06	(3.20 ± 0.87) x 10^8	4.64 ± 0.36
5.6	99.10 ± 0.21	0.05 ± 0.05	1.33 ± 0.10	(3.38 ± 1.12) x 10^8	5.06 ± 0.33
5.8	98.96 ± 0.22	0.15 ± 0.02	1.33 ± 0.03	(2.39 ± 0.78) x 10^8	4.35 ± 0.16
6.0	99.10 ± 0.12	0.26 ± 0.16	1.35 ± 0.05	(2.54 ± 1.21) x 10^8	5.17 ± 0.08

Transmittance and reflectance spectra were also measured for films composed of one- to three-quadlayers after crosslinking for the same PAA pH range (**Figure 5.11a-f**). The transmittance maxima and the reflectance minima peak magnitudes (%) were then averaged for interlayer ISAM ARC films with peak anti-reflection in the visible wavelength range (**Table 5.2**). For interlayer ISAM ARCs with $PAA_{6.0}$, the average transmittance maxima and reflectance minima levels were 99.10% and 0.26%, respectively. A decrease of the PAA pH to $PAA_{5.0}$, $PAA_{4.0}$, and $PAA_{3.0}$ degraded the films' average transmittance to 96.95%, 95.39%, and 83.88%, respectively. The average reflectance values dramatically increased with decreased PAA pH; at $PAA_{5.0}$, $PAA_{4.0}$, and $PAA_{3.0}$, the average reflectance was 1.09%, 1.22%, 0.95%. The reflection minima of $PAA_{3.0}$ and

$PAA_{4.0}$ blue-shifted into the UV range as a result of large degrees of optical scattering. The films' average A_s slope increased with a decrease in PAA pH from $PAA_{6.0}$ to $PAA_{3.0}$. Specifically, films with $PAA_{6.0}$ and $PAA_{3.0}$ had an average A_s slope of 2.54×10^8 and 2.36×10^9, respectively, which was nearly a factor of 10 increase in the scattering.

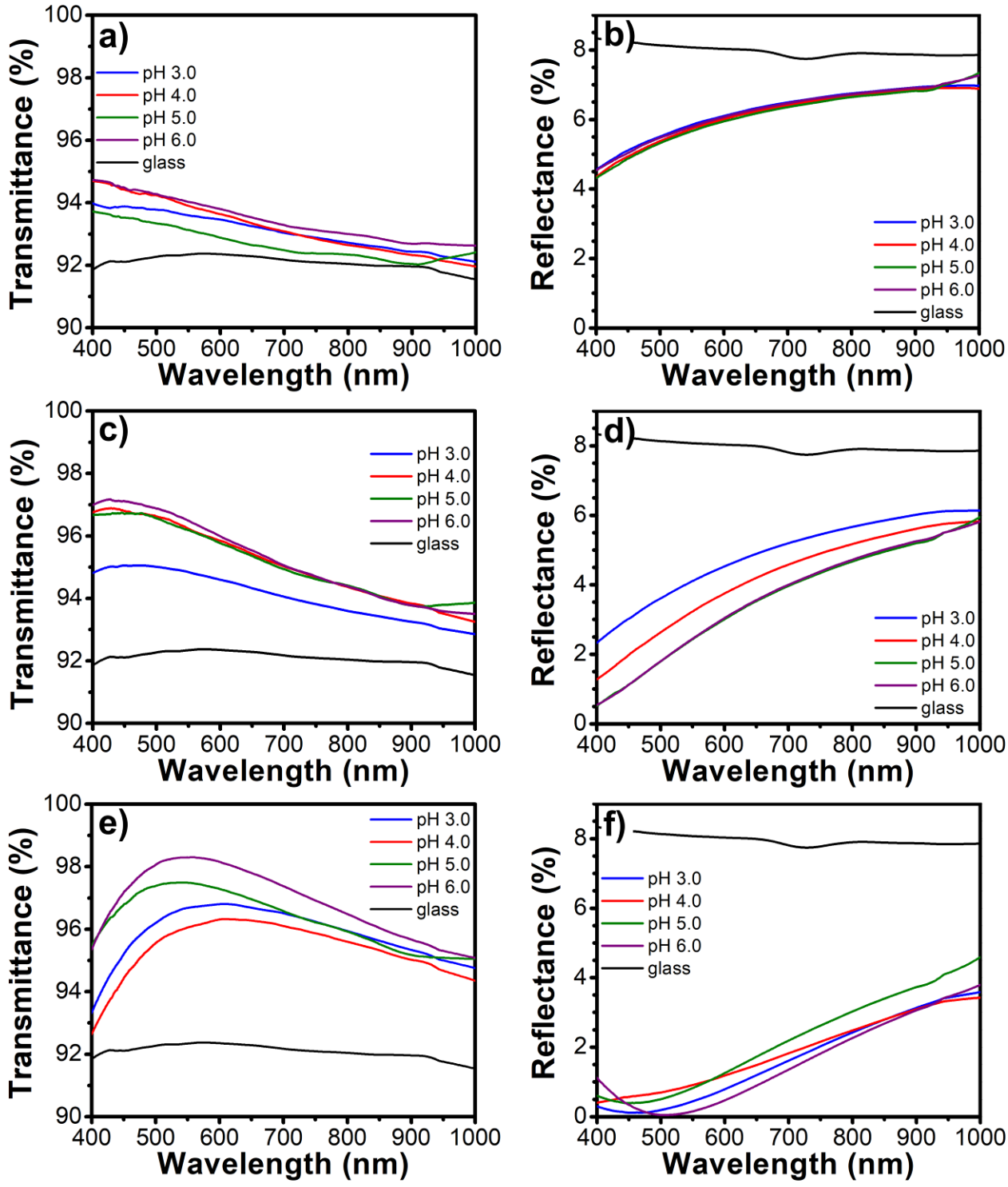

Figure 5.11. Measurements of (**a**) one-quadlayer transmittance, (**b**) one-quadlayer reflectance, (**c**) two-quadlayer transmittance, (**d**) two-quadlayer reflectance, (**e**) three-quadlayer transmittance, (**f**) three-quadlayer reflectance for interlayer ISAM ARCs with PAA pH varied from $PAA_{3.0}$ to $PAA_{6.0}$

by increments of 1.0. All of the films were thermally crosslinked at 200 ºC for 2 h under 20 in. Hg vacuum.

Since the anti-reflection shifted from excellent (transmittance ≥99%) at $PAA_{6.0}$ to fair at $PAA_{5.0}$, four-quadlayer interlayer ISAM ARCs were constructed with PAA pH from $PAA_{5.0}$ to $PAA_{6.0}$ with 0.2 pH increments, in order to pinpoint the critical PAA pH. After thermal crosslinking of the films with PAA pH between $PAA_{5.0}$ to $PAA_{6.0}$, the transmittance and reflectance was measured, and A_s was calculated (**Figure 5.12a-c**). The peak transmittance maxima and reflectance minima were again averaged for all four-quadlayer interlayer ISAM ARCs (**Table 5.2**). For this PAA pH range, one to three quadlayers films were also fabricated, and the transmittance and reflectance was measured (**Figure 5.13a-f**). As the pH was decreased from $PAA_{6.0}$ to $PAA_{5.2}$, the films' transmittance stayed consistent, and then drastically degraded at $PAA_{5.0}$. The average reflectance values decreased by a factor of 5 from $PAA_{6.0}$ to $PAA_{5.6}$, remained mostly consistent from $PAA_{5.6}$ to $PAA_{5.2}$. From $PAA_{5.2}$ to $PAA_{5.0}$, the average reflectance substantially increased by nearly a factor of 18. The average A_s slope values were relatively similar for $PAA_{6.0}$ and $PAA_{5.8}$, and then increased by 41% to $PAA_{5.6}$ and mostly plateaued to $PAA_{5.2}$. From $PAA_{5.2}$ to $PAA_{5.0}$, the average A_s slope increased by 13%.

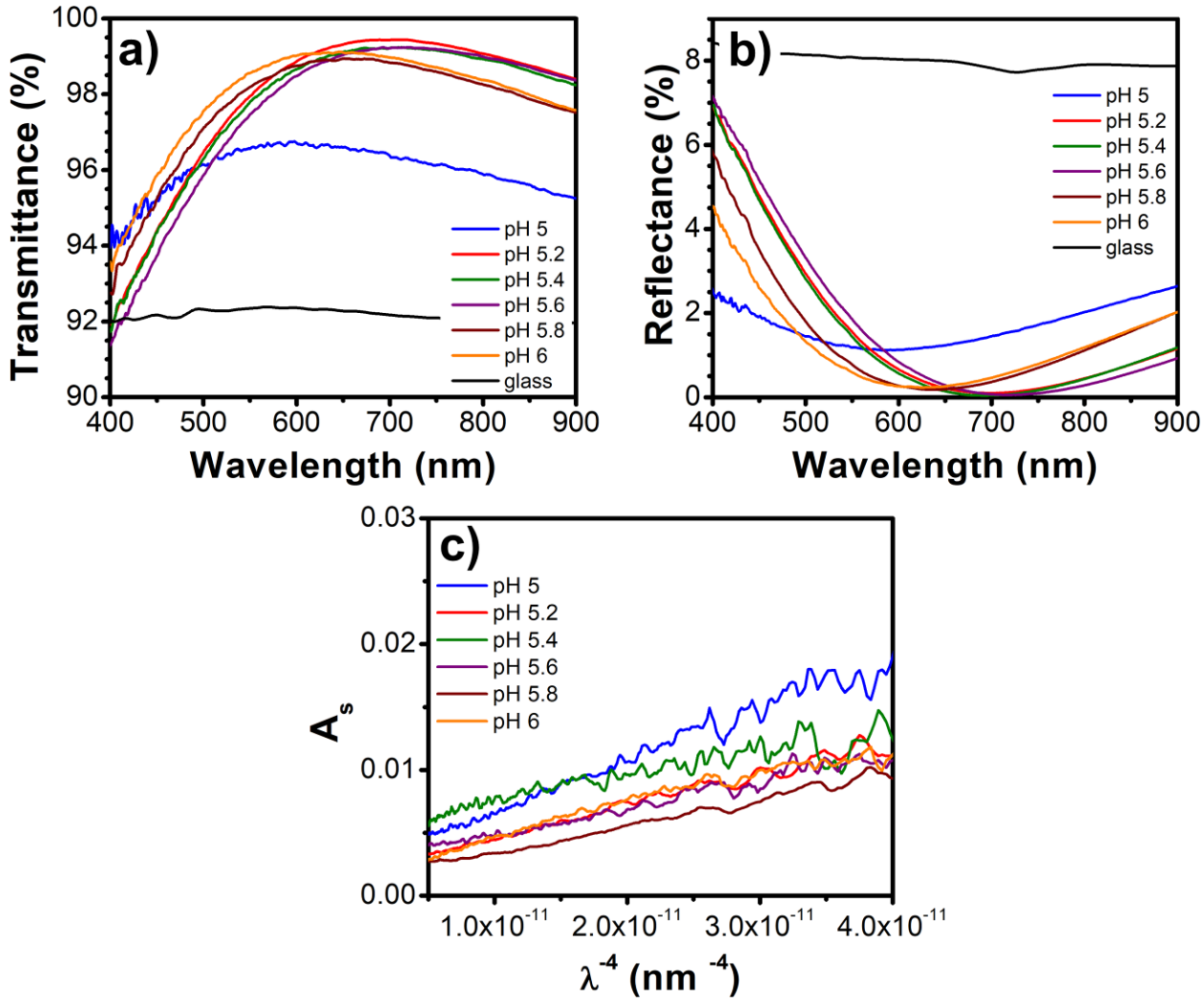

Figure 5.12. Measurements of (**a**) transmittance, (**b**) reflectance, and (**c**) absorbance due to scattering (A_s) for four-quadlayer interlayer ISAM ARCs with PAA pH varied from $PAA_{5.0}$ to $PAA_{6.0}$ by increments of 0.2. All of the films were thermally crosslinked at 200 ºC for 2 h under 20 in. Hg vacuum.

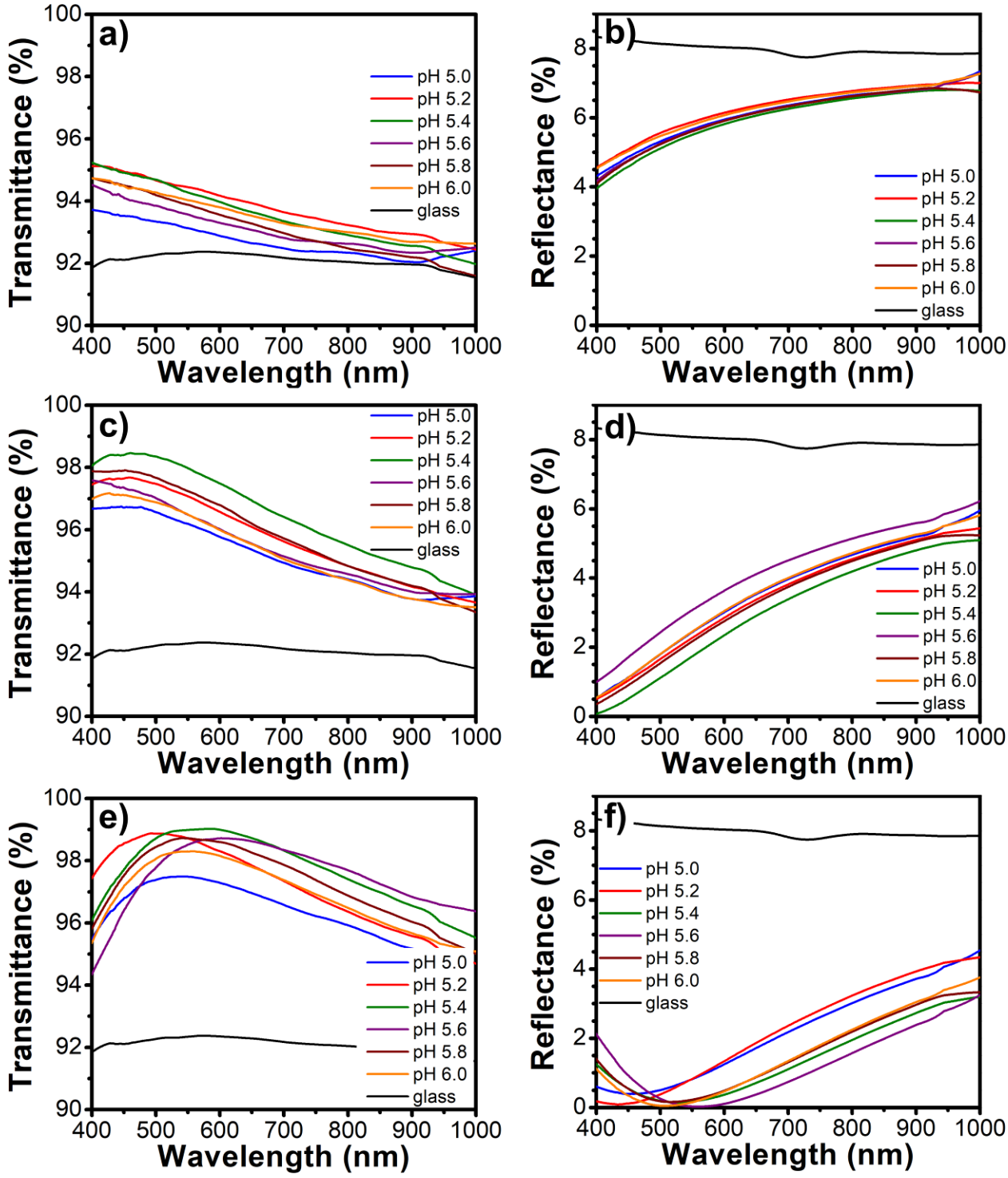

Figure 5.13. Measurements of (**a**) one-quadlayer transmittance, (**b**) one-quadlayer reflectance, (**c**) two-quadlayer transmittance, (**d**) two-quadlayer reflectance, (**e**) three-quadlayer transmittance, (**f**) three-quadlayer reflectance for interlayer ISAM ARCs with PAA pH varied from $PAA_{5.0}$ to $PAA_{6.0}$

by increments of 0.2. All of the films were thermally crosslinked at 200 °C for 2 h under 20 in. Hg vacuum.

The refractive index (n) of the interlayer ISAM ARCs was calculated using the destructive interference relationship represented by

$$(m - 0.5)\lambda = 2nd; \quad m = 1, 2, 3 \ldots \tag{5.5}$$

where m is the interference order, λ is the wavelength, n is the refractive index, and d is the physical thickness. The refractive indices were calculated and averaged from both the transmittance maxima and reflectance minima spectra for the interlayer ISAM ARCs with three- and four-quadlayers (**Figure 5.14** and **Table 5.2**). The average refractive index was 1.43 for the interlayer ISAM ARC with $PAA_{3.0}$, and with an increase of PAA pH from $PAA_{4.0}$ to $PAA_{5.2}$, the average refractive index dropped substantially and plateaued approximately at 1.18. At a PAA pH to $PAA_{5.4}$, the average refractive of the films increased to 1.22. With a further increase of the PAA pH in the range of $PAA_{5.6}$ to $PAA_{6.0}$, the average refractive index increased and plateaued again at approximately 1.34.

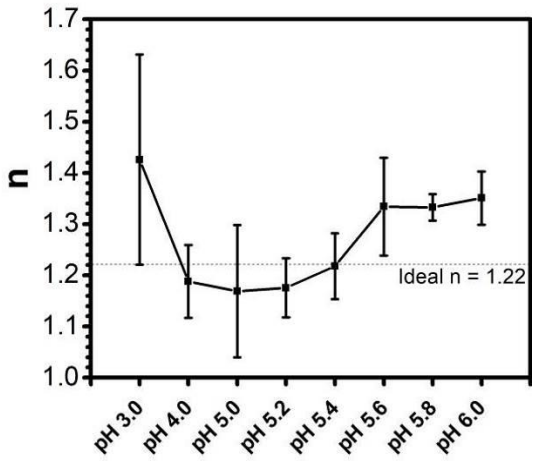

Figure 5.14. Refractive index for three- and four-quadlayer interlayer ISAM ARCs from $PAA_{6.0}$ to $PAA_{3.0}$. The error bars represent the standard deviation.

Along with the optical properties of the interlayer ISAM ARCs, the thickness and RMS roughness values were measured for all films (one to four quadlayers) using profilometry (**Figure 5.15a-d**). The interlayer ISAM ARC average thickness was constant with a change in the PAA pH as the thickness is primarily determined by the SiO_2 NPs. The RMS roughness values were averaged for the four-quadlayer films (**Table 5.2**). The average RMS roughness was statistically unchanged from $PAA_{6.0}$ to $PAA_{5.0}$, and then dramatically increased at $PAA_{4.0}$, and again at $PAA_{3.0}$. From $PAA_{6.0}$ to $PAA_{3.0}$, the average RMS roughness increased by a factor of 14.

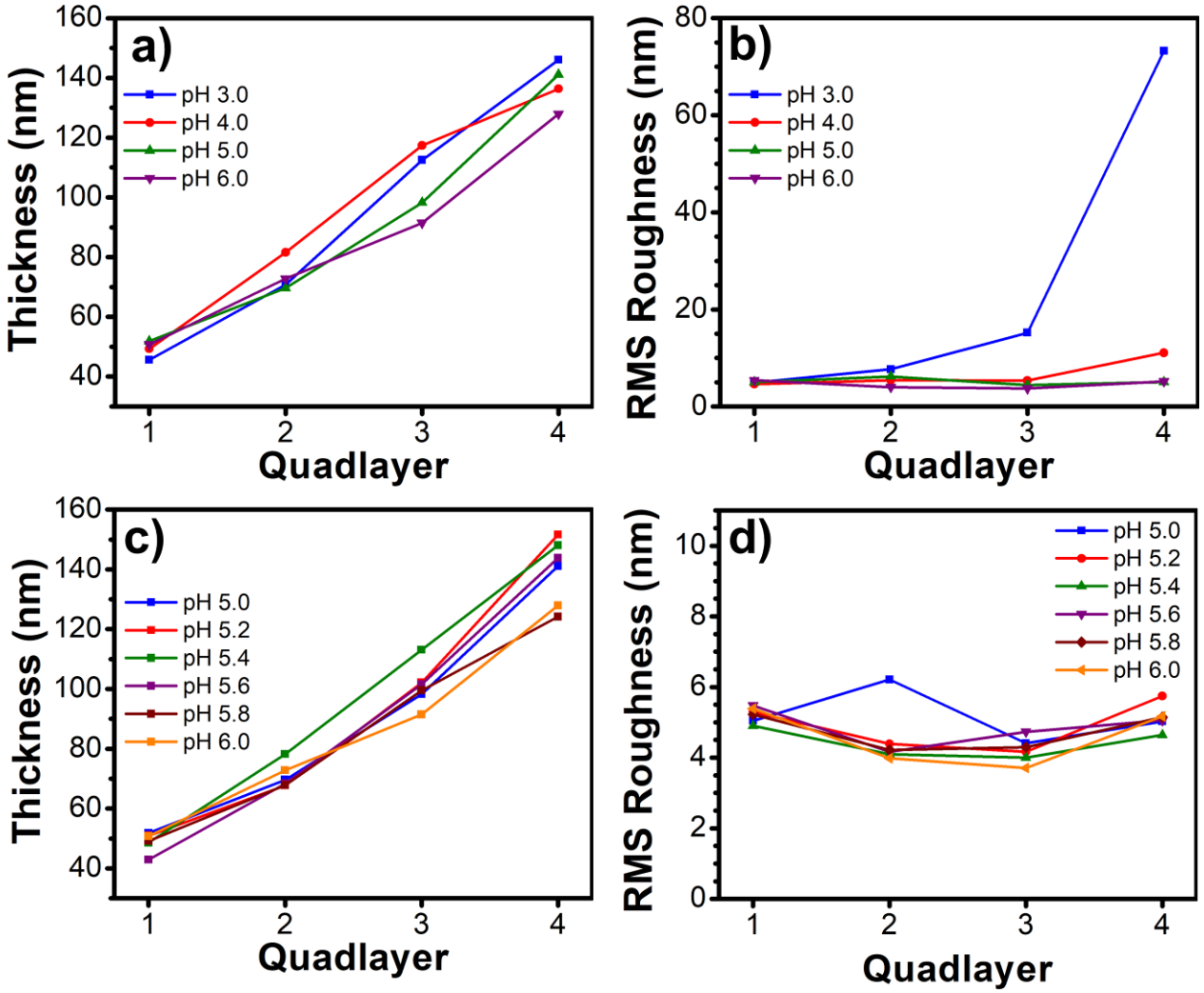

Figure 5.15. Thickness measurements for one- to four-quadlayer interlayer ISAM ARCs with PAA pH in the range of (**a**) $PAA_{3.0}$ to $PAA_{6.0}$ and (**c**) $PAA_{5.0}$ to $PAA_{6.0}$. RMS roughness measurements for one- to four-quadlayer interlayer ISAM ARCs with PAA pH in the range of (**b**) $PAA_{3.0}$ to $PAA_{6.0}$ and (**d**) $PAA_{5.0}$ to $PAA_{6.0}$.

The consistency of the interlayer ISAM ARC thickness in the range of $PAA_{3.0}$ to $PAA_{6.0}$ illustrated that a change in PAA pH did not have a significant effect on the overall thickness of the films. Exponential-growth was not seen in the interlayer thickness measurements primarily because the bulk of the film thickness was determined by the diameter of the SiO_2 NPs. As discovered by the SEM images, the change in the PAA pH simply increased the polyelectrolyte thickness between SiO_2 NPs and changed the morphology of the encapsulated SiO_2 NP islands (**Figure 5.7a-d**).

The correlation between interfacial surface roughness and optical scattering loss has been widely established.[31-32] Clearly, the heightened roughness directly correlated to a rise in the A_s slope for the interlayer ISAM ARCs. In the SEM images, the larger roughness was apparent from $PAA_{5.0}$ to $PAA_{4.0}$ due to greater size of the SiO_2 NP encapsulations. At $PAA_{3.0}$, the roughness increased even more dramatically with the presence of the large microporous formations. Additionally, the increased cloudiness of the films confirmed the presence of optical scattering.

The variable refractive index of the interlayer ISAM ARCs was correlated to the change in void space of the SiO_2 NPs RCP structure and the thickness of the polyelectrolytes. At the higher PAA pH values of $PAA_{6.0}$ to $PAA_{5.6}$, the polyelectrolyte thickness was low due to the lack of free PAA polymer chain diffusion (linear-growth in PAH/PAA multilayers) and increased charge density on the polyelectrolyte chains. Thus, films at higher PAA pH's had a tightly packed structure with a reduced void volume. The refractive index for the interlayer ISAM ARCs with the higher PAA pH was nearly the same as from previous reports in our group.[2] In the range of $PAA_{5.4}$ to $PAA_{4.0}$, the refractive index decreased from $PAA_{5.6}$, but remained relatively consistent. From $PAA_{5.4}$ to $PAA_{4.0}$, the heightened diffusion of the free PAA polymer chains increased the polyelectrolyte

thickness, the size of the SiO_2 encapsulations, and consequently, the amount of void space. Since higher polyelectrolyte thickness and void space would increase and decrease the refractive index, respectively, the trade-off between the two was associated with the relatively consistent refractive index values. From $PAA_{4.0}$ to $PAA_{3.0}$, the refractive index increased dramatically due to the substantial increased polyelectrolyte thickness seen in the microporous formations that filled in much of the void space.

For ARCs, the transmittance and reflectance levels (%) are mainly dependent on the refractive index of the film and optical scattering loss (represented here by the A_s slope). With a change in PAA pH in the interlayer ISAM ARCs, the reflectance levels were mostly unaffected. However, the four-quadlayers films $PAA_{3.0}$ and $PAA_{4.0}$ had reflectance minima shifted into the UV because of the strong scattering in these films. The transmittance remained relatively consistent from $PAA_{6.0}$ to $PAA_{5.2}$, and then degraded below the PAA pH of $PAA_{5.2}$. We attributed the decreased transmittance levels to the increased A_s slope values with a decrease in PAA pH as well as the increased refractive index for the $PAA_{3.0}$ case. The large refractive index at pH 3.0 reduces the destructive interference between the reflections. The similar transmittance levels between $PAA_{6.0}$ and $PAA_{5.2}$ were correlated to a low A_s slope for the higher PAA pH and more ideal refractive index for the low PAA pH. However, the lower average reflectance from $PAA_{5.6}$ to $PAA_{5.2}$ was correlated to the more ideal refractive indices at these values. Therefore, the most excellent anti-reflection properties were found in the interlayer ISAM ARCs with any PAA pH between $PAA_{5.6}$ and $PAA_{5.2}$.

5.3.5 Microscopic Scratch Testing. A TriboIndenter was used to study the scratch resistance (bulk cohesive) properties of the interlayer ISAM ARCs at the micro-scale. In polymeric-based films, deformation is characterized by three different regimes including 1) the quasi-elastic

(thinning) regime, 2) the scratch deformation (also known as ductile ploughing) regime, and 3) the severe damage regime.[33-34] In the microscopic scratch testing, the normal force at initiation of the scratch deformation regime (L_{c1}) was designated as the primary parameter for the comparison of the films. The determination of the L_{c1} required a combination of qualitative and quantitative analysis through inspection of the SPM image, the scratch height profile, and the corresponding normal force. Along with the L_{c1}, the penetration depth of the scratch (P_d) was calculated as the difference between the average height of the non-scratched area film and the height of scratch section. The ratio of normal force divided by scratch penetration depth (L/P_d) was then calculated along the scratch length, and the average value was used as a comparison among the interlayer ISAM ARCs. The critical load due to delamination (L_{c2}), which quantifies the adhesive properties between the film and the substrate, was not focused on here as it is considered difficult to determine through scratch testing.[34] Along with the L_{c2}, the use of nanoindentation to acquire hardness and Young's modulus was not reported for this particular study, since the thicknesses of these films were dominated by the SiO_2 NP's and the results lacked dependence on the PAA pH.

Prior to the fabrication and analysis of the interlayer ISAM ARCs discussed above, the relationship of the scratch-resistance to the crosslinking conditions was assessed. Since these parameters were investigated in the initial exploration stages for this study, the interlayer ISAM ARC architecture was somewhat different. The set of films tested contained ten-bilayer stacks of PAH/PAA before and after the quadlayer interlayers, and the pH of both PAH and PAA was fixed at 7.0. The abbreviated design for four-quadlayer films were as follows: $(PAH_7/PAA_7)_{10}$-$(PAH_7/PAA_7/PAH_7/SiO_9)_4$-$(PAH_7/PAA_7)_{10}$. The L_{c1} was examined for the film set after thermal crosslinking at maximum temperatures of 180 ºC and 200 ºC and with dwell times (at those maximum temperatures) of 1, 2, and 10 h (under 20 in. Hg vacuum) (**Table 5.3**).

Table 5.3. Thermal crosslinking conditions (maximum temperature and dwell time) to the critical load (L_{c1}) for $(PAH_7/PAA_7)_{10}$-$(PAH_7/PAA_7/PAH_7/SiO_9)_4$-$(PAH_7/PAA_7)_{10}$ interlayer ISAM ARCs. Note that this interlayer architecture is different from that used elsewhere in this chapter.

Duration	**L_{c1} (μN)**	
	180 ºC	200 ºC
1 hr	13.34	22.46
2 hr	22.75	**41.23**
10 hr	17.23	34.38
24 hr	-	22.38

Consistently among the films, thermal crosslinking conditions of 200 ºC for 2 h was found to maximize the L_{c1}. An increase of the maximum temperature from 180 ºC to 200 ºC for all of the dwell times produced a rise in the L_{c1} by approximately a factor of 2. Since the heating and cooling rate was set to 1 ºC/min, it should be noted that the 200 ºC films were actually heated for approximately 40 min more than the 180 ºC films. It was apparent that a dwell time of 1 h was inadequate, while a dwell time of 10 h or more led to a possible film degradation. Thus, the crosslinking conditions of 200 ºC for 2 h were applied to all subsequent interlayer ISAM ARCs.

Scratch testing was performed on thermally crosslinked four-quadlayer interlayer ISAM ARCs for the PAA pH range of 3.0 to 6.0. For interlayer ISAM ARCs with $PAA_{3.0}$, $PAA_{6.0}$, as well as a film with the architecture of $(PAH_7/PAA_7)_{10}$-$(PAH_7/PAA_7/PAH_7/SiO_9)_4$-$(PAH_7/PAA_7)_{10}$ (thermally crosslinked at 200 ºC for 2 h in **Table 5.3**), examples of the SPM images, normal force, and the height profile are provided (**Figure 5.16a-f**). It was found that a decrease in the PAA pH directly correlated to a dramatic enhancement of the microscopic scratch resistance, despite the

degradations in anti-reflection (**Table 5.4**). As the PAA pH was decreased by an increment of 0.2 from $PAA_{5.6}$ to $PAA_{5.0}$ for the interlayer ISAM ARCs, the L_{c1} increased by approximately a factor of 2. From $PAA_{6.0}$ to $PAA_{3.0}$, the L_{c1} and L/P_d increased by 2,237% and 372%, respectively. The SPM image features and scratched section for the interlayer ISAM ARCs with $PAA_{3.0}$ were similar to $PAA_{4.0}$ (not shown). For both of these two films, the scratch tip moved across the sample with increasing force, until it punctured the sample at the L_{c1}, and then subsequently rose back up to a lesser depth height for the majority of the scratch (**Figure 5.16a-b**). The apparent "pile-up" pads on either side of the scratch can be explained by an excavation of thicker polymer layers within the film.

For comparison, a thermally crosslinked ten bilayer $PAH_{7.0}/PAA_{7.0}$ ISAM film (no SiO_2 NPs) was also scratch tested with similar parameters used for the interlayer ISAM ARCs (**Figure 5.17**). That film had a significantly larger L_{c1} than any of the films containing SiO_2 NPs (**Table 5.4**).

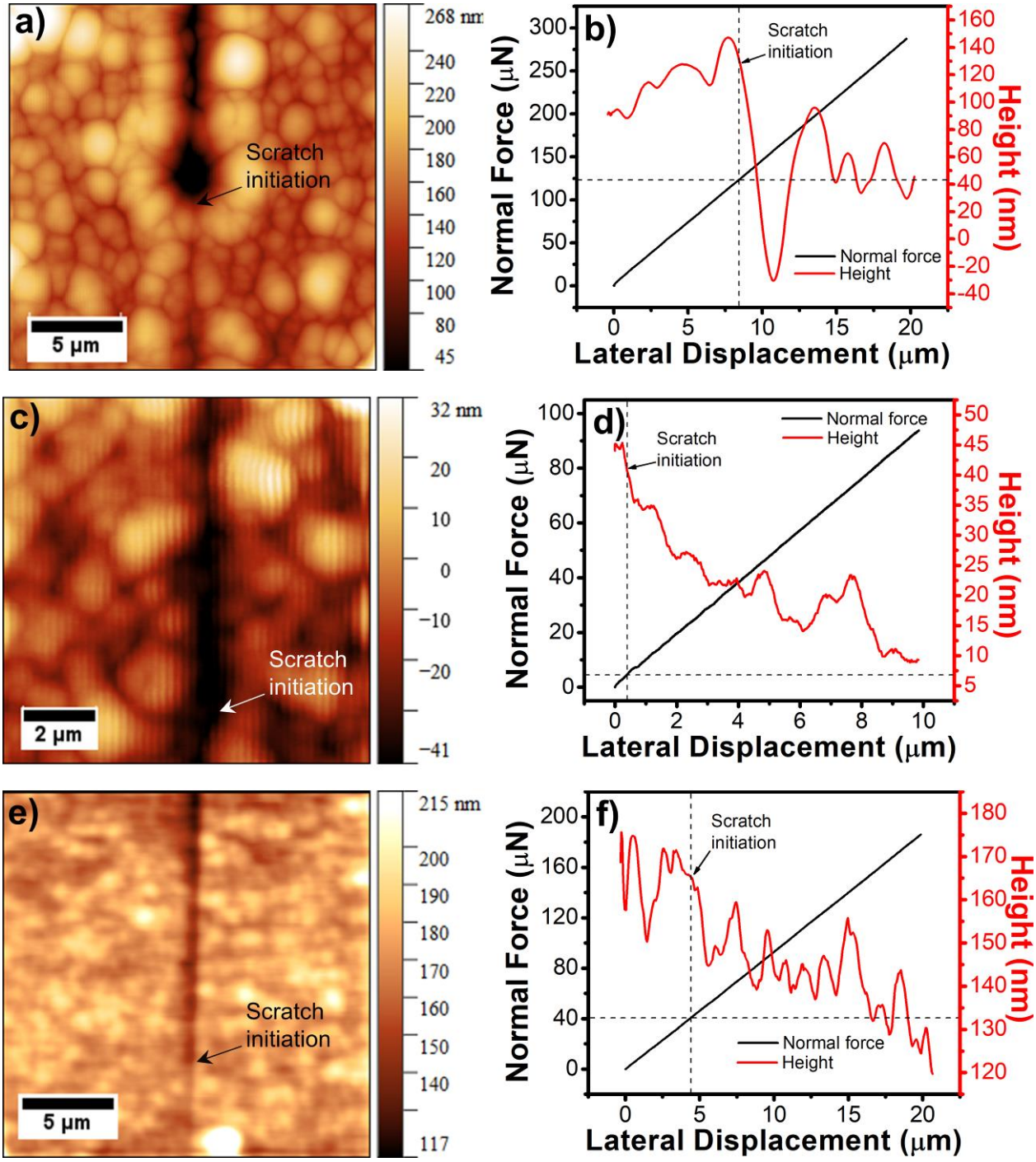

Figure 5.16. *In-situ* SPM image, ramped normal force, and height profile of scratched area for four quadlayer interlayer ISAM ARCs with (**a,b**) $PAA_{3.0}$ and (**c,d**) $PAA_{6.0}$, and (**e,f**) $(PAH_{7.0}/PAA_{7.0})_{10}$-$(PAH_{7.0}/PAA_{7.0}/PAH_{7.0}/SiO_{2\ 9.0})_4$-$(PAH_{7.0}/PAA_{7.0})_{10}$.

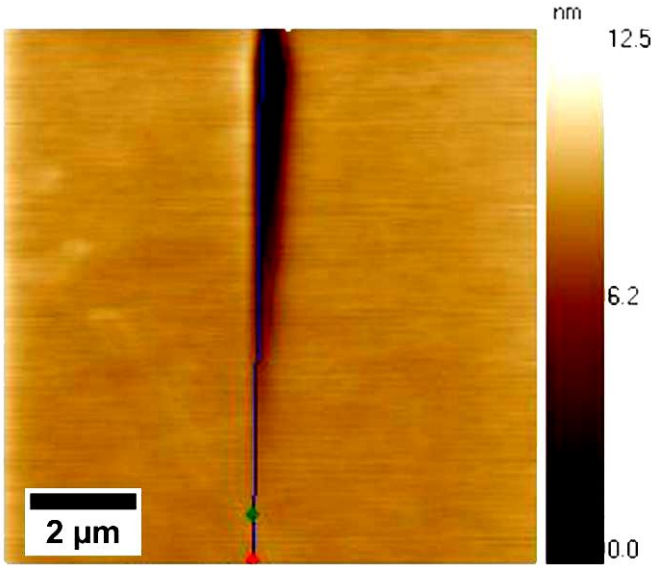

Figure 5.17. *In-situ* SPM characterization of a 10-bilayer $PAH_{7.0}/PAA_{7.0}$ film scratched up to 1000 µN.

Table 5.4. Transmittance maxima, L_{c1}, and L/P_d for four quadlayer interlayer ISAM ARCs. A $PAH_{7.0}/PAA_{7.0}$ ISAM film was included for critical load comparison.

Interlayer PAA pH	3.0	4.0	5.0	**5.2**	5.4	5.6	5.8	6.0	10-bilayer PAH/PAA
Transmittance Maxima (%)	83.9	95.4	97.0	**99.22**	99.08	99.10	99.0	99.10	N/A
L_{c1} (µN)	126	88.0	54.5	**35.7**	19.8	9.37	8.45	5.39	171.2
L/P_d (µN nm^{-1})	7550	7420	5910	**4910**	3410	2570	2000	1600	-

For the interlayer ISAM ARCs with lower PAA pH, the thicker polyelectrolyte SiO_2 NP encapsulations were attributed to an increased interfacial connectivity and scratch resistance. A greater quantity of polyelectrolytes also potentially increased the presence of covalent amide bond

formation after crosslinking. Additionally, the diffusion of free PAA polymer chains correlated to an improved interpenetration of the polyelectrolytes, which further improved the resilience of the film. Given that the L_{c1} for the interlayer ISAM ARC with $PAA_{3.0}$ approached that of the 10-bilayer PAH_7/PAA_7 film, a greater quantity of crosslinked polyelectrolytes was associated with enhanced scratch resistance. However, the same mechanism that caused an enhancement in the scratch resistance, also degraded the anti-reflection. The PAA pH was optimized at $PAA_{5.2}$ for the interlayer ISAM ARCs, as this PAA pH had both excellent anti-reflection and suitable scratch resistance.

5.3.6 Macroscopic Scratch Testing. While the TriboIndenter is an excellent method for pinpointing film failure on a micro-scale, a thorough macro-scale characterization was also necessary to develop fuller representation of the interlayer ISAM ARCs resistance to abrasion. The macroscopic scratch resistance was investigated by sliding laboratory cleaning tissues (secured on a stainless steel rod) over the surface of the films, which simulated cleaning by rubbing. In order to quantify the degree of scratch resistance for each film set, the respective film's haze was measured before and after scratching. Haze is the percentage of diffuse luminous transmittance to total luminous transmittance, in relation to wide angle scattering (light scattered at angles greater than 2.5°).[35] An increase in haze correlated to surface abrasion, since haze is dependent on light scattering, and light scattering is augmented with increased film roughness.[31-32] Previous reports have also used macro-scale scratching testing with a change in haze to define the level of scratch resistance for a film.[36-37]

Thermally crosslinked and uncrosslinked interlayer ISAM ARCs from $PAA_{3.0}$ to $PAA_{6.0}$ were scratched by the abrasive rod setup, and the haze before and after scratching was measured. For each PAA pH, the percent difference was calculated as ratio of the numerical difference of the

haze before and after scratching, divided by the haze after scratching. The percent difference in haze after scratching provided an appropriate scratch resistance comparison for the interlayer ISAM ARCs across the PAA pH range (**Figure 5.18** and **Table 5.5**).

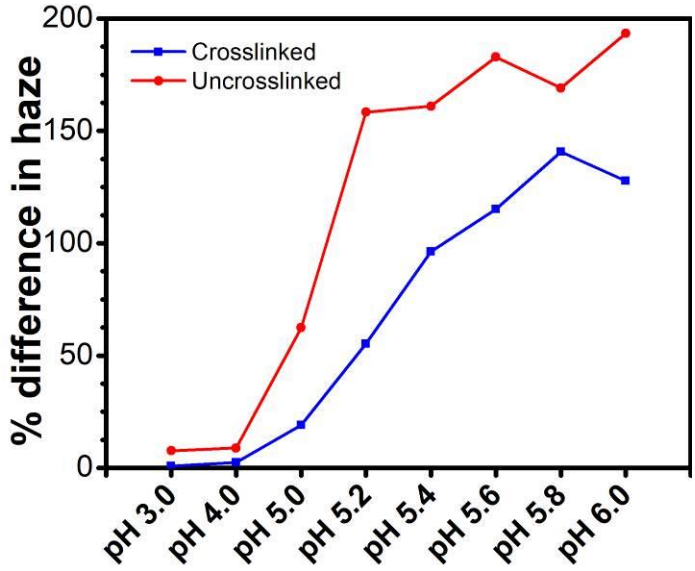

Figure 5.18. Percent differences in haze measurements after scratching for the uncrosslinked and crosslinked four quadlayer interlayer ISAM ARCs.

Table 5.5. Haze measurements before scratching, after scratching, and the respective percent differences for four quadlayer interlayer ISAM ARCs.

	Uncrosslinked ARCs			Crosslinked ARCs (200 °C, 2 h)		
Interlayer PAA pH	Haze (%) before scratch	Haze (%) after scratch	% difference	Haze (%) before scratch	Haze (%) after scratch	% difference
PAA 3.0	25.40 ± 2.2	27.35 ± 1.5	**8%**	23.15 ± 2.5	23.35 ± 1.8	**1%**
PAA 4.0	5.62 ± 0.09	6.12 ± 1.1	**9%**	5.56 ± 0.3	5.70 ± 0.3	**3%**
PAA 5.0	0.86 ± 0.05	1.40 ± 0.2	**62%**	0.78 ± 0.1	0.93 ± 0.05	**19%**
PAA 5.2	0.44 ± 0.03	1.14 ± 0.2	**158%**	0.37 ± 0.01	0.58 ± 0.06	**56%**
PAA 5.4	0.53 ± 0.08	1.37 ± 0.2	**161%**	0.44 ± 0.08	0.87 ± 0.2	**96%**
PAA 5.6	0.35 ± 0.04	0.99 ± 0.04	**183%**	0.38 ± 0.05	0.83 ± 0.04	**115%**
PAA 5.8	0.42 ± 0.06	1.13 ± 0.07	**169%**	0.39 ± 0.05	0.95 ± 0.02	**141%**
PAA 6.0	0.45 ± 0.03	1.32 ± 0.1	**193%**	0.40 ± 0.04	0.90 ± 0.04	**128%**
Blank glass	0.76 ± 0.1	-	**-**	-	-	**-**

As expected, the dependency of haze on PAA pH for interlayer ISAM ARCs was closely correlated to the A_s slope values discussed earlier (**Table 5.2**). At lower PAA pH, the heightened haze levels were unacceptable for excellent anti-reflection properties. Above $PAA_{5.2}$, the films' haze decreased drastically, which was associated with a lower surface roughness and smaller polyelectrolyte encapsulations. At $PAA_{5.2}$, the haze values drop below 0.5, which is attributed to the increased levels of optical transmittance, shown previously. Additionally, the decreased level in haze after thermal crosslinking was correlated to a reduction in film roughness, as discussed previously.[11]

Along with the improved optical properties, thermal crosslinking clearly improved the scratch resistance of the interlayer ISAM ARCs, as shown by the decreased percent difference in haze after scratching. Regardless of the PAA pH, thermal crosslinking of the films induced the formation of covalent amide bonds between the PAH and PAA polyelectrolytes, which provided stronger linkages than their original ionic bonds.

Besides the thermal crosslinking, the PAA pH held the greatest impact on the interlayer ISAM ARCs scratch resistance. Similar to the TriboIndenter results, the change in haze after scratching for $PAA_{3.0}$ and $PAA_{4.0}$ was very minimal, which represented superior scratch resistance for lower PAA pH's. This was true for the uncrosslinked films as well, which implied that even without amide bond formation, simply increased polyelectrolyte thickness and interpenetration within the SiO_2 NP matrix boosted the scratch resistance. For both uncrosslinked and crosslinked films, the change in haze after scratching rapidly increased with increased PAA pH, until reaching a plateau above $PAA_{5.4}$. As a crossover from exponential to linear-growth was found for PAH/PAA multilayer films at $PAA_{5.4}$, this PAA pH signified a reduction in the polyelectrolyte thickness and interpenetration. Therefore, the decreased levels of polyelectrolytes in the films facilitated an ease of abrasion. As discussed previously, there was a sharp transition of the anti-reflection performance of the films from fair to excellent, as the pH of PAA was increased from $PAA_{5.0}$ to $PAA_{5.2}$. Since the interlayer ISAM ARC with $PAA_{5.2}$ possessed the greatest scratch resistance among the films with high levels of anti-reflection, this PAA pH provided the best compromise between excellent anti-reflection and improved mechanical integrity.

5.4 CONCLUSIONS

A pair of PAH and PAA layers were added into the original PAH/SiO_2 NP ARC design to make PAH/PAA/PAH/SiO_2 NP films (interlayer ISAM ARCs) for scratch resistance improvements,

while maintaining excellent anti-reflection. In this study, we focused how the alteration of the PAA pH in the films dramatically changed their character. Starting with pure PAH/PAA multilayer films (without SiO_2 NPs), the establishment of covalent amide linkages between the polyelectrolytes after thermal crosslinking at 200 ^oC was confirmed by FTIR. In addition, a decrease in the PAA pH in PAH/PAA films caused a distinct transition from linear to exponential-growth in film thickness between the PAA pH of $PAA_{5.6}$ and $PAA_{5.4}$. The exponential-growth was attributed to the presence of diffusive PAA chains and low charge densities, as shown in previous reports. Additionally, the RMS roughness of the PAH/PAA films increased dramatically at a low PAA pH of $PAA_{3.0}$, as this pH was far below the solution pK_a. PAH/PAA/PAH/SiO_2 interlayer films were then constructed, thermally crosslinked at 200 ^oC, and examined by SEM. At the highest PAA pH of $PAA_{6.0}$, the films showed remarkable homogeneity and no visible polyelectrolytes. With a decrease of the PAA pH to $PAA_{5.0}$, $PAA_{4.0}$, and $PAA_{3.0}$, the SiO_2 encapsulations enlarged and the increased polyelectrolyte thicknesses became especially apparent. At $PAA_{3.0}$, SEM revealed large-scale microporous polyelectrolytes formations that extended across the majority of the film, a consequence of the pH being far below the pK_a. Examination of the films by UV-vis spectrometry showed a progressive improvement to the anti-reflection with an increase of the PAA pH from $PAA_{3.0}$ to $PAA_{5.2}$. From $PAA_{5.2}$ to $PAA_{6.0}$, the anti-reflection was consistently excellent with transmittance maxima ≥99% and reflectance minima close to or below 0.2%. In the range of $PAA_{5.2}$ to $PAA_{5.6}$, the reflectance minima remained below 0.1%. The improved anti-reflection was attributed to lower absorption due to scattering (A_s) slopes, decreased RMS roughness, and lower polyelectrolyte thickness levels. The scratch resistance of the films was assessed on a microscopic and macroscopic level. The microscopic scratch testing involved tribology (TriboIndenter), and the critical load that initiated the scratch track (L_{c1}) was measured through in-situ SPM imaging

and height profiles. The L_{c1} served as a mode of comparison for scratch resistance between thermally crosslinked interlayer ISAM ARCs and was found to drastically increase as the PAA pH was decreased. For macroscopic scratch testing of the films, the haze of films was measured before and after scratching by a home-made abrasive rod setup. The haze levels were found to decrease after thermal crosslinking and follow similar trends to the A_s slopes. Thermal crosslinking of the films for the entire PAA pH range decreased percent difference in haze after scratching, which established that crosslinking substantially enhanced the scratch resistance. Additionally, the macroscopic scratch testing showed that the scratch resistance for the interlayer ISAM ARCs dramatically improved as the pH of PAA was decreased, which confirmed the microscopic scratch testing results. The same mechanisms that caused scratch resistance enhancements were attributed degradation in the anti-reflection, mainly polyelectrolyte thickness. The interlayer ISAM ARCs fabricated with $PAA_{5.2}$ showed the highest scratch resistance that still maintained excellent anti-reflection.

This work emphasized that the properties of pure polyelectrolyte films can be used within composite films for substantial enhancements. The procedures outlined here demonstrated that simple changes in the fabrication parameters, including additional polyelectrolyte layers and manipulation of the polyelectrolyte solution pH, resulted in a dramatic change of a range of properties. The methods presented can induce a wide range thin film improvements for a large number of applications.

REFERENCES

(1) Metzman, J. S.; Wang, G.; Morris, J. R.; Heflin, J. R. Enhanced Scratch Resistance of Self-Assembled Silica Nanoparticle Anti-Reflection Coatings. *Journal of Materials Chemistry C* **2018,** *6* (4), 823-835, DOI: 10.1039/C7TC04457G.
(2) Yancey, S.; Zhong, W.; Heflin, J. R.; Ritter, A. L. The Influence of Void Space on Antireflection Coatings of Silica Nanoparticle Self-Assembled Films. *Journal of applied physics* **2006,** *99* (3), 034313.

(3) Harris, J. J.; DeRose, P. M.; Bruening, M. L. Synthesis of Passivating, Nylon-Like Coatings through Cross-Linking of Ultrathin Polyelectrolyte Films. *Journal of the American Chemical Society* **1999,** *121* (9), 1978-1979.
(4) Hiller, J. A.; Mendelsohn, J. D.; Rubner, M. F. Reversibly Erasable Nanoporous Anti-Reflection Coatings from Polyelectrolyte Multilayers. *Nature materials* **2002,** *1* (1), 59-63.
(5) Pavoor, P. V.; Bellare, A.; Strom, A.; Yang, D.; Cohen, R. E. Mechanical Characterization of Polyelectrolyte Multilayers Using Quasi-Static Nanoindentation. *Macromolecules* **2004,** *37* (13), 4865-4871.
(6) Zhai, L.; Cebeci, F. C.; Cohen, R. E.; Rubner, M. F. Stable Superhydrophobic Coatings from Polyelectrolyte Multilayers. *Nano letters* **2004,** *4* (7), 1349-1353.
(7) Han, J. T.; Zheng, Y.; Cho, J. H.; Xu, X.; Cho, K. Stable Superhydrophobic Organic-Inorganic Hybrid Films by Electrostatic Self-Assembly. *The Journal of Physical Chemistry B* **2005,** *109* (44), 20773-20778.
(8) Zhang, S.-w.; Feng, D.; Wang, D. Tribological Behaviors of Composite Molecular Deposition Films. *Tribology international* **2005,** *38* (11), 959-965.
(9) Dai, X.; Zhang, Y.; Guan, Y.; Yang, S.; Xu, J. Mechanical Properties of Polyelectrolyte Multilayer Self-Assembled Films. *Thin Solid Films* **2005,** *474* (1), 159-164.
(10) Zhao, Y.; Li, M.; Lu, Q.; Shi, Z. Superhydrophobic Polyimide Films with a Hierarchical Topography: Combined Replica Molding and Layer-by-Layer Assembly. *Langmuir* **2008,** *24* (21), 12651-12657.
(11) Yang, G.; Ma, H.; Yu, L.; Zhang, P. Preparation and Characterization of Layer-by-Layer Self-Assembled Polyelectrolyte Multilayer Films Doped with Surface-Capped Sio 2 Nanoparticles. *Journal of colloid and interface science* **2009,** *333* (2), 776-781.
(12) Liu, X.; Zhou, L.; Liu, F.; Ji, M.; Tang, W.; Pang, M.; Sun, J. Exponential Growth of Layer-by-Layer Assembled Coatings with Well-Dispersed Ultrafine Nanofillers: A Facile Route to Scratch-Resistant and Transparent Hybrid Coatings. *Journal of Materials Chemistry* **2010,** *20* (36), 7721-7727.
(13) Matsuda, M.; Shiratori, S. Correlation of Antithrombogenicity and Heat Treatment for Layer-by-Layer Self-Assembled Polyelectrolyte Films. *Langmuir* **2011,** *27* (7), 4271-4277.
(14) Choi, J.; Rubner, M. F. Influence of the Degree of Ionization on Weak Polyelectrolyte Multilayer Assembly. *Macromolecules* **2005,** *38* (1), 116-124.
(15) Shiratori, S. S.; Rubner, M. F. Ph-Dependent Thickness Behavior of Sequentially Adsorbed Layers of Weak Polyelectrolytes. *Macromolecules* **2000,** *33* (11), 4213-4219.
(16) Yoo, D.; Shiratori, S. S.; Rubner, M. F. Controlling Bilayer Composition and Surface Wettability of Sequentially Adsorbed Multilayers of Weak Polyelectrolytes. *Macromolecules* **1998,** *31* (13), 4309-4318.
(17) Mendelsohn, J.; Barrett, C. J.; Chan, V.; Pal, A.; Mayes, A.; Rubner, M. Fabrication of Microporous Thin Films from Polyelectrolyte Multilayers. *Langmuir* **2000,** *16* (11), 5017-5023.
(18) Sun, B.; Jewell, C. M.; Fredin, N. J.; Lynn, D. M. Assembly of Multilayered Films Using Well-Defined, End-Labeled Poly (Acrylic Acid): Influence of Molecular Weight on Exponential Growth in a Synthetic Weak Polyelectrolyte System. *Langmuir* **2007,** *23* (16), 8452-8459.
(19) Fu, J.; Ji, J.; Shen, L.; Küller, A.; Rosenhahn, A.; Shen, J.; Grunze, M. Ph-Amplified Exponential Growth Multilayers: A Facile Method to Develop Hierarchical Micro-and Nanostructured Surfaces. *Langmuir* **2008,** *25* (2), 672-675.
(20) Zhang, S.-w.; Feng, D.; Wang, D. Tribological Behaviors of Composite Molecular Deposition Films. *Tribology international* **2006,** *38* (11), 959-965.

(21) Jabs, A. Determination of Secondary Structure in Proteins by Fourier Transform Infrared Spectroscopy (Ftir) http://jenalib.leibniz-fli.de/ImgLibDoc/ftir/IMAGE_FTIR.html#Amide%20vibrations.
(22) Krimm, S.; Bandekar, J. Vibrational Spectroscopy and Conformation of Peptides, Polypeptides, and Proteins. *Advances in protein chemistry* **1986,** *38* 181-364.
(23) Hübsch, E.; Ball, V.; Senger, B.; Decher, G.; Voegel, J.-C.; Schaaf, P. Controlling the Growth Regime of Polyelectrolyte Multilayer Films: Changing from Exponential to Linear Growth by Adjusting the Composition of Polyelectrolyte Mixtures. *Langmuir* **2004,** *20* (5), 1980-1985.
(24) Picart, C.; Lavalle, P.; Hubert, P.; Cuisinier, F.; Decher, G.; Schaaf, P.; Voegel, J.-C. Buildup Mechanism for Poly (L-Lysine)/Hyaluronic Acid Films onto a Solid Surface. *Langmuir* **2001,** *17* (23), 7414-7424.
(25) Lavalle, P.; Gergely, C.; Cuisinier, F.; Decher, G.; Schaaf, P.; Voegel, J.; Picart, C. Comparison of the Structure of Polyelectrolyte Multilayer Films Exhibiting a Linear and an Exponential Growth Regime: An in Situ Atomic Force Microscopy Study. *Macromolecules* **2002,** *35* (11), 4458-4465.
(26) Porcel, C.; Lavalle, P.; Ball, V.; Decher, G.; Senger, B.; Voegel, J.-C.; Schaaf, P. From Exponential to Linear Growth in Polyelectrolyte Multilayers. *Langmuir* **2006,** *22* (9), 4376-4383.
(27) Bieker, P.; Schönhoff, M. Linear and Exponential Growth Regimes of Multilayers of Weak Polyelectrolytes in Dependence on Ph. *Macromolecules* **2010,** *43* (11), 5052-5059.
(28) Metzman, J. S.; Ridley, J. I.; Khalifa, M. B.; Heflin, J. R. Stability of Anti-Reflection Coatings Via the Self-Assembly Encapsulation of Silica Nanoparticles by Diazo-Resins. *Journal of Physics and Chemistry of Solids* **2015,** *87* 271-277.
(29) Podsiadlo, P.; Michel, M.; Lee, J.; Verploegen, E.; Wong Shi Kam, N.; Ball, V.; Lee, J.; Qi, Y.; Hart, A. J.; Hammond, P. T. Exponential Growth of Lbl Films with Incorporated Inorganic Sheets. *Nano letters* **2008,** *8* (6), 1762-1770.
(30) McAloney, R. A.; Sinyor, M.; Dudnik, V.; Goh, M. C. Atomic Force Microscopy Studies of Salt Effects on Polyelectrolyte Multilayer Film Morphology. *Langmuir* **2001,** *17* (21), 6655-6663.
(31) Duparré, A. Light Scattering of Thin Dielectric Films. *Thin films for optical coatings* **1995,** *1* 273-304.
(32) Jakobs, S.; Duparré, A.; Truckenbrodt, H. Interfacial Roughness and Related Scatter in Ultraviolet Optical Coatings: A Systematic Experimental Approach. *Applied optics* **1998,** *37* (7), 1180-1193.
(33) Briscoe, B. J.; Evans, P. D.; Pellilo, E.; Sinha, S. K. Scratching Maps for Polymers. *Wear* **1996,** *200* (1), 137-147.
(34) Bull, S.; Berasetegui, E. An Overview of the Potential of Quantitative Coating Adhesion Measurement by Scratch Testing. *Tribology International* **2006,** *39* (2), 99-114.
(35) ASTM, D. 1003-00," Standard Test Method for Haze and Luminous Transmittance of Transparent Plastics. *ASTM International," ASTM International, West Conshohoken, PA* **2000**.
(36) Carnegie, M. R.; Sherine, A.; Sivagami, D.; Sakthivel, S. Anti-Reflection Coatings with Enhanced Abrasion and Scratch Resistance Properties. *Journal of Sol-Gel Science and Technology* **2016,** *78* (1), 176-186.
(37) Kourtakis, K.; Bekiarian, P.; Blackman, G.; Lewittes, M.; Subramoney, S. Novel Thermal and Photo Curable Anti-Reflective Coatings Using Fluoroelastomer Nanocomposites and Self-Assembly of Nanoparticles. *Journal of Coatings Technology and Research* **2016,** *13* (5), 753-762.

Chapter 6

Self-assembly of the Hole-transport Layer and Encapsulated Silver Nanoplates in Organic Photovoltaics

6.1 INTRODUCTION

The introduction of bulk heterojunctions (BHJ) dramatically improved the performance of organic photovoltaics (OPVs) through the formation of interpenetrated phases of conjugated polymers (electron donor) and fullerene derivatives (electron acceptor). The interpenetrated phases have a high interfacial area and small domains for efficient exciton dissociation and diffusion.[1-2] However, despite the improvements to donor/acceptor materials[3-5] and morphology of the active layer,[6-10] the power conversion efficiency (PCE) of OPV devices are still limited by charge transport, specifically low charge carrier mobilities and short exciton diffusion lengths.[11-13] Because of these limitations, the optimal thickness of the BHJ's active layer and the maximum light absorption are limited in OPVs. The most efficient OPV devices are typically no more than 100-200 nm thick.

The addition of plasmonic metallic nanoparticles to OPV devices has proven to be a promising approach for increasing the light absorption without modifications to the active layer thickness.[14] The exposure of incident light onto plasmonic nanoparticles induces resonance of the conduction electrons within their metallic core, which creates local electric field enhancements in the vicinity of the nanoparticles, often referred to as localized surface plasmon resonance (LSPR).[15-18] When the nanoparticle LSPR frequency couples with the OPV absorption frequency, the OPV optical absorption can be substantially increased. Anisotropic silver nanoplates (AgNPs) are especially

attractive as their peak LSPR (λ_{LSPR}) is widely tunable in the visible wavelength range.[19-20] In comparison to other noble metals, Ag possesses exceptional optical properties and lower cost.[21-23]

Plasmonic nanoparticles are typically mixed into the hole-transport layer (HTL, PEDOT:PSS) or active layer solutions before device processing.[21, 24-26] However, compatibility with OPV materials solutions generally requires nanoparticle functionalization. Additionally, nanoparticles degradation are likely to occur when dispersed with OPV materials, due to the acidic nature of PEDOT:PSS and chlorinated organic solvents for the active layer.[27-30]

Layer-by-layer ionic self-assembled multilayers (ISAM) deposition is an effective way for the addition of AgNPs in OPVs. Sodium citrate capping surfactants used in nanoparticle synthesis provide a strong negative surface charge to the AgNPs,[31] which makes them suitable for ISAM deposition. The PEDOT:PSS dispersion, which has also been used extensively in conductive ISAM films for electrochromics,[32-33] can be integrated into films with the AgNPs. Recent advances in water-based active layer components introduces the possibility of OPVs processed purely by ISAM growth for large-scale, eco-friendly (without toxic solvents) development.[34-36]

In the first half of this chapter, the optimization of the annealing conditions and active layer thicknesses for standard reference OPV devices are overviewed. The second half of this chapter is dedicated to the extensive work done on encapsulation of AgNPs and ISAM film production for the HTL in the OPVs. For the second half of the chapter, the results are reported in chronological order. As experimental modifications to the reference devices were made throughout all of the work on OPVs (including the work done in the next chapter), their performance is reflective of the best conditions at each given time. Unfortunately, the methods in the second half of this chapter were ineffective for providing performance enhancements to the OPVs, but they are expected to be helpful for future work in the field.

6.2 EXPERIMENTAL

6.2.1 Synthesis of Ag Nanoplates. Ag nanoplates (AgNPs) were synthesized in the group of Greg Liu via a seed-mediated method following previous reports with slight modifications.[17, 20, 25, 37] To prepare Ag seeds, 4.5 mL of ultrapure deionized (DI) water (resistance, 18.2 MΩ·cm) was mixed vigorously with 0.5 mL of 25 mM sodium citrate tribasic dihydrate (purity ≥99.0%) and 0.25 mL of 0.5 mM poly(sodium 4-styrenesulfonate) (PSSS; $M_w \sim 1000$ kg mol^{-1}) aqueous solutions. Next, 0.3 mL of 10 mM ice-cold sodium borohydride ($NaBH_4$; purity ≥99.99%) solution was introduced, followed by the addition of 5 mL of 0.5 mM silver nitrate ($AgNO_3$; purity ≥99.9999%) at a rate of 2 mL/min using a syringe pump. Once all of the silver nitrate was added, the seed solution was stirred for ~2 min and then ready for use in the next step.

To synthesize AgNPs, 75 μL of 10 mM ascorbic acid (purity ≥99.0%) solution was added to 10 mL of DI water, and a certain volume (75 – 175 μL) of Ag seed solution was added to the growth solution under vigorous stirring. Immediately afterwards, 3 mL of 0.5 mM $AgNO_3$ was dispensed into the growth solution at a rate of 1 mL/min using a syringe pump. The solution initially appeared yellow, then changed rapidly, and eventually stabilized towards the completion of the growth to a color representative of the size range of the AgNPs. Promptly following the complete addition of $AgNO_3$, 0.5 mL of 25 mM sodium citrate was added to stabilize the AgNPs. The final solution volume was approximately 13.68 mL. The AgNP synthesis was reiterated with different volumes of Ag seed solutions to synthesize AgNPs of different sizes and λ_{LSPR}. After synthesis, the solutions were sealed and stored in the dark.

6.2.2 Gold Coating of Ag Nanoplates. Gold coating of the AgNPs (AuAgNPs) was carried out immediately after the synthesis of AgNPs similar to the methods from previous reports with various modifications.[30, 38] While vigorously stirring, 150 μL of 10 mM ascorbic acid solution was

added to the AgNP solution, followed by the addition of a calculated volume of 0.5 mM gold(III) chloride trihydrate ($HAuCl_4$; purity ≥99.9%; Sigma-Aldrich) solution (based on the Au:Ag ratio) at a rate of 0.2 mL/minute. After the solution was stirred vigorously for ~2 minutes, it was sealed and stored in the dark. The following example describes how the AgNPs were coated at an Au:Ag ratio of 0.06:1. Given the AgNP solution had 3 mL of 0.5 mM $AgNO_3$ in a total solution volume of 13.68 mL, then there would be 0.22 mL of 0.5 mM $AgNO_3$ per mL of DI water. For an Au-Ag ratio of 0.06-1, the product of 0.22 with 0.06 equals 0.0132 mL of 0.5 mM $HAuCl_4$ per mL of DI water. For the AgNP solution volume of 13.68 mL, a total volume of 0.18 mL of 0.5 mM $HAuCl_4$ was added.

6.2.3 Solution Formation. For ISAM film processes, poly(allylamine hydrochloride) (PAH) solutions were formed by mixing PAH powder (average Mw ~17,500; Sigma-Aldrich) into DI for a final polymer concentration of 10 mM. For PAH encapsulation processes, high concentrations of PAH powder were vortex-mixed with DI water in scintillation vials. Dispersions of poly(3,4-ethylenedioxythiophene): poly(styrenesulfonate) (PEDOT:PSS; Heraeus; CLEVIOS™ P VP AI 4083) were filtered through a 0.45 μm PVDF syringe filter, diluted with DI water at a ratio of (1:20) or (1:40) (PEDOT:PSS / DI water), and then vortex-mixed before ISAM growth. For spin-coating use, PEDOT:PSS dispersions were filtered through a 0.45 μm PVDF syringe filter, and IPA was added (PEDOT:PSS / IPA = 3/1). The PEDOT:PSS/IPA blend was vortex mixed before each use. The addition of IPA significantly improved the homogeneity of the PEDOT:PSS film. The pH of the solutions was altered with the addition of 1.0 M hydrochloric acid (HCl, Certified ACS Plus) and 1.0 M sodium hydroxide (NaOH, Certified ACS, Pellets, Z97.0%).

6.2.4 PAH Encapsulation of Ag Nanoplates. For the PAH encapsulation of the AgNPs, DI water and a concentrated PAH solution were added to AgNP solution. After mixing of the

components, the final AgNP solution concentration was decreased by a factor of 2 and the desired PAH concentration was achieved. For instance, 20 mL of DI water was vigorously stirred with 25 mL of AgNP solution. After several minutes of vigorous stirring, 5 mL of 40 mM PAH solution was added to the AgNP solution, for a final PAH concentration of 4 mM.

6.2.5 Formation of ISAM Films. A programmable immersion machine was used to fabricate ISAM films onto ARC/glass/ITO substrates. The ARC side of the substrate and the top 1/10 of the ITO strip was covered with electrical tape to prevent film coverage of those areas. The immersion machine has eight solution locations, with the ability to also spin the substrate at those locations (refer to the **Chapter 3** for more details). The immersion steps for each film type are shown in **Table 6.1**, in the order discussed in the chapter.

Table 6.1. Various ISAM film processing steps. One full cycle consists of eight solution immersion steps. For each step, the solution is listed on the top and the immersion time, in minutes, is listed on the bottom. The (*) means that the substrate was spun at 600 rpm in the solution.

Film	Immersion Step – Solution and Time (minutes)							
	1	2	3	4	5	6	7	8
A) PAH/AgNP	PAH	H_2O*	H_2O*	H_2O*	AgNP*	H_2O*	H_2O*	H_2O*
	5	0.75	0.75	0.75	120	0.75	0.75	0.75
B) PAH/PEDOT:PSS	PAH	H_2O*	H_2O*	H_2O*	PEDOT:PSS*	H_2O*	H_2O*	H_2O*
	5	0.75	0.75	0.75	15	0.75	0.75	0.75
C) PAH/PEDOT:PSS (1-20)/PAH/ AuAgNP	PAH	H_2O*	PEDOT:PSS*	H_2O*	PAH	H_2O*	AgNP*	H_2O*
	5	2.25	15	2.25	5	2.25	120	2.25

PEDOT:PSS/IPA was spin-coated at 4000 rpm on top of ISAM film A to create the conventional PEDOT:PSS thickness. For OPV devices with ISAM films B and C (**Table 6.1**), PEDOT:PSS/IPA was spin-coated at 8000 rpm to make a thin layer on top of the ISAM film, and the entire film was annealed at 140 ^{o}C. The thin PEDOT:PSS layer was utilized to increase the coverage and homogeneity of the next layer (P3HT:PCBM).

6.3 RESULTS

6.3.1 Optimization of Annealing Conditions. The design of reference OPV devices examined in this work consisted of the glass/ITO/PEDOT:PSS/P3HT:PCBM/Al architecture . In this section, we first focus upon the optimization of the annealing conditions, as annealing was performed on every OPV device reported.

Immediately after the thermal evaporation of the aluminum cathodes, annealing was performed on the devices at 130 ^{o}C for 15 minutes in a box filled with argon gas. In the early stages of this project, a preliminary test was done to compare pre-annealing (before the evaporation of Al) and post-annealing (following the evaporation of Al). The experimental parameters (active layer thickness, annealing conditions, etc.) were not optimized in this preliminary experiment, so neither was the performance. The current density to voltage (J-V) OPV performance of the pre-annealed and post-annealed devices under the air mass 1.5 (AM1.5g, 100 mW/cm^2) illumination were measured and compared (**Figure 6.1)**. The shunt resistance (R_{sh}) values of the OPV devices (**Table 6.2**) were determined by the reciprocal slopes of the J-V curves at zero bias (*i.e.*, 0 V) according to

$$R_{sh} = \left(\frac{dV}{dJ}\right)_{V\to 0} \quad (\mathbf{6.1})$$

The series resistance (R_s) (**Table 6.2**) was determined by the reciprocal slope of the J-V curves at voltages much larger than V_{oc}, according to

$$R_S = \left(\frac{dV}{dJ}\right)_{V\to\infty} \quad \textbf{(6.2)}$$

It is clear that the OPV performance substantially increased from the post-annealing compared to the pre-annealing. Specifically, the post-annealed device had a 2% increase in the J_{sc}, a 15% increase in the V_{oc}, a 6% increase in the fill-factor (FF), a 30% decrease in the R_s, a 17% increase in the R_{sh}, and a 22% increase in the PCE.

The significant improvements to the R_s signified the improvement of contact resistance, charge carrier extraction, and interfacial quality at the Al electrodes.[39-40] It has been suggested that during post-annealing, the metal cap of Al binds P3HT:PCBM and promotes more efficient phase separation.[41-42] There also is strong evidence that the metal cap restricts the layer laterally, but permits phase separation in the vertical direction (into the Al).[42] This is made possible as the thermal evaporation of aluminum films is reported to consist of grains and voids.[43] Additionally, post-annealing is reported to substantially increase the PCBM uniformity at the interfacial surface, which reduces the amount of defects and trap-assisted recombination rates.[39] The decreased recombination rates are evident in the increased R_{sh} values for the post-annealed devices, which was also reported previously.[39] The decrease of the R_s and increase of the R_{sh} together improved the FF for the post-annealed devices.

The J_{sc} parameter is primarily dependent on absorption, processing conditions, charge carrier mobility, and R_s.[12, 40, 44] The marginally increased J_{sc} levels can be attributed to the reduced R_s values for the post-annealed devices. As the active layer thickness of all these devices was held constant, the absorption was unaffected, so J_{sc} improvements were essentially minimal.

The larger V_{oc} values in the post-annealed devices certainly had a strong impact on their overall performance. An increase in the device V_{oc} has been previously reported to be associated with an increase in the R_{sh},[39, 42, 45-48] which is verified by our results. Essentially, the decreased

recombination rates at the active layer/Al interface interfacial resulted in a dramatic improvement to the V_{oc}.

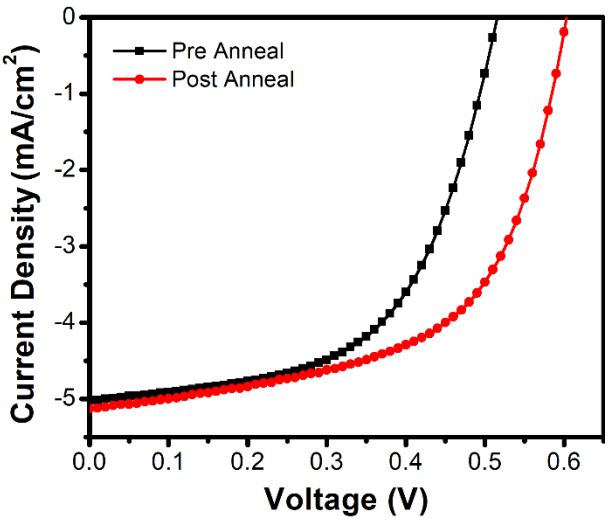

Figure 6.1. The current density – voltage (J-V) characteristics of OPV devices with a pre-annealed or post-annealed Al cathode.

Table 6.2. The J-V characteristics of the OPV devices with a pre-annealed or post-annealed Al cathode.

Anneal	J_{sc} (mA/cm^2)	V_{oc} (V)	FF	R_s (Ω·cm^2)	R_{sh} (Ω·cm^2)	PCE (%)	Best PCE (%)
Pre	-5.02 ± 0.08	0.53 ± 0.01	0.55 ± 0.01	14.15 ± 0.3	958 ± 158	1.48 ± 0.01	1.49
Post	-5.13 ± 0.04	0.61 ± 0.01	0.58 ± 0.01	9.92 ± 0.1	1124 ± 291	1.81 ± 0.03	1.83

Although it was found that a higher evaporation rate (>5 Å/s) can be used for pre-annealing, it is critical that for post-annealing, the evaporation rate of the Al must be maintained below 2.5 Å/s for a good FF and PCE. It has been reported that higher evaporation rates create significantly

larger grain sizes, roughness, and voids than lower evaporation rates,[43] and the post-annealing of the P3HT:PCBM films in this condition led to shunts and pin-holes. Previous reports also found that high deposition rates associate with inhomogeneity and degradation of the interface.[12] The sigmoidal shaped J-V curve shown in **Figure 6.2** for an Al deposition rate >>2.5 Å/s is a result of space-charge limited current due to charge accumulation at an electrode and correlated to the low FF, low R_{sh}, and high R_s.[12]

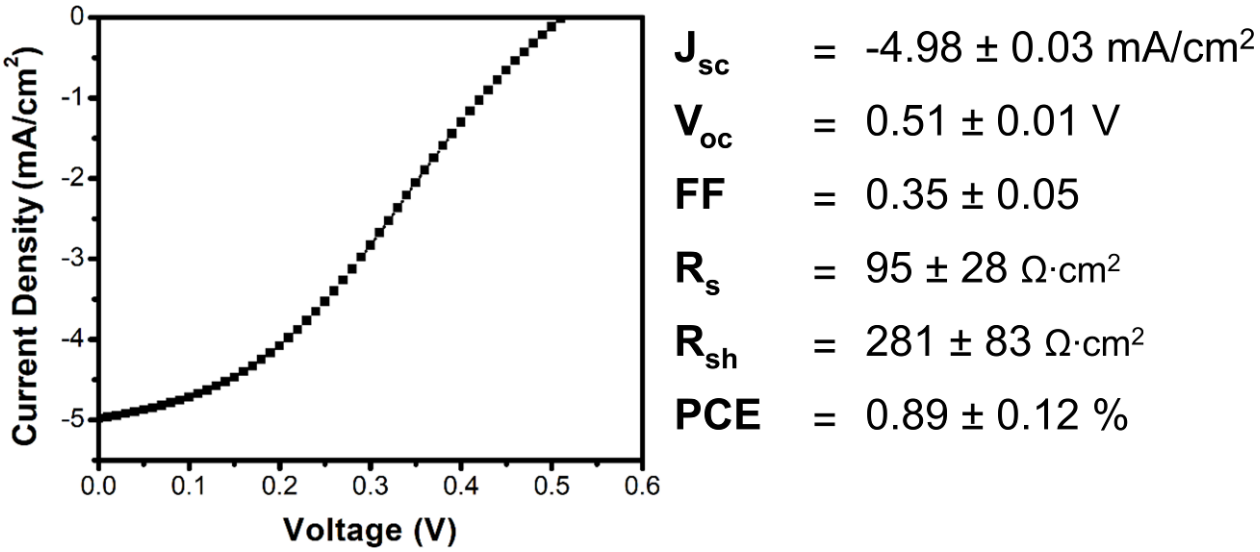

Figure 6.2. The current density – voltage (J-V) characteristics of an OPV device that was post-annealed after high Al deposition rates (>>2.5 Å/s). The electrical characteristics are listed next to the figure.

6.3.2 Optimization of Active Layer Thickness. Along with the annealing conditions, optimization of the active layer (P3HT:PCBM) thickness is essential to maximize the performance of the reference devices. While the active layer thickness can be found through the use of a profliometer or AFM, these methods are more time consuming compared to determination of the thickness from the absorption. The transmittance (T) and reflectance (R) spectra were recorded by

a Filmetrics F10-RT-EXR spectrometer. The absorption (A) spectra were calculated according to Beer-Lambert's law

$$A = -\log(\frac{T}{1-R}) \quad (6.3)$$

where T and R are the transmittance and reflectance for a given wavelength. The absorption spectrum of P3HT:PCBM was obtained by subtracting the absorption spectrum of glass/ITO/PEDOT:PSS from that of glass/ITO/PEDOT:PSS/P3HT:PCBM. This is exemplified for a sample in **Figure 6.3**.

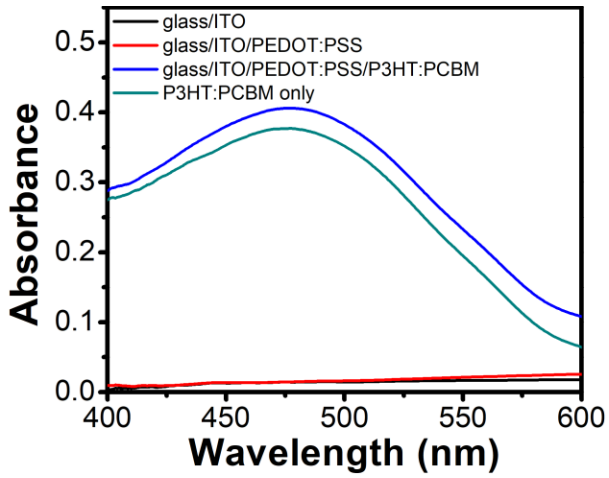

Figure 6.3. Optical absorption of glass/ITO, glass/ITO/PEDOT:PSS, glass/ITO/PEDOT:PSS/P3HT:PCBM, and P3HT:PCBM subtracted spectra.

As shown, the visible wavelength absorption of glass/ITO and PEDOT:PSS are both small, which limits unnecessary light blocking from P3HT:PCBM. The absorption of these initial layers is not negligible, however, and therefore their subtraction was critical for an accurate representation of the P3HT:PCBM absorption spectrum.

A Veeco DekTak 150 Stylus Profilometer was used to measure the thickness of a few reference PEDOT:PSS and P3HT:PCBM films. By measuring the thickness of the P3HT:PCBM films, the absorption coefficient (α) of P3HT:PCBM was then calculated by

$$\alpha = \frac{\ln(10) * A}{l} \qquad (6.4)$$

where l is the thickness of the film. The absorption coefficient is dependent on wavelength (**Figure 6.4**). With the determination of the absorption coefficient, the thickness of the P3HT:PCBM films could then be calculated from a sample's absorbance using **Equation 6.4**.

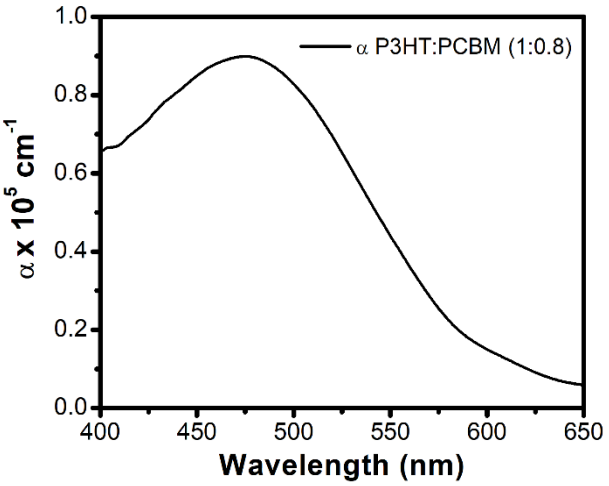

Figure 6.4. Absorption coefficient (α) of P3HT:PCBM (1:0.8) as a function of wavelength.

The active layer thickness was varied systematically through a manipulation of the spin-coating speed for thicknesses ranging from 75 to 130 nm (**Figure 6.5a)**. For all of the P3HT:PCBM as-casted films, the peak absorption wavelength (λ_{max}) was 473 nm, which was associated with the combined absorption from the separate P3HT (λ_{max} = 514 nm) and PCBM ($\lambda_{max} \approx$ 340 nm) BHJ components at a ratio of 1:0.8 (P3HT:PCBM). The thickness of the films was always calculated at this peak absorption wavelength. A greater thickness corresponded directly with increased absorption, as a larger volume of P3HT polymer chains and PCBM molecules were present for the collection of the incident photons. After post-annealing of the glass/ITO/PEDOT:PSS/P3HT:PCBM devices with different P3HT:PCBM thicknesses, absorption measurements were again performed (**Figure 6.5b**).

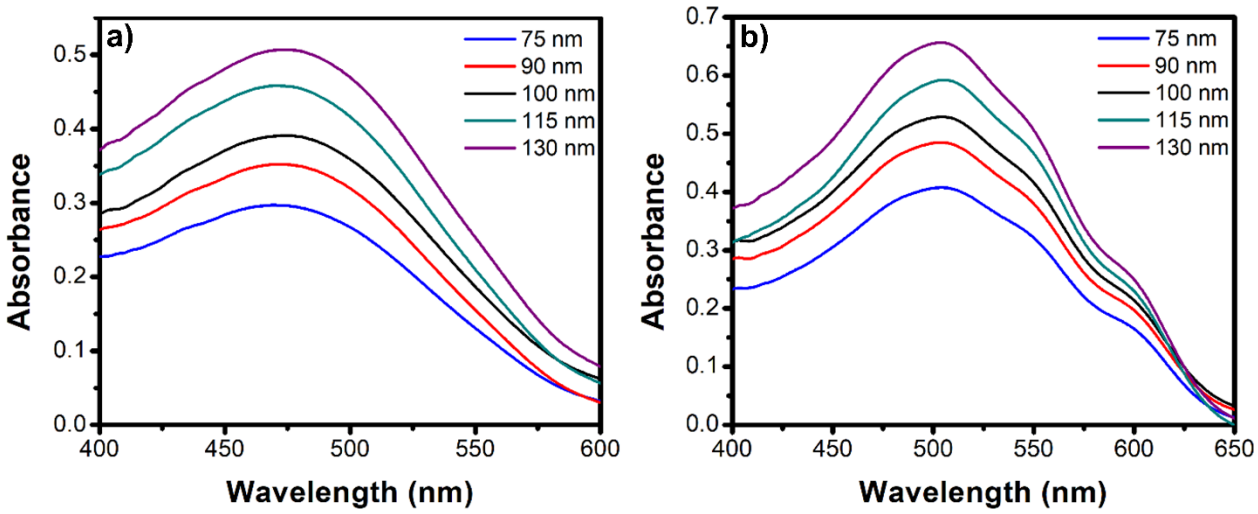

Figure 6.5. (**a**) The optical absorption spectra of the as-cast P3HT:PCBM films with thicknesses of 75, 90, 100, 115, and 130 nm. (**b**) The optical absorption of the same P3HT:PCBM films after thermal annealing.

The J-V OPV performance under AM1.5G illumination for these thicknesses was next examined (**Figure 6.6**). The performance was best for the 100 nm P3HT:PCBM thickness (**Table 6.3**). At this thickness, the average device J_{sc} was -7.88 mA/cm^2, the V_{oc} was 0.61 V, the FF was 0.51, and the average PCE was 2.45%, with a maximum PCE at 2.61%. The V_{oc} stayed relatively steady for thicknesses lower than 100 nm and then decreased for higher thicknesses (115 nm and 130 nm). The FF and the R_{sh} were the highest at 75 nm and continued to drop with greater thickness for the entire range of data. From a thickness of 75 nm to 100 nm, the R_{sh} dropped by 67%, and from 75 nm to 130 nm, the R_{sh} decreased by 75%. The PCE steadily increased with thickness, peaked at a P3HT:PCBM thickness of 100 nm, and then progressively decreased with greater thickness.

Several interesting trends took place within this data set. First, the average J_{sc} initially increased with P3HT:PCBM thickness, and then decreased with thicknesses larger than 100 nm. A heightened J_{sc} can generally be expected for a larger P3HT:PCBM thickness, as increased absorption is correlated with an increased photogenerated exciton and charge carrier yield.[49-50] The

decrease of J_{sc} with thicknesses above 100 nm have been correlated in OPVs to a variation in light intensity within the active layer due to optical interference effects.[51-53] Despite a continuous increase in overall absorption with active layer thickness, the light intensity variations within the active layer cause the average light intensity, overall exciton generation, and the J_{sc} to not monotonously increase with device active layer thickness, but rather in an oscillatory manner with distinct interference maxima.[51-53] Additionally, it has been reported that at large active layer thicknesses and at the location of the secondary interference maxima (~200 nm), the charge carrier collection efficiency declines due to the formation of space-charge and alteration of the electric-field.[51] For our optimization, it is evident that the first interference maxima occurred for an active layer thickness of 100 nm. It is more plausible that the J_{sc} degraded due to optical effects rather than electrical as the device R_s values are invariant with an increase in active layer thickness, and these are often responsible for J_{sc} deccreases.[47] Contrarily, the R_{sh} consistently decreased with increased active layer thickness, representative of heightened recombination levels, as previously reported.[48, 54-55] Recombination levels have also been reported to increase with active layer thickness for BHJ devices.[51] The interpenetrated BHJ network naturally consists of "dead-ends" in the nanodomains, which restrict the transport of charge and eventually lead to bimolecular recombination of the separated charges.[56] As previously discussed, decreased R_{sh} values were correlated with a V_{oc} deterioration, which is shown here with an increase in active layer thickness as well as in previous reports.[51] The decreased R_{sh} also caused a decline in the FF, which continuously decreased with greater active layer thickness. A degradation in the FF with increased active layer thickness is typical for all types of OPVs,[41, 51, 53] besides those formed with specialized processing conditions.[6, 57] Since the devices with an active layer of 100 nm had the highest product of $J_{sc}V_{oc}FF$, those devices had the highest average PCE. For the devices with an active layer of

just 10 nm thinner (90 nm), the PCE decreased by 11%, which signified the importance of active layer optimization.

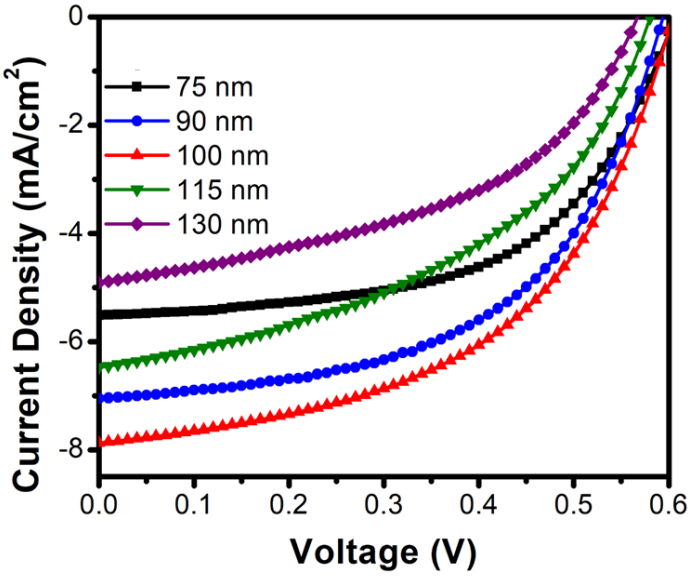

Figure 6.6. The current density – voltage (J-V) characteristics of OPV devices with thicknesses of 75, 90, 100, 115, and 130 nm.

Table 6.3. The J-V characteristics of the OPV devices with thicknesses of 75, 90, 100, 115, and 130 nm.

Thickness	J_{sc} (mA/cm^2)	V_{oc} (V)	FF	R_s (Ω·cm^2)	R_{sh} (Ω·cm^2)	PCE (%)	Largest PCE (%)
75 nm	-5.51 ± 0.08	0.61 ± 0.01	0.57 ± 0.03	11.58 ± 0.77	1432 ± 200	1.89 ± 0.06	1.96
90 nm	-7.05 ± 0.02	0.60 ± 0.01	0.52 ± 0.03	13.16 ± 0.92	890 ± 153	2.18 ± 0.27	2.40
100 nm	-7.88 ± 0.15	0.62 ± 0.01	0.51 ± 0.02	12.10 ± 2.2	502 ± 159	2.45 ± 0.05	2.61
115 nm	-6.47 ± 0.72	0.59 ± 0.01	0.46 ± 0.02	11.65 ± 0.96	447 ± 160	1.70 ± 0.11	1.89
130 nm	-4.91 ± 0.44	0.57 ± 0.01	0.45 ± 0.03	13.47 ± 0.92	376 ± 60	1.28 ± 0.19	1.61

6.3.3 Synthesis of AgNPs. As the active layer thickness of 100 nm was optimal for the reference devices, this limited thickness restricts the maximum light absorption and ultimately the performance. The addition of plasmonic nanoparticles can increase the absorption of the devices through the localized surface plasmon resonance (LSPR). For effective optical absorption enhancement of the active layer, the localized surface plasmonic resonance (LSPR) of the AgNPs should couple with the absorption peak (λ_{max}) of P3HT:PCBM. Anisotropic nanoplates were selected because the λ_{LSPR} is easily tunable over a wide range of visible wavelengths (**Figure 6.7**) by a simple adjustment of the Ag seed concentration during synthesis.[19-20] During synthesis, a lower Ag seed concentration correlates with an larger final lateral dimension (edge length) of the AgNPs, along with a greater aspect ratio (edge length to thickness) and λ_{LSPR} in solution.[15, 20] Based on experimental conditions, a varying percentage of the AgNPs were triangular-shaped prisms, which have been reported to create significant local electric field enhancements.[15, 58-59]

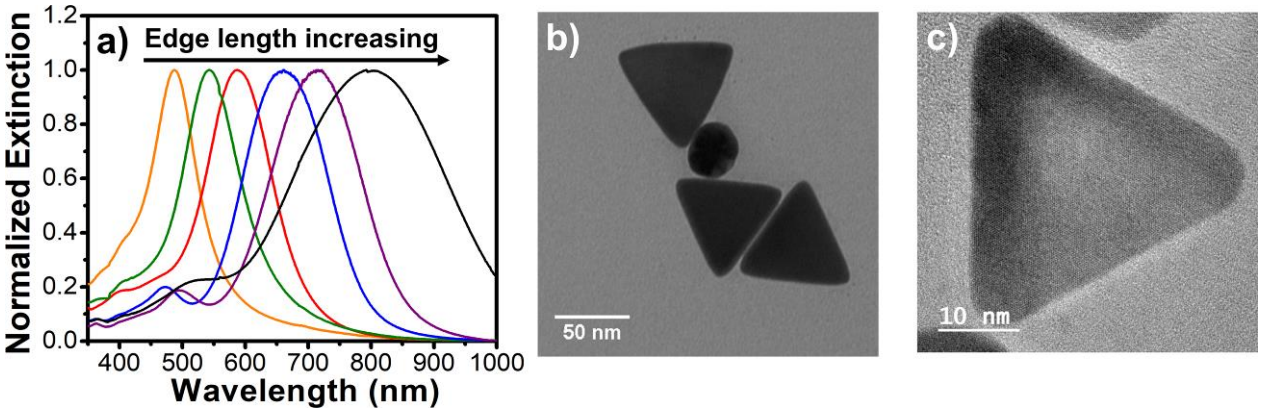

Figure 6.7. AgNPs characterization. (**a**) Normalized extinction spectra of the AgNPs with a variety of lateral dimensions (edge lengths) and corresponding λ_{LSPR}. TEM images of the AgNPs from the (**b**) Philips EM420 and (**c**) JEOL 2100.

6.3.4 PAH/AgNP ISAM films in OPV Devices. The deposition of ISAM films onto the ITO anode is a logical choice for the inclusion of AgNPs in OPV devices because it is does not require

centrifugation of the original AgNP solution. The AgNPs are a good candidate for ISAM fabrication as they are dispersed in an aqueous solution and hold a strong anionic surface charge due to the citrate capping layer.[31] PAH was chosen as the polycation since its functional amine groups ($–NH3^+$) provide a sufficient positive charge for successful ISAM growth. The pH of PAH was adjusted to a neutral value of 7.0, as at this pH, the majority of the PAH chains are ionized and are reported to tightly conform to the previous layer in a multilayer film.[60-61] The pH of the AgNP solution was found to be inherently neutral at 7.0 without any adjustment. ζ-potential measurements confirmed a positive surface charge for the PAH solution, and a negative surface charge for both the AgNP solutions and a diluted solution of PEDOT:PSS (to be used later) (**Figure 6.8**). All of the average ζ-potential magnitudes were similar and at a value that indicated solution stability (more discussion about ζ-potential solution stability later in this chapter).

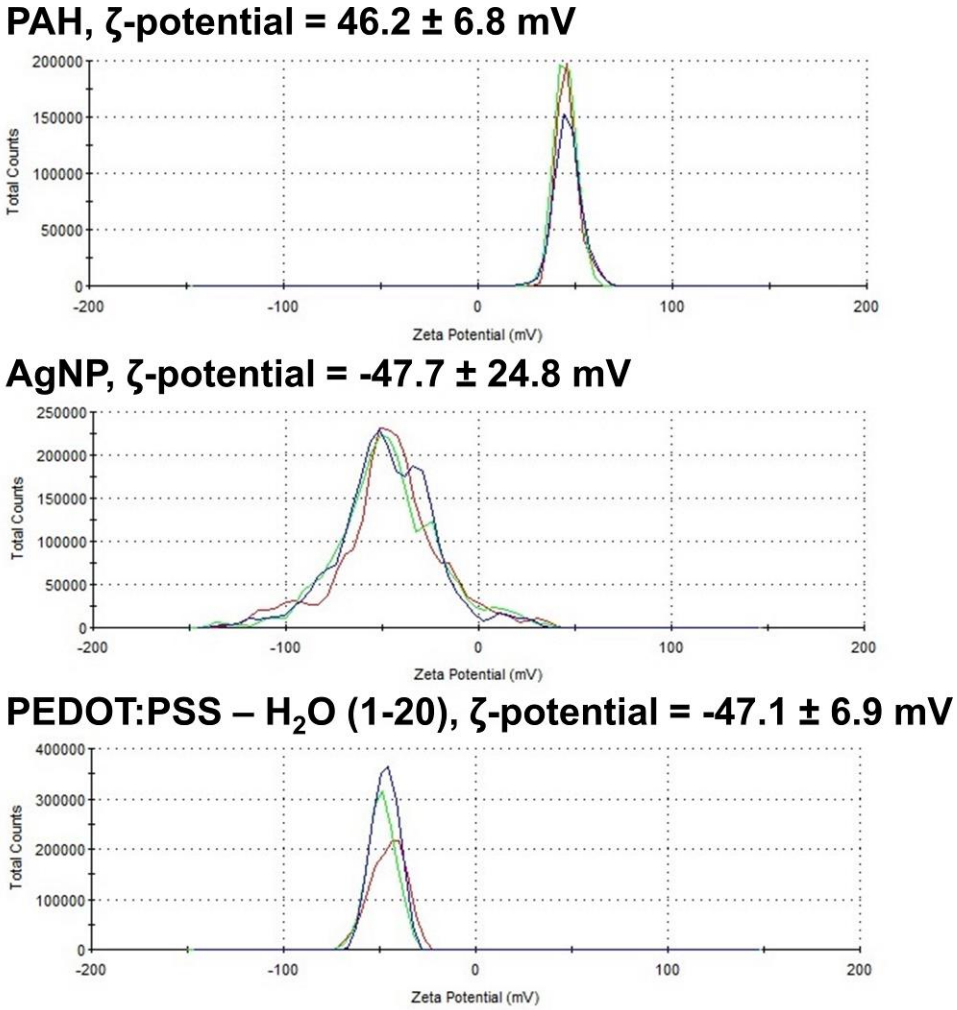

Figure 6.8. Raw ζ-potential measurements from PAH, AgNPs, and PEDOT:PSS – H_2O (1-20) solutions. The ζ-potential for each solution was averaged after three runs.

Preliminary testing involved growth of PAH/AgNP films for one, two, and three bilayers onto a blank glass slide, using a AgNP solution with λ_{LSPR} at 648 nm. With an increase in PAH/AgNP bilayers, the optical absorption intensity increased (**Figure 6.9a and 6.9b**), which is expected due to a larger density of AgNPs on the film. Furthermore, a greater number of PAH/AgNP bilayers caused a substantial broadening of the film absorption and a progressive red-shift of the λ_{LSPR} position. This red-shift has previously been reported to be caused by interparticle plasmonic coupling, which occurs when neighboring plasmonic nanoparticles are within close proximity.[62-

[64] Surface analysis of the films by SEM showed dense AgNP coverage, even for one bilayer (**Figure 6.9c**).

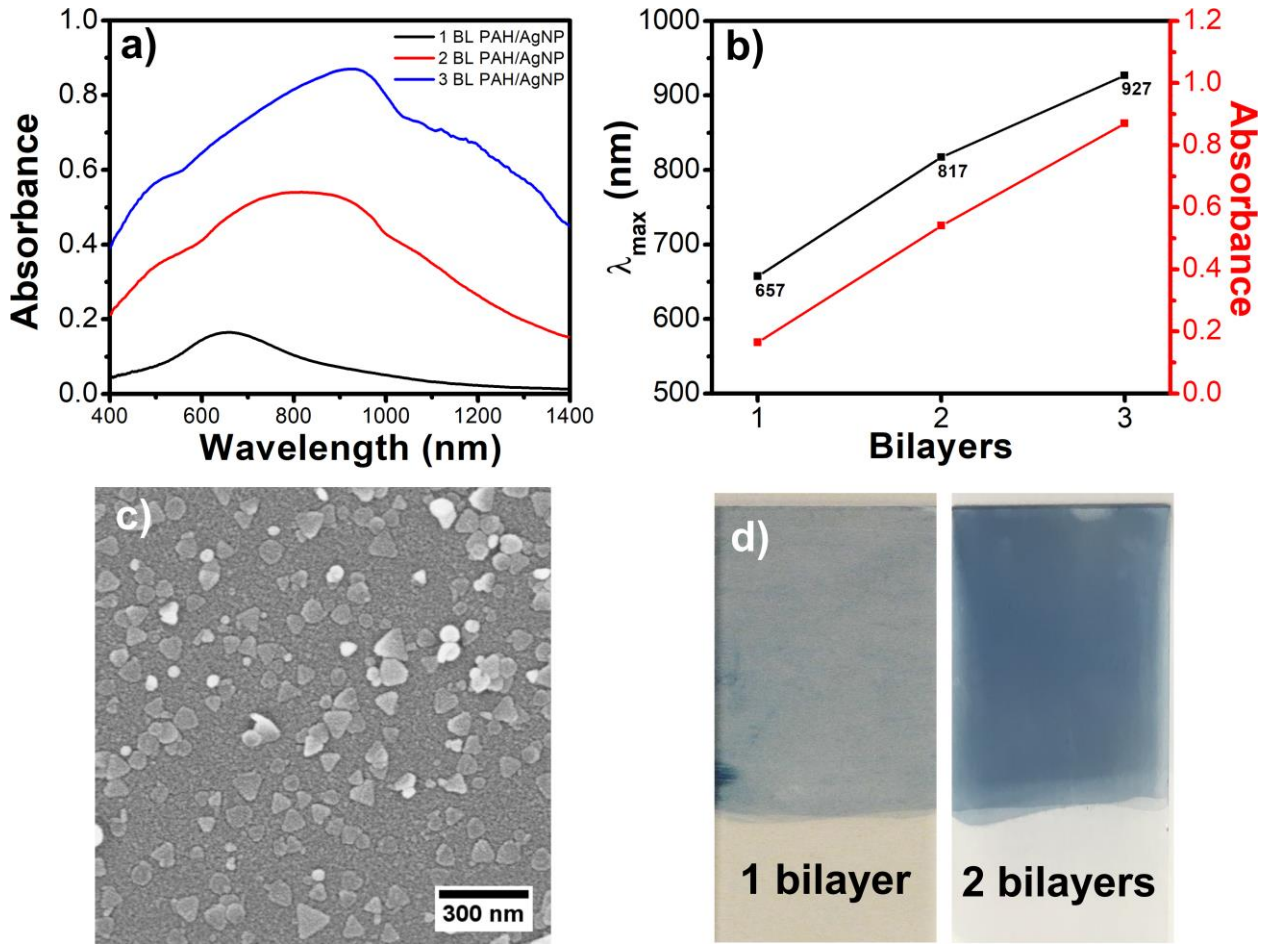

Figure 6.9. Characterization of PAH/AgNP ISAM films, using AgNP solution with λ_{LSPR} equal to 648 nm. (**a**) Optical absorption spectra for one, two, and three bilayers of PAH/AgNP. (**b**) The λ_{max} and peak absorption for one, two, and three bilayers of PAH/AgNP. (**c**) Representative SEM image of one bilayer of PAH/AgNP on glass. (**d**) Photograph of a one and two bilayer film of PAH/AgNP.

PAH/AgNP ISAM films were grown onto the ARC/glass/ITO substrate to be used for OPV devices (**Figure 6.10a**). For continuation of the OPV device fabrication, PEDOT:PSS/IPA was spin-coated on top of the PAH/AgNP film, which resulted in a complete elimination of the LSPR

absorption. The deterioration of the LSPR absorption signified the destruction of the AgNPs by PEDOT:PSS, which resulted from the susceptibility of AgNPs to acidic etching and the highly acidic properties of PEDOT:PSS (pH = 1.64).[27-28] Unfortunately, it has been reported that an increase in the pH above a value of 2.0 causes a continuous decline in the PEDOT:PSS electrical conductivity, and the AgNPs are etched when immersed in any solution with a pH below the neutral value of 7.0 (also confirmed in our own trials).[27-28] Due to the incompatibility of the AgNPs with PEDOT:PSS, other methods involving direct contact with the two materials, such as dispersing the AgNPs into PEDOT:PSS, were unsuccessful (**Figure 6.10b**). Here, AgNPs mixed with PEDOT:PSS/IPA solution at a 5 to 1 ratio and PEDOT:PSS/IPA (without AgNPs) were each spin-coated onto a blank glass slide. The λ_{LSPR} of the AgNPs is completely absent from the optical absorption of the films with the AgNPs, which signified that the AgNPs were destroyed by the PEDOT:PSS solution.

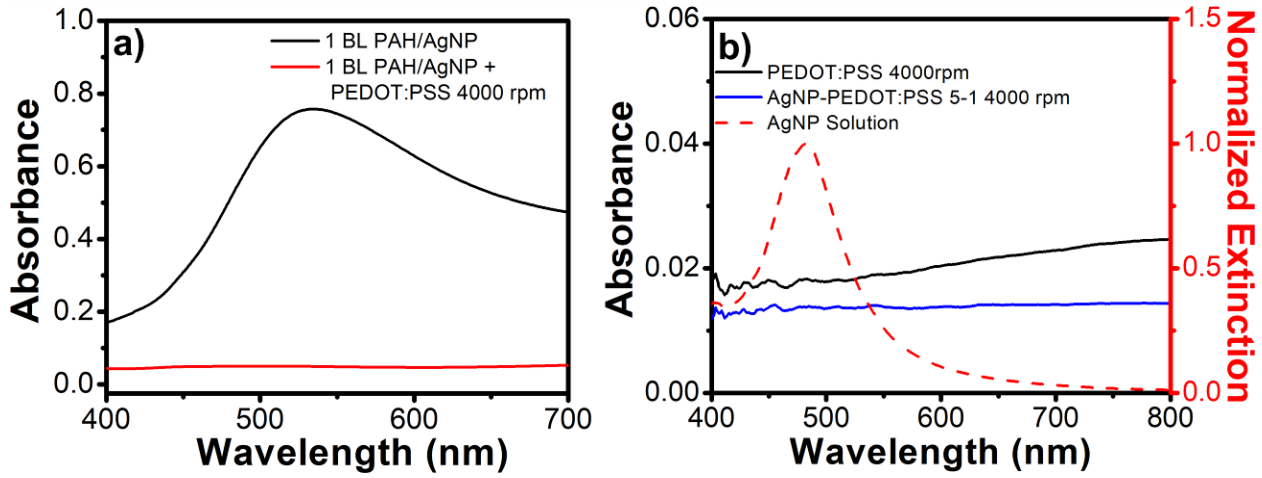

Figure 6.10. (**a**) Optical absorption spectra of one bilayer of PAH/AgNP and PEDOT:PSS spin-coated on top of the same film at 4000 rpm. (**b**) Optical absorption spectra of PEDOT:PSS spin-coated on to glass, and spin-coated AgNPs mixed with PEDOT:PSS at a ratio of 5-1 on glass. The normalized extinction of the AgNP solution is shown by the red dotted line.

6.3.5 PAH/PEDOT:PSS ISAM films as the Hole-Transport Layer. As stated by the manufacturer (Heraeus), the PEDOT:PSS used here (Clevios™ P VP AI 4083) has a PEDOT to PSS ratio of 1:6, mean particle size of 75 nm, a resistivity of 750 Ω-cm, and a work function of 5.2 eV.[65] Globular dispersion particles form in the aqueous solution due to the electrostatic attraction between the positively-charged, hydrophobic PEDOT and the negatively-charged, hydrophilic PSS.[65-67] The PEDOT:PSS 5.2 eV work function is critical for hole transport, as it is within the range of the work function of ITO (4.7 eV) and the HOMO level of P3HT (5.2 eV).[68] PEDOT:PSS is highly acidic due to the sulfonic acid on PSS, although this is essential for its electrical conductivity and work function.[27] Additionally, PEDOT:PSS in the spin-coated, dry form is reported to have a thin layer of PSS on top, which assists in the blocking of electrons.[66]

Next, PEDOT:PSS was utilized as a polyanion solution for ISAM films. The ultimate goal was to incorporate AgNPs with etching-resistant encapsulating layers into the ISAM films with PEDOT:PSS, but first a reference point was established with PAH/PEDOT:PSS ISAM films. After filtering, the concentrated PEDOT:PSS colloidal dispersion was diluted with DI water at a 1 to 20 ratio for ISAM film growth. Higher PEDOT:PSS-H_2O ratios, such as 1:50, required a very high number bilayers to produce a thickness comparable to the spin-coated PEDOT:PSS. PAH/PEDOT:PSS ("(1:20)" and "H_2O" are left out of the name for succinctness) ISAM films of 15 and 30 bilayers were constructed. All films containing PEDOT:PSS were annealed at 140 ºC for 20 minutes for OPV devices, as annealing removes the aqueous solvent, improves the conductivity of the film, and assists in lowering the work function to the appropriate value (5.2 eV).[69] However, even after annealing of the PAH/PEDOT:PSS ISAM films, partial dewetting and lack of uniformity of the spin-coated P3HT:PCBM layer occurred. Spin-coating a thin layer of PEDOT:PSS at 8000 rpm on top of the ISAM layer resolved the dewetting issue, while being thin

enough to preserve the LSPR enhancement effects of AgNPs, to later be included in the ISAM films. One annealing step for the entire HTL was performed after spin-coating the thin PEDOT:PSS layer on top of the ISAM film.

To investigate the variation in the P3HT:PCBM wettability, AFM height images (**Figure 6.11**), mean roughness (R_a), and the RMS roughness (R_q) (**Table 6.4**) were measured for the different HTL configurations before and after annealing. As revealed by the AFM height images, the PEDOT:PSS nanoparticles were clearly present in all of the films. After annealing, the spin-coated PEDOT:PSS R_a increased by 11%, whereas the PAH/PEDOT:PSS ISAM film's R_a decreased by 23%. Compared to the spin-coated PEDOT:PSS film, the PAH/PEDOT:PSS ISAM film had a 161% and 80% higher R_a before and after annealing, respectively. After spin-coating the thin layer of PEDOT:PSS on top of the ISAM film, the roughness values were significantly lower than both the PAH/PEDOT:PSS ISAM and the spin-coated PEDOT:PSS film.

The two primary factors that influence wettability are surface energy and roughness.[70-71] To maximize hydrophilic wettability, the surface energy and roughness should be as high and low as possible, respectively; whereas for hydrophobic wettability, surface energy and roughness must be as low and high as possible, respectively.[70] The surface energy (γ) of the active layer constituents and the underlying surface ($\gamma_{P3HT} \approx 27$ mN m^{-2}, $\gamma_{PCBM} \approx 38$ nM m^{-2}, $\gamma_{PEDOT:PSS} \approx 45$ mM m^{-2})[71-72] strongly govern the active layer phase separation morphology and performance.[71-72] It was previously reported that the surface energy of ZnO can be tuned through self-assembled monolayers (SAMs);when the ZnO surface energy was largely decreased ($\gamma \approx 30$ mN m^{-1}), partial dewetting occurred for the reported P3HT:PCBM film.[71] The increased roughness of the PAH/PEDOT:PSS ISAM film is associated with greater hydrophobicity and possibly lower surface energy (contact angle measurements are required for confirmation), which contributed to

the decreased wettability. Thus, the spin-coating of the thin PEDOT:PSS layer smoothed the PAH/PEDOT:PSS ISAM surface, which improved the wettability for the P3HT:PCBM layer.

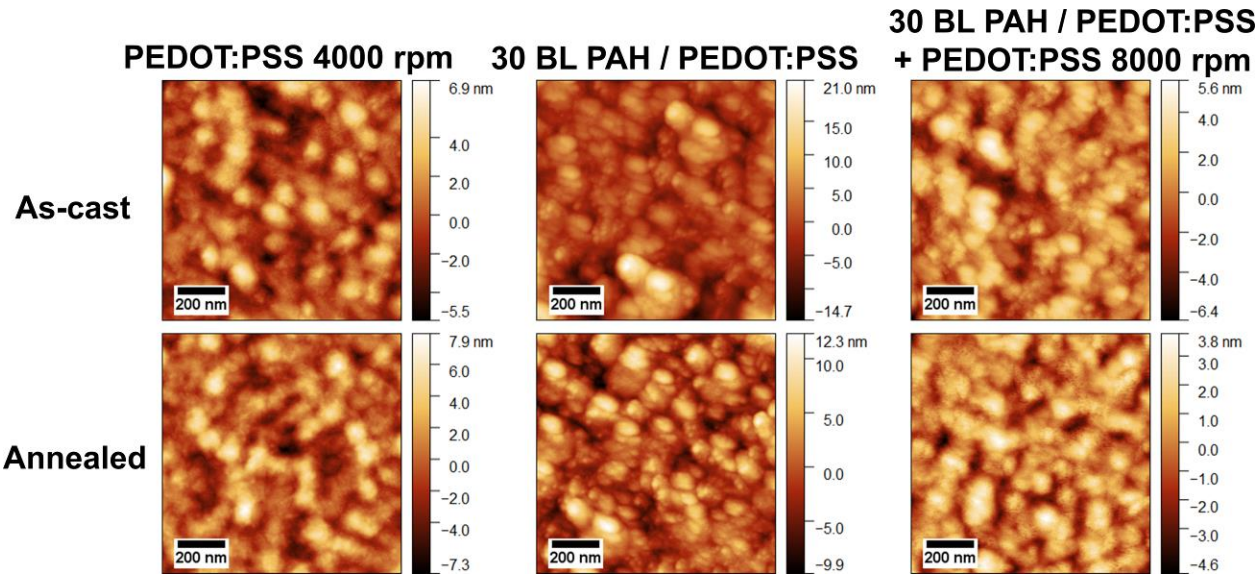

Figure 6.11. AFM height images of as-cast and thermally annealed films of spin-coated PEDOT:PSS (4000 rpm), 30 bilayers of PAH/PEDOT:PSS, and 30 bilayers of PAH/PEDOT:PSS with a thin layer of PEDOT:PSS spin-coated on top.

Table 6.4. Arithmetic mean roughness (R_a) and RMS roughness (R_q) of the AFM height images. The films include as-cast and thermally annealed films of spin-coated PEDOT:PSS (4000 rpm), 15 and 30 bilayers of PAH/PEDOT:PSS with a thin layer of PEDOT:PSS spin-coated.

Hole-transport layer	As-cast		Annealed (140 ^{o}C 20 min)	
	R_a (nm)	R_q (nm)	R_a (nm)	R_q (nm)
PEDOT:PSS spin-coat 4000rpm	1.8 ± 0.3	2.3 ± 0.4	2.0 ± 0.2	2.7 ± 0.6
30 BL PAH/PEDOT:PSS	4.7 ± 0.9	7.1 ± 1.8	3.6 ± 0.8	5.0 ± 1.7
30 BL PAH/PEDOT:PSS + PEDOT:PSS 8000rpm	1.5 ± 0.2	2.0 ± 0.3	1.3 ± 0.2	1.7 ± 0.3

The optical properties of the PAH/PEDOT:PSS ISAM films were measured and compared to the spin-coated PEDOT:PSS. Although PEDOT:PSS is mostly optically absorbing in the UV and IR wavelengths,[66] its absorption in the visible wavelengths can still be used as a comparison for thickness.[73] The optical absorption levels of the spin-coated PEDOT:PSS film were nearly the same as the 15 bilayer PAH/PEDOT:PSS ISAM film and slightly less than 30 bilayer films (both with a thin layer PEDOT:PSS), which indicated that the amount of PEDOT:PSS in all of the films was in the same range (**Figure 6.12a**). The optical absorption for the 15 bilayer PAH/PEDOT:PSS ISAM film, the spin-coated PEDOT:PSS, and the 30 bilayer PAH/PEDOT:PSS ISAM film was 0.024, 0.025, and 0.041, respectively. The film transmittance followed a reciporical trend to the optical absorption, in which the 15 bilayer PAH/PEDOT:PSS ISAM film, the spin-coated PEDOT:PSS, and the 30 bilayer PAH/PEDOT:PSS ISAM film had 89.48%, 88.65%, and 86.08% transmittance at 525 nm, respectively (**Figure 6.12b**).

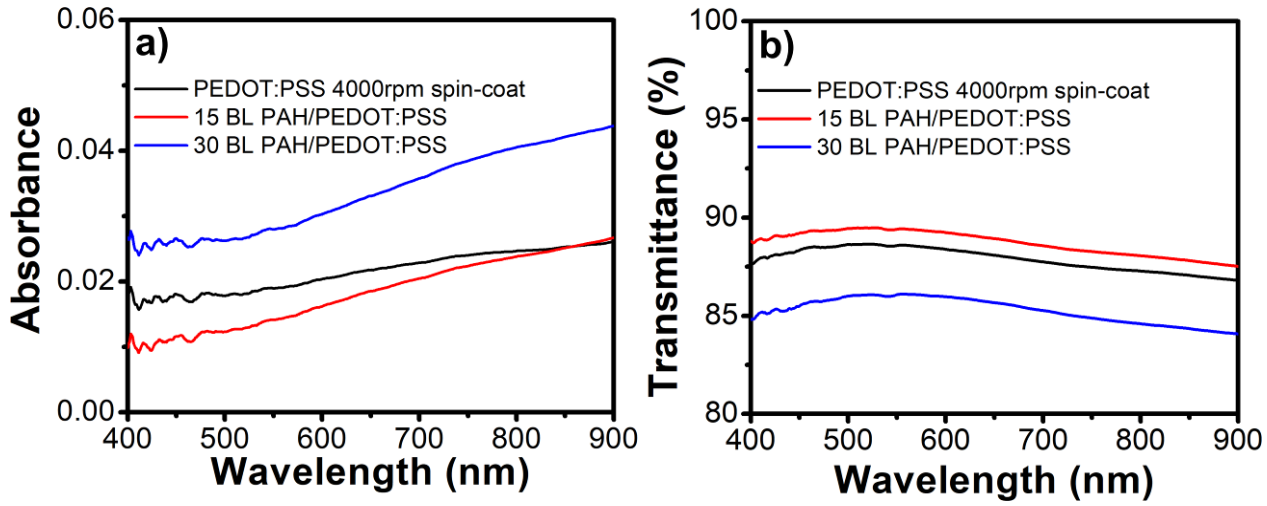

Figure 6.12. The (**a**) optical absorption and (**b**) transmittance of spin-coated PEDOT:PSS at 4000 rpm, 15 and 30 bilayer of PAH/PEDOT:PSS ISAM films with a thin layer of PEDOT:PSS spin-coated on top.

Increased thickness of the spin-coated PEDOT:PSS layer is also associated with lower sheet resistance.[65-66] Sheet resistance is defined as the ratio of resistivity to thickness. With resistivity kept constant, the sheet resistance should decrease with increased thickness (higher absorption). However, despite the smaller thickness of the spin-coated PEDOT:PSS film, its sheet resistance was slightly lower than the 30 bilayer PAH/PEDOT:PSS ISAM film (**Table 6.5**). Additionally, the 15 bilayer PAH/PEDOT:PSS ISAM film's sheet resistance was above the limit of the four-point probe (~70 MΩ/□). Therefore, either the addition of the PAH or the ISAM film morphology caused a decreased resistivity.

Table 6.5. Sheet resistance of spin-coated PEDOT:PSS (4000 rpm), and 30 bilayers of PAH/PEDOT:PSS with a thin layer of PEDOT:PSS spin-coated on top. "Contact limit" indicates that the sheet resistance was higher than the limit of the four-point probe.

Film	15 BL PAH/PEDOT:PSS	30 BL PAH/PEDOT:PSS	Spin-coated PEDOT:PSS
Sheet Resistance	Contact Limit	50 ± 18 MΩ/□	47 ± 9 MΩ/□

OPV devices were assembled with the different HTLs: spin-coated PEDOT:PSS 4000 rpm (reference), 15 and 30 bilayers of PAH/PEDOT:PSS ISAM films with PEDOT:PSS spin-coated on top. The J-V OPV performance was measured under the AM1.5G illumination (**Figure 6.13**), along with the calculation of the OPV device electrical and performance characteristics (**Table 6.6**). The 15 bilayer PAH/PEDOT:PSS ISAM film devices average PCE was 27% lower than the reference, although the 30 bilayer PAH/PEDOT:PSS devices average PCE was only 3% lower than the reference. The 15 bilayer PAH/PEDOT:PSS ISAM devices had a 49% higher R_s and a 26% lower R_{sh} compared to the reference devices. The 30 bilayer PAH/PEDOT:PSS ISAM devices had a 65% higher R_s and a 25% lower R_{sh} compared to the reference devices. The degradation of the parasitic resistances attributed to a decreased FF, J_{sc}, and the PCE.

R_s is directly related to the collective OPV device's active layer, electrode, and contact resistance.[40] The increased R_s was correlated to heightened sheet resistance of the PAH/PEDOT:PSS ISAM films in comparison to the spin-coated PEDOT:PSS films. Furthermore, energy level alignment is essential to limit charge carrier barrier heights, avoid Schottky contacts between layers, and reduce parasitic resistances.[71, 74] The addition of SAMs with functional amines

(similar to PAH) have been reported to reduce the ITO anode work function from 4.8 eV to 4.0 eV, which is favorable for inverted OPVs.[74] The addition of PAH to PEDOT:PSS likely increased the work function of either the ITO anode or the entire PEDOT:PSS film, which further contributed to resistance degradations. Future work would involve studying the thickness and number of the PEDOT:PSS and PAH layers in relation to conductivity. Other future development would consist of replacing PAH with a positively-charged, conjugated polymer such as polyaniline (PANI) that has a work function similar to PEDOT:PSS.[75]

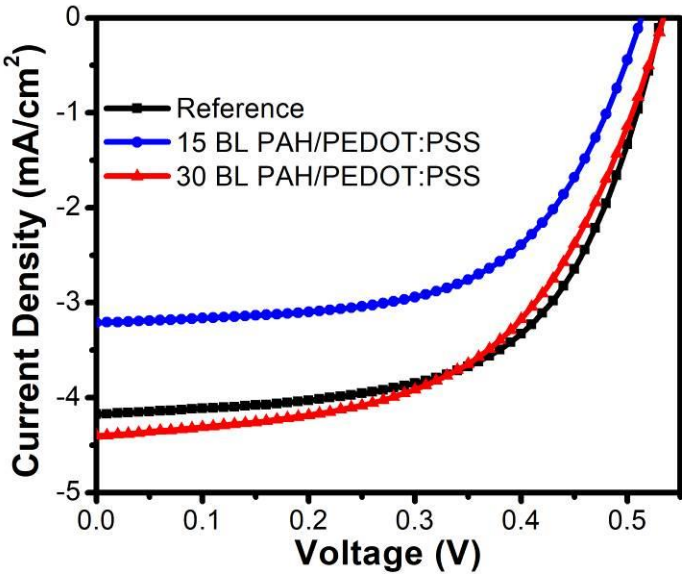

Figure 6.13. The current density – voltage (J-V) characteristics of OPV devices with HTLs of spin-coated PEDOT:PSS (4000 rpm), 15 and 30 bilayers of PAH/PEDOT:PSS with a thin layer of PEDOT:PSS spin-coated on top.

Table 6.6. The J-V characteristics of the OPV devices with HTLs of spin-coated PEDOT:PSS (4000 rpm), 15 and 30 bilayers of PAH/PEDOT:PSS with a thin layer of PEDOT:PSS spin-coated on top.

Film	J_{sc} (mA/cm^2)	V_{oc} (V)	FF	R_s (Ω·cm^2)	R_{sh} (Ω·cm^2)	PCE (%)
Reference	-4.18 ± 0.24	0.54 ± 0.01	0.59 ± 0.01	13.6 ± 0.7	2626 ± 312	1.33 ± 0.06
15 BL PAH/PEDOT:PSS	-3.21 ± 0.19	0.52 ± 0.01	0.55 ± 0.04	20.2 ± 3.0	1943 ± 297	0.97 ± 0.05
30 BL PAH/PEDOT:PSS	-4.42 ± 0.01	0.54 ± 0.00	0.53 ± 0.01	22.5 ± 1.7	1965 ± 343	1.29 ± 0.01

6.3.6 PAH Encapsulation of AgNPs. The encapsulation and functionalization of AgNPs by PAH provides a positive surface charge to the AgNPs, which would allow for the growth of ISAM films with the negatively-charged PEDOT:PSS. Theoretically, the final ISAM film would be comprised of the AgNPs evenly dispersed throughout the thickness. We used our experience and methods from the diazo-resin encapsulation of SiO_2 nanoparticles (as discussed in Chapter 4), and applied them to the AgNPs. In encapsulation of the AgNPs, the AgNP solution was diluted by a factor of 2 to avoid aggregation occurring from the PAH polymer chains attaching to multiple nanoparticles. The encapsulation of AgNPs (ENPs) involved the addition of dissolved PAH to the AgNP solution, and the ENPs were mixed overnight (12 h) for a final PAH concentration in the range of 0.5 to 10.0 mM (**Figure 6.14**). Visible inspection showed that in the range of 1.0 to 2.0 mM, the ENPs had precipitated out of the solution, which indicated solution instability. For concentrations above 3.0 mM, an increased PAH concentration caused the solution color to progressively shift towards a yellow color, characteristic of AgNP etching.[28]

The ζ-potential was measured for all of the ENP solutions to model how the surface charge changed with PAH concentration (**Figure 6.14a**). The negative ζ-potential at the lowest PAH concentration of 0.5 mM signified that an inadequate amount of PAH was in the solution to reverse the surface charge of the AgNPs. In the PAH range of 1.0 to 2.0 mM, the ζ-potential was close to zero and this explained why these solutions had instability (shown by the instability regime). For PAH concentrations above 3.0 mM, the ζ-potential remained positive and relatively constant in magnitude, meaning that the ENPs had successfully gained a positive surface charge.

The extinction spectra were measured for the ENP solutions with PAH concentrations of 3.0, 4.0, and 10.0 mM (**Figure 6.14b**). For ENPs with a PAH concentration closest to the instability regime, such a 3 mM, the extinction intensity increased toward the UV wavelengths, which has previously been reported to be distinctive of nanoparticle clustering.[76] The ENP solution with a PAH concentration of 4 mM was chosen for further ENP work, as it had the lowest PAH concentration that also exhibited solution stability without clustering. The extinction spectra also confirmed that the shift in the solution color represented AgNP etching, since the λ_{LSPR} peak blue-shifted with increased PAH concentration. At a PAH concentration of 10 mM, the λ_{LSPR} and solution color are identical to the AgNP seeds used for synthesis,[20] which indicated that the etching rendered the AgNPs to small and spherical. The blue-shifting of the ENPs also continued with increased time (**Figure 6.14c**) and the rate decreased as the λ_{LSPR} approached similar wavelengths as AgNP seeds.

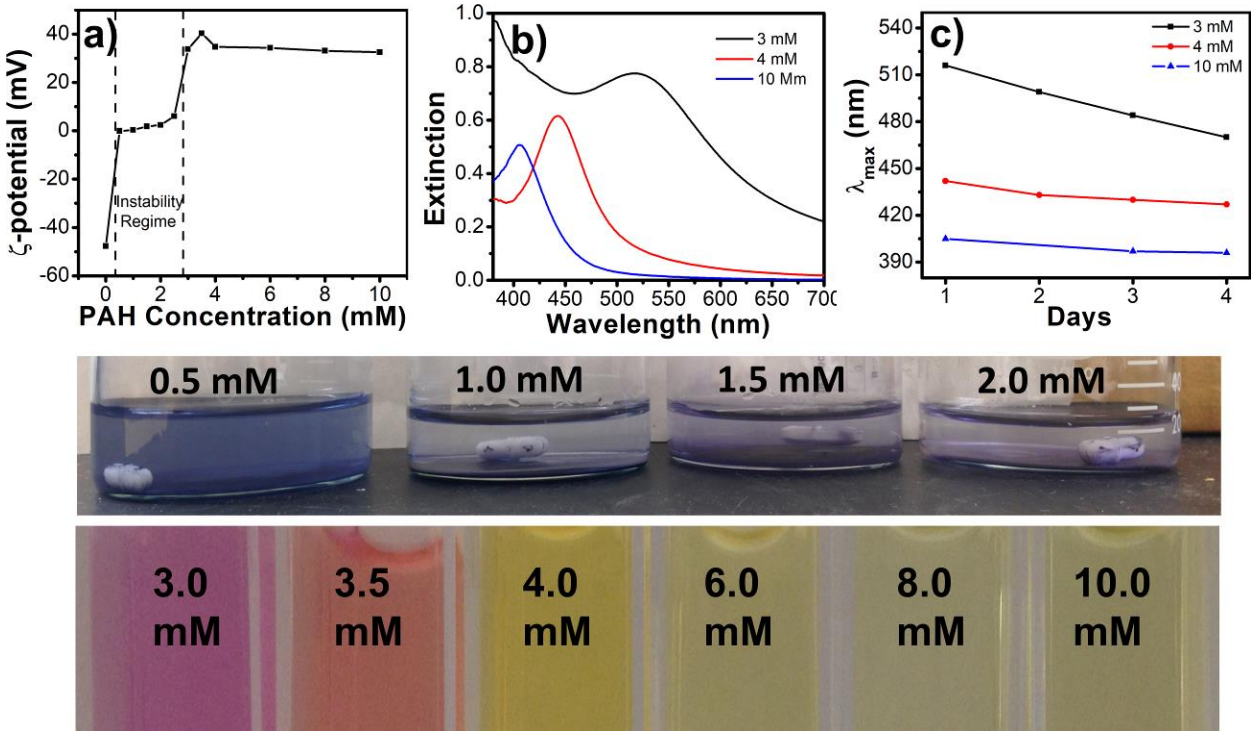

Figure 6.14. Characterization of encapsulated AgNPs (ENPs) with PAH concentration in the range of 0.5 mM to 10.0 mM. (**a**) ζ-potential measurements for ENPs for a range of final PAH concentrations (0.5 – 10.0 mM). (**b**) Extinction of the ENP solutions with the PAH concentration of 3.0 mM, 4.0 mM, and 10.0 mM after one day. (**c**) The change in the ENPs extinction λ_{LSPR} peak over the course of three days.

According to previous reports of AgNP etching,[28-29] it was hypothesized that the etching of the ENPs was attributed to either a low pH or from excess chloride counterions in the PAH solution. Previously, we found that etching occurred with any pH below neutral value. As freshly dissolved PAH powder in the aqueous solution was found to have a pH of 4.0, the pH of the PAH solution was adjusted to 7.0 to alleviate AgNP etching. For PAH with a neutral pH added to AgNPs for a final concentration of 4 mM, the λ_{LSPR} peak of the extinction spectra showed no blue-shift (**Figure 6.15a**), and therefore a neutral pH for PAH was used for all work with the ENPs. After formation of the ENP solution with a final PAH concentration of 4 mM, the solution was used to produce 15,

20, and 30 bilayer ENP/PEDOT:PSS ISAM films. However, optical absorption revealed that the PEDOT:PSS etched the ENPs in the film form, as shown by the absence of the extinction λ_{LSPR} peak (**Figure 6.15b**). Even with the coverage of the AgNPs by PAH, they lacked resistance to etching from the acidic PEDOT:PSS.

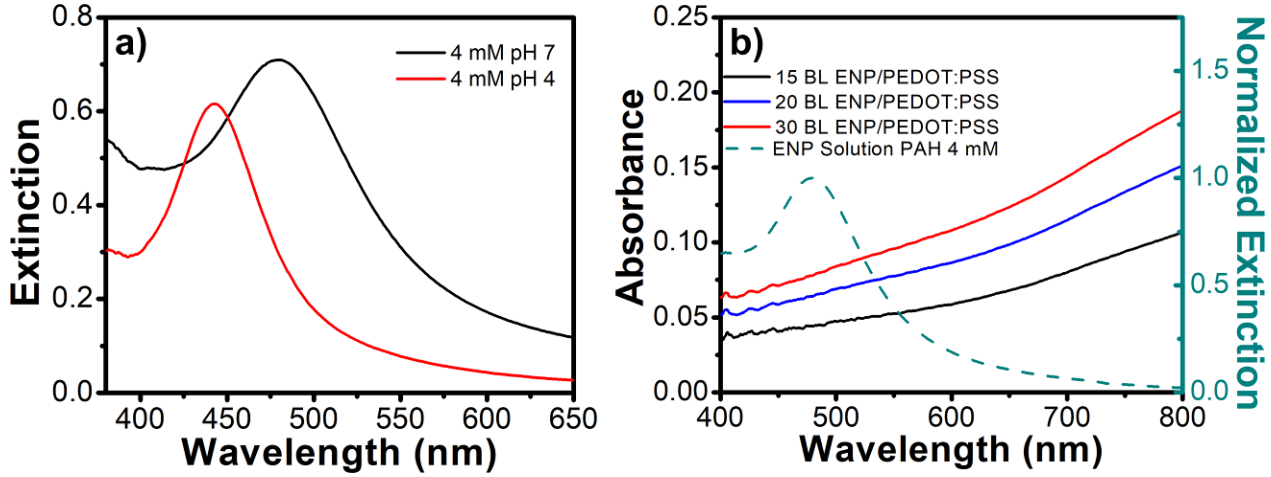

Figure 6.15. (**a**) Extinction spectra of ENPs with PAH at a final concentration of 4 mM. The starting pH of the PAH solution was tested at both 4 and 7. (**b**) Optical absorption of 15, 20, and 30 ENP/PEDOT:PSS ISAM films. The normalized extinction of the ENP with PAH at a final concentration of 4 mM and a starting pH of 7 is shown by the green dotted line.

6.3.6 Gold coating of AgNPs for Etching-Resistance. The high surface energy of [100] edges on AgNPs is an important aspect for their anisotropic growth, but these facets are unstable due to their abundance in defects that are especially susceptible to etching and rounding.[30, 38] Protection against etching is possible by the epitaxial growth of gold atoms onto the high-energy [100] edges of the AgNPs, without modification to the stable silver [111] face.[30, 38] The end result is particles with the superior optical properties of silver, while harnessing the enhanced stability of gold. However, optimization is required for the deposition of gold to avoid galvanic replacement, an

unfavorable process in which gold ions ($AuCl_4^-$) are reduced by a rapid oxidation and dissolving of silver from the [111] face.

Gold chloride ($HAuCl_4$) was reduced to $AuCl_4^-$ in solution by ascorbic acid and mixed with the AgNPs for the ratios of Au:Ag at 0.01:1, 0.033:1, 0.06:1, and 0.085:1 to produce gold-coated silver nanoplates (AuAgNPs). As gold was deposited directly onto the AgNP edges, the extinction λ_{LSPR} peak red-shifted with an increase of gold concentration due to the increase in lateral dimension (edge length) of the AuAgNPs and the higher dielectric constant of gold compared to silver (**Figure 6.16a**).[30, 38] The λ_{LSPR} red-shift was additionally apparent by the change in the AuAgNP solution color after the addition of gold. For an Au:Ag ratio of 0.06:1, TEM revealed that the AuAgNPs were free of pinholes from galvanic replacement and their shape was similar to the original AgNP (**Figure 6.16b**). A faint, rough gold coating of the AuAgNPs edges with the ratio 0.06:1 was clearly seen by zooming in one of the edges and increasing the contrast of the TEM image (**Figure 6.16d**). For the highest ratio of 0.085:1, the gold coating could be clearly seen by the dark outline around the AuAgNPs, however, galvanic replacement of the AuAgNPs and the formation of small gold nanospheres (due to the excess of gold) was widely present throughout this sample (**Figure 6.16b**).

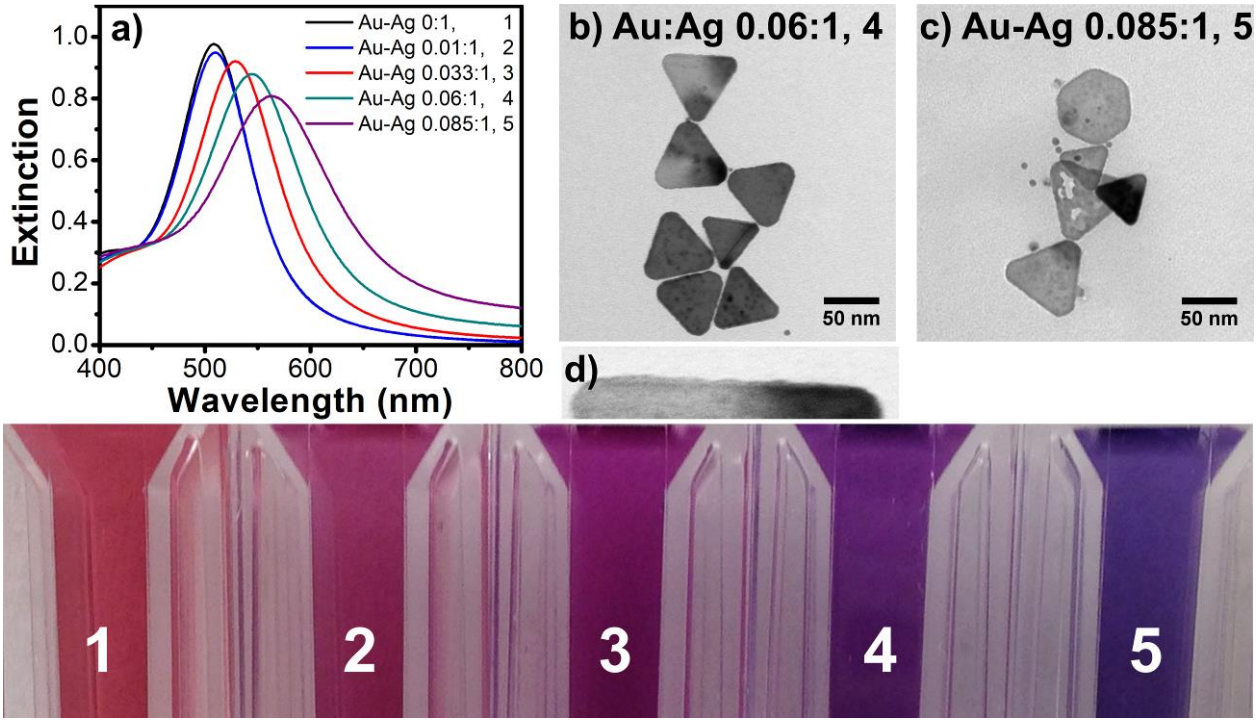

Figure 6.16. Characterization of gold-coated AgNPs (AuAgNPs). (**a**) Extinction spectra of AuAgNPs at Au:Ag ratios of 0:1, 0.01:1, 0.033:1, 0.06:1, and 0.085:1. TEM images for AuAgNPs with Au:Ag ratios of (**b**) 0.06:1, (**c**) 0.08:1, and (**d**) 0.06:1 with a zoom-in on one of the edges. The photograph represents the AuAgNP for the range of Au:Ag ratios, labelled with the number corresponding to the extinction spectra.

Previous reports related to AuAgNPs analyze their resistance against chloride (NaCl) etching, but lack pertinent information about stability in acidic conditions.[30, 38] The inclusion of the AuAgNPs in the HTL required their compatibility with the acidic PEDOT:PSS and specifically the sulfonic acid group on PSS. Sulfuric acid was used to assess the acidic stability of the AuAgNP. As the pH of PEDOT:PSS is approximately 1.6,[27] H_2SO_4 concentrations of 1, 5, and 10 mM of pH was 2.7, 2, 1.7, respectively were added to the AuAgNPs . For AuAgNPs with ratios 0:1 (bare AgNPs) and 0.01:1, the extinction λ_{LSPR} peak was significantly blue-shifted as the H_2SO_4 concentration was increased from 0 to 5 mM, and the AuAgNPs were completely dissolved at

concentration of 10 mM (**Figure 6.17**). The blue-shift in the λ_{LSPR} indicated rapid etching of the AuAgNPs by the acid, due to inadequate gold coverage at Au:Ag ratio of 0.01:1. For Au:Ag ratios of 0.033:1, 0.06:1, and 0.085:1, the addition of H_2SO_4 at a concentration of 5 mM and 10 mM caused a small blue-shift in the λ_{LSPR} attributed to a marginal number of AuAgNPs in each sample without a complete coating of gold. Thus, for Au:Ag ratios at and above 0.033:1, the gold coverage provided the AuAgNPs stability against acidic etching. Since 0.06:1 was the highest Au:Ag ratio without galvanic replacement, it was chosen for additional work with AuAgNPs.

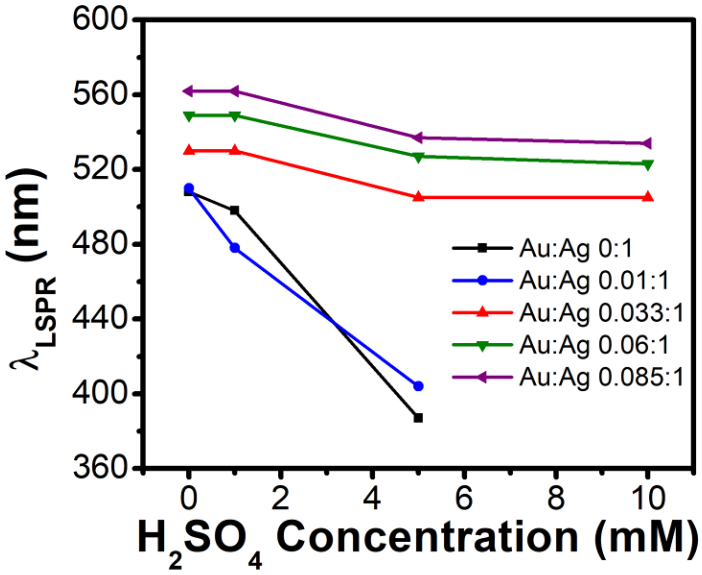

H_2SO_4 (mM)	pH
1	2.7
5	2
10	1.7

For H_2SO_4: $[H^+] = 2 \times H_2SO_4$ M
pH = - log ([H+])

i.e. 1 mM H_2SO_4 :
pH = - log (0.002) = 2.7

$pH_{PEDOT:PSS} \approx 1.6$ (10 mM H_2SO_4)

Figure 6.17. Relationship of the extinction λ_{LSPR} peak for AuAgNPs with Au:Ag ratios of of 0:1, 0.01:1, 0.033:1, 0.06:1, and 0.085:1. Table of H_2SO_4 concentration and the respective pH value, as well as information on calculation of pH.

6.3.7 AuAgNPs in the HTL for OPV Devices. OPV devices were processed with one and three bilayer PAH/AuAgNP ISAM films onto the ITO anode using AuAgNPs (Au:Ag = 0.06:1) with λ_{LSPR} of 584 nm in the aqueous solution. The optical absorption of the one and three bilayers of PAH/AuAgNP ISAM films had average λ_{max} at 642 and 646 nm (before spin-coating

PEDOT:PSS), respectively (**Figure 6.18a**). Both the one and three bilayer films had nearly identical red-shifts from the solution λ_{LSPR} to the film λ_{max}, which was substantially different than the previously discussed PAH/AgNP ISAM films (**Figure 6.9a**). These distinctions are attributed to the different processing techniques and substrates (glass compared to ITO), but their evaluation would require future analysis not reported here. After spin-coating PEDOT:PSS on the ISAM films, the one bilayer films' average λ_{max} remained at 642 nm, and the absorption intensity increased by 25% (0.019 to 0.026) because of the added PEDOT:PSS absorption (**Figure 6.18a**). The three bilayer films' average λ_{max} blue-shifted from 646 to 621 nm, and the absorption intensity decreased by 36% (0.069 to 0.044). Therefore, the optical absorption revealed that although a minimal amount of etching occurred, the AuAgNPs were significantly more resistant to the acidic PEDOT:PSS etching than the bare AgNPs.

The optical absorption of the active layer was significantly enhanced with the incorporation of the PAH/AuAgNP ISAM films (**Figure 6.18b**). As discussed previously (**Figure 6.3**), the HTL and ITO optical absorption were subtracted from the total absorption for isolation of the P3HT:PCBM optical absorption spectra ($A_{P3HT:PCBM} = A_{Total} - A_{HTL} - A_{ITO}$). In comparison to the reference device active layer films, the average absorption intensity of the active layer increased by 15% (0.40 to 0.46) and 18% (0.40 to 0.47) for the devices with the one and three bilayer PAH/AuAgNP ISAM films, respectively. The increased active layer absorption intensity was attributed to the coupling of the AuAgNP LSPR to P3HT:PCBM, as well as possible light scattering enhancements from the AuAgNPs.

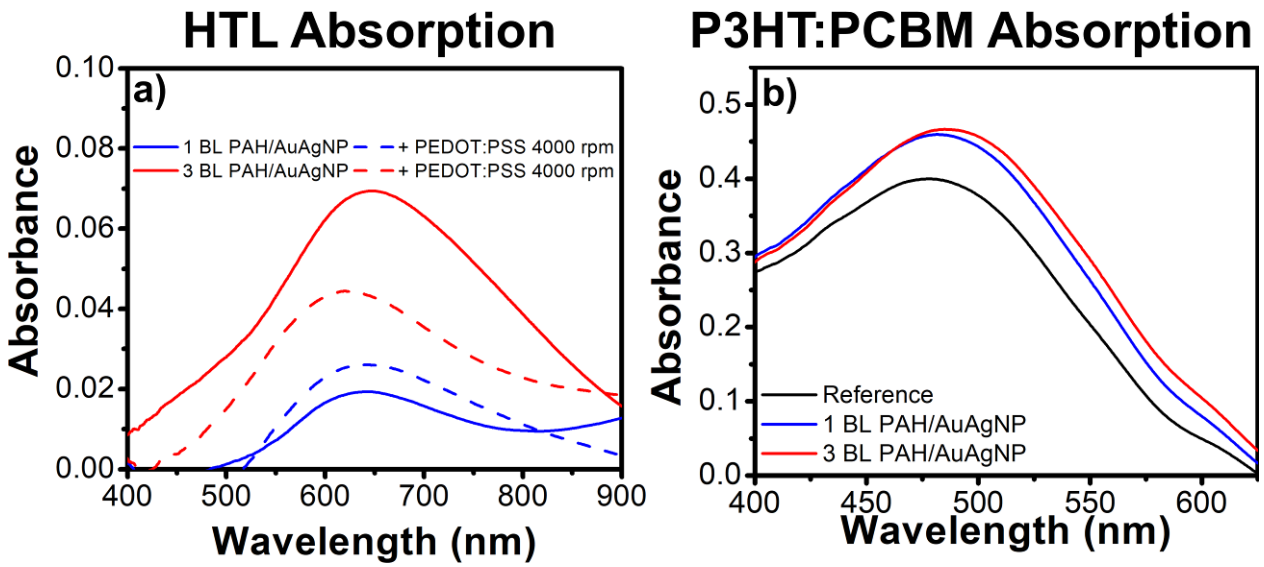

Figure 6.18. (**a**) Optical absorption of just the HTL: one and three bilayers of PAH/AuAgNP ISAM films on ITO before (solid lines) and after spin-coating PEDOT:PSS at 4000 rpm (dashed lines). (**b**) Optical absorption of just P3HT:PCBM with the different HTL absorptions subtracted out.

The J-V curves were measured under AM1.5G illumination for OPV devices with one and three bilayers of PAH/AuAgNP on the ITO anode (**Figure 6.19a**). The reference devices at this time had J_{sc} of -4.18 mA/cm^2, V_{oc} of 0.54 V, FF of 0.59, and PCE of 1.33% (**Table 6.7**). In comparison to the reference devices, the one bilayer PAH/AuAgNP ISAM film OPV device had a 17% higher J_{sc}, a 7% lower V_{oc}, a 19% lower FF, and a 14% lower PCE. Also in comparison to the reference devices, the three bilayer PAH/AuAgNP ISAM film OPV device had nearly the same J_{sc} and V_{oc}, a 12% lower FF, and a 14% lower PCE. The decreased performance was reflected in the average external quantum efficiency (EQE) spectra where the reference, one, and three bilayer PAH/AuAgNP ISAM film OPV devices had peak EQE of 50.5% @ 470 nm, 43.3% @ 475 nm, and 33.7% @ 490 nm, respectively (**Figure 6.19b**).

The substantially higher R_s, lower R_{sh}, and consequently, lower FF, are clearly responsible for the decreased PCE for the one and three bilayer PAH/AuAgNP ISAM film devices. Interestingly, the R_s and R_{sh} values improved with more bilayers. The comparative decrease in R_s with more bilayers, may suggest that the AuAgNPs were assisting hole-transport to the ITO anode, but the overall increase in R_s compared to the reference devices was linked to the presence of the PAH (as discussed previously). Even with the heightened R_s values, the J_{sc} increased for the OPV devices with the one bilayer PAH/AuAgNP ISAM films, which was correlated to the enhanced optical absorption from the active layer. This increase in the J_{sc} was promising, as it signified that a thin layer of AuAgNPs could potentially lead to device enhancements with future ISAM film modifications.

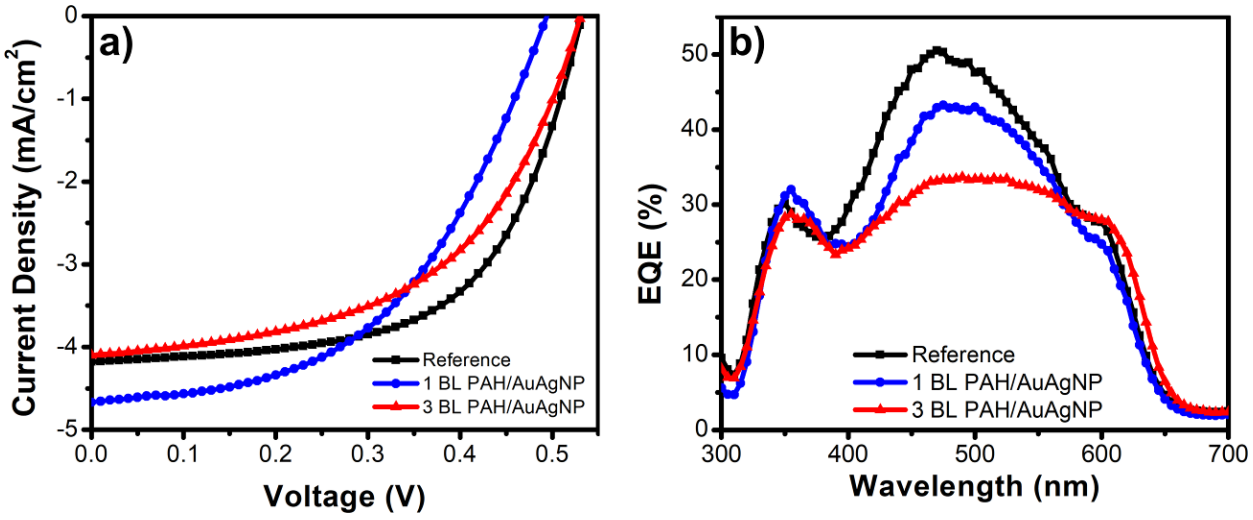

Figure 6.19. (**a**) The current density – voltage (J-V) characteristics of OPV devices with one and three bilayers of PAH/AuAgNP ISAM films on ITO, and the reference device. (**b**) The corresponding external quantum efficiency (EQE) spectra.

Table 6.7. The J-V characteristics of the OPV devices with one and three bilayers of PAH/AuAgNP ISAM films on ITO, and the reference device.

Film	J_{sc} (mA/cm^2)	V_{oc} (V)	FF	R_s (Ω·cm^2)	R_{sh} (Ω·cm^2)	PCE (%)
Reference	-4.18 ± 0.24	0.54 ± 0.01	0.59 ± 0.01	13.57 ± 0.7	2626 ± 312	1.33 ± 0.06
1 BL PAH/AuAgNP	-4.79 ± 0.03	0.50 ± 0.00	0.48 ± 0.02	25.90 ± 3.3	863 ± 208	1.15 ± 0.04
3 BL PAH/AuAgNP	-4.10 ± 0.41	0.54 ± 0.01	0.52 ± 0.03	18.19 ± 2.1	1038 ± 120	1.14 ± 0.07

The final method explored here integrated PAH/PEDOT:PSS and PAH/AuAgNP ISAM films together to make PAH/PEDOT:PSS/PAH/AuAgNP quadlayers for use in OPV devices. Two and three PAH/PEDOT:PSS/PAH/AuAgNP quadlayers were grown onto ITO, and the AuAgNPs had an Au:Ag ratio of 0.06:1 and a λ_{LSPR} of 532 nm in the aqueous solution. The two and three quadlayer ISAM films showed an optical absorption λ_{max} at 549 and 595 nm with absorption intensities of 0.107 and 0.161, respectively (**Figure 6.20a**). Although the acidic PEDOT:PSS layers were in close contact with the AuAgNPs within the films, the absorption intensities for the three quadlayer ISAM films were more than doubled compared to the PAH/AuAgNP ISAM films for the same number of AuAgNP layers (0.161 compared to 0.069). Even though the increased absorption was partially attributed to the added PEDOT:PSS absorption, this showed that multiple layers of PEDOT:PSS did not lead to drastic AuAgNP degradations. Similar to the PAH/PEDOT:PSS films, a thin layer of PEDOT:PSS was spin-coated at 8000 rpm on top of the quadlayer ISAM films to improve the wettability of P3HT:PCBM. After spin-coating PEDOT:PSS on top of the two quadlayer ISAM film, the λ_{max} red-shifted from 549 to 586 nm, and the absorption intensity decreased by 28% (0.107 to 0.071). When PEDOT:PSS was spin-coated onto the three

quadlayer ISAM film, the λ_{max} blue-shifted slightly from 595 to 590 nm, and the absorption intensity decreased by 22% (0.161 to 0.125). The strong optical absorption intensities before and after spin-coating PEDOT:PSS again displayed the AuAgNP acidic etching resistance.

The inclusion of the quadlayer ISAM films into the OPV devices resulted in active layer optical absorption enhancements (**Figure 6.20b**). For the P3HT:PCBM spectra, the two and three quadlayer films increased the average optical absorption intensity by 8% (0.40 to 0.43) and 13% (0.40 to 0.45) compared to the reference films, respectively. The optical absorption enhancements were correlated to the LSPR effects from the AuAgNPs.

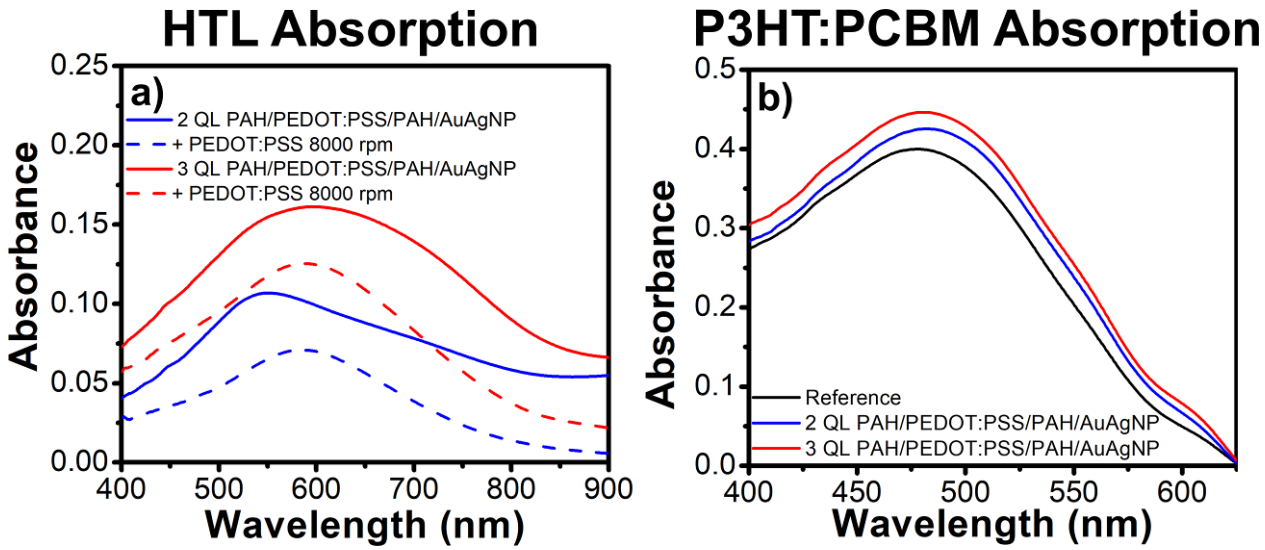

Figure 6.20. (**a**) Optical absorption of just the HTL: two and three quadlayers of PAH/PEDOT:PSS/PAH/AuAgNP on ITO before (solid lines) and after spin-coating PEDOT:PSS at 8000 rpm (dashed lines). (**b**) Optical absorption of just P3HT:PCBM with the different HTL absorptions subtracted out.

J-V curves were measured for both reference OPV devices and devices with HTLs that consisted of two and three quadlayers of PAH/PEDOT:PSS/PAH/AuAgNP with a thin layer of spin-coated PEDOT:PSS (**Figure 6.21a**). The reference OPV devices at this time had J_{sc} of -6.40 mA/cm^2, V_{oc}

of 0.60 V, FF of 0.54, and PCE of 2.07% (**Table 6.8**). Compared to the reference devices, the devices with the two quadlayer films showed significant degradations with a 18% lower J_{sc}, a 12% lower V_{oc}, a 24% lower FF, and a 37% lower PCE. For the devices with the three quadlayer films, the J_{sc} and PCE were 27% and 32% lower than the reference devices, respectively, but the V_{oc} was only 5% lower, and the FF was identical. For the comparison of the EQE spectra, the reference devices had a peak of 44.7% @ 475 nm, and the three quadlayer OPV devices did not have a discernible peak, but had a maximum of 37.5% @ 405 nm.

The R_s, R_{sh}, and FF dramatically improved from two to three quadlayers of PAH/PEDOT:PSS/PAH/AuAgNP. The sigmoidal shape of the J-V curve for the two quadlayer device is signature of space-charge limited current (as discussed previously for the high deposition rates of aluminum),[12] and has also been reported for devices with inadequate PEDOT:PSS thicknesses.[69] The two quadlayer device simply lacked the necessary amount of PEDOT:PSS for practical device operation. Surprisingly, the three quadlayer device had equivalent R_s, R_{sh}, and FF values compared to the reference devices, which indicated that the HTLs for these devices were effectively transporting holes to the ITO anode. Future exploration would provide a greater understanding for the charge transport properties for these quadlayer ISAM films in OPV devices.

The J_{sc} diminished with a greater number AuAgNPs layers in quadlayer ISAM film devices, despite the increased optical absorption of the active layer. The three quadlayer ISAM film devices' EQE spectra was partially equal to the reference devices', but with a mostly flattened peak and the EQE (%) values decreased as wavelengths trended from 395 to 610 nm. The flattened EQE spectra was puzzling as the optical absorption was increased for the active layer, and the R_s and R_{sh} were relatively unchanged, but future work would be required to answer this question.

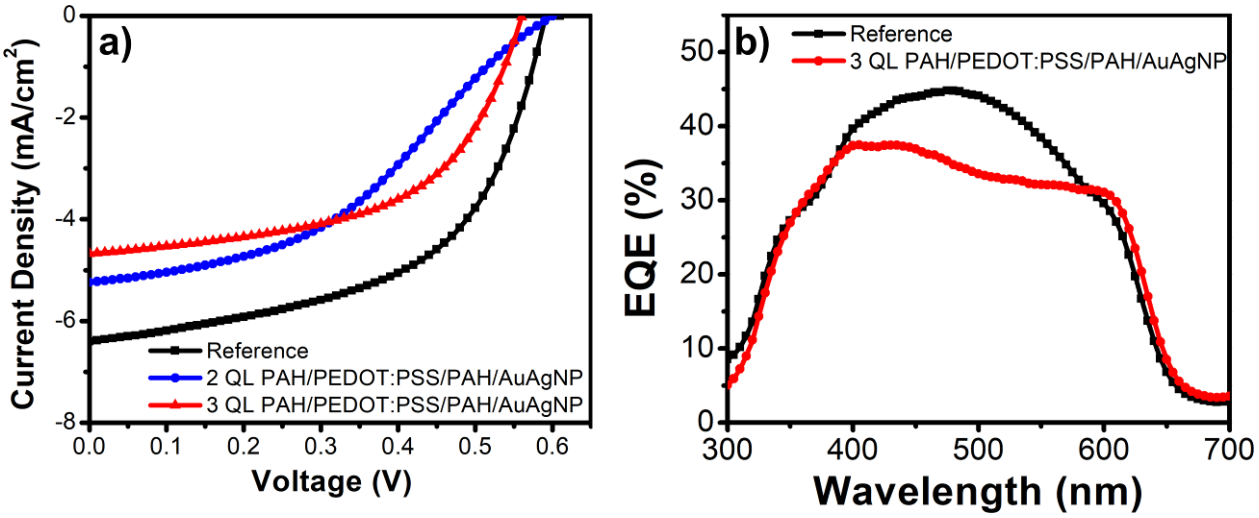

Figure 6.21. (**a**) The current density – voltage (J-V) characteristics of OPV devices with two and three quadlayers of PAH/PEDOT:PSS/PAH/AuAgNP ISAM films on ITO with PEDOT:PSS spin-coated on top at 8000 rpm, and the reference device. (**b**) The corresponding external quantum efficiency (EQE) spectra.

Table 6.8. The J-V characteristics of the OPV devices with two and three quadlayers of PAH/PEDOT:PSS/PAH/AuAgNP ISAM films on ITO with PEDOT:PSS spin-coated on top at 8000 rpm, and the reference device.

Film	J_{sc} (mA/cm^2)	V_{oc} (V)	FF	R_s (Ω·cm^2)	R_{sh} (Ω·cm^2)	PCE (%)
Reference	-6.40 ± 0.14	0.60 ± 0.01	0.54 ± 0.01	14.56 ± 0.7	1110 ± 180	2.07 ± 0.05
2 QL PAH/PEDOT:PSS/ PAH/AuAgNP	-5.24 ± 0.33	0.53 ± 0.01	0.41 ± 0.04	136.14 ± 67.4	592 ± 155	1.30 ± 0.18
3 QL PAH/PEDOT:PSS/ PAH/AuAgNP	-4.68 ± 0.21	0.57 ± 0.01	0.54 ± 0.01	15.00 ± 0.5	1080 ± 128	1.41 ± 0.02

6.4 CONCLUSIONS

In this chapter we (1) presented the optimization processes of reference OPV devices with the P3HT:PCBM active layer and (2) discussed the enhancement of the active layer optical absorption with the addition of encapsulated plasmonic silver nanoplates (although other factors prevented increased PCE increases in all cases). Post-annealing of the reference devices after the deposition of the Al cathode was found to increase the power conversion efficiency significantly and improved all the J-V device characteristics. We emphasized the importance of low Al deposition rates for effective post-annealing performance enhancements. Along with annealing conditions, it was confirmed that an increase of thickness of the P3HT:PCBM active layer intensified the optical absorption. The optimal OPV device active layer thickness was found to be 100 nm, and these devices had average short-circuit current (J_{sc}) and power conversion efficiency (PCE) of -7.88 mA/cm^2 and 2.45%, respectively. However, the performance and the optical absorption were essentially capped for the reference devices at this active layer thickness, as increasing the thickness further led to fill-factor and performance degradations.

Enhancement of the optical absorption was accomplished through coupling of the localized surface plasmon resonance (LSPR) frequency of anisotropic silver nanoplates (AgNPs) with the active layer maximum absorption frequency. AgNPs synthesis was carried out by a seed-mediated growth method, in which the AgNP LSPR frequency and edge length were highly tunable, and the particles primarily had a triangular morphology. Ionic self-assembled multilayer films were constructed with the polycation, poly(allylamine hydrochloride) (PAH), and the negatively-charged AgNPs for devices, but it was found that the devices' hole-transport material, PEDOT:PSS, severely etched the AgNPs. Next, we modified the hole-transport layer (HTL) with PAH/PEDOT:PSS ISAM films with the intent to eventually include AgNPs. The wettability of

PAH/PEDOT:PSS ISAM films was improved by spin-coating a thin layer of PEDOT:PSS on top, which decreased the roughness. However, due to the high sheet resistance and the insulating properties of PAH, the PAH/PEDOT:PSS ISAM films slightly degraded the device performance compared to the reference devices. We then investigated the encapsulation of AgNPs by PAH (ENPs), and found that a neutral pH and final PAH concentration of 4 mM was optimal. Unfortunately, ENP/PEDOT:PSS ISAM films again led to etching of the AgNPs. The prevention of etching by PEDOT:PSS was accomplished by coating the AgNPs with gold (AuAgNPs) at an Au:Ag ratio of 0.06:1, which exhibited acidic etching resistance when exposed to sulfuric acid. The addition of PAH/AuAgNP ISAM films on the ITO anode significantly enhanced the optical absorption of the active layer in OPV devices, as etching of the AuAgNPs from PEDOT:PSS was minimized. The OPV device performance was lower than the reference devices, but a slight improvement to the J_{sc} was made for devices with one bilayer of PAH/AuAgNP, correlated to the increased optical absorption of the active layer. A final method explored involved the addition of PAH/PEDOT:PSS/PAH/AuAgNPs ISAM films on the ITO anode, which also substantially improved the optical absorption of the active layer in OPV devices. Although the OPV device performance was degraded with PAH/PEDOT:PSS/PAH/AuAgNPs ISAM films, the shunt and series resistances were equivalent to the reference devices for the devices with three quadlayers. While the methods here were ineffective at OPV device performance increases, we present a unique method for the HTL design involving ISAM films, which can further be improved through the use of conductive polyelectrolytes. Additionally, we introduce a new method for the encapsulation of AgNPs with PAH to be used ISAM films, which is relevant to a wide range of plasmonic applications even beyond OPV devices. Finally, here we showed how coating of

anisotropic AgNPs with gold facilitated resistance against acidic etching, an important study for the future use of AgNPs in conjunction with the HTL.

REFERENCES

(1) Lu, L.; Zheng, T.; Wu, Q.; Schneider, A. M.; Zhao, D.; Yu, L. Recent Advances in Bulk Heterojunction Polymer Solar Cells. *Chemical reviews* **2015,** *115* (23), 12666-12731.
(2) Li, G.; Zhu, R.; Yang, Y. Polymer Solar Cells. *Nat. Photonics* **2012,** *6* (3), 153-161.
(3) Zhao, F.; Dai, S.; Wu, Y.; Zhang, Q.; Wang, J.; Jiang, L.; Ling, Q.; Wei, Z.; Ma, W.; You, W. Single-Junction Binary-Blend Nonfullerene Polymer Solar Cells with 12.1% Efficiency. *Adv. Mater.* **2017,** *29* (18).
(4) Zhao, J.; Li, Y.; Yang, G.; Jiang, K.; Lin, H.; Ade, H.; Ma, W.; Yan, H. Efficient Organic Solar Cells Processed from Hydrocarbon Solvents. *Nat. Energy* **2016,** *1* 15027.
(5) He, Z.; Xiao, B.; Liu, F.; Wu, H.; Yang, Y.; Xiao, S.; Wang, C.; Russell, T. P.; Cao, Y. Single-Junction Polymer Solar Cells with High Efficiency and Photovoltage. *Nat. Photonics* **2015,** *9* (3), 174-179.
(6) Li, G.; Shrotriya, V.; Huang, J.; Yao, Y.; Moriarty, T.; Emery, K.; Yang, Y. High-Efficiency Solution Processable Polymer Photovoltaic Cells by Self-Organization of Polymer Blends. *Nat. Mater.* **2005,** *4* (11), 864-868.
(7) Marsh, R. A.; Hodgkiss, J. M.; Albert-Seifried, S.; Friend, R. H. Effect of Annealing on P3ht: Pcbm Charge Transfer and Nanoscale Morphology Probed by Ultrafast Spectroscopy. *Nano Lett.* **2010,** *10* (3), 923-930.
(8) Wang, T.; Pearson, A. J.; Lidzey, D. G.; Jones, R. A. Evolution of Structure, Optoelectronic Properties, and Device Performance of Polythiophene: Fullerene Solar Cells During Thermal Annealing. *Adv. Funct. Mater.* **2011,** *21* (8), 1383-1390.
(9) Erb, T.; Zhokhavets, U.; Gobsch, G.; Raleva, S.; Stühn, B.; Schilinsky, P.; Waldauf, C.; Brabec, C. J. Correlation between Structural and Optical Properties of Composite Polymer/Fullerene Films for Organic Solar Cells. *Adv. Funct. Mater.* **2005,** *15* (7), 1193-1196.
(10) Li, H.; Tang, H.; Li, L.; Xu, W.; Zhao, X.; Yang, X. Solvent-Soaking Treatment Induced Morphology Evolution in P3ht/Pcbm Composite Films. *J. Mater. Chem.* **2011,** *21* (18), 6563-6568.
(11) Bartesaghi, D.; del Carmen Pérez, I.; Kniepert, J.; Roland, S.; Turbiez, M.; Neher, D.; Koster, L. J. A. Competition between Recombination and Extraction of Free Charges Determines the Fill Factor of Organic Solar Cells. *Nat. Commun.* **2015,** *6*, 7083.
(12) Gupta, D.; Bag, M.; Narayan, K. Correlating Reduced Fill Factor in Polymer Solar Cells to Contact Effects. *Appl. Phys. Lett.* **2008,** *92* (9), 70, 093301.
(13) Park, S. H.; Roy, A.; Beaupré, S.; Cho, S.; Coates, N.; Moon, J. S.; Moses, D.; Leclerc, M.; Lee, K.; Heeger, A. J. Bulk Heterojunction Solar Cells with Internal Quantum Efficiency Approaching 100%. *Nat. Photonics* **2009,** *3* (5), 297.
(14) Atwater, H. A.; Polman, A. Plasmonics for Improved Photovoltaic Devices. *Nat. Mater.* **2010,** *9* (3), 205-213.
(15) Pastoriza-Santos, I.; Liz-Marzán, L. M. Colloidal Silver Nanoplates. State of the Art and Future Challenges. *J. Mater. Chem.* **2008,** *18* (15), 1724-1737.
(16) Kelly, K. L.; Coronado, E.; Zhao, L. L.; Schatz, G. C. The Optical Properties of Metal Nanoparticles: The Influence of Size, Shape, and Dielectric Environment. *J. Phys. Chem. B.* **2003**.

(17) Khan, A. U.; Scruggs, C.; Hicks, D.; Liu, G. Two-Dimensional Plasmonic Nanoparticle as a Nanoscale Sensor to Probe Polymer Brush Formation. *Analytical Chemistry* **2017,** *89* (14), 7541-7548.
(18) Khan, A. U.; Zhao, S.; Liu, G. Key Parameter Controlling the Sensitivity of Plasmonic Metal Nanoparticles: Aspect Ratio. *J. Phys. Chem. C* **2016,** *120* (34), 19353-19364.
(19) Kulkarni, A. P.; Noone, K. M.; Munechika, K.; Guyer, S. R.; Ginger, D. S. Plasmon-Enhanced Charge Carrier Generation in Organic Photovoltaic Films Using Silver Nanoprisms. *Nano Lett.* **2010,** *10* (4), 1501-1505.
(20) Aherne, D.; Ledwith, D. M.; Gara, M.; Kelly, J. M. Optical Properties and Growth Aspects of Silver Nanoprisms Produced by a Highly Reproducible and Rapid Synthesis at Room Temperature. *Adv. Funct. Mater.* **2008,** *18* (14), 2005-2016.
(21) Baek, S.-W.; Noh, J.; Lee, C.-H.; Kim, B.; Seo, M.-K.; Lee, J.-Y. Plasmonic Forward Scattering Effect in Organic Solar Cells: A Powerful Optical Engineering Method. *Sci. Rep.* **2013,** *3*, 1726.
(22) Lindquist, N. C.; Nagpal, P.; McPeak, K. M.; Norris, D. J.; Oh, S.-H. Engineering Metallic Nanostructures for Plasmonics and Nanophotonics. *Rep. Prog. Phys.* **2012,** *75* (3), 036501.
(23) West, P. R.; Ishii, S.; Naik, G. V.; Emani, N. K.; Shalaev, V. M.; Boltasseva, A. Searching for Better Plasmonic Materials. *Laser Photonics Rev.* **2010,** *4* (6), 795-808.
(24) Li, X.; Choy, W. C. H.; Lu, H.; Sha, W. E.; Ho, A. H. P. Efficiency Enhancement of Organic Solar Cells by Using Shape-Dependent Broadband Plasmonic Absorption in Metallic Nanoparticles. *Advanced Functional Materials* **2013,** *23* (21), 2728-2735.
(25) Du, P.; Jing, P.; Li, D.; Cao, Y.; Liu, Z.; Sun, Z. Plasmonic Ag@ Oxide Nanoprisms for Enhanced Performance of Organic Solar Cells. *Small* **2015,** *11* (20), 2454-2462.
(26) Fung, D. D.; Qiao, L.; Choy, W. C.; Wang, C.; Wei, E.; Xie, F.; He, S. Optical and Electrical Properties of Efficiency Enhanced Polymer Solar Cells with Au Nanoparticles in a Pedot–Pss Layer. *J. Mater. Chem.* **2011,** *21* (41), 16349-16356.
(27) Kim, H.; Nam, S.; Lee, H.; Woo, S.; Ha, C.-S.; Ree, M.; Kim, Y. Influence of Controlled Acidity of Hole-Collecting Buffer Layers on the Performance and Lifetime of Polymer: Fullerene Solar Cells. *J. Phys. Chem. C* **2011,** *115* (27), 13502-13510.
(28) Chen, Y.; Wang, C.; Ma, Z.; Su, Z. Controllable Colours and Shapes of Silver Nanostructures Based on Ph: Application to Surface-Enhanced Raman Scattering. *Nanotechnology* **2007,** *18* (32), 325602.
(29) An, J.; Tang, B.; Zheng, X.; Zhou, J.; Dong, F.; Xu, S.; Wang, Y.; Zhao, B.; Xu, W. Sculpturing Effect of Chloride Ions in Shape Transformation from Triangular to Discal Silver Nanoplates. *J. Phys. Chem. C* **2008,** *112* (39), 15176-15182.
(30) Aherne, D.; Charles, D. E.; Brennan-Fournet, M. E.; Kelly, J. M.; Gun'ko, Y. K. Etching-Resistant Silver Nanoprisms by Epitaxial Deposition of a Protecting Layer of Gold at the Edges. *Langmuir* **2009,** *25* (17), 10165-10173.
(31) Munro, C.; Smith, W.; Garner, M.; Clarkson, J.; White, P. Characterization of the Surface of a Citrate-Reduced Colloid Optimized for Use as a Substrate for Surface-Enhanced Resonance Raman Scattering. *Langmuir* **1995,** *11* (10), 3712-3720.
(32) Rydzek, G.; Ji, Q.; Li, M.; Schaaf, P.; Hill, J. P.; Boulmedais, F.; Ariga, K. Electrochemical Nanoarchitectonics and Layer-by-Layer Assembly: From Basics to Future. *Nano Today* **2015,** *10* (2), 138-167.
(33) DeLongchamp, D. M.; Kastantin, M.; Hammond, P. T. High-Contrast Electrochromism from Layer-by-Layer Polymer Films. *Chemistry of Materials* **2003,** *15* (8), 1575-1586.

(34) Xi, J.; Wu, Z.; Jiao, B.; Dong, H.; Ran, C.; Piao, C.; Lei, T.; Song, T. B.; Ke, W.; Yokoyama, T. Multichannel Interdiffusion Driven Fasni3 Film Formation Using Aqueous Hybrid Salt/Polymer Solutions toward Flexible Lead-Free Perovskite Solar Cells. *Adv. Mater.* **2017,** *29* (23).
(35) D'Olieslaeger, L.; Pirotte, G.; Cardinaletti, I.; D'Haen, J.; Manca, J.; Vanderzande, D.; Maes, W.; Ethirajan, A. Eco-Friendly Fabrication of Pbdttpd: Pc71bm Solar Cells Reaching a Pce of 3.8% Using Water-Based Nanoparticle Dispersions. *Org. Electron.* **2017,** *42* 42-46.
(36) Søndergaard, R.; Helgesen, M.; Jørgensen, M.; Krebs, F. C. Fabrication of Polymer Solar Cells Using Aqueous Processing for All Layers Including the Metal Back Electrode. *Adv. Energy Mater.* **2011,** *1* (1), 68-71.
(37) Khan, A. U.; Zhou, Z.; Krause, J.; Liu, G. Poly (Vinylpyrrolidone)-Free Multistep Synthesis of Silver Nanoplates with Plasmon Resonance in the near Infrared Range. *Small* **2017,** *13* (43).
(38) Shahjamali, M. M.; Salvador, M.; Bosman, M.; Ginger, D. S.; Xue, C. Edge-Gold-Coated Silver Nanoprisms: Enhanced Stability and Applications in Organic Photovoltaics and Chemical Sensing. *J. Phys. Chem. C* **2014,** *118* (23), 12459-12468.
(39) Kumar, M.; Dubey, A.; Reza, K. M.; Adhikari, N.; Qiao, Q.; Bommisetty, V. Origin of Photogenerated Carrier Recombination at the Metal–Active Layer Interface in Polymer Solar Cells. *Physical Chemistry Chemical Physics* **2015,** *17* (41), 27690-27697.
(40) Servaites, J. D.; Yeganeh, S.; Marks, T. J.; Ratner, M. A. Efficiency Enhancement in Organic Photovoltaic Cells: Consequences of Optimizing Series Resistance. *Advanced Functional Materials* **2010,** *20* (1), 97-104.
(41) Li, G.; Shrotriya, V.; Yao, Y.; Yang, Y. Investigation of Annealing Effects and Film Thickness Dependence of Polymer Solar Cells Based on Poly (3-Hexylthiophene). *Journal of Applied Physics* **2005,** *98* (4), 043704.
(42) Kim, H.; So, W.-W.; Moon, S.-J. The Importance of Post-Annealing Process in the Device Performance of Poly (3-Hexylthiophene): Methanofullerene Polymer Solar Cell. *Solar Energy Materials and Solar Cells* **2007,** *91* (7), 581-587.
(43) Semaltianos, N. Thermally Evaporated Aluminium Thin Films. *Applied surface science* **2001,** *183* (3), 223-229.
(44) Mihailetchi, V.; Blom, P.; Hummelen, J.; Rispens, M. Cathode Dependence of the Open-Circuit Voltage of Polymer: Fullerene Bulk Heterojunction Solar Cells. *Journal of Applied Physics* **2003,** *94* (10), 6849-6854.
(45) He, C.; Zhong, C.; Wu, H.; Yang, R.; Yang, W.; Huang, F.; Bazan, G. C.; Cao, Y. Origin of the Enhanced Open-Circuit Voltage in Polymer Solar Cells Via Interfacial Modification Using Conjugated Polyelectrolytes. *Journal of Materials Chemistry* **2010,** *20* (13), 2617-2622.
(46) Proctor, C. M.; Nguyen, T.-Q. Effect of Leakage Current and Shunt Resistance on the Light Intensity Dependence of Organic Solar Cells. *Applied Physics Letters* **2015,** *106* (8), 23_1.
(47) Luque, A.; Hegedus, S. Handbook of Photovoltaic Science and Engineering, *John Wiley & Sons*, **2011**.
(48) Li, Y. Three Dimensional Solar Cells Based on Optical Confinement Geometries, *Springer Science & Business Media*, **2012**.
(49) Piris, J.; Dykstra, T. E.; Bakulin, A. A.; Loosdrecht, P. H. v.; Knulst, W.; Trinh, M. T.; Schins, J. M.; Siebbeles, L. D. Photogeneration and Ultrafast Dynamics of Excitons and Charges in P3ht/Pcbm Blends. *The Journal of Physical Chemistry C* **2009,** *113* (32), 14500-14506.
(50) Hwang, I.-W.; Moses, D.; Heeger, A. J. Photoinduced Carrier Generation in P3ht/Pcbm Bulk Heterojunction Materials. *The Journal of Physical Chemistry C* **2008,** *112* (11), 4350-4354.

(51) Kirchartz, T.; Agostinelli, T.; Campoy-Quiles, M.; Gong, W.; Nelson, J. Understanding the Thickness-Dependent Performance of Organic Bulk Heterojunction Solar Cells: The Influence of Mobility, Lifetime, and Space Charge. *The journal of physical chemistry letters* **2012,** *3* (23), 3470-3475.
(52) Hoppe, H.; Shokhovets, S.; Gobsch, G. Inverse Relation between Photocurrent and Absorption Layer Thickness in Polymer Solar Cells. *physica status solidi (RRL)-Rapid Research Letters* **2007,** *1* (1).
(53) Sievers, D. W.; Shrotriya, V.; Yang, Y. Modeling Optical Effects and Thickness Dependent Current in Polymer Bulk-Heterojunction Solar Cells. *Journal of applied physics* **2006,** *100* (11), 114509.
(54) Topp, K.; Borchert, H.; Johnen, F.; Tunc, A.; Knipper, M.; Von Hauff, E.; Parisi, J.; Al-Shamery, K. Impact of the Incorporation of Au Nanoparticles into Polymer/Fullerene Solar Cells. *J. Phys. Chem. A* **2009,** *114* (11), 3981-3989.
(55) Tang, J.; Wang, X.; Brzozowski, L.; Barkhouse, D. A. R.; Debnath, R.; Levina, L.; Sargent, E. H. Schottky Quantum Dot Solar Cells Stable in Air under Solar Illumination. *Advanced materials* **2010,** *22* (12), 1398-1402.
(56) Yang, B.; Yuan, Y.; Huang, J. Reduced Bimolecular Charge Recombination Loss in Thermally Annealed Bilayer Heterojunction Photovoltaic Devices with Large External Quantum Efficiency and Fill Factor. *The Journal of Physical Chemistry C* **2014,** *118* (10), 5196-5202.
(57) Jo, J.; Na, S. I.; Kim, S. S.; Lee, T. W.; Chung, Y.; Kang, S. J.; Vak, D.; Kim, D. Y. Three-Dimensional Bulk Heterojunction Morphology for Achieving High Internal Quantum Efficiency in Polymer Solar Cells. *Advanced Functional Materials* **2009,** *19* (15), 2398-2406.
(58) Haes, A. J.; Haynes, C. L.; McFarland, A. D.; Schatz, G. C.; Van Duyne, R. P.; Zou, S. Plasmonic Materials for Surface-Enhanced Sensing and Spectroscopy. *MRS Bull.* **2005,** *30* (5), 368-375.
(59) Kelly, K. L.; Coronado, E.; Zhao, L. L.; Schatz, G. C., The Optical Properties of Metal Nanoparticles: The Influence of Size, Shape, and Dielectric Environment. ACS Publications: 2003.
(60) Choi, J.; Rubner, M. F. Influence of the Degree of Ionization on Weak Polyelectrolyte Multilayer Assembly. *Macromolecules* **2005,** *38* (1), 116-124.
(61) Shiratori, S. S.; Rubner, M. F. Ph-Dependent Thickness Behavior of Sequentially Adsorbed Layers of Weak Polyelectrolytes. *Macromolecules* **2000,** *33* (11), 4213-4219.
(62) Zhao, L.; Kelly, K. L.; Schatz, G. C. The Extinction Spectra of Silver Nanoparticle Arrays: Influence of Array Structure on Plasmon Resonance Wavelength and Width. *J. Phys. Chem. B* **2003,** *107* (30), 7343-7350.
(63) Ung, T.; Liz-Marzán, L. M.; Mulvaney, P. Optical Properties of Thin Films of Au@ Sio2 Particles. *J. Phys. Chem. B* **2001,** *105* (17), 3441-3452.
(64) Yuan, W.; Li, C. M. Direct Modulation of Localized Surface Plasmon Coupling of Au Nanoparticles on Solid Substrates Via Weak Polyelectrolyte-Mediated Layer-by-Layer Self Assembly. *Langmuir* **2009,** *25* (13), 7578-7585.
(65) Simpson, J. Advances and Applications of Baytron® Conductive Polymer Technologies https://www.aimcal.org/uploads/4/6/6/9/46695933/simpson_presentation.pdf.
(66) Alemu, D.; Wei, H.-Y.; Ho, K.-C.; Chu, C.-W. Highly Conductive Pedot: Pss Electrode by Simple Film Treatment with Methanol for Ito-Free Polymer Solar Cells. *Energy & environmental science* **2012,** *5* (11), 9662-9671.

(67) Valtakari, D.; Bollström, R.; Toivakka, M.; Saarinen, J. J. Influence of Anionic and Cationic Polyelectrolytes on the Conductivity and Morphology of Poly (3, 4-Ethylenedioxythiophene): Poly (Styrenesulfonate) Films. *Thin Solid Films* **2015,** *590* 170-176.
(68) Das, S.; Alford, T. Improved Efficiency of P3ht: Pcbm Solar Cells by Incorporation of Silver Oxide Interfacial Layer. *Journal of Applied Physics* **2014,** *116* (4), 044905.
(69) Kim, Y.; Ballantyne, A. M.; Nelson, J.; Bradley, D. D. Effects of Thickness and Thermal Annealing of the Pedot: Pss Layer on the Performance of Polymer Solar Cells. *Org. Electron.* **2009,** *10* (1), 205-209.
(70) Feng, X.; Feng, L.; Jin, M.; Zhai, J.; Jiang, L.; Zhu, D. Reversible Super-Hydrophobicity to Super-Hydrophilicity Transition of Aligned Zno Nanorod Films. *Journal of the American Chemical Society* **2004,** *126* (1), 62-63.
(71) Bulliard, X.; Ihn, S. G.; Yun, S.; Kim, Y.; Choi, D.; Choi, J. Y.; Kim, M.; Sim, M.; Park, J. H.; Choi, W. Enhanced Performance in Polymer Solar Cells by Surface Energy Control. *Adv. Funct. Mater.* **2010,** *20* (24), 4381-4387.
(72) Germack, D. S.; Chan, C. K.; Kline, R. J.; Fischer, D. A.; Gundlach, D. J.; Toney, M. F.; Richter, L. J.; DeLongchamp, D. M. Interfacial Segregation in Polymer/Fullerene Blend Films for Photovoltaic Devices. *Macromolecules* **2010,** *43* (8), 3828-3836.
(73) Nah, Y.-C.; San Choi, W.; Kim, D.-Y. Preparation and Electrochromic Properties of Spin Self-Assembled Polyelectrolyte Multilayer Films Composed of Pedot: Pss and Pah. *Sol. Energy Mater. Sol. Cells* **2008,** *92* (12), 1547-1551.
(74) Kang, H.; Hong, S.; Lee, J.; Lee, K. Electrostatically Self-Assembled Nonconjugated Polyelectrolytes as an Ideal Interfacial Layer for Inverted Polymer Solar Cells. *Adv. Mater.* **2012,** *24* (22), 3005-3009.
(75) Bozano, L.; Carter, S.; Scott, J.; Malliaras, G.; Brock, P. Temperature-and Field-Dependent Electron and Hole Mobilities in Polymer Light-Emitting Diodes. *Appl. Phys. Lett.* **1999,** *74* (8), 1132-1134.
(76) Templeton, A. C.; Pietron, J. J.; Murray, R. W.; Mulvaney, P. Solvent Refractive Index and Core Charge Influences on the Surface Plasmon Absorbance of Alkanethiolate Monolayer-Protected Gold Clusters. *J. Phys. Chem. B* **2000,** *104* (3), 564-570.

Chapter 7

Polystyrene-Coated Plasmonic Silver Nanoplates for Enhancement of Organic Photovoltaics

The majority of this chapter is from a manuscript under review for the journal ACS Applied Materials and Interfaces. Additional studies not reported in that manuscript are also included.

7.1 INTRODUCTION

Plasmonic nanoparticles can create large local electric field enhancements in organic photovoltaics (OPVs), substantially enhance the absorption of light, and, consequently, improve the device efficiency. The nanoparticle location in the OPV device is crucial. Nanoparticles can be positioned within OPV devices at virtually any layer or interface. For instance, the hole-collecting buffer layer, poly(3,4-ethylenedioxythiophene):poly(styrenesulfonate) (PEDOT:PSS), is widely used as a location for plasmonic nanoparticles.[1-6] Although the aqueous PEDOT:PSS mixtures are miscible with hydrophilic plasmonic nanoparticles, the electrical conductivity of PEDOT:PSS requires highly acidic conditions (pH ≈ 1.6),[7] which cause rapid deterioration of Ag nanoparticles (as shown in the previous chapter). Nanoparticles added directly to the active layer have the closest proximity to the light absorbing donor/acceptors, so in principle should yield the largest device improvements. However, nanoparticles coated with short-chain ligands,[8-9] thiols,[10-11] or surfactants[12] added to the active layer have been repeatedly shown to increase exciton quenching and non-radiative charge carrier recombination, which are detrimental to the device performance.[6, 13] Charge carrier recombination in the active layer can be avoided if nanoparticles

are coated with insulating oxides,[10, 14] or are synthesized by laser ablation to be surfactant-free,[12, 15] but these methods are time-consuming and difficult. Alternatively, the incorporation of the plasmonic nanoparticles directly outside the active layer (*i.e.*, at the organic/electrode interfaces[3, 16]) can mitigate the recombination effect while still providing strong performance enhancements.

In addition to the location, dispersion is also crucial to avoid nanoparticle aggregation and performance degradation.[1, 9, 11, 17] Coating nanoparticles with high-molecular-weight functional groups[2, 18-20] is a facile method for effective nanoparticle dispersion and deterrence of charge carrier recombination. Due to the steric repulsion, polymer chains prevent detrimental aggregation of nanoparticles.[21-23] Since thiol has an affinity for and reacts with the Ag nanoparticle surface, thiol-terminated polystyrene (PS-SH) can be "grafted-to" the Ag nanoparticles and create a hydrophobic polystyrene (PS) layer surrounding the nanoparticles. The protective PS layer provides the nanoparticles with long-term dispersion stability in organic solvents, which otherwise is difficult.[21-23] The polystyrene layer provides an insulating layer to prevent parasitic charge recombination.[18] In one report, Ag nanospheres functionalized by PS were successfully added to the active layer with controlled dispersion and yielded 13% efficiency enhancements.[19] However, the PS functionalization has not previously been utilized with anisotropic nanoparticles incorporated outside the active layer, where sufficient detail is lacking regarding resistance to charge carrier recombination effects and photoluminescence quenching.

In this chapter, anisotropic Ag nanoplates (AgNPs) were functionalized by thiol-terminated polystyrene (PS-SH) to yield polystyrene-functionalized Ag nanoplates (PS-AgNPs), and then spin-coated directly on the OPV active layer, poly(3-hexylthiophene-2,5-diyl):[6,6]-phenyl C_{61} butyric acid methyl ester (P3HT:PCBM). A systematic variation of the PS-AgNP solution concentration correlated to different nanoparticle densities on the active layer. The localized

surface plasmon resonance (LSPR) of the PS-AgNPs enhanced the light absorption of the active layer, which directly contributed to an increase in exciton yield, demonstrated by the increased photoluminescence emission intensities in P3HT films. In addition, incorporation of the PS-AgNPs decreased the series resistance and increased the photocurrent of the devices. In devices with PS-AgNP at a concentration of 0.57 nM, the power conversion efficiency was 32% higher than the devices without the PS-AgNPs. We also discuss the importance of PS functionalization and its effect on the reduction of exciton quenching and charge trapping. Without polystyrene functionalization, the AgNPs severely deteriorated the performance of the OPV devices regardless of the nanoparticle concentration. We also report a similar performance degradation for OPV devices with added AgNPs functionalized by thiol-terminated poly(ethylene glycol) (PEG-AgNPs).

7.2 EXPERIMENTAL

7.2.1 Synthesis of Ag Nanoplates. Ag nanoplates (Ag NPs) were synthesized in the group of Prof. Greg Liu via a seed-mediated method following previous reports with slight modifications.[10, 24-26] To prepare Ag seeds, 4.5 mL of ultrapure deionized (DI) water (resistance, 18.2 MΩ·cm) was mixed vigorously with 0.5 mL of 25 mM sodium citrate tribasic dihydrate (Purity ≥99.0%) and 0.25 mL of 0.5 mM poly(sodium 4-styrenesulfonate) (PSSS; $M_w \sim 1000$ kg mol^{-1}) aqueous solutions. Next, 0.3 mL of 10 mM ice-cold sodium borohydride ($NaBH_4$; Purity ≥99.99%) solution was introduced, followed by the addition of 5 mL of 0.5 mM silver nitrate ($AgNO_3$; Purity ≥99.9999%) at a rate of 2 mL/min using a syringe pump. Once all of the silver nitrate was added, the seed solution was stirred for ~2 min and then ready for use in the next step.

To synthesize AgNPs, 75 μL of 10 mM ascorbic acid (Purity ≥99.0%) solution was added to 10 mL of DI water, and a certain volume (75 – 175 μL) of Ag seed solution was added to the growth

solution under vigorous stirring. Immediately afterwards, 3 mL of 0.5 mM $AgNO_3$ was dispensed into the growth solution at a rate of 1 mL/min using a syringe pump. The solution initially appeared yellow, then changed rapidly, and eventually stabilized towards the completion of the growth. Promptly following the complete addition of $AgNO_3$, 0.5 mL of 25 mM sodium citrate was added to stabilize the AgNPs. The AgNP synthesis was reiterated with different volumes of Ag seed solutions to synthesize AgNPs of different sizes and λ_{LSPR}. After synthesis, the solutions were sealed and stored in the dark.

7.2.2 Synthesis of Thiol-terminated Polystyrene. Thiol-terminated polystyrene (PS-SH) was synthesized by reversible addition-fragmentation chain transfer (RAFT) polymerization and subsequent reduction of thiocarbonylthio to thiol (**Figure 7.1**). Briefly, styrene (144 mmol) and 2-phenyl-2-propyl benzodithioate (CDB) (0.481 mmol) were mixed in a Schlenk flask using a stirring bar. The mixture in the Schlenk flask was degassed through three freeze-pump-thaw cycles. The Schlenk flask was filled with N_2 and immersed into an oil bath at 110 °C. After heating and stirring for 18 h, the reacted mixture was cooled down to room temperature. The resulting CDB-terminated polystyrene (PS-CDB) was precipitated in methanol twice and then dried in a vacuum oven for 24 h. Based on size exclusion chromatography (SEC), the PS-CDB had a molecular weight (M_n) of ~10.3 kDa and a polydispersity index of 1.1.

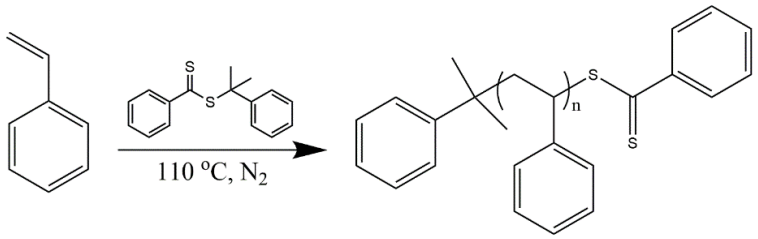

Figure 7.1. Synthesis of polystyrene (PS) using reversible addition-fragmentation chain transfer (RAFT) polymerization. The chain transfer agent used here is 2-phenyl-2-propyl benzodithioate (CDB) and the final polymer is denoted as PS-CDB.

To convert PS-CDB to PS-SH, 1000 mg of PS-CDB was dissolved in 25 mL of THF in a round bottom flask and mixed with 50 molar equivalent (44.51 mg) of $NaBH_4$ dissolved in 2.4 mL of water. This solution was then stirred vigorously at room temperature for 24 h (**Figure 7.2**).[27] The resulting PS-SH was precipitated in methanol twice and dried in a vacuum oven at room temperature for 48 h. The conversion of PS-CDB to PS-SH was confirmed by NMR (**Figure 7.3**).

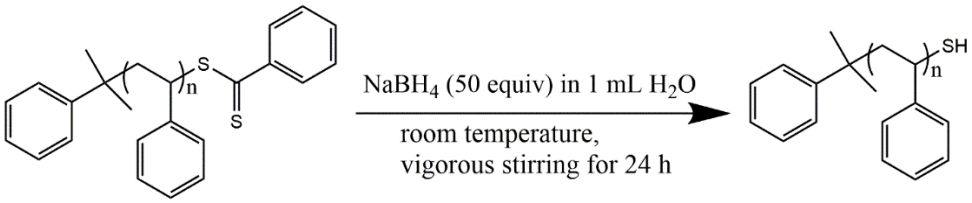

Figure 7.2. Reduction of PS-CDB to thiol terminated polystyrene (PS-SH) by $NaBH_4$.

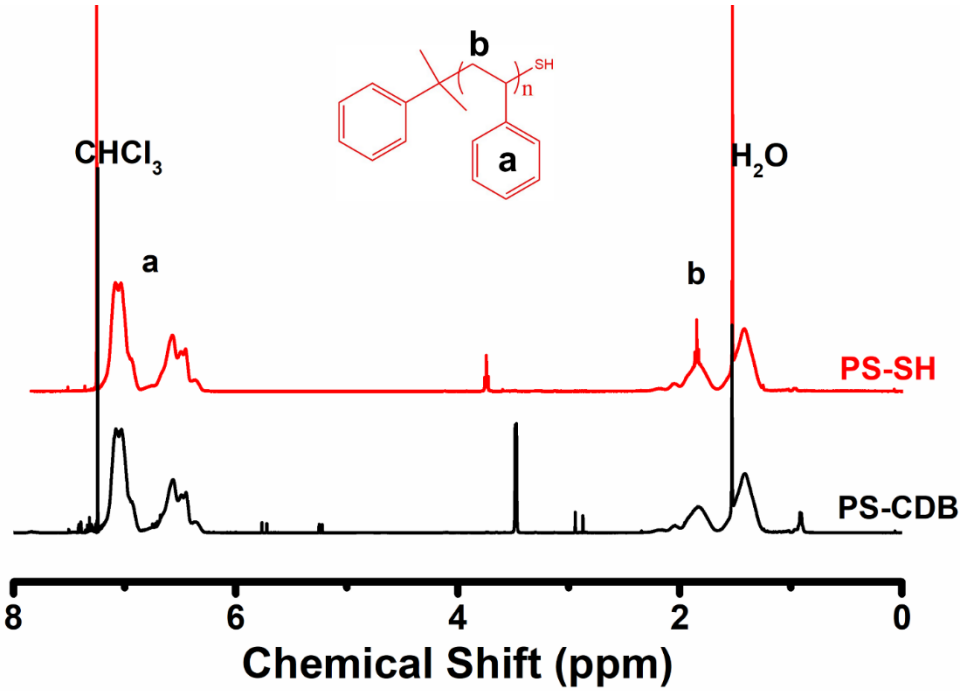

Figure 7.3. 1H NMR spectra of PS-CDB (black) and PS-SH (red). The thiol peak (~1.7 ppm) is indistinguishable in the spectra due to overlap with the backbone polystyrene proton peaks (**b**). Peaks around 5.25 and 5.76 ppm correspond to the residual styrene monomers.

7.2.3 Functionalization of AgNPs with PS-SH and Solution Dispersion. A solution of AgNPs was centrifuged at 10,000 rpm for 30 min. The supernatant was immediately removed and the precipitate was redispersed in an identical volume of N,N-dimethylformamide (DMF; Certified ACS; Purity ≥99.8%). Next, PS-SH powder was added to the DMF solution that contained redispersed AgNPs. The final polymer concentration was 0.1 wt.% (1 mg/mL). After brief sonication, the solution was gently agitated by a vortex mixer for 24 h to make sure PS-SH fully reacted with the AgNPs. After 24 h, the PS-SH functionalized AgNPs (denoted as PS-AgNPs) were stored in the dark and used within 3 d.

Before use in the photovoltaic devices, PS-AgNPs in DMF were centrifuged at 10,000 rpm for 30 min. The supernatant was removed and the precipitate was redispersed in 500 μL of methanol (MeOH; Purity ≥99.9%). Since the starting concentration of AgNPs in DMF was 0.57 nM and the final MeOH solution volume was maintained at a constant of 500 μL, the final nanoparticle concentration depended on the initial volume of the PS-AgNP solution. For example, with starting volumes of 250, 500, 1000, and 2500 μL PS-AgNP solutions in DMF, the final concentrations of PS-AgNPs in MeOH were 0.29, 0.57, 1.14, and 2.90 nM, respectively. After the addition of MeOH, the solution was vortex-mixed and used immediately.

7.2.4 Functionalization of AgNPs with PEG-SH and Solution Dispersion. Poly(ethylene glycol) methyl ether thiol (PEG-SH, average M_n ~6 kDa, $M_w/M_n < 1.2$) powder was added directly to the original AgNP aqueous solution for a polymer concentration of 0.1 wt.% (1 mg/mL). After brief sonication, the solution was gently agitated by a vortex mixer for 24 h to make sure PEG-SH fully reacted with the AgNPs. After 24 h, the PEG-SH functionalized AgNPs (denoted as PEG-AgNPs) were stored in the dark and used within 3 d.

Immediately before use in photovoltaic devices, the PEG-AgNPs were centrifuged at 10,000 rpm for 30 minutes. The supernatant was immediately removed and the precipitate was redispersed in MeOH. The concentration of the PEG-AgNPs in MeOH was altered identically to the method used with the PS-AgNPs. Similarly, after the addition of MeOH, the solution was vortex-mixed and used immediately.

7.2.5 Miscibility Testing. To test miscibility, AgNPs were centrifuged at 10,000 rpm for 30 minutes, the supernatant was removed, and a new solvent was then added to the precipitate. Brief sonication and vortex mixing were used to fully disperse the particles into the solvent.

7.3 RESULTS

7.3.1 AgNP Solvent Miscibility. Miscibility testing was performed on AgNPs that were unfunctionalized, functionalized by poly(ethylene glycol) methyl ether thiol (PEG-SH) (PEG-AgNPs), and functionalized by thiol-terminated polystyrene (PS-SH) (PS-AgNPs). The goal of this testing was a determination of an effective spin-coating solvent (**Table 7.1**). In general, water is a poor solvent for spin-coating of the AgNPs due to its relatively low vapor pressure, which leads to increased drying times and decreased dispersion.[28] Additionally, it important to limit the presence of water on P3HT:PCBM, as the diffusion of water is reported to be a performance degradation pathway.[29]

The AgNPs were either miscible, immiscible, or disintegrated in the solvent. In regards to immiscibility, the AgNPs phase separated completely from the solvent and dispersion was impossible. Unfunctionalized AgNPs were miscible in alcohol-based solvents (methanol, ethanol, isopropyl alcohol), but they lacked stability and formed aggregated precipitates after a short period of time (**Figure 7.15**). The solvent compatibility of the unfunctionalized AgNPs and the PEG-AgNPs was similar, and the PEG-AgNPs had long-term stability in the alcohol-based solvents.

Also, the PEG-AgNPs were immiscible in the solvents that disintegrated the unfunctionalized AgNPs (dichloromethane, chlorobenzene), which was attributed to the PEG layer protecting the AgNPs against etching from chloride ions.[30] The PS-AgNPs were miscible in every tested solvent besides water, due to the hydrophobic nature of the PS layer. Methanol (MeOH) was selected as the spin-coating solvent for all materials, as it had the highest vapor pressure out of all of the solvents compatible with the unfunctionalized AgNPs, functionalized AgNPs, and P3HT:PCBM (as discussed later).

Table 7.1. Solvent miscibility of unfunctionalized AgNPs, PEG-AgNPs, and PS-AgNPs. In the solubility column, miscible, immiscible, and disintegrated is referred to as M, I, and D, respectively. M* refers to only short-term stability.

Solvent	Vapor Pressure, kPA (@ 25 ^{o}C)[31]	Unfunctionalized AgNPs Solubility	PEG-AgNPs Solubility	PS-AgNPs Solubility
Dichloromethane	57.90	D	I	M
Methanol	13.02	M*	M	M
Ethanol	7.91	M*	M	M
Isopropyl alcohol	6.05	M*	M	M
Toluene	3.79	I	I	M
Pyridine	2.77	M*	M	M
Water	2.72	M	M	I
Chlorobenzene	1.59	D	I	M
DMF	0.52	M	M	M

7.3.2 PEG-SH Functionalization of AgNPs. The functionalization of the AgNPs by poly(ethylene glycol) methyl ether thiol (PEG-SH) was thoroughly explored preceding the work related to the functionalization of AgNPs by thiol-terminated polystyrene (PS-SH). Our primary research collaborators, Assad Khan and Dr. Guoliang Liu, had recently completed an extensive investigation on the functionalization of AgNPs with PEG-SH,[25] and their methods and insight were applied to AgNPs for enhancements in OPV devices. The PEG-SH layer would provide electrical insulation for the AgNPs against detrimental charge trapping.[32-33] Additionally, the PEG-SH would increase the stability of the functionalized AgNPs in organic solvents.[34] The results concerning PEG-SH functionalized AgNPs were not included in the submitted manuscript, but they are presented here for completeness and future reference.

Ag nanoplates were synthesized with a λ_{LSPR} located at 507 nm (**Figure 7.4**) in an aqueous solution. After synthesis, the AgNPs were functionalized with 0.1 wt% PEG-SH (PEG-AgNPs) in the aqueous solution and vortex mixed overnight. The PEG-AgNPs were then centrifuged and transferred to a MeOH solvent for spin-coating on top of the active layer. The final λ_{LSPR} had a slight shift to 511 nm due to the change of the surrounding refractive indices (n_{H2O} = 1.33, n_{MEOH} = 1.35, n_{PEG} = 1.44).[35]

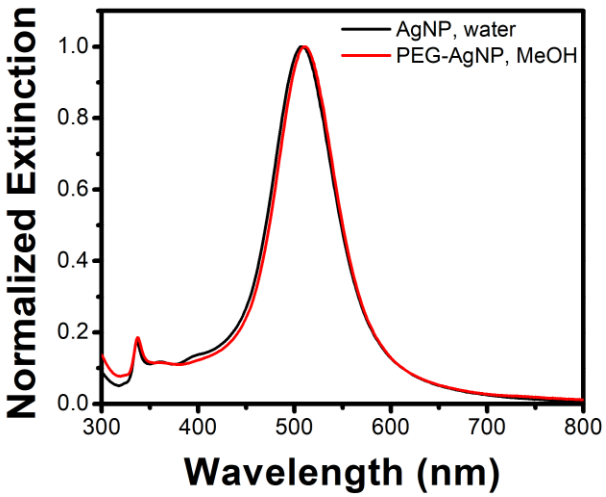

Figure 7.4. Normalized extinction spectra of the AgNPs in solution before and after functionalization with PEG-SH.

7.3.3 Density and Absorption Enhancements of PEG-AgNPs. PEG-AgNPs were transferred to MeOH at concentration of 8.55 nM, and were immediately spin-coated on either a glass substrate or the annealed active layer (P3HT:PCBM) (**Figure 7.5**). As PEG is well-known to be hydrophilic,[36] the PEG-AgNPs had good dispersion on the glass substrate with no stacking of particles or visible aggregates. Contrastingly, the PEG-AgNPs were incompatible with the hydrophobic P3HT:PCBM,[37-38] which caused phase separation and surface aggregation of the spin-coated nanoparticles. We note that these early methods involved spin-coating PEG-AgNPs onto annealed P3HT:PCBM. PS-AgNPs and unfunctionalized AgNPs studied later were spin-coated onto as-cast P3HT:PCBM, as there was found to be greater reproducibility and homogeneity over spin-coating onto annealed films.

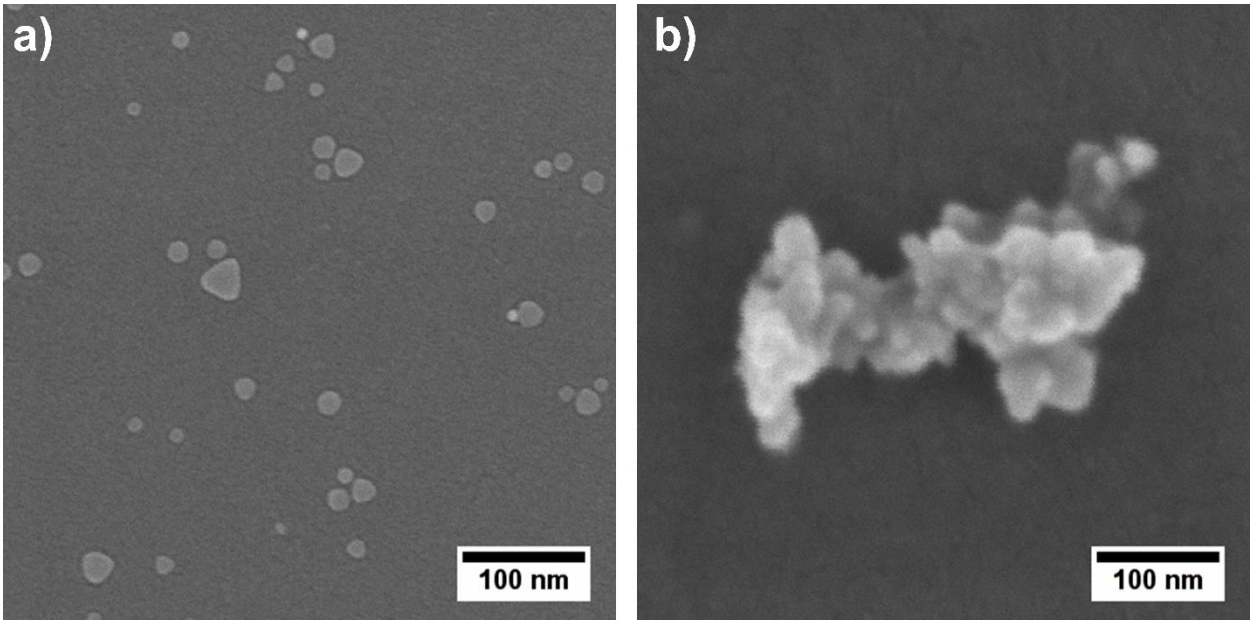

Figure 7.5. Representative SEM images of PEG-AgNPs at a concentration of 8.55 nM spin-coated on (**a**) bare glass and (**b**) an annealed P3HT:PCBM film.

Despite the aggregation of the PEG-AgNPs, the absorption of the annealed P3HT:PCBM was enhanced, although only marginally (**Figure 7.6**). Since the absorption enhancements for lower PEG-AgNPs concentrations (0.29 nM to 2.90 nM) were negligible, the PEG-AgNPs solution concentrations used here were substantially higher than those used in work done on the unfunctionalized AgNPs and PS-AgNPs.

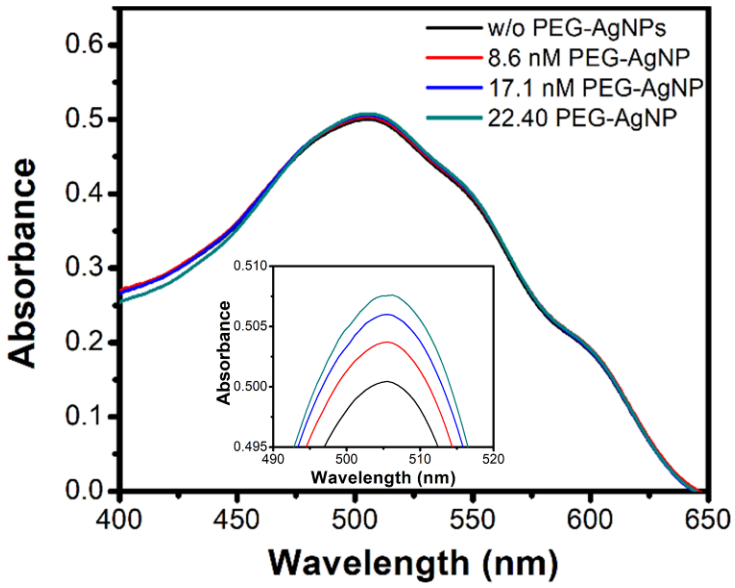

Figure 7.6. The optical absorption spectra of the as-cast P3HT:PCBM films before and after spin-coating PEG-AgNPs. The PEG-AgNP solutions had concentrations of 8.55 nM, 17.10 nM, and 22.40 nM. The inset is a zoomed-in view of the absorption peaks.

7.3.4 OPV Device Performance with PEG-AgNPs. OPV devices were formed with the configuration ITO/PEDOT:PSS/P3HT:PCBM/PEG-AgNPs/Al, and the current density – voltage (J-V) curves were measured under 100 mW/cm^2 Air Mass 1.5 (AM1.5G) illumination (**Figure 7.7**). Similar to the unfunctionalized, aggregated AgNP devices discussed later, the PCE of the devices for every PEG-AgNP concentration was less than the reference devices (**Table 7.2**).

The R_{sh} values of the OPV devices (**Table 7.2**) were determined by the reciprocal slopes of the J-V curves at zero bias (*i.e.*, 0 V) following Equation (1).

$$R_{sh} = \left(\frac{dV}{dJ}\right)_{V\to 0} \quad (1)$$

The series resistance (R_s) (**Table 7.2**) was determined by the reciprocal slope of the J-V curves at voltages much larger than V_{oc}, following Equation (2):

$$R_s = \left(\frac{dV}{dJ}\right)_{V\to \infty} \quad (2)$$

Due to the formation of defects and voids, the V_{oc}, R_{sh}, R_s, FF all show substantial degradations from the reference devices. However, the electrical device characteristics show no clear trend with an increased PEG-AgNP concentrations. Differently than the unfunctionalized AgNPs, the J_{sc} for the PEG-AgNP concentration of 8.55 nM and 17.10 nM show an 7.6% and 5.7% increase over the reference devices, respectively. Despite the aggregation of the PEG-AgNPs, the J_{sc} improvement highlights the importance of an insulating layer on the AgNPs for any incorporation into an OPV device.

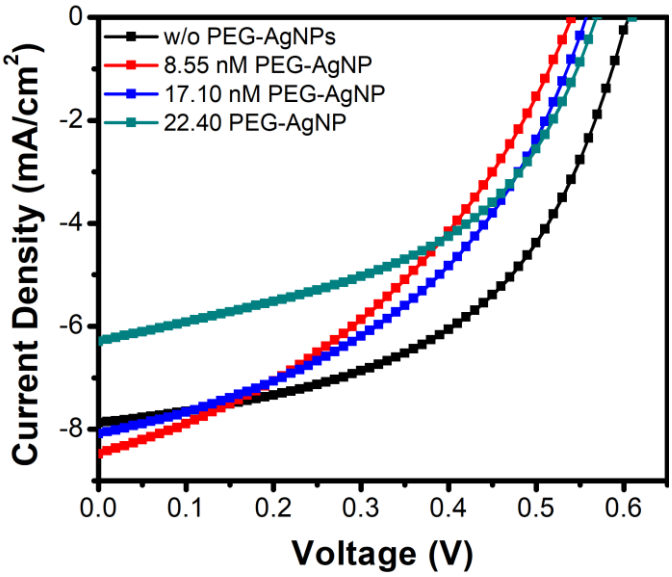

Figure 7.7. The current density – voltage (J-V) characteristics of OPV devices with added PEG-AgNP at concentrations of 8.55 nM, 17.10 nM, and 22.40 nM.

Table 7.2. The J-V characteristics of the OPV devices with PEG-AgNPs of various concentrations ranging from 0 to 22.40 nM in the spin-coating solutions.

PEG-AgNP	J_{sc} (mA/cm^2)	V_{oc} (V)	FF	R_s (Ω·cm^2)	R_{sh} (Ω·cm^2)	PCE (%)	Best PCE (%)
0 mM (ref)	-7.88 ± 0.15	0.62 ± 0.01	0.51 ± 0.02	12.10 ± 2.2	502 ± 159	2.45 ± 0.05	2.61
8.55 nM	-8.48 ± 0.26	0.55 ± 0.01	0.39 ± 0.01	19.55 ± 1.83	208 ± 34	1.79 ± 0.08	1.90
17.10 nM	-8.33 ± 1.02	0.56 ± 0.02	0.43 ± 0.06	18.13 ± 1.88	285 ± 139	1.98 ± 0.24	2.33
22.40 nM	-6.30 ± 0.09	0.56 ± 0.01	0.48 ± 0.04	17.97 ± 0.57	253 ± 56	1.70 ± 0.10	1.90

7.3.5 PS-SH Functionalization of AgNPs. Silver nanoplates (AgNPs) were functionalized with thiol-terminated polystyrene. The resulting PS-AgNPs were dispersed in methanol (MeOH) and spin-coated directly on top of the active layer (**Figure 7.8**). The placement of the PS-AgNPs between the active layer and the electrode is advantageous because 1) the density of the PS-AgNPs can be easily tuned by the nanoparticle solution concentration, and 2) the exciton quenching and charge trapping are potentially low compared to placing them in the active layer.[6]

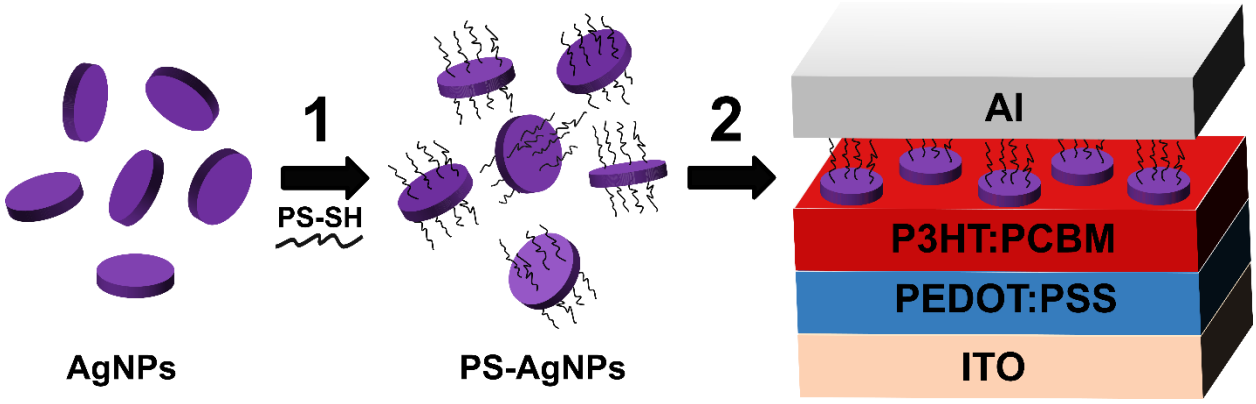

Figure 7.8. Schematic illustration of an OPV device with PS-AgNPs. The AgNPs are (1) functionalized with a layer of thiol-terminated polystryrene (PS-SH). The PS-AgNPs are (2) deposited on top of the active layer (P3HT:PCBM) in OPV devices.

To effectively enhance the optical absorption of the active layer, the LSPR of the AgNPs should couple with the absorption peak (λ_{max}) of P3HT:PCBM. AgNPs with an LSPR peak wavelength (λ_{LSPR}) of 485 nm were synthesized in an aqueous solution (**Figure 7.9a**). As measured with TEM (**Figure 7.9b**), the Ag NPs were primarily nanoplates with an average lateral dimension of 28.3 ± 4.9 nm and an average thickness of 8.6 ± 2.1 nm. Anisotropic Ag nanoplates were selected over spherical particles because the λ_{LSPR} is easily tunable in the visible light range.[13] In addition, the prismatic features in a portion of the nanoplates can further improve the local electric field enhancement effect.[39-41]

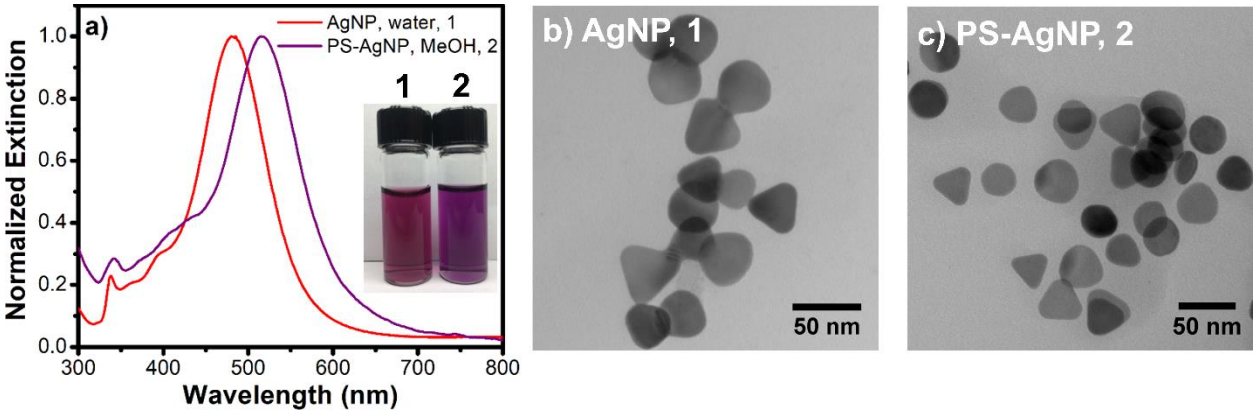

Figure 7.9. Characterization of AgNPs. (**a**) Normalized extinction spectra of the AgNPs in solution before and after functionalization with PS-SH. The unfunctionalized AgNPs and PS-AgNPs were suspended in water and methanol, respectively. (Inset) A photograph of AgNPs in solution (1) and PS-AgNPs in solution (2). (**b, c)** TEM images of the AgNPs and PS-AgNPs.

To effectively place the AgNPs on the organic active layer of P3HT:PCBM (**Figure 7.8**), it is crucial to control the hydrophobicity of the AgNPs.[14, 19] The AgNPs were functionalized with PS-SH in DMF to achieve hydrophobicity. DMF was chosen because both AgNPs and PS-SH are miscible in DMF (**Table 7.1**) to allow PS-SH to react with AgNPs.[42] After functionalization, a layer of polymer was anchored on the AgNPs. The polymer layer enabled the AgNPs to be fully

dispersible in organic solvents and prevented them from aggregating during spin-coating.[21-23] TEM revealed that the PS-SH functionalized AgNPs (PS-AgNPs) had a shape similar to the non-functionalized ones (**Figure 7.9c**), indicating that the shape was not compromised during functionalization. The PS-AgNPs showed long-term stability in organic solvents such as chlorobenzene and MeOH.

The solvent vapor pressure is critical to ensure effective spin-coating.[28] Since MeOH has a vapor pressure of 13.01 kPa at room temperature,[43] which is two orders of magnitude higher than DMF (0.32 kPa)[44], the PS-AgNPs were dispersed in MeOH for fast drying after spin-coating, good surface coverage, and minimal nanoparticle aggregation.[28] Moreover, MeOH is a poor solvent for P3HT:PCBM[45] and thus it has little influence on the active layer during spin-coating (**Figure 7.10**). When dispersed in MeOH, the λ_{LSPR} of the AgNPs red-shifted from 485 to 515 nm (**Figure 7.9a**) due to a change in the refractive index (n_{water} = 1.34, n_{PS} = 1.60, and n_{MeOH} = 1.35).[21] The λ_{LSPR} of PS-AgNPs at 515 nm closely matched the optical absorption peak of P3HT (λ_{max} = 514 nm).

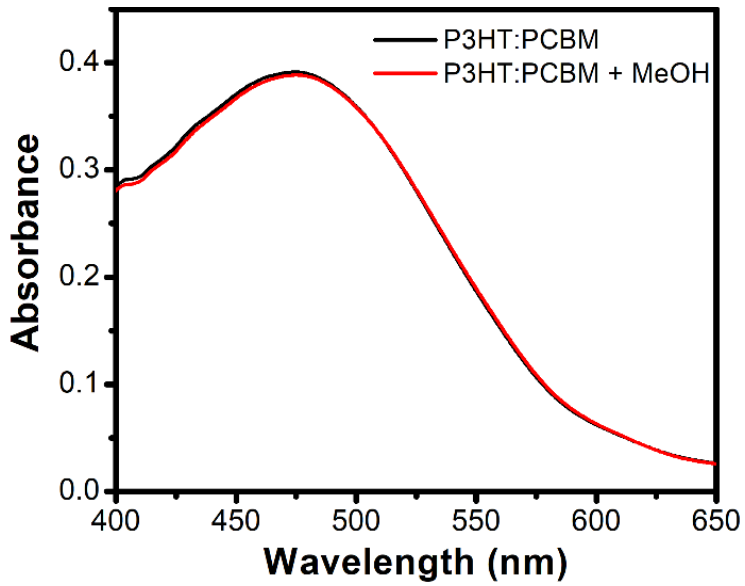

Figure 7.10. Absorption spectrum of P3HT:PCBM before and after spin-coating a blank solution of 500 µl of MeOH at 800 rpm, showing that the P3HT:PCBM is not dissolved.

7.3.6 Density and Structures of PS-AgNPs in Thin Films. The PS-AgNPs were spin-coated on the active layer of P3HT:PCBM. The surface density of the PS-AgNPs was controlled by the solution concentration. As the concentration of the PS-AgNP solution was increased, the density of the PS-AgNPs on the active layer increased (**Figure 7.11**). The PS-AgNP solution of 0.57 nM resulted in a low density and minimal stacking of nanoparticles. At a PS-AgNP solution concentration of 2.90 nM, the surface density was high and the stacking of PS-AgNPs occurred. Thin films of P3HT:PCBM with PS-AgNPs were then thermally annealed and inspected (**Figure 7.12**). The AFM images show that after annealing, the PS-AgNPs remained dispersed on the P3HT:PCBM layer. Additionally, the mean roughness (R_a) and the RMS roughness (R_q) increased with an increasing PS-AgNP concentration (**Table 7.3**) due to the increasing nanoparticle density on the active layer.

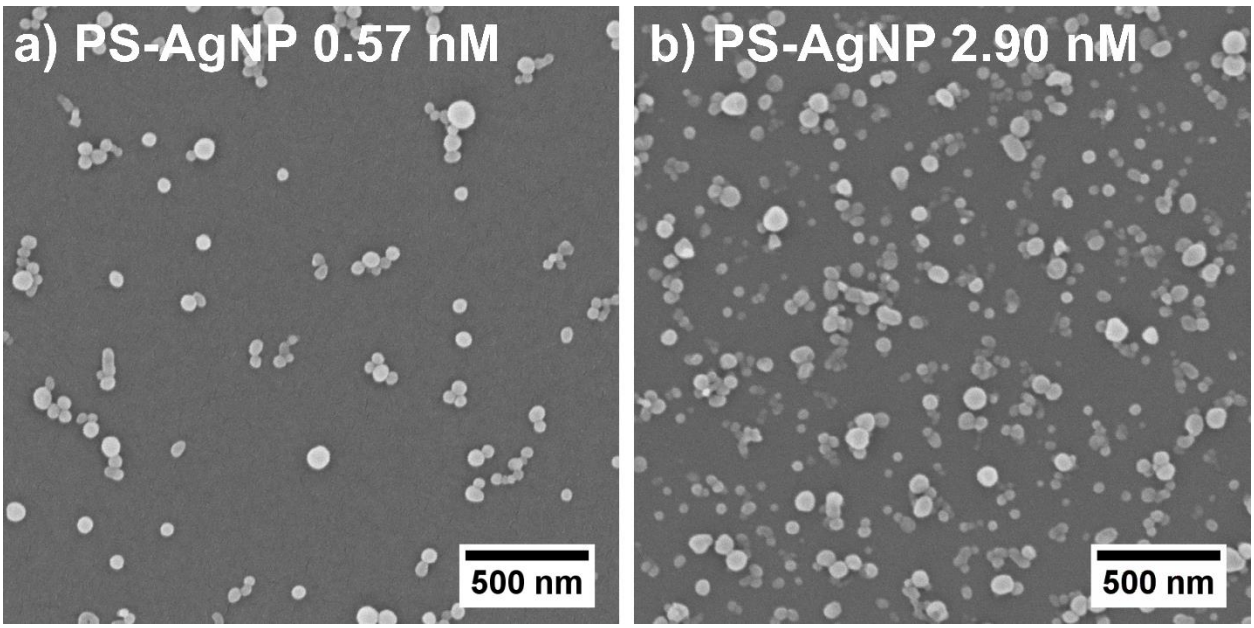

Figure 7.11. Representative SEM images of PS-AgNPs in OPV devices. The PS-AgNPs were spin-coated on the active layer of P3HT:PCBM from solution concentrations of: (**a**) 0.57 nM and (**b**) 2.90 nM.

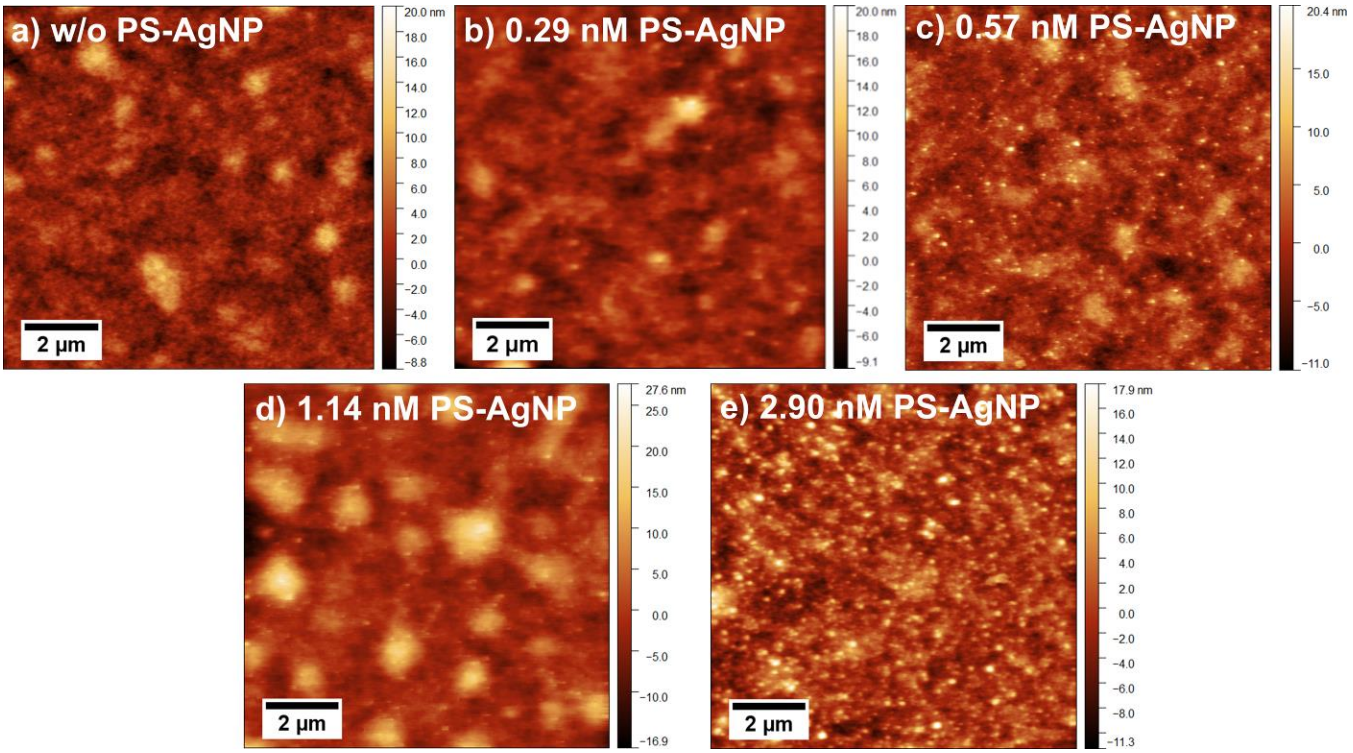

Figure 7.12. AFM height images of thermally annealed P3HT:PCBM films with PS-AgNPs of various concentrations (0 ~ 2.90 nM).

Table 7.3. Arithmetic mean roughness (R_a) and RMS roughness (R_q) of the thermally annealed P3HT:PCBM films with PS-AgNPs of various concentrations (0 ~ 2.90 nM). The roughness values were averaged over at least five AFM images.

PS-AgNPs	R_a (nm)	R_q (nm)
0 nM	1.5 ± 0.3	2.0 ± 0.4
0.29 nM	1.8 ± 0.6	2.4 ± 0.8
0.57 nM	2.2 ± 0.2	2.9 ± 0.2
1.14 nM	3.2 ± 0.2	4.2 ± 0.2
2.90 nM	3.8 ± 0.5	5.0 ± 0.7

7.3.7 Enhancement of Optical Absorption. The addition of PS-AgNPs enhanced the optical absorption of the active layer. **Figure 7.13a** represents the optical absorption of an as-cast active layer of P3HT:PCBM, as well as active layers with PS-AgNPs that were spin-coated from solutions of various concentrations. The optical absorption peak (λ_{max}) of P3HT:PCBM at a mixing ratio of 1:0.8 was at 473 nm, which results from the combined absorption of P3HT (λ_{max} = 514 nm) and PCBM ($\lambda_{max} \approx$ 340 nm). The optical absorption intensity increased continuously as the concentration of PS-AgNPs was increased, similar to that in previous reports.[1, 13] For comparison, the PS-AgNPs were spin-coated on pristine P3HT without PCBM. The absorption of P3HT was also enhanced with an increasing concentration of the PS-AgNPs (**Figure 7.14**). The absorption difference spectra (**Figure 7.13b**) were calculated by subtracting the absorption of P3HT:PCBM from that of the as-cast P3HT:PCBM with PS-AgNPs. The peak positions of the absorption difference spectra were close to the λ_{LSPR} of the PS-AgNPs, suggesting that the absorption enhancements were correlated to the presence of the plasmonic nanoparticles.

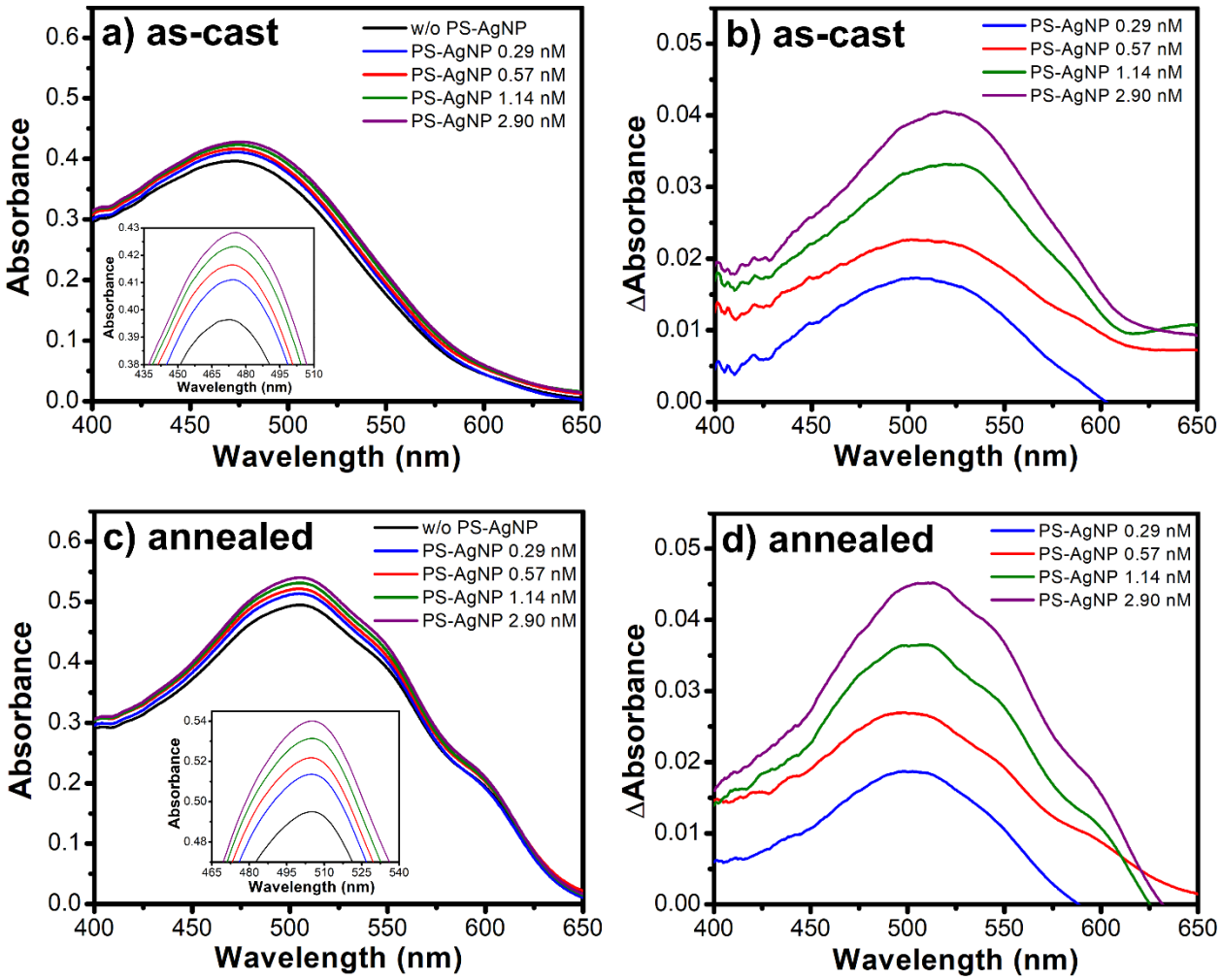

Figure 7.13. (**a**) The optical absorption spectra of the as-cast P3HT:PCBM films before and after spin-coating PS-AgNPs. The PS-AgNP solutions had concentrations of 0.29, 0.57, 1.14, and 2.90 nM. (**b**) The optical absorption difference (ΔAbsorbance) between the P3HT:PCBM films with PS-AgNPs and the as-cast P3HT:PCBM films. (**c, d**) The optical absorption spectra and the difference of the same P3HT:PCBM films after thermal annealing. The insets are zoomed-in view of the absorption peaks.

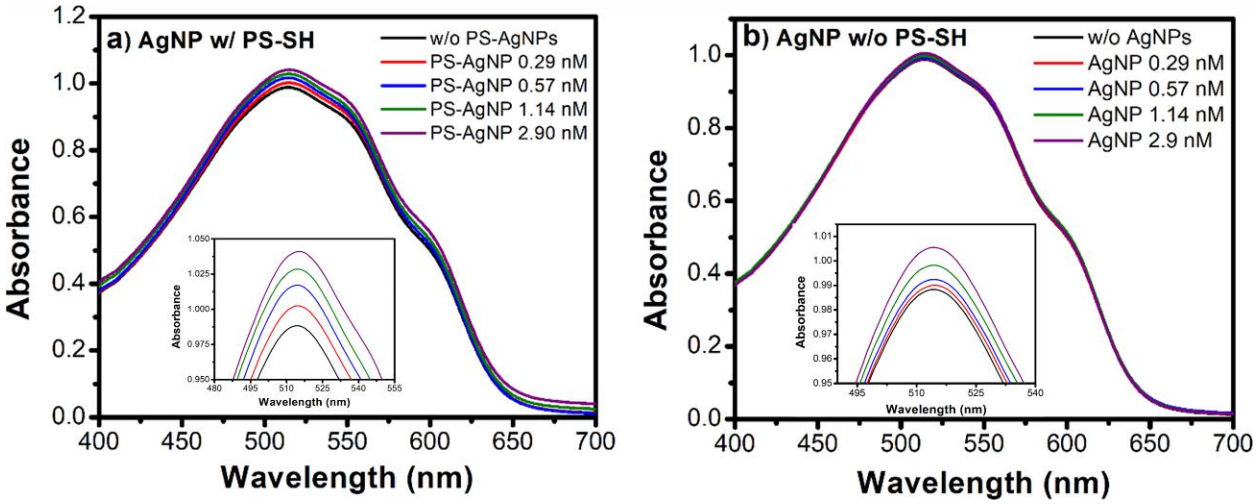

Figure 7.14. Absorption spectra of pristine P3HT films (no PCBM) with a layer of (a) PS-AgNPs and (b) AgNPs of various concentrations. The inset is a zoomed-in view of the absorption peaks.

Thermal annealing of P3HT:PCBM induces further phase separation of P3HT and PCBM, which also increases the planar ordering of P3HT chains and the crystallinity of P3HT/PCBM.[46-49] As a result, thermal annealing often improves the optical absorption, photocurrent, charge carrier mobility, and ultimately device performance.[46-50] As shown in **Figure 7.13c**, the peak optical absorption of P3HT/PCBM increased from 0.39 to 0.49 after annealing. In addition, the absorption peak wavelength (λ_{max}) red-shifted from 473 to 505 nm (**Figure 7.13c**) due to the prominent 0-2 vibronic transition of P3HT.[46] The spectra also developed shoulders at ~550 and ~600 nm, corresponding to the 0-1 and 0-0 vibronic transitions of P3HT, respectively.[46] Similar to the non-annealed films, the optical absorption of the annealed P3HT:PCBM films increased as the concentration of the PS-AgNPs was increased. Additionally, the absorption intensity differences were higher due to the strong coupling between the PS-AgNPs and the annealed P3HT:PCBM (**Figure 7.13d**).

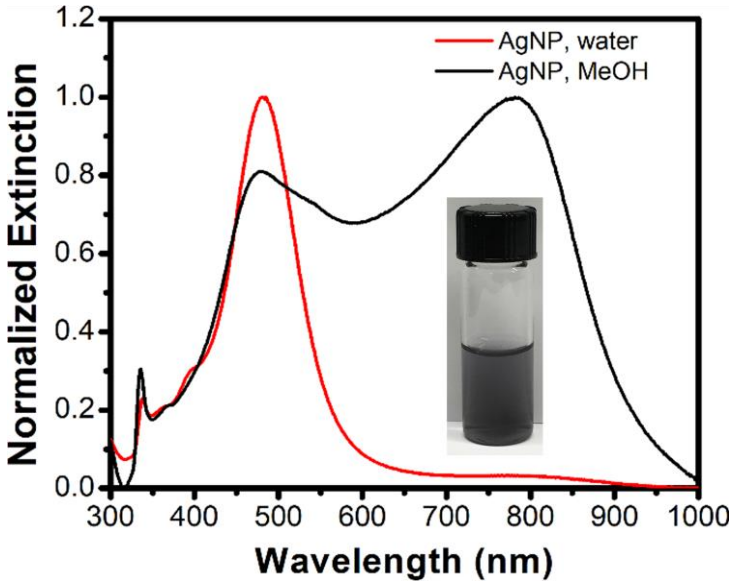

Figure 7.15. Absorption spectra of (red curve) AgNPs in water right after the synthesis and (black curve) aggregated AgNPs after transferring to a solution of MeOH. (inset) A photograph of an aggregated AgNP solution in MeOH.

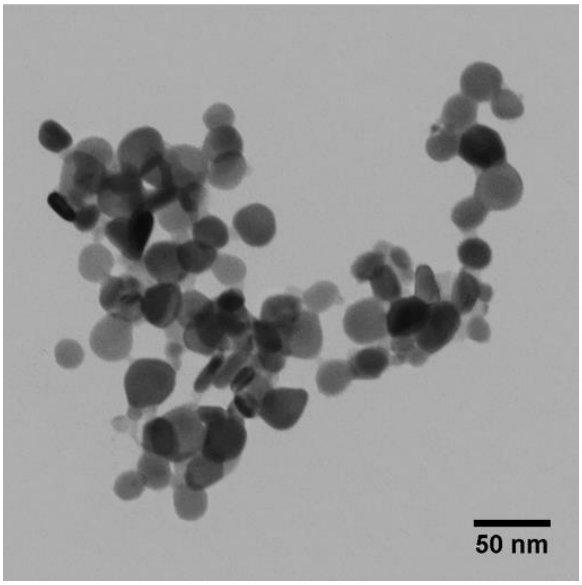

Figure 7.16. TEM image of aggregated AgNPs in MeOH.

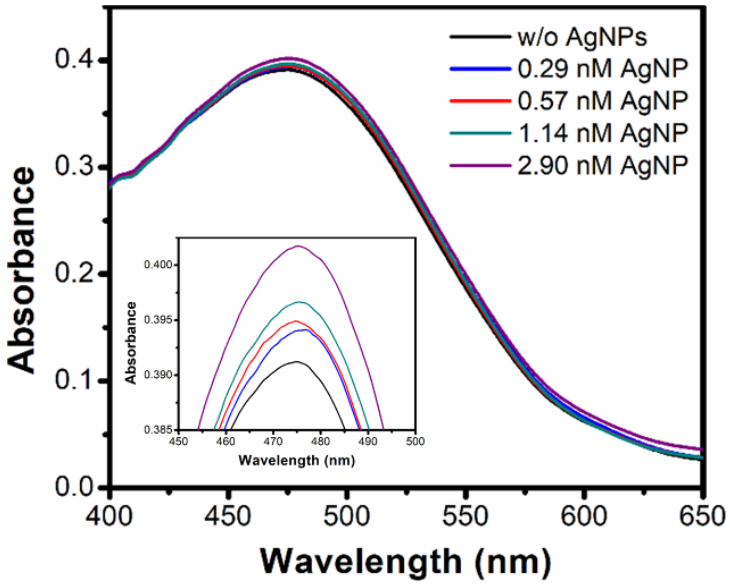

Figure 7.17. Absorption spectra of the aggregated bare AgNPs on P3HT:PCBM.

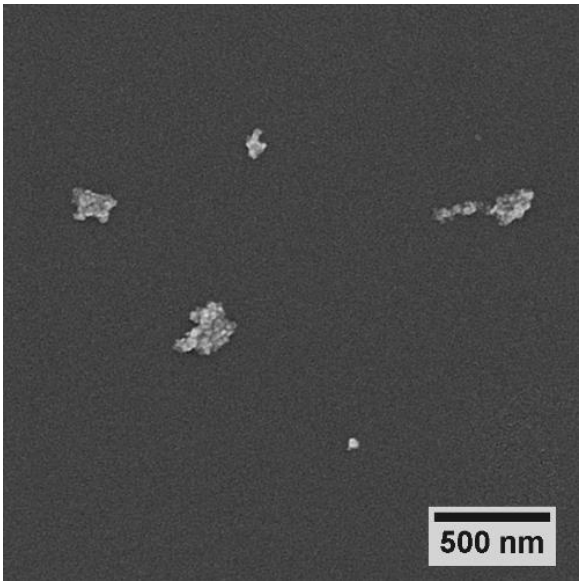

Figure 7.18. SEM image of the aggregated unfunctionalized AgNPs on P3HT:PCBM.

To examine the importance of the polymer coating, unfunctionalized AgNPs in as-synthesized aqueous solutions were centrifuged and directly re-dispersed in MeOH. Without the protective polymer layer, the AgNPs lost their distinct LSPR color and the solution turned black (**Figure 7.15 inset**). As revealed by UV-vis spectroscopy, the solution maintained an absorption peak at λ_{LSPR}

= 485 nm and gained another peak with a greater intensity at λ = 782 nm (**Figure 7.15**). The new extinction peak is attributed to interparticle plasmonic coupling,[9, 51] which is due to the AgNP aggregation in the solvent. The formation of AgNP aggregates in solutions was confirmed by TEM (**Figure 7.16**) with an average aggregated cluster size of 278.2 ± 80.0 nm. The aggregated AgNPs on P3HT:PCBM films were confirmed by SEM (**Figure 7.18**). Although the unfunctionalized, aggregated AgNPs enhanced the optical absorption of both pristine P3HT and P3HT:PCBM (**Figures 7.14b** and **7.17**), the aggregated AgNPs were detrimental to the performance of OPV devices (**Figure 7.21**), demonstrating the importance of a polymer layer on the AgNPs.

7.3.8 Enhancement of Steady-state Photoluminescence. Steady-state photoluminescence (PL) spectroscopy can indirectly measure the amount of photogenerated excitons at a given PL quantum efficiency.[4-5, 10, 12, 15, 52] When P3HT films (without the PCBM electron acceptor) were excited by a laser at 488 nm, at which wavelength P3HT strongly absorbs, the PL intensity increased with the surface density of the PS-AgNPs (**Figure 7.19a**). The primary PL peak was at λ = 718 nm, which corresponds to the singlet exciton emission of P3HT.[8, 46] Higher densities of nanoparticles amplified the plasmon resonance and increased the amount of excitons generated by P3HT. The elevated PL intensity is in agreement with the enhanced optical absorption of P3HT:PCBM and pristine P3HT films.

In contrast, the PL intensity of P3HT films with unfunctionalized AgNPs showed an opposite trend, *i.e.*, an increase in the AgNP concentration resulted in a decrease in the PL intensity (**Figure 7.19b**). The causes are likely twofold. First, despite that the aggregated AgNPs produced enhanced optical absorption (**Figures 7.14b** and **7.17**), the unfunctionalized AgNPs had no insulating polymer layer on the surface and were in direct contact with P3HT, thus providing convenient sites for exciton dissociation, non-radiative recombination, and photoluminescence

quenching.[10-11] Second, the PL emission spectra of P3HT overlapped the extinction peak of the unfunctionalized AgNPs, which increased the probability of non-radiative recombination by Förster resonance energy transfer.[8, 53] Therefore, it is important to functionalize the AgNPs with polymers to enhance the PV device performance.

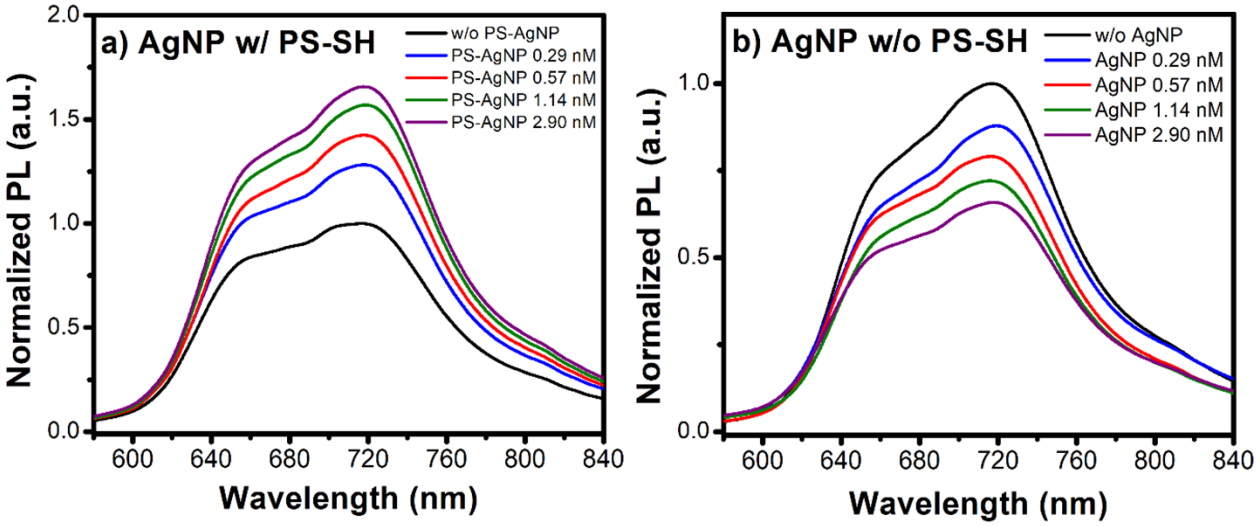

Figure 7.19. Photoluminesence emission spectra of P3HT films with a layer of (**a**) PS-AgNPs and (**b**) AgNPs. The intensities are normalized to the reference films without PS-AgNPs or AgNPs.

7.3.9 OPV Device Performance with PS-AgNPs. OPV devices were assembled following the architecture of ITO/PEDOT:PSS/P3HT:PCBM/PS-AgNPs/Al. The current density (J) – voltage (V) curves were measured under 100 mW/cm^2 AM1.5G illumination. Reference devices without PS-AgNPs were also assembled and measured. The reference devices had an average short-circuit current density (J_{sc}) of -7.88 mA/cm^2, an open circuit voltage (V_{oc}) of 0.62 V, a fill factor (FF) of 0.51, and an average power conversion efficiency (PCE) of 2.45% (**Figure 7.20a**). After adding a low concentration of the PS-AgNPs, the J-V characteristics improved substantially from the reference devices. At a PS-AgNP concentration of 0.57 nM, the devices performed the best with a J_{sc} of -9.77 mA/cm^2, a V_{oc} of 0.63 V, a FF of 0.53, and an average PCE of 3.23%, which was 32% higher than the average PCE of all reference devices (**Table 7.4**). Additionally, the average

external quantum efficiency (EQE) spectra peaked at λ = 505 nm with an efficiency of at 75.1%, which was 25% higher than the reference devices (peak EQE = 60.4% at λ = 505 nm) (**Figure 7.20b**). The performance gradually deteriorated when the PS-AgNPs concentration was increased beyond 0.57 nM. At a PS-AgNP concentration of 2.90 nM, the device characteristics dropped below the reference devices. J-V curves and EQE spectra of OPV devices with unfunctionalized AgNPs were also measured (**Figure 7.21**). In contrast, all devices in this case showed worse performance than the reference devices (**Table 7.5**).

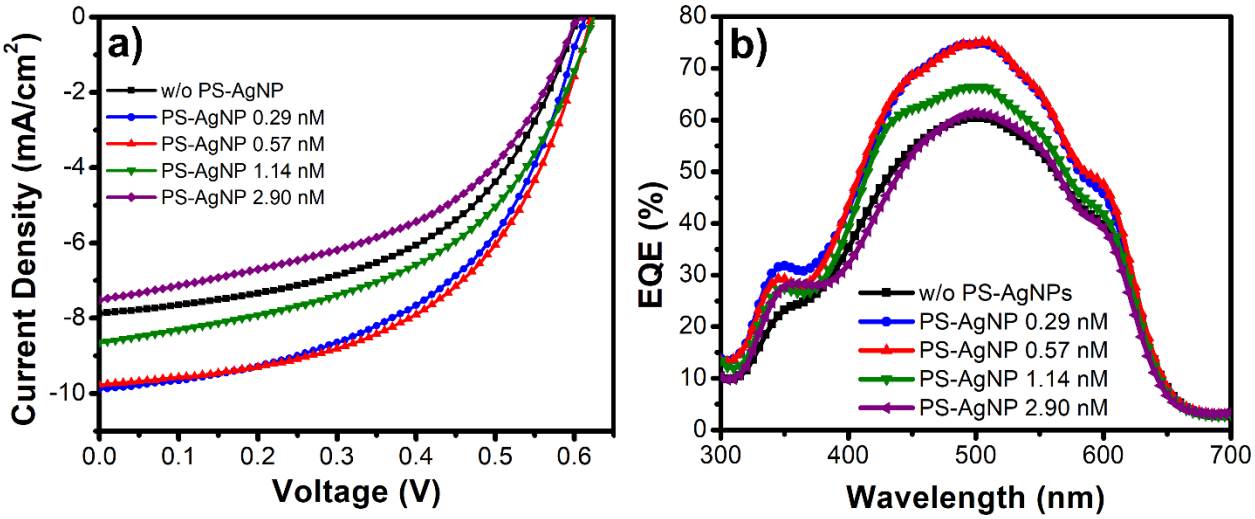

Figure 7.20. (**a**) The current density – voltage (J-V) characteristics and (**b**) the corresponding external quantum efficiency (EQE) of OPV devices.

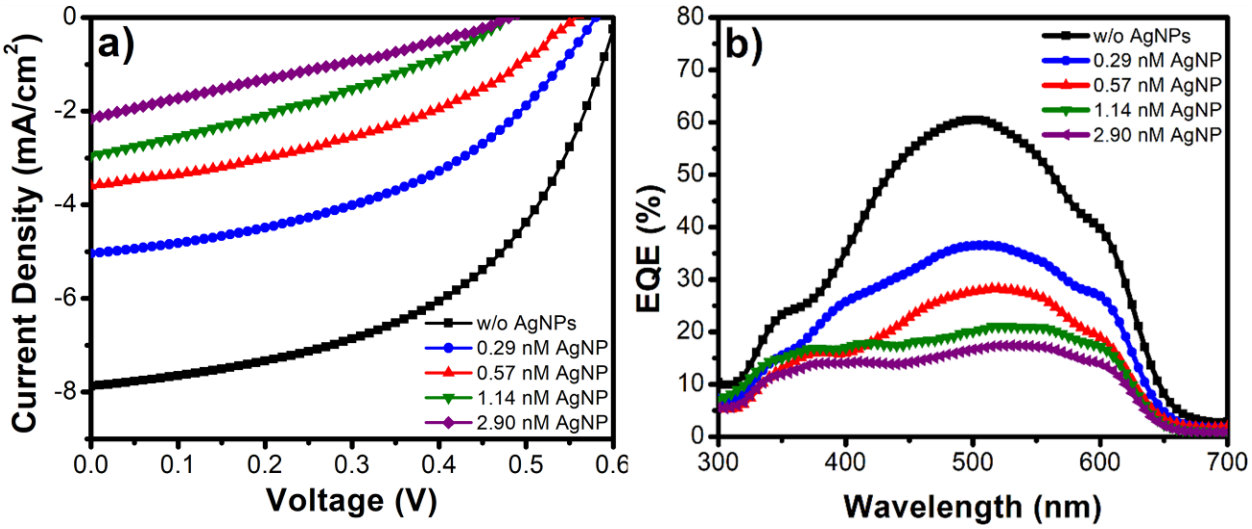

Figure 7.21. (**a**) The current density – voltage (J-V) characteristics of OPV devices with bare AgNPs and (**b**) the corresponding external quantum efficiency (EQE).

Table 7.4. The J-V characteristics of the OPV devices with PS-AgNPs of various concentrations ranging from 0 to 2.90 nM in the spin-coating solutions. All values are averaged over at least 5 devices. The "%diff" is the percentage of the average PCE improvement compared to the reference devices.

PS-AgNPs	J_{sc} (mA/cm^2)	V_{oc} (V)	FF	R_s (Ω·cm^2)	R_{sh} (Ω·cm^2)	PCE (%)	Best PCE (%)	%diff
0 nM (ref)	-7.88 ± 0.16	0.62 ± 0.01	0.51 ± 0.02	12.10 ± 2.2	502 ± 159	2.45 ± 0.05	2.61	-
0.29 nM	-9.88 ± 0.05	0.62 ± 0.01	0.52 ± 0.003	9.27 ± 0.5	505 ± 67	3.10 ± 0.04	3.14	27%
0.57 nM	-9.77 ± 0.11	0.63 ± 0.01	0.53 ± 0.01	11.02 ± 1.1	470 ± 117	3.23 ± 0.1	3.40	32%
1.14 nM	-8.65 ± 0.23	0.63 ± 0.01	0.50 ± 0.03	14.05 ± 1.7	330 ± 48	2.69 ± 0.2	2.90	10%
2.90 nM	-7.52 ± 0.15	0.61 ± 0.01	0.48 ± 0.02	17.35 ± 2.9	250 ± 32	2.21 ± 0.06	2.27	-10%

Table 7.5. The J-V characteristics of the OPV devices with unfunctionalized AgNPs of various concentrations ranging from 0 to 2.90 nM in the spin-coating solutions. All values are averaged over at least 5 devices.

AgNP	J_{sc} (mA/cm^2)	V_{oc} (V)	FF	R_s (Ω·cm^2)	R_{sh} (Ω·cm^2)	PCE (%)	Best PCE (%)
0 nM (ref)	-7.88 ± 0.16	0.62 ± 0.01	0.51 ± 0.02	12.10 ± 2.2	502 ± 159	2.45 ± 0.05	2.61
0.29 nM	-5.04 ± 0.18	0.59 ± 0.01	0.45 ± 0.003	29.10 ± 0.5	503 ± 36	1.31 ± 0.05	1.36
0.57 nM	-3.59 ± 0.10	0.56 ± 0.02	0.40 ± 0.04	34.85 ± 6.2	367 ± 42	0.81 ± 0.08	0.86
1.14 nM	-2.96 ± 0.22	0.51 ± 0.05	0.36 ± 0.05	39.07 ± 3.0	278 ± 114	0.68 ± 0.29	0.75
2.90 nM	-2.16 ± 0.15	0.50 ± 0.03	0.28 ± 0.02	51.98 ± 14.7	223 ± 35	0.30 ± 0.05	0.37

In an ideal device, R_{sh} should be as high as possible. After adding a small amount of the PS-AgNPs (0.29 nM), R_{sh} did not change significantly. However, R_{sh} decreased continuously as the PS-AgNP concentration was increased from 0.29 to 2.90 nM (**Table 7.4**). At a PS-AgNP concentration of 2.90 nM, the average R_{sh} values decreased by 50% compared to the reference devices. R_{sh} is referred to as the parallel resistance,[54] which is inversely proportional to the level of leakage current as a result of linear ohmic shunts (*i.e.*, short circuits) and nonlinear local shunts.[9, 55-56] The local shunts, where charge carriers recombine, are usually caused by nanoparticle aggregation,[9, 11, 17] poor interface quality, and crystal defects.[56] An examination of the PS-AgNPs on the active layer (**Figures 7.11a** and **7.11b**) reveals the cause of the decreasing R_{sh}. At low PS-AgNP concentrations, the aggregation of the PS-AgNPs was insignificant and R_{sh} was similar to the reference devices. As the nanoparticle concentration was increased, the face-to-face stacking of the PS-AgNPs was unavoidable. The stacked PS-AgNPs behaved as small aggregates and caused local shunts as shown in previous reports.[9, 11, 17] In addition, the stacked PS-AgNPs caused surface defects and voids, which immobilized the charge carriers and increased the charge

recombination.[17] In devices with unfunctionalized AgNPs, the stacking and aggregation were more prevalent and R_{sh} dropped more intensely than the OPV devices with PS-AgNPs (**Table 7.5**).

In contrast to R_{sh}, R_s should be as low as possible in an ideal device. R_s decreased favorably by ~25% after adding a small amount of PS-AgNPs (0.29 nM); then it increased as the PS-AgNP concentration was increased from 0.29 to 2.90 nM (**Table 7.4**). At a PS-AgNP concentration of 2.90 nM, R_s increased by 43% compared to the reference devices. R_s is the combined resistance of the active layer, electrodes, and interfacial contacts.[57] The decrease in R_s after adding 0.29 nM of PS-AgNPs is attributed to a beneficial drop in the contact resistance between the active layer and the cathode, since all other parameters were constant such as the device processing conditions, the active layer thickness, and the electrode materials. At low PS-AgNP concentrations, the resistance most likely decreased due to the increased surface roughness of the active layer (**Figure 7.12**), which led to an increase of the interfacial surface area between the active layer and the cathode.[49, 58-59] Although the polymer layer largely insulated the AgNPs,[18] it was shown in previous reports that due to the strong citrate adsorption on NPs, a complete citrate-to-thiol ligand exchange is difficult and a small portion of the total particle surface area is possibly uninsulated.[51] As a result, there was possible charge injection[59] from P3HT:PCBM to the PS-AgNPs and subsequent charge transport[16, 20] from the PS-AgNPs to the aluminum electrodes. Although charge injection may remain in devices with stacked PS-AgNPs of high concentrations and aggregated unfunctionalized AgNPs, the average R_s values increased disadvantageously due to the creation of defects, voids, and decreased contact between the active layer and the cathode.[17]

FF mostly depends on the resistances R_{sh} and R_s.[60] To maximize the FF, the R_s and R_{sh} should be as low and as high as possible, respectively. At low PS-AgNP concentrations of 0.29 and 0.57 nM, the R_s values were lower than that of the reference devices and thus their FF values were

higher. In devices with high PS-AgNP concentrations of 1.14 and 2.90 nM or unfunctionalized AgNPs, R_s increased and R_{sh} decreased and thus FF decreased.

J_{sc} is related to R_s, optical absorption, film morphology, charge carrier mobility, and others.[45, 47, 49, 57, 61-65] The optical absorption of the OPV devices were enhanced by the nanoparticle LSPR[13] (**Figure 7.13**). In the devices with PS-AgNPs, the J_{sc} was mainly dependent on a competition between the optical absorption and R_s. Thanks to the improved optical absorption and the lowest R_s, the OPV devices with the lowest PS-AgNP concentration of 0.29 nM exhibited the highest J_{sc}, which was 25% more than the reference devices. When the PS-AgNP concentration was above 0.29 nM, however, the increasing R_s overwhelmed the effect of the increasing optical absorption and thus J_{sc} continuously declined. The effect of R_s was more prominent in the devices with unfunctionalized AgNPs, where J_{sc} substantially degraded as the AgNP concentration was increased. EQE exhibited a similar trend: EQE increased significantly compared to the reference devices when the PS-AgNP concentration was at 0.29 or 0.57 nM; it declined continuously when the concentration was further increased to 2.90 nM. For devices with the unfunctionalized AgNPs, both EQE and J_{sc} deteriorated substantially due to the increase in R_s.

V_{oc} is determined by the difference between the lowest unoccupied molecular orbital (LUMO**)** of the acceptor and the highest occupied molecular orbital (HOMO**)** of the donor, along with the voltage losses due to band bending at the electrodes,[50, 66] energetic disorder[64, 66] and charge recombination.[64, 66] It is reported that trap-assisted recombination, which could be induced by the ligand-capped AgNPs, causes drops in V_{oc}.[8, 11] In addition, since R_{sh} is inversely correlated to the charge recombination level, a decrease in R_{sh} can deteriorate the V_{oc},[17, 60] especially at low light intensities where the leakage current dominates.[54] In this work, V_{oc} showed no appreciable changes after adding PS-AgNPs but steadily declined after adding an increasing amount of

unfunctionalized AgNPs. The defects and voids created by the unfunctionalized AgNP aggregates enhanced the recombination rates and reduced the shunt resistance,[17] which ultimately resulted in a severely degraded $V_{oc.}$

FF, J_{sc}, and V_{oc} collectively determine the PCE of an OPV device. At a PS-AgNP concentration of 0.57 nM, the devices showed the highest combined effects of FF, J_{sc}, and V_{oc}. As a result, the PCE increased by 32% compared to the reference devices. With a PS-AgNP concentration of 0.29 nM, the devices showed a slightly lower PCE increase of 27%, due to the marginally lower FF and V_{oc}. When the PS-AgNP concentration was above 0.57 nM, PCE decreased continuously due to the deteriorated characteristics of FF, J_{sc}, and V_{oc}. At a PS-AgNP concentration of 2.90 nM, the PCE was even lower than the reference devices due to the worse FF, J_{sc}, and V_{oc}. In OPV devices with unfunctionalized AgNPs, the FF, J_{sc}, and V_{oc} all decreased and the PCE values were lower at all concentrations than the reference devices. Even at the lowest concentration of 0.29 nM, the AgNPs caused a PCE decrease by 47%. The continuously declined performance with an increasing concentration of the AgNPs highlights that unfunctionalized AgNPs are detrimental to the OPVs, despite the enhanced optical absorption. The polymer layer effectively insulated the PS-AgNPs, minimized the nanoparticle aggregation, and provided significant enhancements to the PCE of the OPV devices.

7.4 CONCLUSIONS

We have shown that the polymer functionalized PS-AgNPs effectively increase the optical absorption and improve the power conversion efficiency of organic photovoltaics. We demonstrate that an insulating polymer layer on the plasmonic nanoparticles, such as polystyrene, is essential for reducing the detrimental effects such as exciton quenching and charge trapping, even when the nanoparticles are placed between the active layer and the cathode. The polystyrene layer on the

nanoparticles also enables their stable dispersion in organic solvents and effective spin-coating on the active layer. To effectively improve the light absorption, the λ_{LSPR} of the PS-AgNPs are coupled to the λ_{max} of the active layer. As the concentration of the PS-AgNPs is increased, the light absorption of the active layer is enhanced. The power conversion efficiency, however, increases only at low PS-AgNP concentrations, peaks at a concentration of 0.57 nM (32% improvement compared to the reference devices), and then decreases at high concentrations. Unfunctionalized AgNPs and PEG-AgNPs deteriorate the performances of the OPV devices regardless of the concentration due to particle aggregations.

REFERENCES

(1) Baek, S.-W.; Noh, J.; Lee, C.-H.; Kim, B.; Seo, M.-K.; Lee, J.-Y. Plasmonic Forward Scattering Effect in Organic Solar Cells: A Powerful Optical Engineering Method. *Sci. Rep.* **2013,** *3*, 1726.

(2) Fung, D. D.; Qiao, L.; Choy, W. C.; Wang, C.; Wei, E.; Xie, F.; He, S. Optical and Electrical Properties of Efficiency Enhanced Polymer Solar Cells with Au Nanoparticles in a Pedot–Pss Layer. *J. Mater. Chem.* **2011,** *21* (41), 16349-16356.

(3) Yao, K.; Salvador, M.; Chueh, C. C.; Xin, X. K.; Xu, Y. X.; deQuilettes, D. W.; Hu, T.; Chen, Y.; Ginger, D. S.; Jen, A. K. Y. A General Route to Enhance Polymer Solar Cell Performance Using Plasmonic Nanoprisms. *Adv. Energy Mater.* **2014,** *4* (9).

(4) Wu, J.-L.; Chen, F.-C.; Hsiao, Y.-S.; Chien, F.-C.; Chen, P.; Kuo, C.-H.; Huang, M. H.; Hsu, C.-S. Surface Plasmonic Effects of Metallic Nanoparticles on the Performance of Polymer Bulk Heterojunction Solar Cells. *ACS Nano* **2011,** *5* (2), 959-967.

(5) Yang, Y.; Lin, X.; Qing, J.; Zhong, Z.; Ou, J.; Hu, C.; Chen, X.; Zhou, X.; Chen, Y. Enhancement of Short-Circuit Current Density in Polymer Bulk Heterojunction Solar Cells Comprising Plasmonic Silver Nanowires. *Appl. Phys. Lett.* **2014,** *104* (12), 123302.

(6) Stratakis, E.; Kymakis, E. Nanoparticle-Based Plasmonic Organic Photovoltaic Devices. *Materials Today* **2013,** *16* (4), 133-146.

(7) Kim, H.; Nam, S.; Lee, H.; Woo, S.; Ha, C.-S.; Ree, M.; Kim, Y. Influence of Controlled Acidity of Hole-Collecting Buffer Layers on the Performance and Lifetime of Polymer: Fullerene Solar Cells. *J. Phys. Chem. C* **2011,** *115* (27), 13502-13510.

(8) Wu, B.; Wu, X.; Guan, C.; Tai, K. F.; Yeow, E. K. L.; Fan, H. J.; Mathews, N.; Sum, T. C. Uncovering Loss Mechanisms in Silver Nanoparticle-Blended Plasmonic Organic Solar Cells. *Nat. Commun.* **2013,** *4*.

(9) Topp, K.; Borchert, H.; Johnen, F.; Tunc, A.; Knipper, M.; Von Hauff, E.; Parisi, J.; Al-Shamery, K. Impact of the Incorporation of Au Nanoparticles into Polymer/Fullerene Solar Cells. *J. Phys. Chem. A* **2009,** *114* (11), 3981-3989.

(10) Du, P.; Jing, P.; Li, D.; Cao, Y.; Liu, Z.; Sun, Z. Plasmonic Ag@ Oxide Nanoprisms for Enhanced Performance of Organic Solar Cells. *Small* **2015,** *11* (20), 2454-2462.

(11) Xue, M.; Li, L.; Tremolet de Villers, B. J.; Shen, H.; Zhu, J.; Yu, Z.; Stieg, A. Z.; Pei, Q.; Schwartz, B. J.; Wang, K. L. Charge-Carrier Dynamics in Hybrid Plasmonic Organic Solar Cells with Ag Nanoparticles. *Appl. Phys. Lett.* **2011,** *98* (25), 119.
(12) Kymakis, E.; Spyropoulos, G. D.; Fernandes, R.; Kakavelakis, G.; Kanaras, A. G.; Stratakis, E. Plasmonic Bulk Heterojunction Solar Cells: The Role of Nanoparticle Ligand Coating. *ACS Photonics* **2015,** *2* (6), 714-723.
(13) Kulkarni, A. P.; Noone, K. M.; Munechika, K.; Guyer, S. R.; Ginger, D. S. Plasmon-Enhanced Charge Carrier Generation in Organic Photovoltaic Films Using Silver Nanoprisms. *Nano Lett.* **2010,** *10* (4), 1501-1505.
(14) Shen, W.; Tang, J.; Yang, R.; Cong, H.; Bao, X.; Wang, Y.; Wang, X.; Huang, Z.; Liu, J.; Huang, L. Enhanced Efficiency of Polymer Solar Cells by Incorporated Ag–Sio 2 Core–Shell Nanoparticles in the Active Layer. *RSC Adv.* **2014,** *4* (9), 4379-4386.
(15) Spyropoulos, G. D.; Stylianakis, M. M.; Stratakis, E.; Kymakis, E. Organic Bulk Heterojunction Photovoltaic Devices with Surfactant-Free Au Nanoparticles Embedded in the Active Layer. *Appl. Phys. Lett.* **2012,** *100* (21), 213904.
(16) Kalfagiannis, N.; Karagiannidis, P.; Pitsalidis, C.; Panagiotopoulos, N.; Gravalidis, C.; Kassavetis, S.; Patsalas, P.; Logothetidis, S. Plasmonic Silver Nanoparticles for Improved Organic Solar Cells. *Sol. Energy Mater. Sol. Cells* **2012,** *104* 165-174.
(17) Li, P.; Jiu, T.; Tang, G.; Wang, G.; Li, J.; Li, X.; Fang, J. Solvents Induced Zno Nanoparticles Aggregation Associated with Their Interfacial Effect on Organic Solar Cells. *ACS applied materials & interfaces* **2014,** *6* (20), 18172-18179.
(18) Butcher, D. P.; Wadams, R. C.; Drummy, L.; Koerner, H.; Bailey, C.; Scheltens, F.; Mccomb, D.; Fabris, L.; Durstock, M. F.; Tabor, C. Controlled Dispersion of Polystyrene‐Capped Au Nanoparticles in P3ht: Pc61bm and Consequences Upon Active Layer Nanostructure. *J. Polym. Sci. B* **2016,** *54* (7), 709-720.
(19) Woo, Y. J.; Park, K. H.; Park, O. O.; Wang, D. H. Dispersion Control of Ag Nanoparticles in Bulk-Heterojunction for Efficient Organic Photovoltaic Devices. *Org. Electron.* **2015,** *16* 118-125.
(20) Li, X.; Choy, W. C. H.; Lu, H.; Sha, W. E.; Ho, A. H. P. Efficiency Enhancement of Organic Solar Cells by Using Shape‐Dependent Broadband Plasmonic Absorption in Metallic Nanoparticles. *Advanced Functional Materials* **2013,** *23* (21), 2728-2735.
(21) Lombardo, M. T.; Pozzo, L. D. Clusters and Inverse Emulsions from Nanoparticle Surfactants in Organic Solvents. *Langmuir* **2015,** *31* (4), 1344-1352.
(22) Bokern, S.; Getze, J.; Agarwal, S.; Greiner, A. Polymer Grafted Silver and Copper Nanoparticles with Exceptional Stability against Aggregation by a High Yield One-Pot Synthesis. *Polymer* **2011,** *52* (4), 912-920.
(23) Pletsch, H.; Peng, L.; Mitschang, F.; Schaper, A.; Hellwig, M.; Nette, D.; Seubert, A.; Greiner, A.; Agarwal, S. Ultrasound–Mediated Synthesis of High–Molecular Weight Polystyrene–Grafted Silver Nanoparticles by Facile Ligand Exchange Reactions in Suspension. *Small* **2014,** *10* (1), 201-208.
(24) Aherne, D.; Ledwith, D. M.; Gara, M.; Kelly, J. M. Optical Properties and Growth Aspects of Silver Nanoprisms Produced by a Highly Reproducible and Rapid Synthesis at Room Temperature. *Adv. Funct. Mater.* **2008,** *18* (14), 2005-2016.
(25) Khan, A. U.; Scruggs, C.; Hicks, D.; Liu, G. Two-Dimensional Plasmonic Nanoparticle as a Nanoscale Sensor to Probe Polymer Brush Formation. *Analytical Chemistry* **2017,** *89* (14), 7541-7548.

(26) Khan, A. U.; Zhou, Z.; Krause, J.; Liu, G. Poly (Vinylpyrrolidone) - Free Multistep Synthesis of Silver Nanoplates with Plasmon Resonance in the near Infrared Range. *Small* **2017,** *13* (43).
(27) Nishi, H.; Kobatake, S. Reduction Reaction to Thiol Group of Dithiobenzoate End Group in Polystyrene Polymerized by Reversible Addition–Fragmentation Chain Transfer. *Chem. Lett.* **2008,** *37* (6), 630-631.
(28) Picart, C.; Lavalle, P.; Hubert, P.; Cuisinier, F.; Decher, G.; Schaaf, P.; Voegel, J.-C. Buildup Mechanism for Poly (L-Lysine)/Hyaluronic Acid Films onto a Solid Surface. *Langmuir* **2001,** *17* (23), 7414-7424.
(29) Norrman, K.; Gevorgyan, S. A.; Krebs, F. C. Water-Induced Degradation of Polymer Solar Cells Studied by H218o Labeling. *ACS Appl. Mater. Interfaces* **2008,** *1* (1), 102-112.
(30) An, J.; Tang, B.; Zheng, X.; Zhou, J.; Dong, F.; Xu, S.; Wang, Y.; Zhao, B.; Xu, W. Sculpturing Effect of Chloride Ions in Shape Transformation from Triangular to Discal Silver Nanoplates. *J. Phys. Chem. C* **2008,** *112* (39), 15176-15182.
(31) Han, J. T.; Zheng, Y.; Cho, J. H.; Xu, X.; Cho, K. Stable Superhydrophobic Organic-Inorganic Hybrid Films by Electrostatic Self-Assembly. *The Journal of Physical Chemistry B* **2005,** *109* (44), 20773-20778.
(32) Pérez-Madrigal, M. M.; Armelin, E.; Puiggalí, J.; Alemán, C. Insulating and Semiconducting Polymeric Free-Standing Nanomembranes with Biomedical Applications. *Journal of Materials Chemistry B* **2015,** *3* (29), 5904-5932.
(33) Wang, T.; Qi, Y.; Xu, J.; Hu, X.; Chen, P. Effects of Poly (Ethylene Glycol) on Electrical Conductivity of Poly (3, 4-Ethylenedioxythiophene)–Poly (Styrenesulfonic Acid) Film. *Applied surface science* **2005,** *250* (1-4), 188-194.
(34) Alkilany, A. M.; Yaseen, A. I. B.; Park, J.; Eller, J. R.; Murphy, C. J. Facile Phase Transfer of Gold Nanoparticles from Aqueous Solution to Organic Solvents with Thiolated Poly(Ethylene Glycol). *RSC Adv.* **2014,** *4* (95), 52676-52679, DOI: 10.1039/C4RA11928B.
(35) Polyanskiy, M. N. Refractive Index Database. https://refractiveindex.info/.
(36) Balazs, A. C.; Emrick, T.; Russell, T. P. Nanoparticle Polymer Composites: Where Two Small Worlds Meet. *Science* **2006,** *314* (5802), 1107-1110.
(37) Oh, J. Y.; Jang, W. S.; Lee, T. I.; Myoung, J.-M.; Baik, H. K. Driving Vertical Phase Separation in a Bulk-Heterojunction by Inserting a Poly (3-Hexylthiophene) Layer for Highly Efficient Organic Solar Cells. *Appl. Phys. Lett.* **2011,** *98* (2), 6.
(38) Karagiannidis, P.; Georgiou, D.; Pitsalidis, C.; Laskarakis, A.; Logothetidis, S. Evolution of Vertical Phase Separation in P3ht: Pcbm Thin Films Induced by Thermal Annealing. *Materials Chemistry and Physics* **2011,** *129* (3), 1207-1213.
(39) Haes, A. J.; Haynes, C. L.; McFarland, A. D.; Schatz, G. C.; Van Duyne, R. P.; Zou, S. Plasmonic Materials for Surface-Enhanced Sensing and Spectroscopy. *MRS Bull.* **2005,** *30* (5), 368-375.
(40) Pastoriza-Santos, I.; Liz-Marzán, L. M. Colloidal Silver Nanoplates. State of the Art and Future Challenges. *J. Mater. Chem.* **2008,** *18* (15), 1724-1737.
(41) Kelly, K. L.; Coronado, E.; Zhao, L. L.; Schatz, G. C. The Optical Properties of Metal Nanoparticles: The Influence of Size, Shape, and Dielectric Environment. *J. Phys. Chem. B.* **2003**.
(42) Galati, E.; Tebbe, M.; Querejeta-Fernández, A.; Xin, H. L.; Gang, O.; Zhulina, E. B.; Kumacheva, E. Shape-Specific Patterning of Polymer-Functionalized Nanoparticles. *ACS Nano* **2017,** *11* (5), 4995-5002.
(43) Gibbard, H. F.; Creek, J. L. Vapor Pressure of Methanol from 288.15 to 337.65. Deg. K. *J. Chem. Eng. Data* **1974,** *19* (4), 308-310.

(44) Cui, X.; Chen, G.; Han, X. Experimental Vapor Pressure Data and a Vapor Pressure Equation for N, N-Dimethylformamide. *J. Chem. Eng. Data* **2006,** *51* (5), 1860-1861.
(45) Li, H.; Tang, H.; Li, L.; Xu, W.; Zhao, X.; Yang, X. Solvent-Soaking Treatment Induced Morphology Evolution in P3ht/Pcbm Composite Films. *J. Mater. Chem.* **2011,** *21* (18), 6563-6568.
(46) Marsh, R. A.; Hodgkiss, J. M.; Albert-Seifried, S.; Friend, R. H. Effect of Annealing on P3ht: Pcbm Charge Transfer and Nanoscale Morphology Probed by Ultrafast Spectroscopy. *Nano Lett.* **2010,** *10* (3), 923-930.
(47) Wang, T.; Pearson, A. J.; Lidzey, D. G.; Jones, R. A. Evolution of Structure, Optoelectronic Properties, and Device Performance of Polythiophene: Fullerene Solar Cells During Thermal Annealing. *Adv. Funct. Mater.* **2011,** *21* (8), 1383-1390.
(48) Erb, T.; Zhokhavets, U.; Gobsch, G.; Raleva, S.; Stühn, B.; Schilinsky, P.; Waldauf, C.; Brabec, C. J. Correlation between Structural and Optical Properties of Composite Polymer/Fullerene Films for Organic Solar Cells. *Adv. Funct. Mater.* **2005,** *15* (7), 1193-1196.
(49) Li, G.; Shrotriya, V.; Huang, J.; Yao, Y.; Moriarty, T.; Emery, K.; Yang, Y. High-Efficiency Solution Processable Polymer Photovoltaic Cells by Self-Organization of Polymer Blends. *Nat. Mater.* **2005,** *4* (11), 864-868.
(50) Bartesaghi, D.; del Carmen Pérez, I.; Kniepert, J.; Roland, S.; Turbiez, M.; Neher, D.; Koster, L. J. A. Competition between Recombination and Extraction of Free Charges Determines the Fill Factor of Organic Solar Cells. *Nat. Commun.* **2015,** *6*, 7083.
(51) Park, J.-W.; Shumaker-Parry, J. S. Strong Resistance of Citrate Anions on Metal Nanoparticles to Desorption under Thiol Functionalization. *ACS nano* **2015,** *9* (2), 1665-1682.
(52) Piris, J.; Dykstra, T. E.; Bakulin, A. A.; Loosdrecht, P. H. v.; Knulst, W.; Trinh, M. T.; Schins, J. M.; Siebbeles, L. D. Photogeneration and Ultrafast Dynamics of Excitons and Charges in P3ht/Pcbm Blends. *The Journal of Physical Chemistry C* **2009,** *113* (32), 14500-14506.
(53) Hodgkiss, J. M.; Albert‐Seifried, S.; Rao, A.; Barker, A. J.; Campbell, A. R.; Marsh, R. A.; Friend, R. H. Exciton‐Charge Annihilation in Organic Semiconductor Films. *Adv. Funct. Mater.* **2012,** *22* (8), 1567-1577.
(54) Proctor, C. M.; Nguyen, T.-Q. Effect of Leakage Current and Shunt Resistance on the Light Intensity Dependence of Organic Solar Cells. *Appl. Phys. Lett.* **2015,** *106* (8), 083301.
(55) Li, Y. Three Dimensional Solar Cells Based on Optical Confinement Geometries, *Springer Science & Business Media*, **2012**.
(56) Breitenstein, O.; Rakotoniaina, J.; Al Rifai, M. H.; Werner, M. Shunt Types in Crystalline Silicon Solar Cells. *Prog. Photovoltaics* **2004,** *12* (7), 529-538.
(57) Servaites, J. D.; Yeganeh, S.; Marks, T. J.; Ratner, M. A. Efficiency Enhancement in Organic Photovoltaic Cells: Consequences of Optimizing Series Resistance. *Adv. Funct. Mater.* **2010,** *20* (1), 97-104.
(58) Park, H. I.; Lee, S.; Lee, J. M.; Nam, S. A.; Jeon, T.; Han, S. W.; Kim, S. O. High Performance Organic Photovoltaics with Plasmonic-Coupled Metal Nanoparticle Clusters. *ACS nano* **2014,** *8* (10), 10305-10312.
(59) Salvador, M.; MacLeod, B. A.; Hess, A.; Kulkarni, A. P.; Munechika, K.; Chen, J. I.; Ginger, D. S. Electron Accumulation on Metal Nanoparticles in Plasmon-Enhanced Organic Solar Cells. *Acs Nano* **2012,** *6* (11), 10024-10032.
(60) Luque, A.; Hegedus, S. Handbook of Photovoltaic Science and Engineering, *John Wiley & Sons*, **2011**.
(61) Li, G.; Zhu, R.; Yang, Y. Polymer Solar Cells. *Nat. Photonics* **2012,** *6* (3), 153-161.

(62) Lu, L.; Zheng, T.; Wu, Q.; Schneider, A. M.; Zhao, D.; Yu, L. Recent Advances in Bulk Heterojunction Polymer Solar Cells. *Chemical reviews* **2015,** *115* (23), 12666-12731.
(63) Gupta, D.; Bag, M.; Narayan, K. Correlating Reduced Fill Factor in Polymer Solar Cells to Contact Effects. *Appl. Phys. Lett.* **2008,** *92* (9), 70, 093301.
(64) He, Z.; Xiao, B.; Liu, F.; Wu, H.; Yang, Y.; Xiao, S.; Wang, C.; Russell, T. P.; Cao, Y. Single-Junction Polymer Solar Cells with High Efficiency and Photovoltage. *Nat. Photonics* **2015,** *9* (3), 174-179.
(65) Zhao, F.; Dai, S.; Wu, Y.; Zhang, Q.; Wang, J.; Jiang, L.; Ling, Q.; Wei, Z.; Ma, W.; You, W. Single‐Junction Binary‐Blend Nonfullerene Polymer Solar Cells with 12.1% Efficiency. *Adv. Mater.* **2017,** *29* (18), 1700144.
(66) Collins, S. D.; Proctor, C. M.; Ran, N. A.; Nguyen, T. Q. Understanding Open‐Circuit Voltage Loss through the Density of States in Organic Bulk Heterojunction Solar Cells. *Advanced Energy Materials* **2016,** *6* (4).

Chapter 8

Conclusions and Future Work

In this dissertation, the coating of nanoparticles by polymer or metallic coatings for integration into both anti-reflection coatings (ARCs) and organic photovoltaics (OPVs) is examined. The coating layers induced dispersion, stability, and performance enhancements in both of the applications. Here, we present a summary of the conclusions and the potential future work for this area of research.

8.1 ENCAPSULATION OF SILICA NANOPARTICLES BY DIAZO-RESINS

8.1.1 Summary. The introduction of the covalent crosslinking reaction between diazo-resins (DAR) and poly(styrene sulfonate) (PSS) provides increased chemical stability in silica nanoparticle (SiO_2 NP) ISAM ARCs. The crosslinking reaction was first confirmed in pure DAR/PSS ISAMs. Upon UV-irradiation of the DAR/PSS films, the absorption peak of the diazonium group in DAR at λ = 380 nm disappeared, which signified the formation of covalent bonds between the two polyelectrolytes. Silica nanoparticles (SiO_2 NPs) were encapsulated in solution by DAR at an optimal concentration of 0.25 mM, to develop cationic modified SiO_2 NPs (MSNPs) with an average particle size of 96 nm. Two to four bilayer MSNP/PSS ISAM ARCs displayed excellent anti-reflection with transmittance and reflectance levels >98% and <0.2%, respectively and refractive indices from 1.25 – 1.26. The ARCs also possessed exceptional homogeneity, as confirmed by SEM. The UV crosslinking reaction between DAR on the MSNPs and PSS produced significant film chemical stability. The stability was confirmed by UV-vis spectrometry and AFM film analysis, after the films were exposed to a ternary solvent (H2O:DMF:ZnCl2, 3:5:2, w/w/w).

This work presents a simple encapsulation method that harnesses the covalent crosslinking properties of pure films into composite films. The encapsulation process can be used in other applications to prevent agglomerations and induce stability.

8.1.2 Future Work. Future work would involve further measure of induced stability within ARCs by the incorporation of DAR. First, the ISAM film design could be reconfigured as DAR/PSS/MSNPs/PSS quadlayers, to would ensure that more crosslinking polymer layers were present. Also, PAA could be a suitable substitute for PSS, which would exchange a weak polyelectrolyte for a strong polyelectrolyte, and allow for manipulation of the charge density by pH adjustments. Future films could also contain a stack of pure DAR/PSS ISAMs (5-10 bilayers) prior to the MSNP layers would support the adhesion and stability of the films. Finally, examination of the covalent bonding between DAR and polyanions would be confirmed by FTIR for different crosslinking conditions. Mechanical stability would also be quantified using the Triboindenter and macroscopic scratch testing methods employed in **Chapter 5**.

8.2 COVALENT CROSSLINKED PAH/PAA INTERLAYERS IN SILICA NANOPARTICLE ISAM ARCS

8.2.1 Summary. The incorporation of additional PAH/PAA bilayers into the original ISAM ARC design to make a covalently-crosslinked PAH/PAA/PAH/SiO_2 NP ISAM film significantly improved the mechanical stability without sacrificing the anti-reflection with appropriate selection of the PAA solution pH. The stability in ISAM films containing cationic PAH amine groups and anionic PAA carboxylate groups can be dramatically enhanced through thermal crosslinking (~200 ^{o}C) to form covalent amide bonding between the two polyelectrolytes. The thermal crosslinking reaction was first confirmed on pure PAH/PAA through FTIR. Next, the growth properties of pure PAH/PAA ISAMs were studied using ellipsometry for a manipulation of the PAA pH from 3.0 to

6.0. It was found that as the PAA pH was decreased from 5.6 to 5.4, the growth changed from linear to exponential, which was attributed to a decrease in polymer chain charge density and an increase in concentration of free, diffusing chains. As the PAA pH was decreased further, the exponential-growth slope continued to increase revealing an amplification of the effect.

PAH/PAA/PAH/SiO_2 NP quadlayer ISAM interlayers were then developed and examined with SEM. At higher PAA pH, the polymer chains had higher charge densities with less diffusion, so the SiO_2 NP encapsulations were thin and the NPs were tightly packed. However, with a decrease in PAA pH, the decreased polymer chain charge density and increased concentration of free, diffusing chains caused a dramatic increase in the encapsulation size (often more than one SiO_2 NP), but with increased void space as the NPs were not packed as tightly. At the lowest PAA pH of 3.0 (close to PAA's pK_a in the film), large-scale microporous polymer structures were present across the film. The 2 to 4-quadlayer interlayer ISAM ARCs were then analyzed by UV-vis spectrometry, and it was found that the anti-reflectivity remained excellent (transmittance ≈ 99%) as the PAA pH was decreased from 6.0 to 5.2. However, the anti-reflection rapidly degraded with a reduction of the PAA pH below 5.2 (similar PAA pH value for the crossover of linear to exponential-growth in PAH/PAA films). With a decrease in the PAA pH from 5.2 to 5.0, 4.0, and 3.0, the transmittance decreased from 99.22% to 96.95%, 95.39%, and 83.88%, respectively. The optical scattering and roughness both continuously increased with a reduction of the PAA pH below 5.2, while the thickness remained relatively independent of pH. From PAA pH of 5.2 to 3.0, the scattering slope and the roughness increased by a factor of 6 and 13, respectively. The thermally crosslinked ARCs were then scratch tested on both a microscopic and macroscopic scale to examine their mechanical robustness. A nanoindenter (Hysitron TriboIndenter) was used for microscopic scratch testing, and it was discovered that the critical load (L_{c1}) continuously

increased with a decrease in PAA pH. The increases in the L_{c1} were significantly more dramatic at lower PAA pH's. With a reduction of the PAA pH from 6.0 to 5.2 and 3.0, the L_{c1} increased by a factor of 7 and 23, respectively, which represents the massive difference in magnitude between the mechanical properties. For macroscopic scratch testing, a change in haze of the films after abrasion was used as the metric for mechanical robustness. A homemade abrasive rod setup was developed, and haze of the films was measured before and after abrasion. It was discovered that thermal crosslinking of the films improved the scratch resistance for all PAA pH's. Also, with a reduction in PAA pH, the change in haze after scratching was substantially reduced, which confirmed an increased scratch resistance of these films. For example, the change in haze after scratching for the crosslinked ARCs with PAA pH 6.0, 5.2, 4.0, and 3.0, was 128%, 56%, 3%, and 1%. The similar trends between the microscopic and macroscopic scratch testing methods confirmed the substantial changes in the mechanical properties with a variation of the PAA pH. The interlayer ISAM ARC with PAA pH 5.2 represented the optimal trade-off point between mechanical robustness and excellent anti-reflection.

This work presented the ability to include the stability-enhancing properties from pure polyelectrolytes into nanocomposite films. Also, this work shows how simple adjustments to conventional experimental properties, e.g. pH, can induce dramatic changes in properties to the nanocomposite film in terms of morphology, optical, and mechanical properties.

8.2.2 Future Work. Further exploration of this study would first involve the inclusion of amine groups directly to the SiO_2 NPs. ISAM films of aminopropyl-functionalized SiO_2 NPs and PAA could then be thermally crosslinked similarly to the interlayer ISAMs. Alternatively, SiO_2 NPs could be encapsulated by PAH in solution for fabrication of PAH-SiO_2 NPs/PAA ISAMs. Furthermore, investigation of the SiO_2 NP diameters may reveal improved scratch resistance at

different diameters. Next, the adhesion to the substrate could be augmented by the attachment of SAMs terminated by carboxylic acid groups, for thermal crosslinking between PAH. Also, a thick stack (5-10 bilayers) of PAH/PAA layers at pH 7 (to reduce optical scattering) prior to the formation of PAH/PAA/PAH/SiO_2 NP quadlayers could also improve the adhesion. Additionally, the pH of PAH and PAA could be manipulated together from 2.5 to 9.0 for the interlayer ARCs to determine any connection of the pH regimes to the optical or mechanical properties. Also, ellipsometry could be used more extensively to determine the void space and refractive index of the interlayer ARCs at different pH values. Finally, the exponential-growth could be more deeply investigated. In our study, the thickness of the interlayer ARCs remained relatively constant at all PAA pH's, since the SiO_2 NPs dominated the majority of the film, but it would be possible to determine more through QCM. Through QCM, we could study exponential increases in mass by the diffusion of free PAA chains. The diffusive properties in the interlayer film could also be studied through confocal laser scanning microscopy (CLSM).

8.3 SELF-ASSEMBLY OF THE OPV HOLE-TRANSPORT LAYER WITH SILVER NANOPLATES

8.3.1 Summary. This study focused on a new method of integrating plasmonic silver nanoplates (AgNPs) into the OPV hole-transport layer (usually spin-coated PEDOT:PSS) by the fabrication of ISAMs. Prior to delving into the primary study, the standard reference devices were first optimized to maximize the power conversion efficiency (PCE). First, the device annealing conditions were optimized, and it was found that post-annealing (annealing after the deposition of the Al cathode) lead to a 22% increase in the PCE, as well as generally increased all of the electrical properties of the devices. It was emphasized that low Al deposition rates ($\leq$ 2.5 Å/s) were necessary for favorable outcomes with post-annealing. The active layer thickness was next examined, and it

was found that a thickness of 100 nm consistently resulted in the best performance with an average short-circuit current density (J_{sc}) and PCE of -7.88 mA/cm^2 and 2.45%, respectively. Although greater thicknesses increased the overall optical absorption, they also caused a gradual decrease in both the shunt resistance (R_{sh}) and the fill factor (FF) due to heightened recombination.

The incorporation of AgNPs is a valuable approach to enhance the optical absorption, without manipulation of the active layer thickness. The synthesis of AgNPs was first thoroughly overviewed, along with tuning of the localized surface plasmon resonance (LSPR) wavelength by variation of the seed concentration. The positive charge of PAH and negative charge of citrate on AgNP allowed for the ISAM deposition of particles at a high density on glass with a strong visible color similar to the particle solution. To integrate the particles into the OPV devices, PAH/AgNP films were first successfully deposited onto the ITO anode, and the rest of the device was fabricated on top. However, spin-coating of the highly acidic PEDOT:PSS (the HTL material) over the AgNPs caused an immediate deterioration of the particles. Since the acidic properties of PEDOT:PSS were necessary for its electrical properties, a protective particle coating was absolutely critical. First, the HTL design was revamped as PAH/PEDOT:PSS ISAMs, and this reference HTL arrangement was first tested without AgNPs. It was discovered that a very thin layer of PEDOT:PSS (spin-coated at 8000 rpm) on top of the ISAM drastically improved the wettability of P3HT:PCBM, as a result of substantially decreased surface roughness (as found by AFM). Despite wettability improvements, the PAH/PEDOT:PSS ISAMs consistently had an overall higher sheet resistance than the standard PEDOT:PSS spin-coated layer. For instance, although the optical absorption (proportional to the amount of PEDOT:PSS) in the 30 bilayer PAH/PEDOT:PSS film was 48% greater than the spin-coated PEDOT:PSS, the sheet resistance for the 30 bilayer and the spin-coated film was 50 and 47 MΩ/□, respectively. The higher sheet

resistance caused a slight decrease in the OPV device performance, mainly due to the degraded series resistance (R_s) and FF. While simultaneously improving the reference ISAM HTL design, the encapsulation of the AgNPs by PAH (ENPs) was also examined, and it was found that a PAH concentration of 4 mM at pH 7 was optimal. Despite the successful creation of the ENPs, the particles were still damaged by the acidic PEDOT:PSS. Next, gold was epitaxially grown onto the AgNPs edges (AuAgNPs) at an optimal ratio of Au:Ag 0.06:1, which displayed excellent resistance to the exposure of sulfuric acid. PAH/AuAgNP ISAMs were then fabricated on ITO for the OPV devices, and the ISAM layers finally displayed PEDOT:PSS etching resistance, as well as drastically enhanced the optical absorption of the active layer. For example, the one- and three-bilayer PAH/AuAgNP ISAM films enhanced the optical absorption by 15% and 18%, respectively. Although OPV device performance for one bilayer of PAH/AuAgNP was marginally lower than the reference device (1.33% and 1.15% PCE for reference and one bilayer of PAH/AuAgNP ISAM, respectively), the J_{sc} was improved by 15%, which signified the optical absorption enhancement of the active layer. Finally, PEDOT:PSS was included as an ISAM layer with the AgNPs, and PAH/PEDOT:PSS/PAH/AuAgNPs ISAMs were fabricated onto the ITO anode. Although the AuAgNPs displayed etching resistance and the active layer absorption improvements, the OPV device performance was again degraded by 32 – 37% from the reference devices. Regardless, the three-quadlayer PAH/PEDOT:PSS/PAH/AuAgNPs ISAMs in OPV devices exhibited equivalent shunt and series resistances to the reference devices, which suggested their potential with further tuning.

Although none of the approaches explored were able to show increases in the PCE of the OPV devices, this study presents a unique method for developing the HTL primarily from ISAM deposition. The techniques used can be expanded on for fabrication of entire OPV devices purely

from ISAMs. Furthermore, we introduce insight on the methodology for the encapsulation of AgNPs by PAH, significant for a range of plasmonic applications. Finally, the acidic etching resistance of gold-coated AgNPs in exposure to PEDOT:PSS is thoroughly demonstrated, which can surely be applied to future studies.

8.3.2 Future Work. Continuation of this work would first involve the investigation of the PEDOT:PSS ISAM layer thickness. By using a higher concentration PEDOT:PSS solution for the ISAM layers, increased PEDOT:PSS thicknesses could potentially counteract the insulating PAH layers. Besides increased PEDOT:PSS thickness, the cationic PAH layers can be simply replaced with a conductive cationic polyelectrolyte layers such as polyaniline (PANI). Additionally, the ENP processing could be substantially improved upon, such as removal of the excess citrate from the original AuAgNP solution and slow addition of the particles to a concentrated PAH solution. The ENPs could then be thoroughly examined by TEM to inspect the polymer coverage. Successful coverage of the AuAgNPs by PAH would enable ENP/PEDOT:PSS ISAMs, in which both PEDOT:PSS and the AuAgNPs would be extensively distributed throughout the HTL. For all of the HTL ISAM methods, the work function and charge transport (charge carrier mobilities) properties would be deeply examined in order to build a comparison with the conventionally spin-coated PEDOT:PSS layer. Finally, favorable light scattering effects created by the AgNPs in the HTL could also be investigated.

8.4 POLYSTYRENE-COATED SILVER NANOPLATES IN OPVS

8.4.1 Summary. The inclusion of AgNPs into the OPV devices involved the spin-coating of polymer-functionalized particles between the active layer (P3HT:PCBM) and the Al cathode. Other than the addition of AgNPs, the rest of the OPV device fabrication methodology was unchanged from the reference devices. This study systematically investigated the effects of

polymer brush coatings on the AgNP spin-coated dispersion properties at the active layer. The AgNPs were functionalized separately with poly(ethylene glycol) methyl ether thiol (PEG-SH) (PEG-AgNPs) and thiol-terminated polystyrene (PS-SH) (PS-AgNPs) brush coatings, and these were compared to unfunctionalized AgNPs as a control. AgNPs were synthesized with an LSPR peak wavelength in the range of 485 – 507 nm in order to closely couple with the peak optical absorption of the active layer. All three AgNP types were dispersed into various solvents for spin-coating, and methanol (MeOH) was chosen because possessed the highest vapor pressure while also being compatible with all of the functionalization types. The spin-coated density on the film was readily controlled by the AgNP solution concentration. For the unfunctionalized AgNPs and the PS-AgNPs, the concentration was varied from 0 to 2.90 nM, while for the PEG-AgNPs, the concentration was altered from 0 to 22.40 nM. SEM revealed that the spin-coated unfunctionalized and PEG-AgNPs clustered into large aggregates, attributed to incompatible interactions between the hydrophilic functionalization and the hydrophobic P3HT:PCBM. Differently, the hydrophobic PS-AgNPs dispersion on P3HT:PCBM was dramatically more homogeneous with uniform surface coverage. Regardless of the functionalization, all AgNPs exhibited some level of active layer optical absorption enhancement that scaled with the AgNP solution concentration and surface density. However, the absorption enhancements by PS-AgNPs were significantly greater than the two other AgNP types. Furthermore, the unfunctionalized AgNPs resulted in detrimental photoluminescence (PL) quenching of P3HT, whereas the insulated PS-AgNPs induced elevated PL intensities. When incorporated into OPV devices, the unfunctionalized and PEG-AgNP deteriorated the performance for all particles concentrations, correlated to charge trapping at the aggregate-induced defects and voids. Contrastingly, the addition of PS-AgNPs at low concentrations resulted in substantial performance improvements over the reference OPV devices.

At an optimal PS-AgNP concentration of 0.57 nM, the PCE increased by 32% over reference devices.

This study shows that appropriate polymer layers can provide both the essential insulation and dispersion properties on the plasmonic nanoparticles when used in OPV devices. Here, the systematic evaluation of coating composition to produce favorable deposition interactions can be applied to many different fields of study. The work highlights a simple, yet effective method of spin-coating particles to integrate them into OPVs, which can be used in virtually any PV technology.

8.4.2 Future Work. Future work could involve examination of the polymer concentration and molecular weight on the AgNPs. In relation to this, the AgNP edges would be meticulously analyzed by TEM to determine the polymer thickness to assist in the understanding of the LSPR effects. Additionally, the "graft-from" method could be utilized to synthesize polymer chains directly onto AgNPs, to further control the brush density and maximize the insulation.